Understanding the fluid pathways that control the Navan ore body

Brett John Davidheiser-Kroll

Doctor of Philosophy

Scottish Universities Environmental Research Centre
College of Science and Engineering
University of Glasgow

September 2014

DECLARATION

The material presented in this thesis is the result of research carried out between October 2011 and October 2014 at the Scottish Universities Environmental Research Centre College of Science and Engineering, University of Glasgow.

Under the supervision of

Professor Adrian Boyce

and

Darren Mark

This thesis is based on my own independent research and any published or unpublished material used here is given full acknowledgment.

Brett John Davidheiser-Kroll

Adrian J. Boyce

Darren F. Mark

Abstract

This work is focused on carbonate-hosted base metal deposits in the Irish midlands with emphasis on the Navan ore deposit, County Meath, Ireland. The Irish ore deposits were created by the mixing of two fluids, a metal-bearing fluid and a sulfur-rich brine. Herein I aim to further the understanding of the creation, movement, and mixing of these two fluids and how they created the giant Zn and Pb deposit at Navan, as well as how post-ore genesis fluids are recorded in the rocks around Navan.

The first chapter contains a summary of current knowledge and views of the deposit, local lithologies, structures, and mineralization.

The second chapter is original work that examines how metal distribution patterns and 3D meshes of the paleo-surfaces can yield insights into the movement of mineralizing fluid during ore genesis. This work builds on previous work over the many years the mine has been operating. This new work shows the spatial variability in Pb and Zn concentrations and ratios and interprets these values with respect to vertical and horizontal fluid flow. It also builds on the work of others to interrogate the extent to which a major paleo-erosion event and surface has affected the mineralization found above and below this surface. This has significant bearing for the future of exploration in the area.

The third chapter is original work that contains new noble gas data from Navan and deposits across Ireland that elucidate the temperature and tectonic setting that drove the metal bearing fluid that made the Irish midlands so well-endowed in base metals. Sulfides from every major carbonate-hosted base metal mine in Ireland were crushed to release noble gases trapped in fluid inclusions, which had retained $^{3}He/^{4}He$ signatures from the time of mineralization *ca.* 350 Ma. These $^{3}He/^{4}He$ ratios indicate a small but clear contribution of mantle-derived ^{3}He, which reveals that mineralization occurred during an extensional event that introduced heat from the mantle.

The fourth chapter is original work based on new $^{40}Ar/^{39}Ar$ geochronological results that constrain the timing of a later fluid flow event caused by the Variscan compression that inverted the local basin. This inversion event created large wrench and reverse faults and has greatly complicated the local lithology and metal extraction. The timing of this inversion event was interrogated by analyzing the $^{40}Ar/^{39}Ar$ systematics of disturbed feldspars along a large reverse fault. The 293 ± 3 Ma minimum age produced represent the first radiometric age of the Variscan compressional event in central Ireland and confirms the long held assumption that these faults are related to this large scale tectonic event.

The fifth and final chapter is a combination of original and recently published work from others. It focuses on a newly discovered area of mineralization several km to the south of Navan. Mineralization, fluid inclusions, and the structural setting of this new area are evaluated and compared to ‘typical’ Navan mineralization. The new area was created by hotter hydrothermal fluid and did not mix with the surface fluid as effectively as the main deposit.

Table of contents

Figures

Tables

Acknowledgements

Over the course of my PhD and life in Glasgow and Navan, many people have helped make my time fruitful and enjoyable. I would first like to thank Tara Mines and Boliden for their financial support and understanding that Glasgow University and I would make a great fit to further the knowledge of the Navan deposit. While spending the last three years pursuing my PhD, my interactions and experiences can be neatly divided between SUERC and Tara mines.

The types of knowledge and interactions at SUERC have been defined by trying to answer scientific questions with the help of isotopes and mass spectrometers. While attacking the many dead ends and final pathways of my PhD, I have had the great fortune of learning from some of the very best. I have had the great pleasure of learning from my two advisers. Adrian Boyce has always been extremely enthusiastic, helpful, and willing to allow me sufficient latitude to pursue problems I found interesting. He was always willing to work on a problem and put forward the resources necessary to try and tackle them. Darren Mark has been a great sounding board for crazy ideas, mass spectrometry, editing, figures, as well as drawing the lines of what could and could not be done. His willingness to help and efficiency in doing so were a tremendous asset to my time at SUERC.

I have had the pleasure of using many pieces of equipment and interacting with a large number of people at SUERC. I would like to thank Andrew Tait for his helpfulness and endless troubleshooting of both computer and vacuum lines problems that I have dragged him into over the last few years. Thanks as well to Terry Donnelly for his endless knowledge of vacuum lines and parts, and for his willingness to drop what he was doing to help me with whatever problem or trouble I had created. Without Andrew and Terry I would know far less about how and why the instruments we use work and are created, and I would certainly have had less fun over the last three years. I would also like to thank Alison McDonald for her constant helpfulness with running sulfur samples and always looking out for both the safety of my samples and myself. If I continued on this way I would fill several pages of thanks to the many people who have helped me, so I will list a few who have been especially helpful: Julie Dougans, Fin Stuart, Rob Ellam, Jason Newton, Philippa Ascough, Dan Barfod, Ben Cohen, Tracey Doogan, Nicole Doran, Luigia Di Nicola, Ross Dymock, Valerie Olive, Vincent Gallagher, Anne Kelly, Jim Imlach and Robert McLeod. As I have been at SUERC the number of PhD students has gone from just two of us to a roomful of eight students. Being in an office full of a dedicated and multidisciplinary group has been a pleasure, if not always the most

conducive to productivity. Thanks to Domokos Györe, Ana Carracedo Plumed, Sevasti Modestou, Piotr Jacobsson, Kieran Tierney, and Jessica Bownes.

For the 171 days I worked and lived in Navan, Ireland, I had the great pleasure of interacting with the Tara mines staff, academics, and geological consultants working on Navan. While at the mine site Jim Geraghty took great pleasure in asking tough questions and applying doubt while working hard to make sure that I was able to access the information and resources I needed to get any particular job done. The other members of staff, Eugene Hyland, Finn Oman, Paul McDermott, Archie Watts, Eammon Brady, Matthew Walker, Gerry Kelly, and Dessie O'Brien were always helpful getting data, rocks, pints, rides to work, underground visits, lunch, core samples, water samples and helping with the many avenues that I have meandered on my journey. I would like to thank them all for making my job easier and enjoyable.

The Tara mines exploration office became my second office during my PhD. Rob Blakeman was a constant figure during my time with Tara, explaining simple things like the difference between marcasite and pyrite, or that one should not touch melanterite, to pondering the location of the sulphuretum within the Navan system. I am grateful for the many decisions and debates that Rob and I had and believe that they have helped test many of the ideas put forward in this thesis. My bungalow office was always well-neighbored by Rowan Lee and Simon Huleatt and their down-to-earth views on geology and exploration. Gráinne Byrne's igneous perspective was helpful, and nights out with Paul Henry and Gráinne were always pleasant. Brendan O'Donovan, Imelda McGroggan, and Natasha McWalter were ever helpful with maps, databases, hotels, tea time and the general oddities of an exploration department. Richard Vetters, John Harrington and Brian Cosgrove never grumbled over my need to access core that was invariably at the bottom of a palate in a mud puddle and were nicer then they had any need to be.

While working at Tara mines exploration department I was fortunate to interact with and learn from two great geology consultants: David Coller and Mike Philcox. David's knowledge of faults and intense push to deliver motivated me to keep my ideas grounded and always improving. The many hours spent with Mike in the core shed and at our dinners proved him to be a great mentor on how quality observations are the best way to drive geological interpretations.

Working on her own contemporaneous PhD, which I often called my sister PhD, Freya Marks and her work on the halo to the Navan deposit gave another perspective into the same system. The many other students, Mike Treloar, Simon Large, Sean Johnson,

Humphrey Knight, Alexander Gillespie, Megan Nugent, Olivia Chant and Chris C, passed though Tara while I was coming and going. Their questions, projects, and insights were helpful in always keeping the big picture and the many things left unknown in perspective. I would also like to thank Jamie Wilkinson for taking time to share his knowledge on carbonates and fluid inclusions.

Lastly from Tara mines I would like to thank John Ashton for a great many things. Firstly my personal life was greatly simplified by his effort to secure from Boliden a fully-funded PhD for me based at the University of Glasgow. I would also like to thank him for his no-nonsense management that mixed a healthy level of skepticism with quick understanding of a useful new thought.

I would like to thank Philippa Ascough for removing any stress before my viva with her work as my convener. I would like to thank Iain McDonald for taking time out of his busy schedule to give this work the time and effort it needed to be fully vetted.

I would like to thank Tony Fallick who was just retiring as I came to SUERC but still found time to spark great questions and give his pragmatic and knowledgeable thoughts on some tough questions. Tony was also generous enough to agree to read my thesis and give many useful and intelligent comments on this thesis.

Thanks Mom, Dad, Sis and Bro.

Lastly I would like to thank Leah Morgan. She has been my partner in crime for over nine years and the drive behind my continued education. She may be the only person to have read every word of this thesis, and without her editing and copy editing this document would be much harder to read and full of spelling mistakes. It is safe to say that without her daily reminder of how to be driven, scientific, and rebound from setbacks, I would never have completed this PhD.

Chapter 1

Introduction

1 Introduction

The world uses Zn and Pb for many industrial processes. These important elements are usually found as sulfide minerals, mainly galena (PbS) and sphalerite (ZnS), in three major types of deposits: volcanogenic massive sulfide (VMS), stratiform sedimentary exhalative (SEDEX), and Mississippi Valley Type (MVT). Irish type deposits form a smaller subset of these base metal deposits, as they do not clearly fall into one of these three groups. This study focuses on the sources, timing and pathways of fluids involved in the ore genesis of sulfide minerals in the Irish orefield, and particularly the Navan orebody. The three types of deposits are described in detail below, followed by descriptions of the stratigraphy, structure, and mineralization found at Navan. The chapter is completed by a short introduction to the isotopic methods used herein.

1.1.1 Volcanogenic massive sulfide (VMS)

Volcanogenic massive sulfide (VMS) or volcanic hosted massive sulfide (VHMS) deposits can vary, but they mainly consist of Cu-Zn deposits with minor Pb and Au. These deposits are usually formed on the seafloor by hydrothermal fluids related to volcanic activity. The timing of ore genesis for VMS deposits is related to the time of emplacement of the volcanic body from which the metals and heat to move the fluids were derived.

Black smoker hydrothermal vents are thought to be modern analogues to VMS deposits (Francheteau et al., 1979). Black smokers can be found in every major ocean as well as in the Mediterranean Sea. They are produced by cold sea water descending into the basement, being heated by volcanic activity, then stripping metals from the surrounding rocks along their ascent to the surface (Scott, 1997). This process is shown by the relationship between metal ratios found in various deposits with metal ratios present in surrounding basement

rocks. As the fluids vent to the seafloor, they mix with seawater (Webber et al., 2011) and create chimneys that are dominated by sulfates (anhydrite and barite), but also contain significant amounts of sulfides (zinc and copper-rich sulfides along with minor but widespread iron sulfides) (Styrt et al., 1981).

Comparisons of active and non-active vents show that the vents have distinct mineralogies, suggesting that mineralogical reordering occurred shortly after cooling (Styrt et al., 1981). The Cyprus Cu-Zn deposits in the obducted ophiolites of the Troodos Massif represent the best example of mid-ocean-ridge (MOR) VMS deposits (Figure 1.1). Field relationships show that venting occurred through pillow basalts (Constantinou and Govett, 1973). Some have suggested that VMS deposits are generally found along extensional faults off the main spreading axis and are likely related to secondary intrusions (Eddy et al., 1998). Many VMS deposits also form in non-MOR tectonic settings such as back arc basins, greenstone belts, and island arc environments. For example, the Kuroko deposits in Japan formed in an island arc setting and have distinctly more Zn than other VMS deposits due to the felsic nature of the surrounding basement rocks (Robb, 2009).

Whilst a conceptual model, including driving mechanisms and metal sources is well understood the source of sulfur for VMS deposits has been debated. One view is that the sulfur is thermochemically reduced from seawater sulfate prior to venting on the sea floor (Robb, 2009, Roberts et al., 2003). This is supported by the presence of a 17‰ offset (the maximum possible thermochemical fractionation is 20‰) in $\delta^{34}S$ in VMS sulfide deposits compared with seawater sulfate (see sulfur isotope section below) through time (Large, 1992). Modern-day seafloor chimneys from black smokers have a typical isotopic range of 0-4‰ in $\delta^{34}S$ (Robb, 2009) that could represent either magmatic sulfur or the reduction of seawater sulfate from the present value of +21‰ (Rees et al., 1978). VMS deposits exhibit well-developed vertical and horizontal metal zonation of Cu-Pb-Zn-Ba, in that order, with distance from the feeder vent (Velasco et al., 1998).

VMS deposits differ from Irish type deposits in their association with volcanic rocks, low quantities of Pb, and in the nature of their host rocks (igneous rather than sedimentary).

1.1.2 Stratiform sedimentary exhalative (SEDEX)

Stratiform sedimentary exhalative (SEDEX) deposits can be larger and higher grade than VMS deposits and include more than half of the world's exploitable Pb and Zn (Robb, 2009). They are believed to be created when hydrothermal fluids are exhaled onto the seafloor, carrying metals that are precipitated as sulfides. Many very large and high-grade deposits are characterized as SEDEX, including the Australian H.Y.C, Broken Hill, Mt. Isa, and Century, as well as the North American Howards Pass, Sullivan and Red Dog deposits.

SEDEX deposits are typically hosted in marine clastic or chemical sediments in intracratonic rift basins and are not directly associated with volcanic rocks. There is a correlation of SEDEX deposits with failed rift systems (Goodfellow, 2004). The Red Dog deposit in Alaska has been well dated by Re-Os geochronology to show that the main stage sulfides are synchronous with rifting (Morelli et al., 2004). Many deposits contain thin volcanic ashes interbedded within the sedimentary sequence, suggestive of regional volcanism, such as the Rammelsberg (Germany) massive sulfide deposit (Large and Walcher, 1999). SEDEX deposits are often hosted in basins with evidence for synsedimentary extension, high heat flow and some magmatism, hydrothermal alteration, and large quantities of hydrothermal sediments (Goodfellow, 2004). SEDEX deposits show conformable discrete lenses of syngenetic or early diagenetic replacement in interlayered barren or scarcely mineralized sediments. These mineralized beds show gradual but distinct metal zoning and thicken towards the feeder vent (Goodfellow, 2004).

Approximately 20% of SEDEX deposits have feeder vents and altered footwall rocks present and represent the classical exhalative model. The remainder are found distal

to vent structures (Sangster and Hillary, 1998) and are thought to occur where dense brines vent onto the seafloor, move downhill in turbidity currents, and deposit synsedimentary metals at a location distal to the hot feeder (Sangster, 2002). The existence of interlayering is considered by many as diagnostic of an exhalative feature. Others, however, debate this, preferring to interpret these textures as fine-scale replacement of individual beds (Leach et al., 2010). When syngenetic mineralization interbedded with the host rock occurs, ore genesis can be dated by the timing of deposition of the host rock.

It was originally proposed that the Irish deposits are a subset of the SEDEX deposits (Russell, 1978). However it was later realized that the majority of mineralization in Irish deposits was likely deposited sub-seafloor and replaced existing lithologies, and only a minor portion of the mineralization was likely precipitated on the seafloor (Anderson et al., 1998, Ashton et al., in press), which presents a fundamental distinction to the classic SEDEX deposit.

The best modern analogues for SEDEX deposits are the Red Sea and the Salton Sea in the Gulf of California rift system. The Salton Sea was created over a two-year period when engineers lost control of an irrigation canal tapping the Colorado River. The influx of water on the actively extending salt plain created brines that began leaching metals from depth and re-precipitating them at surface, consistent with models proposed by Russell et al. (1981). This occurrence has given workers an insight into to the type of brines thought to create SEDEX deposits and has shown the importance of chlorine complexes in metal migration (Helgeson, 1965, Skinner et al., 1967). The Red Sea, another modern analogue, is a young rift that is host to many seafloor vents, VMS, and SEDEX deposits. The occurrence of both SEDEX and VMS deposits in a single tectonic regime indicates that they represent a continuum of deposit types. SEDEX deposits form in cooler areas distal to the volcanic centers, whereas VMS deposits form closer to the volcanic centers (Pirajno, 2008).

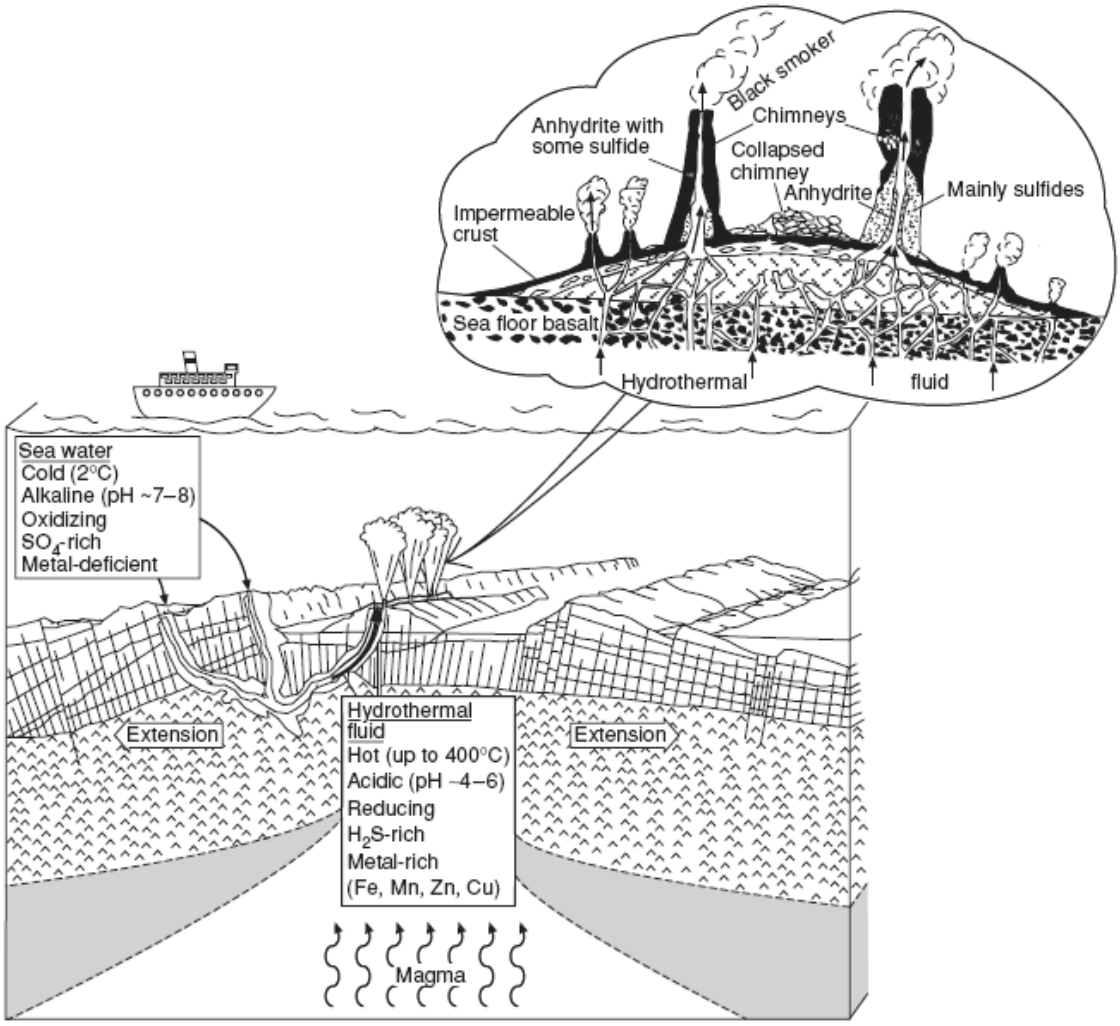

Figure 1.1. A cartoon of VMS deposition at a mid-ocean ridge setting. The hydrothermal fluids are derived from seawater scavenging metals from the basement. The driving force of heat from the magma pushes them to the surface (Robb, 2009).

1.1.3 Mississippi Valley Type (MVT)

Mississippi Valley Type (MVT) deposits are the third major type of sediment-hosted Pb and Zn deposits and occur worldwide. The group has many shared characteristics, but the classic style is defined by deposits in the Tri-State district in the United States (Ohle, 1959).

MVT deposits are not associated with potential sources of heat or metals from igneous rocks (Leach et al., 2005, Ohle, 1959). They have simple mineralogy consisting of Pb + Zn ± Ba and sparse fluorite (fluorite is rarely noted in SEDEX deposits, and has no recorded occurrence in the Irish type deposits), while lacking Cu as well as precious metals. MVT deposits form from cool (50-150 °C), high salinity (> 15% NaCl equivalent) brines that contain considerable quantities of SO_4^{2-}, CO_2, CH_4 and other heavy organic molecules (Gize and Barnes, 1987). They are typically hosted by limestones and are stratabound in structurally high areas around the margins of large basins (Ohle, 1959). Host rocks are often brecciated, suggestive of either pre-existing karst features or dissolution by the ore-forming fluid during metal deposition (Anderson, 1983.).

The favored model for MVT emplacement involves brine fluids that are driven hundreds of kilometers through regional aquifers by heavy rainfall on topographic highs created during collisional events (Leach et al., 2001, Rickard et al., 1975) (Figure 1.2). In this model, the timing of ore deposition is disconnected from the deposition of the host rocks, and is rather thought to be related to the supercontinent cycle and collisional tectonic settings (Leach et al., 2010) (Figure 1.2). MVT deposits have proven difficult to date directly because there has been not been an isotopic decay system to directly date the main stage mineral phases present (Sangster, 1983). However efforts have been made to date MVT deposits by dating the associated mineralogy or the effects of a passing fluid. Some examples include U-Pb on calcite and feldspars (Goldhaber et al., 1995), Rb-Sr on sphalerite (Nakai and Halliday, 1990), fission track on zircon or apatite (Ravenhurst et al., 1994), and paleomagnetic techniques (Symons et al., 1996). Each of these dating methods

is limited in scope but results have been used to tie MVT ore genesis events chronologically with supercontinent cycles and collisional events rather than the depositional age of the host rock (Leach et al., 2001).

The metals found in MVT deposits are thought to be leached from the aquifer during fluid migration. The conditions under which metals are dissolved and held in stable solution within the ore-forming fluid have long been debated (Ohle, 1959). The cold and chloride-complexing nature of the fluids is thought to play a major role in maintaining stability of the metal ions. The fluids, however, are thought to be oxidizing (Anderson, 1975), and the high oxidation state of the fluids limits the amount of sulfide that can be carried by the primary ore fluid (Cooke et al., 2000). This then requires either mixing or reduction of sulfate to sulfide prior to precipitation of the metals.

Some authors divide all base metal deposits into groups based on their host rocks. Dividing deposits this way creates a clastic-dominated (CD) group and a MVT group based on passive-margin host lithologies (e.g., carbonates) (Leach et al., 2010). This grouping would place all Irish type deposits in the MVT group, contrary to those who consider the Irish deposits to follow the SEDEX model (discussed above). Many workers who favor the MVT model in the Irish Orefield have considered the Hercynian Orogeny evident in southern Ireland as a potential collisional event to drive fluids via topographic flow (Hitzman and Beaty, 1996, Hitzman, 1999, Johnston, 1999, Peace et al., 2003). This implies that the mineralization event postdates deposition of the host lithologies, that mineralization occurred in a compressional environment, and that topographic fluid flow from a highland source was the major driver of fluids, rather than convection due to heat.

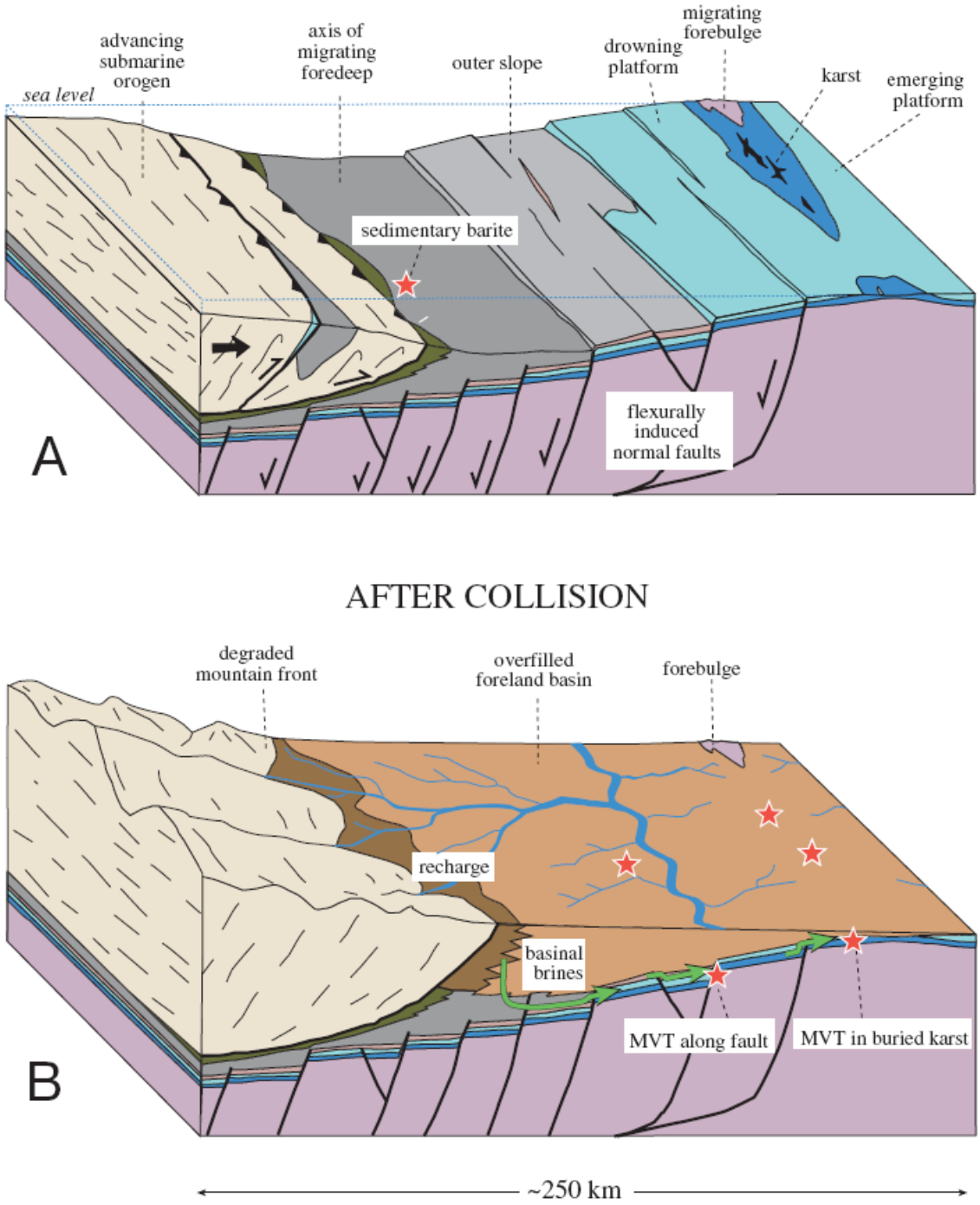

Figure 1.2. A block model showing the creation of MVT host rocks (A), followed by the driving mechanism for fluid flow and location of MVT deposits (B) from Leach et al. (2010).

1.1.4 Irish type deposits

The Irish type ore deposits are not readily grouped into any single deposit type and thus are often categorized in a separate group (Figure 1.3). The Irish deposits are alike in that they are hosted in Carboniferous-age carbonates, formed by the action of cool high-salinity fluids (>15%NaCl, <200°C), have distinct source isotopic signatures, display evidence for precipitation from two sources of sulfur, and are located in the hanging wall of extensional faults. They vary in textures, stratigraphic position, range of fluid temperatures (within 70-200°C), size, and grade. Some are hosted as cavity-fills within the Waulsortian Limestone (Boast et al., 1981), others are found stratigraphically below this unit and fill areas between the Waulsortian Mudbanks (Taylor, 1984), and one is primarily hosted hundreds of meters below the Waulsortian in the Navan group (Ashton et al., in press). A new, recently discovered area in Limerick, however, does not fit the standard Irish type ore deposit, due to its association with diatreme volcanism (Elliot et al., 2013).

There has been much debate over the origin of fluids that created the Irish ore deposits, with many supporting an MVT model (Hitzman, 1999, Hitzman and Beaty, 1996, Johnston, 1999, Leach et al., 2001, Leach et al., 2010, Peace and Wallace, 2000, Peace et al., 2003, Symons et al., 2002) and others a SEDEX model (Altinok, 2005, Andrew and Ashton, 1985, Andrew and Ashton, 1982, Ashton et al., 1992, Ashton et al., 1986, Ashton et al., 2003, Ashton et al., in press, Bischoff et al., 1981, Blakeman et al., 2002, Boyce et al., 1983a, Coller et al., 2005, Davidheiser-Kroll et al., 2014, Dixon et al., 1990, Elliot et al., 2013, Fallick et al., 2001, Ford, 1996, LeHuray et al., 1987, Mills et al., 1987, O'Keeffe, 1986, Russell et al., 1981, Wilkinson et al., 2003). The difference between these two models is significant and is based the timing and tectonic setting of metal deposition. These differences are important because they greatly affect exploration methods used to identify and exploit these deposits (Blakeman, 2002, Leach et al., 2001). In Chapter 3, I present data that indicate an extensional tectonic setting, and thus strongly support the extensional model for the Irish orefield.

The Navan deposit is the largest known of the Irish type deposits and is located at the northern end of the Irish Midlands. It contains over 110 Mt of ore at ca. 8% Zn and 2% Pb (Ashton et al., in press), with 97% of the ore hosted in Carboniferous shallow-water carbonates and the remaining 3% hosted in a Chadian polymictic debris flow (Ford, 1996). Metals were leached from the basement by a sulfide-poor oxidizing hydrothermal fluid (Bischoff et al., 1981, Wilkinson et al., 2009). This metal-rich, sulfide-poor fluid mixed with a lower temperature sulfur-rich brine to cause the precipitation of sulfides within the carbonate host (Andrew and Ashton, 1982).

This study focuses on several elements of Irish type ore deposits, including the pathways, sources, and timing of fluids involved in the ore genesis of sulfide minerals in the Irish orefield, and particularly the Navan orebody. Fluid pathways are investigated in Chapter 2 using metal zoning patterns and 3D lithological maps. Chapter 3 uses He isotopic signatures to show that source fluids for the Irish orefield were derived from an extensional tectonic environment. The timing of the most recent hot fluid to pass through the Navan area is determined by results presented in Chapter 4. Finally, a recently discovered area near the Navan orebody is explored in Chapter 5 and compared with the main deposit at Navan.

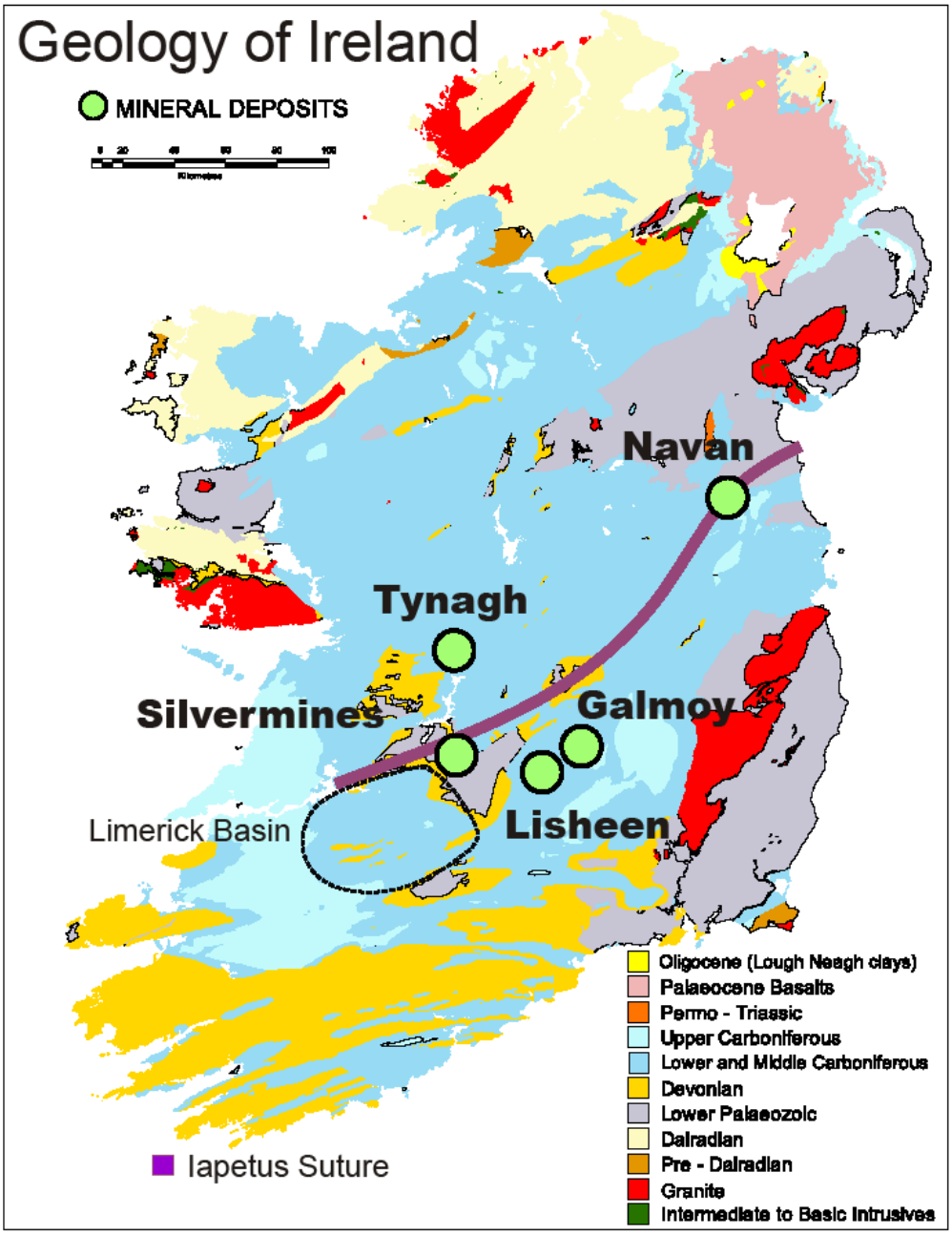

Figure 1.3. Map of Ireland with names of mines. From Davidheiser-Kroll et al. (2014).

1.2 Stratigraphy of the Navan area

1.2.1 Lower Paleozoic

The oldest rocks found in the Navan area are lower Paleozoic in age. These rocks are an amalgamation of terrains that are delineated by lithologies, deformational and metamorphic histories, as well as by faunal ages and provinciality (Murphy et al., 1991). Navan sits on the Navan Fault, which forms the boundary between the Central Terrane and the Grangegeeth Terrane.

1.2.1.1 The Lonford-Down Central Belt

The Longford-Down Central Belt is north of the Navan Fault and outcrops to the northwest of Navan. This terrane is comprised of a variety of intermediate volcanics and epiclastic interbedded with carbonaceous shales (Murphy et al., 1991).

1.2.1.2 The Grangegeeth Terrane

The Grangegeeth Terrane is composed of Ordovician to Silurian rocks which outcrop in a wedge, beginning at Navan and increasing in size to the east, ending in the sea at Clogherhead (Murphy et al., 1991). The Grangegeeth continues beneath the Navan deposit and is bounded to the north by the Navan Fault and to the south by the Slane Fault (Murphy et al., 1991). The oldest member of the Grangegeeth Terrane is the Ordovician Slane Group, which is composed of tuffs and intercalated lavas, and is capped by a basaltic group (Romano, 1980). Unconformably overlying the Slane Group is the Grangeeth Group. This group is composed of three formations: the lowest, which contains volcanic conglomerates with rounded fragments suggestive of significant reworking (Romano, 1980), and two upper units which begin as sandstone and become massive >400m thick shales capped by laminated mudstones with thin, well-bedded volcaniclastic beds (Romano, 1980). The whole of the Grangegeeth is believed to be Caradocian in age, which is well constrained by a large number of fossils such as graptolites (Romano, 1980).

1.2.2 Palaeozoic Stratigraphy

1.2.2.1 Navan Group

1.2.2.1.1 Brownstown Fm (Old Red Sandstone)

Uncomformably above the Grangegeeth Terrane is the Courceyan age Brownstown Formation, which is locally known as the Old Red Sandstone. The Brownstown Formation is a fluvial deposit of conglomerates, sandstones and mudstones. The facies vary laterally and are thought to be indicative of a braided riverbed setting (Mallon, 1997). The thickness of this unit in the Navan area ranges from 0 to 40 m. It thickens to the south, with the thickest area in the Munster Basin (Andrew and Ashton, 1985) (Figure 1.4). The metal source is thought to be predominantly Caledonian granites based on their proximity and lead isotopic values (Everett et al., 2003).

1.2.2.1.2 Liscartan Formation (The Mixed Beds)

1.2.2.1.2.1 Portanclogh Member (The Laminated Beds)

The Portanclogh Member is 40 m thick in the Navan area with a sandier base of carbonates and an upper portion with massive mudstones and Ca-rich silts. Its thinly bedded nature gives the member its local mine name of the Laminated Beds. The paleoenviroment is consistent with a shallow tidal and wave-influenced environment (Strogen et al., 1990). There is evidence for occasional periods of sub-aerial modification. This is expressed in keystone vugs (Inden and Moore, 1983) as well as a chalcedonic silica layer interpreted as a paleo-anhydrite deposit (Ashton et al., 1986).

1.2.2.1.2.2 Bishopscourt Member (Muddy Limestone)

The Bishopscourt Member is defined by the first dark grey calcareous mudstone above the Portanclogh Member. The member is 15-20 m thick at Navan and is composed of a grey nodular bioturbated silty and peloidal wackestone with mud wisps (Strogen et al., 1990) and occasional oncolytic bioclastic micrites and syringopora corals (Blakeman, 2002).

There are some micro-conglomerates that eroded though the Bishopscourt and into the Portanclogh (Anderson et al., 1998). The top of the sequence indicates open-marine conditions with the presence of stenohaline fauna (Strogen et al., 1990).

1.2.2.1.3 Pale Beds

The Pale Beds are a regionally extensive thickly bedded oolitic and bioclastic limestone with thinner interbedded packstones, dolomites, calcareous sandstones, thin shale-silt layers and micrites (Philcox, 1984). The Pale Beds are also known as the Meath Formation (Strogen et al., 1990). Locally to Navan, the base of the Pale Beds is consistently a clean, pale grey, 'birds-eye' micrite that varies in thickness from 3 to 80 m (Andrew and Ashton, 1985). Higher in the unit, the Pale Beds become sandier with more argillaceous interlayers. Several of the more distinctive sandy and argillaceous layers are used as marker horizons. These marker horizons vary in nature but not in stratigraphic position across the Navan area (Ashton et al. in press). There are many instances of erosive channeling through the Pale Beds succession that suggest variable sea levels during deposition (Anderson, 1990, Anderson et al., 1998). The Pale Beds are thought to indicate a quiescent to shallow shelf environment (Ashton et al. in press).

1.2.2.1.4 Shaley Pales

The Shaley Pales are thought to represent a deeper water facies represented by interbedded bioclastic sandstones, siltstones, shales and bioclastic dark shales (Philcox, 1984, Philcox, 1989). The Shaley Pales are found allochthonously within the Navan area and are then called the Shaley Pales Trough. The Shaley Pales are also known as the Moathill Formation.

1.2.2.2 The Argillaceous Bioclastic Calcarenite (ABC) Group

The Argillaceous Bioclastic Calcarenite (ABC) Group is composed of two members: the Argillaceous Bioclastic Limestone and the Waulsortian Limestone. The Argillaceous Bioclastic Limestone (ABL) is a well-bedded crinoidal argillaceous limestone that

diachronously transitions into the Waulsortian mudbank facies limestone (Ashton et al., in press). In the Navan area the Waulsortian varies from crinoidal flank facies to well-developed mudbank facies. The ABC group is predominantly found to the NW of the Liscartan Fault but is also present above the SW extent of the deposit. Although the Waulsortian is very important in hosting mineralization in all other Irish deposits, there is no known mineralization of the ABC group in the Navan area.

1.2.2.3 The Boulder Conglomerate

The Boulder Conglomerate is formed of high energy debris flow material that has been deposited above a Chadian age erosional unconformity that cuts across the Navan area (Boyce et al., 1983a) (Figure 1.5). This definition allows for conformable interbedding with the overlying Thinly Bedded Unit (see Fingal Group) as well as the unit's clear succession of multiple debris flows (Ashton et al., 1992, Ford, 1996). The Boulder Conglomerate beds are unsorted to poorly sorted with clast sizes ranging from tens of meters to sand-sized (Ashton et al., 1986). The Boulder Conglomerate varies in thickness across the deposit from less than a meter to tens of meters and is composed of material from the Pale Beds, the Shaley Pales, and the ABC group, as well as the occasional mafic rock (Ford, 1996). The matrix is generally formed of dark crinoid-bearing argillaceous material. The source and flow direction of the Boulder Conglomerate is thought to be from the north to south west (Ashton et al., in press; M.Philcox pers. comm.).

1.2.2.4 Fingal Group

The Fingal Group is locally known as the Upper Dark Limestones (UDL), with the lowermost section being called the Thinly Bedded Unit (TBU). The TBU consists of a series of well-bedded turbiditic calcarenites and thin dark mudstones (Strogen et al., 1990, Altinok, 2005). The TBU is thickest in areas where the erosion has cut deeply into low stratigraphy. In some areas, Boulder Conglomerate can be found interbedded with TBU. Above the TBU is the Boudin Mudstone Unit that is composed of graded calcarenites, Ca-

rich silts and unfossiliferous black mudstones (Philcox, 1989). The boudins are believed to have been created by soft sediment slumping on unstable slopes and have been demonstrated to onlap onto the shoulders of paleotopographic highs (Philcox, unpublished; Walker, 2004). Above the Boudin Mudstone Unit, the UDL becomes a series of deep water, low energy calcarenites and mudstones (Philcox, 1989, Altinok, 2005). Within this fill sequence there are many marker horizons identified by Philcox (1989). The UDL represents the highest lithology preserved in the Navan area.

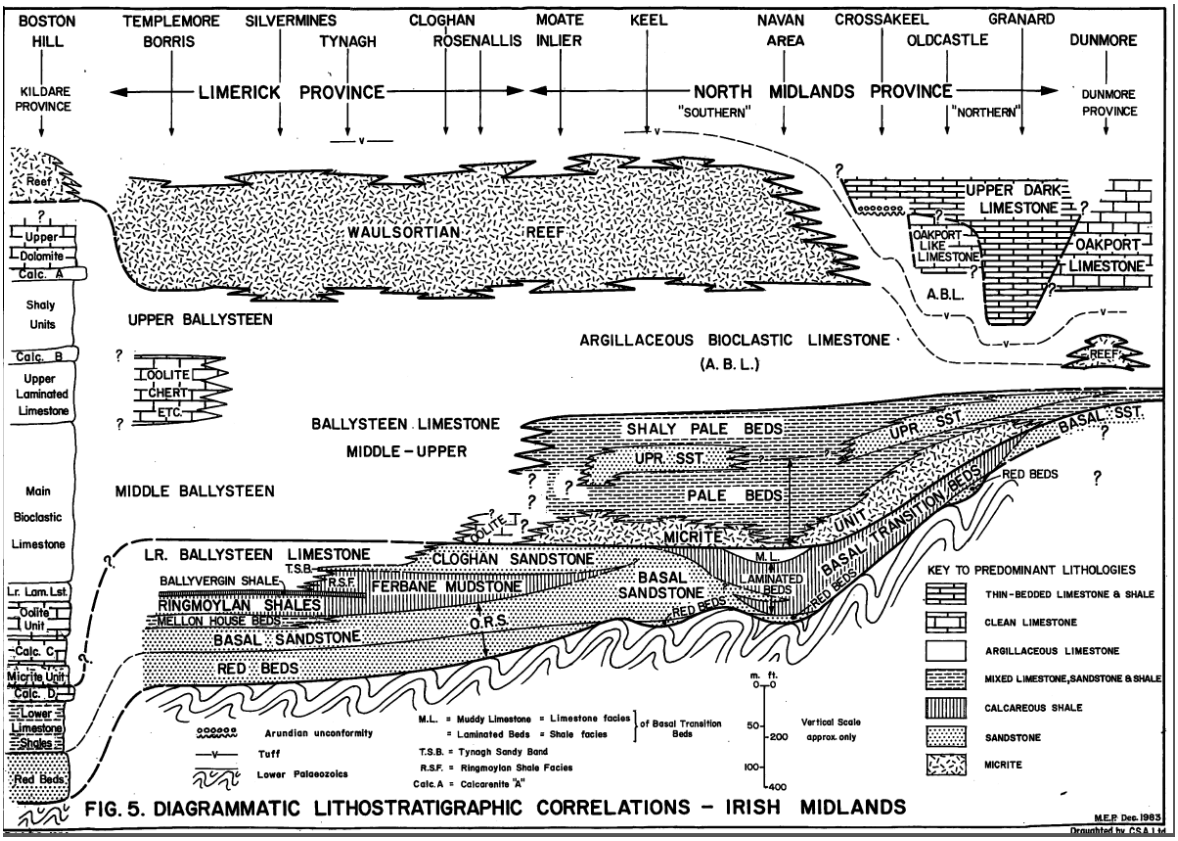

Figure 1.4. Stratigraphic column across the Irish midlands, showing the thinning of the Red Beds to the north and the thinning of Waulsortian Limestone. Taken from Philcox (1984).

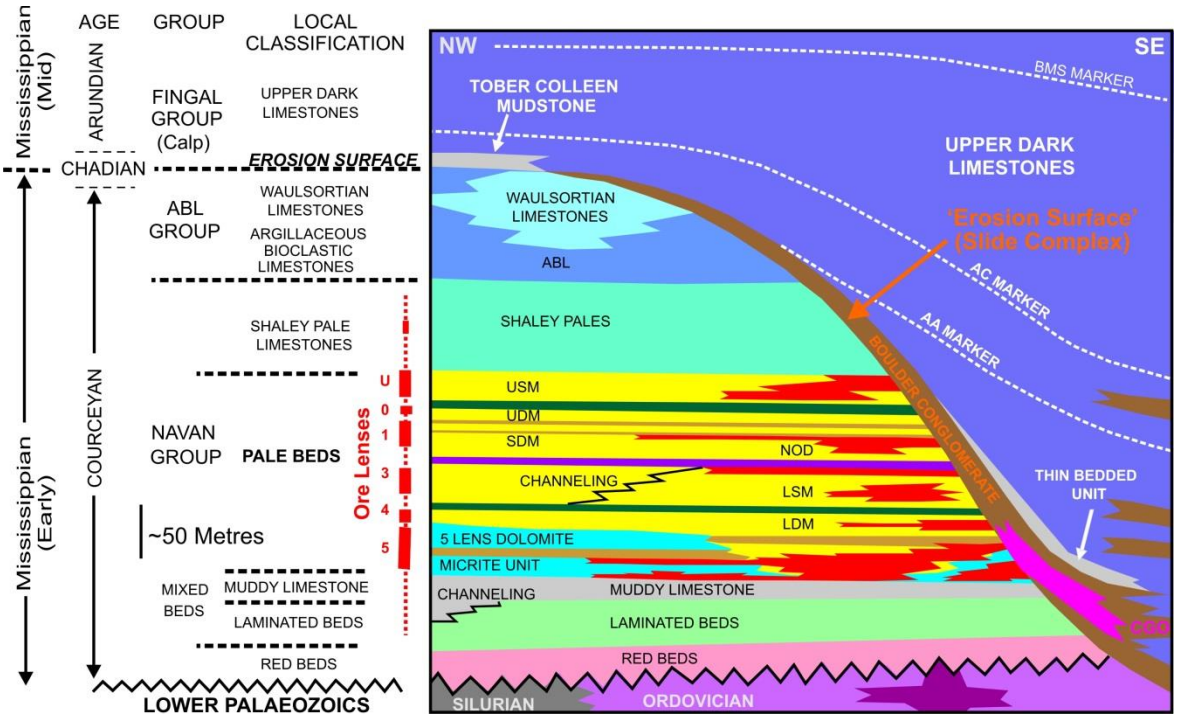

Figure 1.5. A stratigraphic cartoon of the Navan area. Note the erosion surface created in the Chadian cuts deeper into stratigraphy to the SE. From Ashton et al., (in press).

1.3 Structure

The structures in the Navan area were created in three distinct tectonic events: the suture of Laurentia and Avalonia, the extensional rifting that created the Dublin basin, and the inversion created by the Hercynian orogeny.

1.3.1 Basement structures

Avalonia and Laurentia were cratonic blocks with distinct histories. Prior to their collision during the northward subduction of the Iapetus under Laurentia, Andean-type volcanism created Ordovician to Silurian volcanic and volcanoclastic rocks that covered the southern side of Laurentia (Strachan, 2012). The final closure of the Iapetus ocean created an accretionary prism, with the Laurentian block overriding the Avalonian, but very little other tectonic deformation occurred (Woodcock, 2012b). Shortly after closure, regional sinistral strike-slip faulting caused up to 10 km of displacement on individual faults within the suture area (Strachan, 2012). The precise location of the Iapetus suture is difficult to trace in many parts of the British islands, but it can be well-constrained in eastern Ireland and is believed to exist under the Navan area (Vaughan and Johnston, 1992). Drilling into basement below the Navan Group reveals that the immediate basement is composed of volcanic, volcanoclastic, and sedimentary rocks, which are likely part of the accretionary wedge from the Laurentian block (Gillespie, 2013). This history of accretion, collision, and strike-slip faulting likely created many deep-seated structures that remained as crustal weak zones. The basement rocks at Navan are simply called the Lower Paleozoics (LP) regardless of their composition and are readily identified by their low-grade metamorphism, which gives them a glossy sheen.

1.3.2 Normal faults

The oldest faults within the Pale Beds are the two major synthetic NW-dipping normal faults on opposing sides of the orebody that define a topographic high. The northwestern of these, the Liscartan (L) Fault, has 200 m of displacement and was likely active during the

deposition of the ABL group, based on the thicker sequences found on the down-thrown side (Ashton et al., in press). The second of these faults, which defines the SE side of the South West Extension (SWEX) and likely the main orebody (now obscured by inversion faults, as described below), is known simply as the E Fault (Figure 1.6). The E Fault shows more displacement (>500 m) than the L Fault and because of this it has created a boundary between the Pale Beds and basement rocks to the southeast known as the "E Fault Horst" (Ashton et al., 2003). Along the SWEX the succession expected to be present on top of the horst has been completely removed by the erosional event; currently UDL rocks lie conformably on the horst. Within the footwall of the E fault (the NW side) there are several branches that accommodate the large amount of displacement. The largest of these subparallel faults is known as the E Fault Branch, which bounds a complex mixture of Pale Beds and is important to local mineralization. The E and L Faults have similar strikes and timings and may represent a non-breached ramp relay with the orebody situated on the ramp (Ashton et al., in press). Ramp relays are created when faults are not fully aligned and accommodate differential displacement between faults. Regardless of the ramp relay structure, the large normal E and L Faults are similar to faults found at other Irish orebodies.

Between the E and L faults in the proposed relay ramp there are many SE and NW dipping normal faults (named F-X, where X is a number, Figure 1.6). These anastomosing faults vary in size and their maximum displacements and propagate to different heights in the stratigraphy. The SE-dipping faults tend to be larger and can extend up to the ABL. These faults have an extensive fracture network that is generally oriented in a NE-SW direction.

1.3.3 SE-dipping normal faults and listric faults

In the proposed relay ramp between the E and L faults there are two long (ca. 2.5 km) synthetic faults named the B and T Faults. These faults are thought to have been planar normal faults that transitioned to listric normal faults. The displacement along these faults

varies but ranges up to 120 m, with decreasing throws to the northeast. Neither of the faults propagates above the erosion surface, but in some areas the thickness of the Boulder Conglomerate increases on the hanging wall side.

To the southeast of the B and T faults are the listric Y, M, and N Faults (Figure 1.6). These faults are thought to have formed during the transition of the B and T Faults from planar normal faults to listric faults. These listric faults displace and rotate the Pale Beds to varying degrees along their strike. In the hanging wall of these faults, above any displaced Pale Beds, there are beds of allochthonous Shaley Pales and ABL units (Philcox, 1989). These allochthonous units are overturned and are believed to have been transported from the immediate north (Philcox, 2013).

The SE-dipping P Fault is a large (>5 Km) normal fault that is situated east of the E Fault and defines the eastern side of the E Fault Horst. The P fault displaces the BC and UDL, representing large amounts of movement after the Chadian erosional event. Whether the P fault was active during or before the Chadian is difficult to ascertain. The P Fault has seen major inversion and likely merges with the D fault to the northeast (see below).

The last phase of faulting at Navan is compressional. This phase involves the A, C, D, Randalstown (R), and Castle (CS) Faults. These faults have varying degrees of reverse (80 – 200 m) and dextral wrench (500 - 800 m) movements that significantly complicate the stratigraphy, especially in the NE of the main mine (3 zone, see below for zone descriptions). This compression is thought to be Variscan in age, but this has not previously been demonstrated conclusively; this question is addressed in Chapter 4.

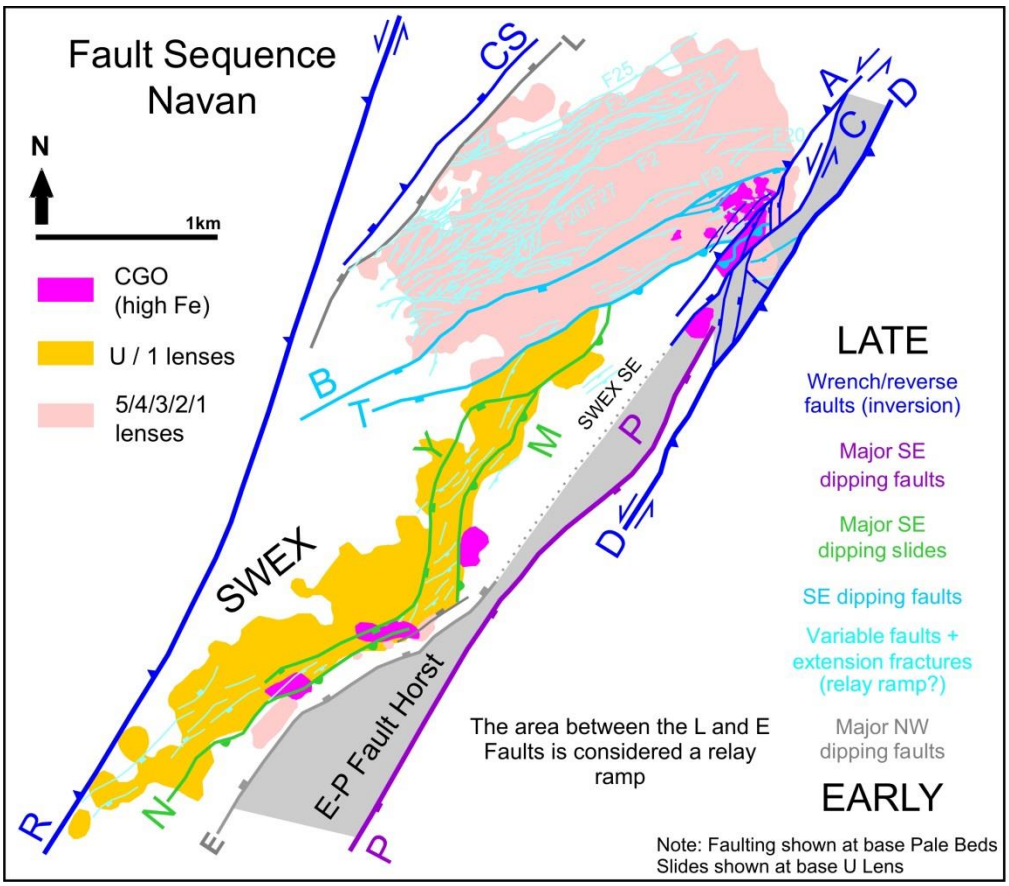

Figure 1.6. Structures in the mine area colored by type and timing, overlying the outline of mineralized areas. From Ashton et al. (in press).

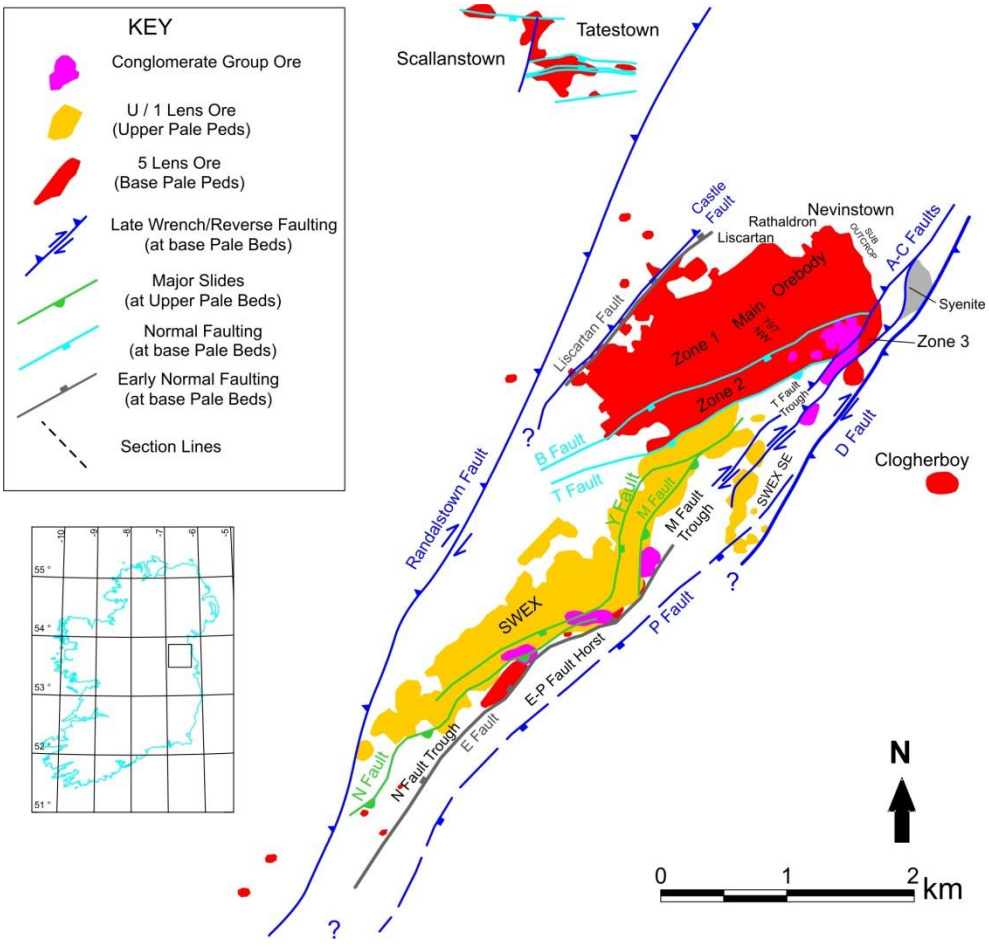

Figure 1.7. Simplified map of mine areas modified from Ashton et al. (in press).

1.4 Mineralization

1.4.1 Mineralogy

Mineralization at Navan consists predominantly of sphalerite (ZnS) and galena (PbS), with a respective ratio of ca. 4:1. Some silver is recovered from the mill, which is believed to be associated with small inclusions of tetrahedrite and pyragyrite and is associated with galena and in areas of low Zn/Cd ratios (Steed, 1980). Antimony sulfosalts, mostly boulangerite, are found as dense lamellae in galena and rarely as individual grains associated with galena (Huhtelin, 1994, Steed, 1980).

The majority of gangue minerals are barite, calcite and dolomite. Pyrite and marcasite abundances vary across the deposit, with pyrite being far more common. Pyrite varies vertically with increasing amounts in the higher stratigraphic horizons. Pyrite represents a major gangue mineral in the Conglomerate Group Ore (>20%) and is also present within the lower UDL (Altinok, 2005, Ashton et al., 1992, Ford, 1996).

1.4.2 Locations

The majority of the mineralization is present within the base of the Pale Beds. Distinct marker beds are used to divide the Pale Beds stratigraphy into 6 units. These units are known as lenses and are labeled stratigraphically from highest to lowest starting with U, followed by 0,1,2,3,4 and 5 (Figure 1.5). Stratigraphically overlying the Pale Beds is mineralization hosted within the Shaley Pales, Boulder Conglomerate and lower UDL (Figure 1.6). The Shaley Pales and UDL mineralization is low-grade and sub-economic, while areas of the Boulder Conglomerate are higher-grade and can be economically extracted.

The deposit is also divided into three geographic zones based on the major listric normal faults (Figure 1.6). Zone 1 is comprised of the area to the NW of the B fault; zone 2 is the smallest area and is bound by the B and T faults; and zone 3 is located to the SE of the T fault and in the NE of the deposit east of the major reverse A fault (Figure 1.7).

These vertically differentiated lenses and horizontally differentiated zones yield a method of naming mineralization by location and stratigraphy. The convention is to name a region by "zone - lens", so mineralization found to the east of the A fault (3 zone) at the base of the Pale Beds (5 lens) would be called the "3-5 lens". The mineable mineralization found within the Boulder Conglomerate is sufficiently distinct that it is called Conglomerate Group Ore (CGO) to differentiate it from Pale Beds Ore (PBO).

The Navan ore body is divided on a larger scale into the main mine, the South West Extension (SWEX), Tatestown/Scallanstown, and Clogherboy (Figure 1.7). The areas of Tatestown/Scallanstown and Clogherboy are small satellite occurrences of mineralization that have not yielded economic-grade ore. The SWEX, on the other hand, has proven to represent a large resource that has been exploited since the early 2000s (Ashton et al. 2003). The SWEX is found SE of the T fault and thus is wholly within the 3 zone; mineralization is largely hosted within the 1 Lens. The main mine is comprised of zones 1 and 2 as well as a small portion of zone 3 in the NE of the deposit (see Figure 1.7), and the majority of mineralization within the main mine is contained within the 5 Lens (the lowest lens). The zonation and grade of areas within the main mine and the SWEX are discussed in Chapter 2.

Exploration in areas near the Navan mine has been ongoing and achieved varying degrees of success. Most recently, a new area showing considerable promise has been located to the southeast of the SWEX and has been named the South West Extension-South or SWEXS (Figure 5.1). This area is described in detail for the first time in Chapter 5.

1.4.3 Textures of mineralization

The relatively simple mineralogy is confounded by the complex and varied textures found at Navan. The majority of textures are fine-grained, with grains rarely larger than 2 mm. The majority of mineralization appears to be filling open spaces following dissolution or

fracturing of the carbonate host lithology. The open-space textures present at Navan include cross-cutting veins, dendritic-skeletal, stalactitic, internal sediment, geopetal, breccia, disseminated, and coarse-bladed forms (Anderson et al., 1998, Anderson, 1990). There are replacement textures that range from destructive granular styles to delicate pseudomorphs of bioclasts such as bivalves. The textures of mineralization within the Boulder Conglomerate are distinct and dominated by massive to semi-massive bands of iron sulfides with minor sphalerite and galena. The minor sphalerite and galena can be found in delicately-laminated fabrics, cross-cutting veinlets and irregular ramifying patches (Ashton et al., 1992). The Boulder Conglomerate also contains clasts of mineralized Pale Beds that are thought to have been mineralized prior to transport (Ashton et al., 1992, Blakeman et al., 2002). Layered pyrite and shale are present within in the UDL and the Boulder Conglomerate. The new SWEXS area also displays these textures (see Chapter 5).

1.4.4 Fluid inclusions

Fluid inclusions are trapped bubbles of fluid within a mineral that are thought to represent the fluid at the time of capture. Fluid inclusions at Navan are relatively rare and small, making inclusions studies limited and difficult. However, due to their power to yield temperature and compositional constraints on the fluids responsible for mineralization, many studies have been conducted (Braithwaite and Rizzi, 1997, Everett and Wilkinson, 2001, Knight, 2012, Peace, 1999, Peace et al., 2003, Treloar, 2014, Wilkinson, 2010). These studies were conducted on transparent dolomite, calcite, sphalerite and barite.

There are two main categories of fluid inclusions at Navan: a high temperature, low salinity fluid (100-140 °C, 5-10 wt.% eq. NaCl), and a low temperature, high salinity fluid (70-100 °C, 20-25 wt.% eq. NaCl) (Figure 1.8) (Wilkinson, 2010). The low T fluid is thought to represent an evaporitic brine and is more prevalent in late stages of paragenesis. The high T fluid is thought to represent the hydrothermal metal-bearing fluid, while intermediate values likely represent mixing between these end members (Wilkinson et al.,

2005a). The high T, low salinity fluid at Navan is less saline and lower temperature than the other Irish deposits, a feature that is not fully understood (Wilkinson, 2010). Recent work in the SWEXS has shown evidence of boiling in the form of halite crystals and three-phase inclusions (Figure 16 Treloar, 2014). These inclusions from the SWEXS record temperatures that are 30-70°C higher than those of the main mine or the SWEX (Figure 1.8). Treloar (2014) used the temperatures and salinities to calculate an apparent paleo-boiling depth of ca. 100 m below sea level.

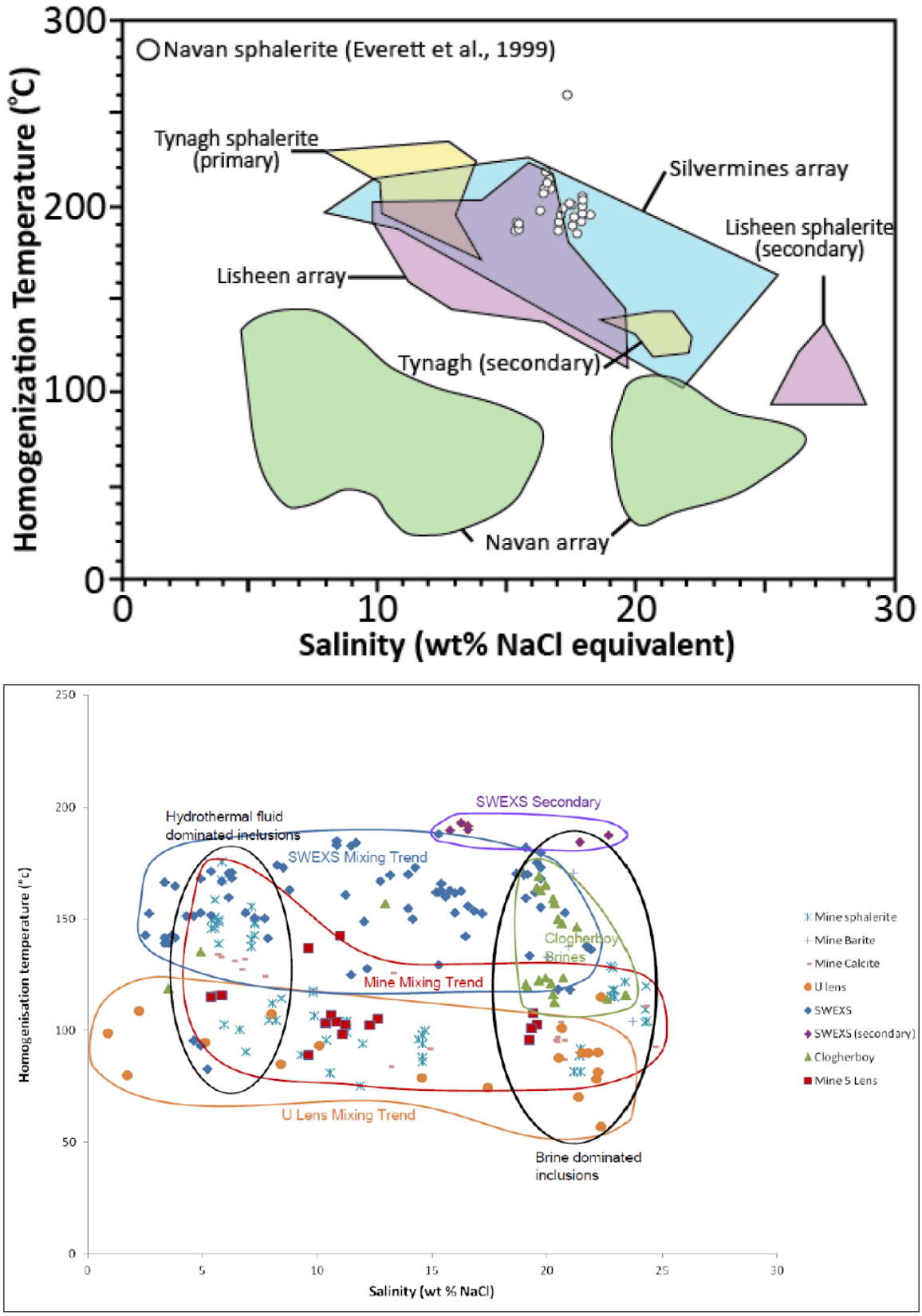

Figure 1.8. Fluid inclusion data for Navan and other deposits in the Irish ore field. Data were aggregated from Everett and Wilkinson (2001), Everett et al. (1999) and Mike Treloar (2014).

1.4.5 Isotopic methods

Isotopes are atoms of differing masses of the same element, formed by the addition or subtraction of neutrons. Because neutrons lack a charge, the addition or subtraction does not greatly affect the chemical properties of the element although there are subtle quantum mechanical effects. However the change in mass does create the possibility for fractionation, the process of separating or concentrating isotopes based on some property (mass, spin etc). One major form of isotope fractionation is mass dependent fractionation. Mass dependent fractionation is caused by the fact that different isotopes behave slightly differently because of their mass. For example, in a molecule the strength of the chemical bond to a given atom will be different for a light isotope compared to a heavy isotope. The isotopically different molecules can have different reaction rates. Also, in a gas a molecule containing the light isotope will move faster than the same chemical species containing the heavy isotope for a given kinetic energy as explained by $E_k = \frac{1}{2}mv^2$, where E_k is the kinetic energy, m is the mass, and v is the velocity. Another example of mass dependent fractionation occurs when biological metabolisms prefer one isotope over another, typically the lighter one. These and other stable isotope fractionation effects can be created by differences between isotopes in bond strength, rates of movement, and preferences in enzymatically-controlled biological processes (Chambers and Trudinger, 1979).

Some isotopes are not stable and will radioactively decay to different elements or isotopes; those created from these radiogenic processes are called radiogenic isotopes. The rate of this decay varies depending on the stability of the isotope, which is apparent in its half-life ($t_{1/2}$), or decay constant (λ), which are related by the equation $\lambda=\ln(2)/t_{1/2}$. Decay follows the exponential function: $N_t = N_o e^{-\lambda t}$ where N_t is the quantity of the parent isotope at time t, λ is the decay constant, and N_0 is the initial quantity of parent isotope, i.e. the quantity at time $t = 0$.

1.4.5.1 Sulfur isotopes

Sulfur has four stable isotopes of ^{32}S, ^{33}S, ^{34}S, and ^{36}S, with ^{32}S and ^{34}S having the major abundances at 95.03% and 4.2%, respectively. The low abundances of ^{33}S and ^{36}S, 0.75% and 0.017% respectively, make routine measurements difficult. The sulfur isotopes typically measured are ^{34}S and ^{32}S; the ratio of these is expressed in permil (‰) as $\delta^{34}S_{sample} = [(R_{sample}/R_{std}) - 1)] \times 1000]$, where $R = {}^{34}S/{}^{32}S$. The values expressed in $\delta^{34}S$ are relative to an international standard, Canyon Diablo troilite, which has been defined as 0‰. Larger values of $\delta^{34}S$ are often referred to as "heavy," while smaller or negative values are referred to as "light."

Sulfur isotopes clearly illustrate the mixing and precipitation of Navan mineralization. The two main fluids involved in the Navan mineralizing system are a hydrothermal metal-bearing fluid and an evaporite-derived brine. The oxygenated hydrothermal metal-bearing fluid is sulfur-poor. The sulfur that is present is relatively enriched in SO_4^{2-} over H_2S and is isotopically heavy, at $\delta^{34}S$ = 10-15‰. The evaporite-derived brine contains both seawater sulfate (SO_4^{2-}) and bacteriogenically-derived H_2S from the same seawater sulfate source. The seawater sulfate (SO_4^{2-}) is isotopically heavy ($\delta^{34}S$ = 20-25‰) where it has been measured in local barite. The H_2S is isotopically lighter than the sulfate by ca. 40‰, having been reduced from sulfate to sulfide by sulfate-reducing bacteria. Thus the hydrothermal fluid and the evaporate-derived brine have distinct and distinguishable sulfide isotopes.

The isotopic analysis of a sulfide mineral within the Navan area can thus reveal the sulfur source. Sulfide from the hydrothermal fluid is present close (within a few meters) to feeder faults and related fractures, while the bacteriogenic sulfide dominates the majority of mineralization (>90% by mass) (Blakeman et al., 2002, Fallick et al., 2001) (Figure 1.9). It has been shown that some textures tend to have isotopically heavy or light sulfur values (Anderson et al., 1998, Anderson, 1990, Gagnevin et al., 2014) (Figure 1.10). The bulk of Boulder Conglomerate- and UDL-hosted ore have been shown to have exceedingly light

values (ca. -35‰) and are thought to have precipitated from sulfur that has been metabolized by sulfate reducing bacteria multiple times (Ford, 1996). For this process to work, the seawater sulfate must be fractionated during reduction by bacteria, only to be reoxidized by some means, and then again bacterially reduced and fractionated. More recently it has been shown that some species of sulfate reducing bacteria can fractionate sulfide by up to 76‰ from the original sulfate (Sim et al., 2011). The presence of these species of bacteria could reduce or remove the need for reoxidation of the sulfide. Values within the CGO have been shown to increase up-section, which has been explained by variations in the availability of sulfide in the water column (Altinok, 2005).

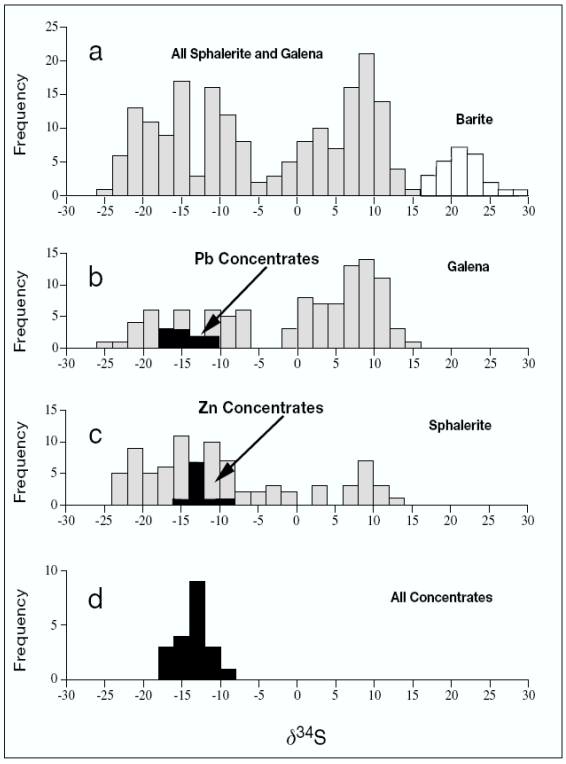

Figure 1.9. A histogram with $\delta^{34}S$ in sulfides from drilled and lasered samples shown in gray and $\delta^{34}S$ from bulk mine concentrates shown in black. The presence of distinct sulfur sources is evident from the bimodal distribution of individual samples (a,b,c), however concentrate data from the entire mine (d) indicates the bacteriogenic endmember (isotopically light) is dominant. Extracted from Fallick et al. (2001).

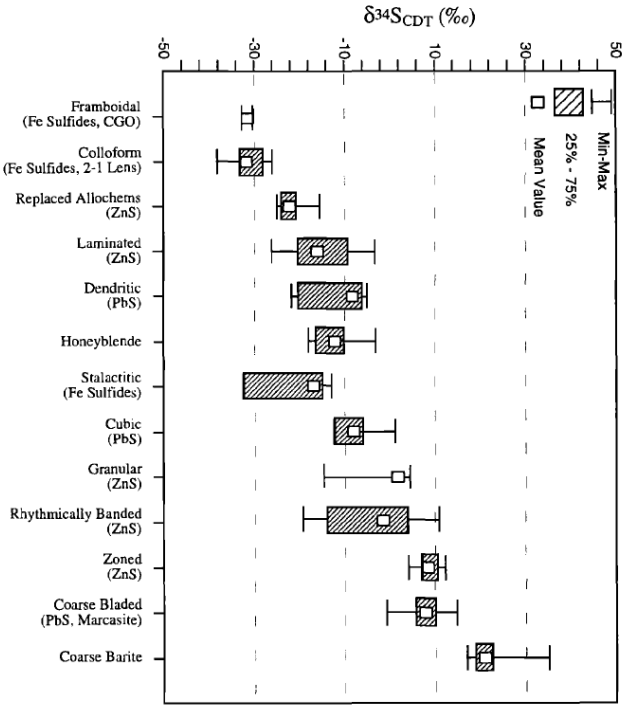

Figure 1.10. $\delta^{34}S$ values for sulfides from Navan with varying minerals and textures, extracted from Anderson et al. (1998).

1.4.5.2 Lead isotopes

Lead has four stable isotopes ^{204}Pb, ^{206}Pb, ^{207}Pb and ^{208}Pb. However ^{206}Pb, ^{207}Pb and ^{208}Pb are the radiogenic daughter products of ^{238}U, ^{235}U, and ^{232}Th respectively. Given differences in $t_{1/2}$ of the parent isotopes, Pb isotopic ratios can change with time. This ingrowth of heavier isotopes has created geographical "isoplumes" that become less radiogenic to the northwest (O'Keeffe, 1986). The Pb isotopes within each Irish deposit are homogeneous and are related to their position over the Lower Paleozoic basement (Caulfield et al., 1986, LeHuray et al., 1987). Some workers have suggested that $^{206}Pb/^{204}Pb$ varied vertically within the deposit and showed a changing source of over time (Mills et al., 1987). However later authors suggest that this earlier work did not identify true basement signatures but instead measured the addition of older detrital Pb (Dixon et al., 1990) (Figure 1.11). It has since been shown that bulk Pb values from Navan mill concentrate yield the best average value, which also matches that of the basement (Fallick et al., 2001).

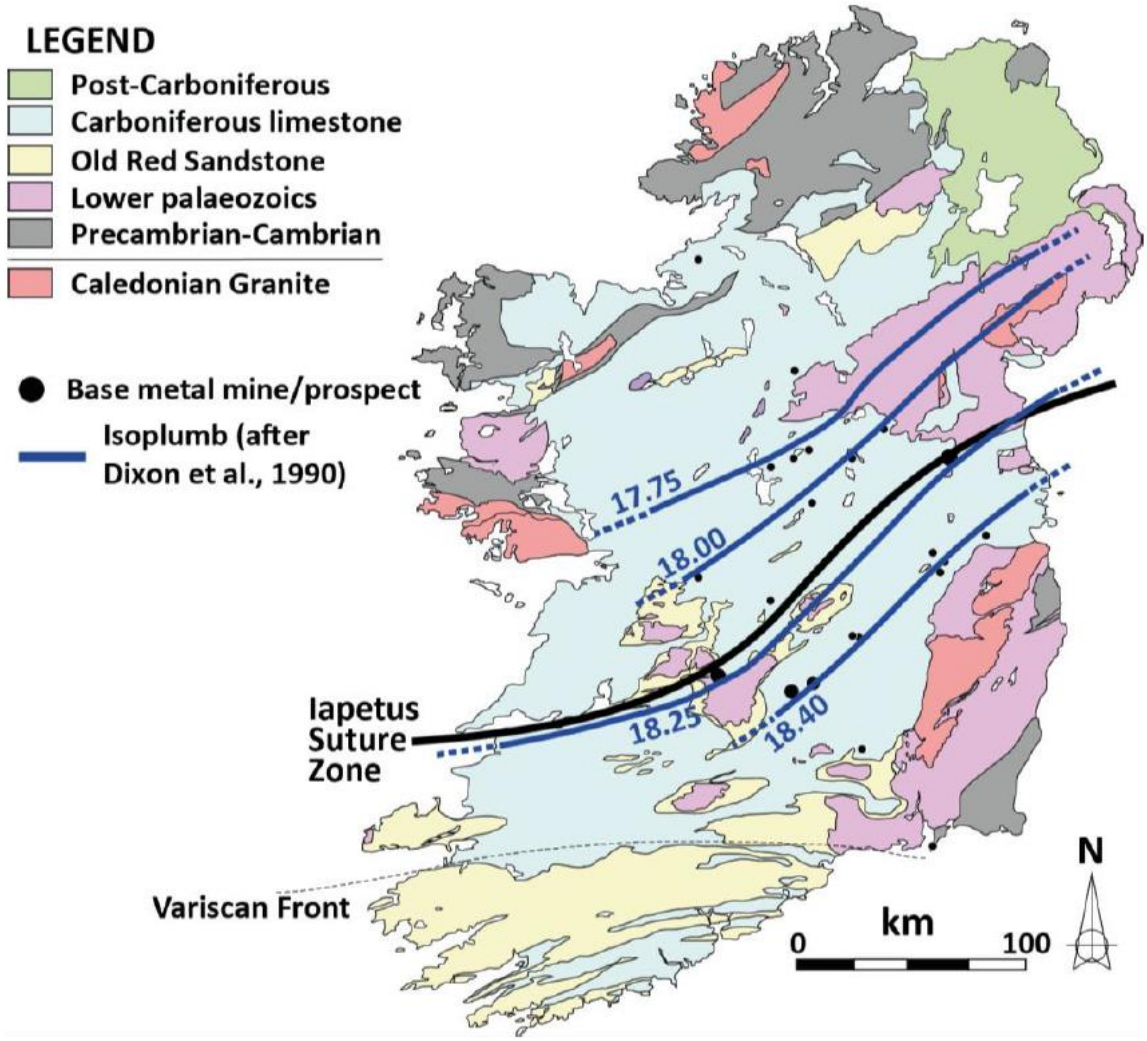

Figure 1.11. A map of Ireland showing the steady northward change in Pb isotopes. Data for the base map from Everett et al., (2003) isoplumbs from Dixon et al (1990), figure sourced from Gillespie (2013).

1.4.5.3 Nd-Sr isotopes

The study of radiogenic $^{87}Sr/^{86}Sr$ and $^{143}Nd/^{144}Nd$ isotopes on gangue minerals can elucidate fluid mixing of distinct ratios. Walshaw et al. (2006) showed that that early dolomite approximated host limestone and seawater while later dolomite, barite, and calcite yielded values closer to basement ratios. The $^{87}Sr/^{86}Sr$ and $^{143}Nd/^{144}Nd$ ratios cannot be explained with a hydrothermal source from the Red Beds and suggest an incorporation of some Precambrian basement within the local source.

1.4.5.4 Helium isotopes

Helium is the lightest of the noble gases and is the second most abundant element in the universe as it is created by the fusion of H in stars. There are two stable isotopes of helium, ^{3}He and ^{4}He, with ^{4}He order of magnitudes more prevalent. The concentrations of the two isotopes vary radically based on the source. As the earth accreted it inherited helium with a relatively high $^{3}He/^{4}He$ value. This helium isotopic signature is then trapped within minerals until they melt and release the helium. This signature can be found today at volcanic centers that are sourced in the deep primordial mantle (Stuart et al., 2003). Volcanic centers that tap mantle that has been melted previously yield a lower $^{3}He/^{4}He$, which suggests ^{4}He has been added to the system. ^{4}He is largely created by alpha particles from the radioactive decay of elements such as U and Th. The crust contains the majority of the Earth's U and Th, thus the crust has the lowest $^{3}He/^{4}He$ ratio of any helium reservoir. Helium in general is very rare in the atmosphere as the Earth's gravitational pull is not sufficiently strong to retain helium, but atmospheric $^{3}He/^{4}He$ has an intermediate ratio between those of the mantle and crust. There are two main processes that create ^{3}He. The bombardment of elements by high-energy cosmic rays can create fission products that include ^{3}He. This process is particularly important for cosmic bodies that are not protected by a magnetic field and atmosphere but can also affect the top few meters of planetary bodies such as the Earth (Gosse and Phillips, 2001). A second means of producing ^{3}He within the earth is by neutron bombardment of ^{6}Li (Andrews and Kay, 1982). The effect

can be quantified by determining the ratio of Li to other neutron absorbers within the sample. The distinct reservoirs of helium in the atmosphere, crust, and mantle are used here to identify the source of He and to recognize mixing between reservoirs at Navan.

1.4.5.5 Argon isotopes

Argon has three stable isotopes: ^{36}Ar, ^{38}Ar, and ^{40}Ar with abundances of 0.34%, 0.06%, and 99.6%, respectively. By operating a gas source mass spectrometer in static mode for the first time it was shown by Aldrich and Nier (1948) that some minerals can contain radiogenic argon as a result of the decay of K. The argon they detected was created by the decay of ^{40}K with a half-life of ca. 1.25×10^9 a. The majority (88.8%) of ^{40}K decays to ^{40}Ca while a considerable amount (11.2%) decays to ^{40}Ar. In a magmatic or metamorphic system, ingrown argon will diffuse out of minerals above a trapping temperature, preventing the accumulation of radiogenic argon. After a mineral has cooled or grown below this temperature, argon is trapped and thus starts a clock. An age can be calculated if the ^{40}K concentration and quantity of non-atmospheric ^{40}Ar (corrected by measurement of ^{36}Ar), of the sample are known. Due to the inherent benefits of measuring a ratio over absolute concentrations of elements, a system of converting ^{39}K to ^{39}Ar was developed by Craig Merrihue and Grenville Turner (1966). This $^{40}Ar/^{39}Ar$ method is enabled by the neutron irradiation of the sample to convert a portion of the ^{39}K to ^{39}Ar, allowing for the measurement of ^{39}Ar as a proxy for parent isotope ^{40}K. To quantify the amount of converted ^{39}K the sample is co-irradiated with a monitor of a known age. Because the sample's effective parent and daughter product are both argon, the sample can then be incrementally heated to release gas in a step-wise manner. The comparison of these heating steps can give great insights into the geological significance of the argon retained within the mineral and thus the thermal and fluid history of the mineral. The $^{40}Ar/^{39}Ar$ method can be used on a wide range of time scales, from late historical to the beginning of the solar system (McDougall and Harrison, 1999, Renne et al., 1997).

1.5 Outline

This thesis focuses on the fluids that created the Navan ore deposit. Chapter 2 integrates the Tara mine's giant drill hole database to understand the lithogeochemical controls of mineralization at Navan. This examines the controls of specific lithological horizons, faults, and fractures, on the grade and ratios of metals. Chapter 3 is a broader chapter that looks into the source and tectonic setting of the Irish ore deposits. Here I use $^{3}He/^{4}He$ ratios in fluid inclusions to constrain the role and implications of the mantle in driving the hydrothermal fluid. The fourth chapter aims to constrain the age of the last hot fluid event within the basement at Navan in hopes of dating the ore genesis event. This chapter details the diffusion model required to interpret the complicated $^{40}Ar/^{39}Ar$ ages and constrain timing of the most recent fluid event. The fifth chapter focuses on a recently discovered area found a few km SE of Navan. This chapter details the petrography, spatial constraints, structures, isotopes, and mineralization within this new area. Finally, chapter 6 synthesizes the chapters and presents some of my views on why Navan is the giant ore deposit it is.

Chapter 2

Base metal variation within the Navan orebody and interactions between submarine paleotopography and hydrothermal fluid flow

B. Davidheiser-Kroll[1], J.H. Ashton[2], R.J. Blakeman[2], A.J. Boyce[1]

[1]Isotope Geosciences Unit, Scottish Universities Environmental Research Centre, Rankine Avenue, East Kilbride, G75 0QF, UK

[2] *Boliden Tara Mines Limited, Navan, Co Meath, Ireland*

Intended for submission to Economic Geology

- J.H. Ashton provided guidance with respect to ideas, data production, figure production, and editing
- R.J. Blakeman provided guidance with respect to ideas and editing
- A.J. Boyce provided supervision and editorial guidance

2.1 Abstract

The giant 110 Mt Navan deposit (8.0% Zn, 2.0% Pb) has been in production for over 35 years. As a result, Tara Mines Ltd. has amassed a comprehensive digitized base metal assay database with over 400,000 assay points in over 28,000 drill cores. The orebody is hosted in extensionally faulted lower Carboniferous limestones and truncated by a submarine debris flow. This Erosion Surface was created by footwall collapse of basin margin faulted blocks. Using the assay database alongside in-house and LeapFrog® software, a comprehensive study of metal and metal ratio patterns has been completed to elucidate controls on hydrothermal fluid flow during ore deposition in both the older Main Orebody and the South West Extension (SWEX), discovered in the 1990s. The data reveal, for the first time, that the Main Orebody has two distinct distributions of Pb/Zn values, while the SWEX is relatively homogeneous. From these maps the southern part of the orebody shows evidence for km-scale horizontal fluid flow, whereas the SWEX and eastern main mine exhibit evidence for vertical fluid flow. Inspection of a 3D map of the Chadian Erosion Surface allows for the identification of detailed correlations between paleotopography and metal concentrations within the Pale Beds and Boulder Conglomerate. The combination of comprehensive metal distribution maps and 3D lithological maps delivers an understanding of the control active extension exerts on fluid pressures and flow during the Chadian mineralization event. This work demonstrates that lithological features present in the Chadian dominantly controlled large-scale fluid flow and mineralization.

2.2 Introduction

The Navan Orebody in Co. Meath, Ireland, is a world-class base-metal deposit with an estimated pre-mining resource of 110 Mt at 8.0% Zn, 2.0% Pb. The deposit (see Figure 2.1) is operated by Boliden Tara Mines Limited, and has been in production since 1977. The deposit can be divided into two sections: the Main Orebody (discovered in the 1970s)

and the South West Extension (SWEX, discovered in the1990s). The SWEX is comprised of 29.5 Mt at 8% Zn+Pb and is described in Ashton et al. (2003); the Main Orebody has been described by Andrew and Ashton (1985), Ashton et al. (1992), Anderson et al. (1998), and Blakeman et al. (2002). Ashton et al. (in press) provide a recent review of the structural setting, geology, and mineralogy. As a consequence of the longevity of modern mining, Boliden has amassed a comprehensive digital assay database for Zn, Pb and Fe comprising 400,000 assay points in over 28,000 drill cores. We have interrogated this massive database to elucidate hydrothermal fluid flow characteristics and controls.

It has long been noted that metal deposits exhibit mineralogical zonation that can be used to understand their history. Some base metal mines show vertical or horizontal zoning while others have little to no zoning (Large, 1980). The causes of metal zoning have been debated but it has been shown that geochemical processes that control metal precipitation can create consistent patterns (Susak and Crerar, 1982). Early metal zoning studies in the Irish ore-field showed the existence of zoning and its ability to locate likely pathways for metal-rich fluids (Taylor and Andrew, 1978; Andrew and Ashton (1982); Taylor (1984). For example, Taylor (1984) identified a strong correlation between high Pb:Zn ratios (Pb/Zn = 10) with textural and isotopic evidence for feeder zones, and thus concluded that metal ratios can be used to determine which faults controlled fluid ingress during ore deposition. Three previous studies of metal zoning patterns of the Navan ore body have been undertaken and focused on the Main Orebody (Figure 2.1). The first was conducted by Andrew and Ashton (1982) and examined 420 intersections of drill holes with the 5 Lens (the lens with the greatest concentration of ore at that time). They addressed Zn, Pb and Fe concentration as well as the elemental ratio of Zn:Pb. The area covered less than 10% of the plan area of the current ore body. The 5 Lens drillhole intersections were vertically averaged and then mapped on contour plots. Andrew and Ashton (1982) noted a parallel enrichment in the 1 Zone, within 200 - 300 m of the ‘B’ fault, and other enrichments in the north following a smaller swarm of ENE-trending normal faults. They

explain that the 2 Zone displays distinct enrichments that are not related to the B Fault and show a more easterly orientation. The Pb data are said to "show broadly similar trends to those displayed by Zn." (Page 41 Andrew and Ashton, 1982). They also note that changes in Zn:Pb ratios match the element zonation within the east of the 2 Zone. No conclusion regarding fluid migration or feeder areas was drawn from this study.

Andrew and Ashton (1985) updated the earlier paper, and revisited the same area but included more drill-hole data and produced metal-distribution maps for the higher lenses, drawing similar conclusions. For the first time, vertical zoning of Zn, Pb, and Fe showing increasing Zn and Fe in higher lenses was attributed to variations in hydrothermal fluid chemistry with time.

The most recent study on metal zoning was conducted by Blakeman et al. (2002). The area covered by this study was approximately 80% of theextent of the Main Orebody and focused on the 5 Lens in Zones 1 and 2. Seeking to expand on the earlier studies these authors examined 3 m vertical aggregates (slices) to locate likely feeder zones and concluded that these are more aligned with minor NW- and SE-dipping, NNE-, NE- and ENE-trending structures associated with the ramp relay in the 1 Zone, rather than the major extensional, SE-dipping, B and T Faults.

This study uses a significantly enlarged database compared to previous work, and we explore metal distributions in the SWEX for the first time. We also incorporate lithological features, as well as structure, in relation to the metal distributions. This study has been enhanced by the ability to explore large databases using 3D visualization software (in house Eagle mining software and Leapfrog®). What emerges is a new view on hydrothermal fluid flow through the various Navan orebodies, both horizontal and vertical, and a greater understanding of the influence exerted by Mississippian tectonism, including active footwall degradation by debris flows, in controlling preferred fluid pathways.

2.3 Geologic Setting

2.3.1 Stratigraphy

The stratigraphy of the Navan area (Figure 2.2) is comprised of a transgressive, carbonate-dominated sequence, ranging from Tournaisian to Visean (Mississippian) age, which unconformably overlies Ordovician and Silurian volcaniclastic and sedimentary rocks of low metamorphic grade. The basal member of the Mississippian sequence is known as the Red Beds (local mine nomenclature is used here and throughout). These largely fluvial, marginal sandstones and mudstones infill the paleotopography of a regional unconformity. Overlying the Red Beds, the onset of a shallow marine environment is marked by thinly bedded siltstones, mudstones, sandstones, and calcarenites termed the Laminated Beds. Above this is the Muddy Limestone, a well-bedded argillaceous micrite unit.

The main host rocks to ore at Navan are termed the Pale Beds, a carbonate-dominated sequence above the Muddy Limestone. The base of the Pale Beds comprises a clean micrite unit overlain by variably oolitic and bioclastic calcarenites, calcareous sandstones, and minor shale-silt layers that record a deepening shelf environment. Some of the minor shale and occasionally dolomitized silt layers are sufficiently uniform in extent to serve as deposit-wide marker horizons (Philcox, 1984), and to locally control mineralization (Anderson et al., 1998). The Pale Beds host the majority of the mineralization, and are comprised of the numerous (n=7) mineralized lenses as described below (Figure 2.2). In the northern part of the deposit an area of dolomite exists that is considered to have formed approximately contemporaneously with mineralization and broadly resembles the shape of a plume (Ashton et al., in press, Rizzi and Braithwaite, 1997).

The Shaley Pales overlie the Pale Beds and are comprised of bioclastic calcargillites and calcarenites with some calcareous sandstones. Above the Shaley Pales, the stratigraphy is composed chiefly of crinoidal argillaceous limestones, termed the Argillaceous Bioclastic

Limestones (ABL), which interfinger with the Waulsortian Limestone mudbank facies (Philcox, 1984).

2.3.2 The Erosion Surface and overlying stratigraphy

A major unconformity known as the Erosion Surface truncates the stratigraphy (including, locally, the complete removal of Mississippian sediments), with generally deeper incision to the southeast (Philcox, 1989). The Erosion Surface is considered to have been caused by foundering of the seafloor due to rapid extension on the northern margin of the developing Dublin Basin during the early Visean (Boyce et al., 1983a). This submarine erosion event yielded high-energy beds composed of coarse chaotic, polymict debris flows collectively termed the Boulder Conglomerate. The Boulder Conglomerate is host to <3% of the total ore andcontrasts with the lower ore horizons by its high pyrite content. Where the Boulder Conglomerate is mineralized it is termed Conglomerate Group Ore (Ashton et al., 1992). Overlying and occasionally interbedded with the Boulder Conglomerate are a series of thinly bedded turbidites. This unit represents the base of a sequence of interbedded shales and calcarenites called the Upper Dark Limestones (UDL). The basal parts of the UDL occasionally contain pyrite-rich horizons that vary from millimeters to half a meter in thickness with some rare and thin bedding-parallel sphalerite-rich horizons. The UDL is the highest preserved stratigraphic unit in the Navan area and represents the infilling of the Dublin Basin (Altinok, 2005, Nolan, 1989).

2.3.3 Structure

The Lower Paleozoic rocks below the Navan deposit form a complex geometry of terranes sitting within the Iapetus Suture Zone and inherit a number of deep-rooted fault zones (Vaughan and Johnston, 1992). Faulting within the deposit area is partly controlled by the reactivation of these structures during both Mississippian extension and Pennsylvanian compression (Coller et al., 2005).

The deposit is bound by two early en echelon, E-NE trending, N-NW dipping normal faults; the E Fault and the Liscartan Fault (see Figure 2.1), which are considered to have moved early in the system, with over 500 and 200 m throws respectively. The geometry of more minor faulting between these large faults strongly suggests a displacement transfer zone, creating a ramp relay (Ashton et al., in press). Later ENE-trending faults with ca. 100 m throw displace portions of the Pale Beds and overlying units to the SE (e.g. the B, T and Y faults, see Figure 2.1). This generation of faulting delivers a shift in the Navan area from a NW- to a SE-dipping regime (Coller et al., 2005): this shift likely reflects the onset of large-displacement faulting to the immediate south of Navan that defines the northern margin of the first order Dublin Basin. Several half-grabens termed the Shaley Pales Troughs (see Figure 2.1) occur in an area bounded to the NW by the T, M and N faults and to the east by the E and C faults. Infilled by allochthonous blocks of Shaley Pales and ABL, the top of the Shaley Pales Trough is truncated by the Erosion Surface and is usually capped by the Boulder Conglomerate and lower parts of the UDL (Philcox, 1989).

Post-Mississippian inversion of many faults peripheral to the orebody (A, C, D, Randalstown, and Castle Faults, see Figure 2.1) created large (ca. 500 m) dextral and significant (ca. 200 m) reverse displacements (Ashton et al., in press). This compression is believed to have taken place at the end of the Hercynian orogeny ca. 300 Ma (Hitzman, 1999).

2.3.4 Navan mine nomenclature

The Navan ore body is divided vertically and horizontally into lenses and zones, respectively. Geographically, it is divided on a large scale into the Main Orebody, the South West Extension (SWEX), Tatestown/Scallanstown, and Clogherboy (Figure 2.1). The areas of Tatestown/Scallanstown and Clogherboy are small satellite occurrences of mineralization that have not yielded economic-grade ore. The Main Orebody is sub-divided in to geographic zones based on the major listric normal faults (Figure 2.1): Zone 1 is comprised of the area to the NW of the B Fault; Zone 2 is the smallest area and is bound

by the B and T Faults; Zone 3 is located to the SE of the T Fault and in the NE of the deposit east of the major reverse A Fault.

Distinct marker beds are used to vertically divide the Pale Beds stratigraphy. These units are known as lenses and are labeled from stratigraphically highest to lowest starting with U, followed by 0,1,2,3,4 and 5 (Figure 2.2). Stratigraphically above the Pale Beds lens is the mineralization hosted within the Shaley Pales, Boulder Conglomerate, and lower UDL (Figure 2.2).

The vertically differentiated ore lenses (Figure 2.2) and horizontally differentiated zones yield a method of naming mineralization by location and stratigraphy. The convention is to name a region by "Zone Lens", so mineralization found to the east of the A Fault (3 Zone) at the base of the Pale Beds (5 Lens) would be called the "3-5 Lens". The mineable mineralization found within the Boulder Conglomerate is sufficiently distinct that it is called Conglomerate Group Ore (CGO) in whichever area of the mine it occurs.

Since its discovery in 1990's, the SWEX, representing a total resource approaching 30 Mt 8% Zn+Pb grades, has been a major Irish source of base metals. The SWEX lies SE of the T Fault and thus is wholly within the 3 Zone. In contrast to the main mine, in which ore is dominantly hosted in 5 Lens, SWEX mineralization is largely hosted within the 1 and U Lenses (Ashton et al., in press).

2.3.5 Sulfur isotopes and metallogenic models

Sulfur isotope analyses have been instrumental in determining sources of sulfide and sulfate, and in elucidating precipitation mechanisms within the Irish Orefield (Boyce et al., 1983a, Boyce et al., 1983b, Coomer and Robinson, 1976, Fallick et al., 2001, Wilkinson et al., 2005b). It is believed that Mississippian seawater-sourced brines descended into the basement (Banks et al., 2002), where they scavenged metals from the basement rocks (e.g. Everett et al., 1999, Everett et al., 2003), as well as acquiring minor amounts of sulfur with a positive isotope signature (Bischoff et al., 1981, Russell et al., 1981). The dominant

process of ore deposition has been shown to be the mixing of surface-derived fluids bearing bacteriogenic sulfide (sourced from Mississippian seawater sulfate), with rising metal-bearing hydrothermal fluids: at Navan, >90% of ore was precipitated using bacteriogenic sulfide (Everett et al., 2001, Fallick et al., 2001, Blakeman et al., 2002). In a study located in the north-eastern part of the Navan deposit, Blakeman et al. (2002) showed that positive sulfur isotope values (associated with the metal-bearing fluid), are focused in and proximal to all extensional fractures examined, with a loss of this signature within 3 meters of the hanging and footwalls of even small NW and SE dipping normal faults. Bacteriogenic sulfide dominates outside of these zones. Within the CGO, pyrite-rich mineralization is dominated by the presence of highly fractionated, biogenically-derived sulfide (Ford, 1996). Thus, at Navan and among all economic deposits to date, there is very strong evidence for the dominance of the mixing of a surficial brines containing bacteriogenic sulfide with upwelling metal-bearing fluids to precipitate ore, and the importance of fault-related fluid flow in bringing that hydrothermal fluid to the site of mineralization (Wilkinson et al., 2005a).

2.4 Methods

2.4.1 Maps and slices

Drill-hole assay data from >35 years delineation and production were composited (as in the Blakeman et al., 2002 study), into notional ~3m slices orientated parallel to the stratigraphy using in-house software (Ashton and Harte, 1989). Using this method the deposit is composed of 66 slices created from almost 400,000 assay points in over 28,000 drill-holes equaling greater than 74,000 meters of analyzed drill-core. These data represent samples between 0.5 and 3.0 m in length, with the vast majority being 1.5 m. Slice composites, when combined, can assist elucidation of the bulk metal distributions within any 3 m section of the host stratigraphy. Previous workers (Andrew and Ashton, 1985, Blakeman et al., 2002) used similar slice composite data to calculate bulk metal values in

10 x 10 m blocks using inverse-distance weighting for specified sections of the stratigraphy.

In this study the input parameters were varied in order to determine the data sensitivity. Different methods of averaging the data, including both mean and inverse distance squared methods, did not yield significant differences in the maps, so inverse-distance weighting was selected for consistency with previous studies (Andrew and Ashton, 1985, Blakeman et al., 2002). Increasing the search distance resulted in the blurring of local trends in favor of regional trends. A final distance of 50 m was selected both to allow the examination of larger-scale trends and to remain consistent with previous studies. Blocks that contain data from only a single drill hole were omitted to avoid over-reliance on single data points; given the large size of the database these omissions do not significantly affect the results..

To investigate potential errors produced by the block-creation algorithms, the composite data were compared with the raw data. We viewed both the 10 x 10 m block data and the raw data using 3D viewing software (Leapfrog™). By comparing the data holistically as well as systematically in cross-section, we are confident that these complex displays reflect true base-metal variations across the deposit.

2.4.2 Filtering

The data presented in the histograms (Figs 2.4, 2.5, and 2.6) were compiled from aggregated block data after filtering of data points with Zn or Pb values < 0.1 wt. %. Filtering the data removed rounding artifacts, particularly in the Pb/Zn and Zn/Pb ratio maps, which caused comb shaped histogram distributions (e.g. now absent in Figs. 4, 5, and 6). The comb shape is largely due to low Pb values; filtering resulted in the omission of <22% of the total data. The histograms are not significantly affected by filtering, excepting the omission of several spikes at integer values. The Fe data remained unfiltered as they were not used in ratio maps and lack comb-shaped histograms.

2.4.3 Erosion Surface contour and sub-crop maps

A contour map of the Erosion Surface (at 20 m intervals) was created in Leapfrog®. Complications due to post-ore reverse faulting were removed and the resulting grid was triangulated to create a 3D mesh. The sub-crop map at the Erosion Surface was extracted from Ashton et al. (in press) and projected onto the Erosion Surface Mesh.

2.5 Metal concentration and ratio distributions

Figures 2.3, 2.4, 2.5, and 2.6 present the complete coverage of every major lens within the current extent of the Navan deposit. The SWEX, NW and SW areas of the main deposit (Figure 2.1), and the majority of the upper lenses are evaluated here for the first time. Other areas shown here were previously reported by Andrew and Ashton (1982), Andrew and Ashton (1985), Ashton et al. (1992) and Blakeman et al. (2002), and this study yields similar results for the areas previously addressed. As with the earlier publications these maps should be viewed as lithogeochemical maps rather than ore outline maps.

2.5.1 Main mine deposit

2.5.1.1Metal concentration distributions, 1-5 and 2-5 lenses

The 5 Lens is stratigraphically the lowest mineralized body in the Navan deposit and in map view forms a rough parallelogram bounded by faults to the NW and SE. This lens has been responsible for the majority of production at Navan (Ashton et al., in press, Blakeman et al., 2002). Quaternary erosion to the E and NE has removed substantial but un-quantified amounts of material, while to the SW the mineralization diminishes gradually to uneconomic values. The largest Zn concentrations are found in the eastern section of the main deposit and are described in detail by Andrew and Ashton (1985), and in Blakeman et al. (2002). Figure 2.4*n* shows four parallel, broadly NE-aligned zones with Zn–grades decreasing to the southwest. These features are concentrated on minor SE- and NW-dipping normal faults.

The distribution of Pb concentrations in the 5 Lens (Figure 2.4*o*) broadly follows that of Zn but also shows an apparent displacement to the SW along the trend of the minor faulting discussed above. Pb concentrations cut across both large and small faults and are not clearly fault-controlled.

Fe in the 5 Lens is enriched to the E and N, and the majority of the lens contains less than 2% Fe (Figure 2.4*p*). The concentrations in Zones 1 and 2 follow rough northerly trends in places, with sporadic enrichments between. The most prominent area of Fe concentration in the 1 Zone is coincident with the hydrothermal dolomite plume (Anderson et al., 1998, Ashton et al., in press, Rizzi and Braithwaite, 1997) but not with Pb or Zn mineralization under the dolomite. High Fe values are also found along the T Fault, grading to lower values to the north. In this area, Fe is inversely correlated with Pb and Zn enrichments.

2.5.1.2 Metal ratio distributions, 1-5 and 2-5 lenses

There are two main areas in the southwestern parts of the main deposit 5 Lens that have higher Pb/Zn values than the remainder. When examining a histogram of these data (Figure 2.4*m*), it is difficult distinguish any variation from a positively skewed distribution. However by inverting and examining the same data in Zn/Pb ratio space, a clearly bi-modal distribution can be observed (Figure 2.5). This is due to the inherent nature of ratios near one, which can conceal variability. The two populations not only occupy distinct Zn/Pb ratio space but are also distinctly geographically distributed within the deposit (Figure 2.5). The area in the southwest of the main deposit has a low Zn/Pb ratio that progressively increases to the northeast. Within the north and northeast of Zones 1 and 2 the Zn/Pb values are relatively homogenous over the 100m scale, with small scale variations forming pods cored by high Zn/Pb values.

2.5.1.3 Metal concentration distributions, 4, 3 and 1 lenses

The significant Zn, Pb and Fe concentrations in the upper lenses of the main deposit are restricted to the E fault area. Outside this area there are several zones of enrichment in the 4 and 3 lenses that are elliptical in shape with the elongate axis following the NE strike of

small normal faults. The higher Zn values in 4 Lens are restricted to the area of the B Fault and directly above the elevated Zn values of the southeastern 5 Lens (Figure 2.4*j*). The Zn maxima in the 3 Lens generally follow those seen in the 4 Lens but with a longer strike (Figure 2.4*f*). Zn values in the 1 Lens are generally lower, with small areas of higher enrichment towards the edges (Figure 2.4*b*). Pb concentration trends in the upper lenses closely follow those for Zn.

Fe concentrations within the main deposit area diminish upwardly through successive lenses. By far the greater concentrations within lenses 4 and 3 are focused in the immediate footwall of the T Fault, and within the horst area in 1 Zone (Figure 2.4*p*). A lesser high is observed in the footwall of the B Fault to the north-east. However, a distinct enrichment in the footwall of the T Fault occurs in the 4 Lens to the north-east of the similar occurrence in the 5 Lens. This concentration increases in the 3 and 1 lenses and is likely associated with the body of Fe-rich CGO sitting in the hanging wall of the T Fault.

The Pb/Zn ratios in the upper lenses of the main deposit are spatially similar to those found in the basal 5 Lens. The areas in the SW have high Pb/Zn values as in the underlying 5 Lens. The areas in the NE show no clear variation between lenses.

2.5.1.4 Conglomerate Group Ore

Conglomerate Group Ore occurs in five distinct lenses along the southern margin of the Main Orebody and SWEX (Figure 2.1). The textures, contours, relationship to Pale Beds-hosted mineralization, observed paragenesis, and cross-sections for the Main Orebody are described in Ford (1996) and Ashton et al. (1992). The latter also reconstructed the 300m of dextral slip on the compressional faults to recreate paleo-metal distribution patterns. The study here did not incorporate any reconstructed areas and thus the Conglomerate Group Ore from this area is not incorporated in the maps presented here.

2.5.2 SWEX deposit

2.5.2.1 Metal concentration distributions, SWEX 3-1 and 3-5 lenses

The 1 and 5 lenses in the SWEX are presented together here because they do not overlap, and each represents the most heavily mineralized lens in their respective areas. Mineralization in the 3-1 and 3-5 lenses is dominantly found between the major listric M and N faults, and the major normal E Fault (Figures. 2.1 and 2.3). Metals are largely concentrated along the western edge of the Shaley Pales Trough (Figure 2.6*j*, *k*). Metal concentrations decrease to the NW, perpendicular to the E Fault, and drop significantly beyond the Y Fault, where concentrations become patchy but are still economically viable. Mineralization in the 1 Lens largely consists of thin massive replacement textures and is present below a dolomitic siltstone that defines the top of 1 Lens (Ashton et al., 2003). Mineralization in the 5 Lens of the SWEX is typified by small ramifying veins. However, close to the zone of faulting created by the E Fault, what is logged as the 5 lens may actually contain material from other lenses due to structural complexities. These horizons are strongly mineralized between the southwest of the M Fault and the northeastern extent of the N Fault (Figure 2.6 *j* and *k*).

Although Fe concentrations in the 3-1 lens are relatively low, the highest values (>2%) are found abutting the M, E and N faults (from north to south).

2.5.2.2 Metal ratio distributions, SWEX 3-1 and 3-5 lenses

The Pb/Zn ratio within the 3-1 and 3-5 Lenses is homogenous at a large scale. There is no correlation of either the Pb/Zn or Zn/Pb ratio with absolute metal concentrations. The variability in Pb/Zn that is evident does not correlate with the high Zn and Pb areas. What variation in Pb/Zn is present expresses itself as cryptic isolated to semi-connected patches centered around high Pb/Zn values (Figure 2.6*i*). There are a few small high Pb/Zn areas on the edge of the northwestern SWEX area but these are based on fewer than 3 drill-holes and are thus poorly supported. The northern end of the SWEX has higher Pb/Zn ratios.

This area is between the Y and T faults and may be related to the adjacent high Pb/Zn zone in the footwall of the T Fault.

2.5.2.3 Metal concentration distributions, SWEX 3-U Lens

Concentrations of Zn and Pb in the U Lens generally grade to higher values towards the east, with isolated pockets of much higher concentrations along the eastern edge. The highest values are found within semi-circular areas that are slightly elongated in the NE direction and vary in size from 200 x 200 m to 100 x 50 m. Occurrences of Conglomerate Group Ore and pockets of high-grade ore are approximately vertically correlated. However the exact extent of these two does not coincide, as the CGO covers a smaller area. There are three high-Fe areas within the body of SWEX. The distribution of Fe in 3-U Lens is directly related to the base of the Boulder Conglomerate. There are three large (>2500 m^2) areas with major concentrations of Fe. These areas occur directly below Conglomerate Group Ore and in the hanging wall of the E Fault and associated with the Y Fault, and are found either in the footwall or straddling the Y Fault. These areas are spaced roughly 600 m apart, along the strike of the eastern edge of the SWEX. These high Fe areas vary slightly in shape but are all slightly elongate along a NW-SE trend. Apart from these areas Fe concentrations are very low (< 1.5%) and patchy. Fe enrichments do not appear to be correlated with Zn or Pb enrichments.

2.5.2.4 Metal ratio distributions, SWEX 3-U Lens

The consistency in Pb and Zn concentration distributions yields homogenous Pb/Zn values in the 3-U Lens. Areas with slightly higher values are generally situated on the edges of the lens or at the northern end of the SWEX. This area is underlain by the southeastern edge of the high Pb area of the main mine. The eastern edge of the modeled space does display some small areas with very low Pb/Zn ratios, however this is likely caused by a biasing effect due to the small amount of data used to calculate the aggregates. This is supported by the fact that areas with fewer drill holes have slightly lower Pb/Zn values.

2.5.2.5 The Conglomerate Group Ore within the SWEX and the Erosion Surface

All intersections of mineralization above the Erosion Surface are contiguous with areas where the Erosion Surface has cut deep enough to reach the Pale Beds (Figure 2.7), as seen in the main deposit (Ashton et al., 2003). In the SWEX, this occurs in the east of the deposit along the major normal faults (E and C). Examination of 3D data of the Erosion Surface indicates that the most intense concentrations of mineralization are associated with deep incision of the Erosion Surface into the Pale Beds (Figure 2.8). These incisions run roughly 60° NW, with a maximum depth of 30 m. The mineralization thickness changes within these incisions but generally thins against their flanks. There are some instances of mineralization within the higher sections of the Boulder Conglomerate but these are much thinner and lower grade. The lowest points of the Erosion Surface in SWEX are underlain by the non-permeable and allochthonous Shaley Pales (Shaley Pales Trough) (Figure 2.8).

The maps presented on Figure 2.6 *a-d* show the slice composite data for two of the three CGO areas within the SWEX (Figure 2.6 *a-d*). These areas are relatively small (ca. 100m^2) but do show elemental zoning. Zn and Pb values in the most northerly occurrence decrease to the west with the highest values found on the southeastern boundary, while Fe values decrease along the western and northern borders (Figure 2.6*d*). As with the main deposit, mineralization within the Boulder Conglomerate has a much higher Fe content than Pale Beds-hosted mineralization (Ashton et al., 2003, also see Figure 6d). The middle area has higher concentrations of Zn and Pb in the western portion, decreasing to the edges. Fe values are more consistent across the area, with a slight decrease at the northern end. The most southerly CGO zone in the SWEX has not been included in the slice aggregate system but is marked by a small ellipse on Figures 6 *a-d*.

2.5.3 The Argillaceous Bioclastic Limestone

The Argillaceous Bioclastic Limestone (ABL) has been intersected by drill holes across the SW of the deposit and in areas to the west of the deposit. The slides and the Erosion Surface have removed the ABL above most of the deposit; it is thin at its eastern extent

and thickens to the west. A subcrop map created by Ashton et al. (in press) shows the extent of the ABL present above the Erosion Surface. In Figure 2.7, the ABL has been projected vertically onto the 5 Lens horizon and compared with mineralization within the ore lenses.

2.6 Discussion

In the following discussion we use the large 3D metal distribution database from Navan, allied with an emerging understanding of the structural and textural evolution of the deposit (e.g. Ashton et al., in press, Boyce et al., in press), to examine whether the Navan deposit was created from primarily vertical flow or large-scale horizontal flow of ore fluids sourced from the basement (Everett et al., 2001, Walshaw et al., 2006). In a primarily vertical flow regime, the emerging hydrothermal source(s) would theoretically be distributed below all mineralized areas of the Pale Beds, as shown in Figure 2.9*a*. This is analogous to mid ocean ridge sites (Webber et al., 2011). The location of vertical flow may move over time but occurs within the same general stress regime (Roberts et al., 2003). Alternatively, the presence of large-scale (km) horizontal flow within mineralizing lenses would allow for a small area to be fed by a single point, fault, or source region that supplies hydrothermal fluids to the entire deposit (Figure 2.9*b*). Data presented here show that the Navan orebody exhibits both flow regimes in different regions, and perhaps at different times. Our analysis indicates that vertical flow is dominant within the SWEX and areas of the main mine with high metal concentrations, including areas near the Erosion Surface and major extensional normal faults. Horizontal flow appears more prevalent in areas of the main mine with low metal concentrations, particularly in areas far from the erosion surface and major faults, such as in the western mine.

2.6.1 Vertical fluid flow

It is clear that some upward component of fluid flow must have occurred to create mineralization in the carbonate sediments above the metal source in the basement (Everett

et al., 2003, LeHuray et al., 1987, O'Keeffe, 1986, Walshaw et al., 2006). The driving force for the hydrothermal fluids is debated; possible mechanisms include continental heat (Russell et al., 1981), mantle heat (Davidheiser-Kroll et al., 2014), volcanic (Wilkinson and Hitzman, in press) and topographic flow (Hitzman and Beaty, 1996).

The presence of vertically similar metal distribution patterns, as demonstrated for Navan below, requires rapid vertical fluid flow, resulting in small changes in metal precipitation activities. Rapid vertical flow can be caused either by over-pressuring and hydraulic jacking (Andrew and Ashton, 1985), or by pervasive fracture-induced faulting (Ashton et al., 1992). Conceptually, the hydraulic jacking and creation of vertical pathways for fluid migration would be assisted by unloading due to the removal of the overlying stratigraphy by the erosional event, and several authors show that mineralization was ongoing at this time (Andrew and Ashton, 1982, Boyce et al., 1983a, Ashton et al., 1992, Ford, 1996, Anderson et al., 1998, Everett et al., 2001, Fallick et al., 2001, Blakeman et al., 2002, Ashton et al., 2003, Ashton et al., in press). Given that the ultimate cause of the erosional event was faulting (Boyce et al., 1983a), there is an obvious potential connection between this faulting, and the fracturing that allowed for the vertical flow: vertical flow may thus have occurred as part of a feedback process, where hydraulic jacking and faulting caused rapid vertical fluid flow. Further, metal precipitation activities must have been relatively constant to prevent vertical variation in metal concentration values. If one considers hydraulic pressure as the main variant during the evolution of rapid vertical flow, and that relative activities (Reed and Palandri, 2006, see figure. 1) of Zn and Pb in chloride complexes (Wilkinson et al., 2009) vary little over the 100 m thickness of ore lenses at Navan, it is clear that changes in pressure would not have been sufficient to induce differential precipitation between Pb and Zn (Susak and Crerar, 1982).

There is abundant evidence for vertical flow at Navan in the form of textures, metal emplacement patterns, and metal ratios. Textural evidence includes ramifying veins that cross-cut bedding, anastomosing veins, collapse breccias, and hydraulic breccias, all of

which have been reported previously (Anderson et al., 1998, Andrew and Ashton, 1982, Andrew and Ashton, 1985, Ashton et al., 1992, Ashton et al., 2003, Blakeman et al., 2002, Ford, 1996). These observations are generally made on the drift scale (ca. 3m vertical), with vertical mineralization seen in places terminating at areas of bedding-parallel mineralization below aquitards (Anderson et al., 1998). On a larger scale, metal distribution patterns across stratigraphic lenses faithfully track the passage of the rising fluids (Figures 2.4 and 2.6). The observed similarities between metal ratios in vertically adjacent sections, even in areas where textural observations demand multiple episodes of ore emplacement (Andrew and Ashton, 1982, Gagnevin et al., 2012), support the notion that vertical fluid incursion was persistent and focused in particular areas (Figures 2.4 and 2.6). Below we provide detailed evidence for vertical flow from two areas at Navan: the SWEX and the areas in the main mine with the highest ore grades.

Ashton et al. (2003), showed that in an area of the SWEX bound geographically by the E Fault and the Y Fault, and vertically by the structurally complex 5 Lens and the Boulder Conglomerate, mineralization is dominated by vertical ore texture relationships, with stratabound mineralization found locally below marker horizons. This is supported by large-scale mapping of metal concentration patterns (Figure 2.6), where the vertical continuity of high-grade areas from the lower-most 5 Lens up to the Boulder Conglomerate (see Boulder Conglomerate and Conglomerate Group Ore section) implies dominantly vertical flow. That Pb/Zn ratio values are homogenous on a km scale indicates that no systematic horizontal flow preferentially enriched one geographic area of the SWEX with one element over the other, as in the main mine 1 Zone (Figure 2.5). The small-scale heterogeneities that do exist in the SWEX 1 Lens Pb/Zn values are not present within the overlying homogenous and slightly lower Pb/Zn U Lens (Figure 2.6 a, e and i).

The highest ore grades at Navan are found in the northeastern area of the main mine (1 and 2 Zones), with grades of up to >30% Zn+Pb over 25m (Andrew and Ashton, 1982). In these areas of intense mineralization it is possible to trace focused high concentrations and

homogenous Pb/Zn from the lowest and most pervasively mineralized lens through all of the overlying lenses (compare Figure 2.4 *e*, I and m with Figure 2.4 *f, g, j, k, n* and *o*). These vertical zonations are generally bound by the local large listric faults (B and T) but are believed to be causally related to the smaller faults and fractures in this region (Andrew and Ashton, 1982, Blakeman et al., 2002). Although these are relatively small faults, meshes with numerous small extensional and related faults are thought to be able to accommodate large scale fluid flow (Sibson, 1996). These vertically mineralized areas do not show any significant variation in Pb/Zn ratios as seen at other deposits, such as Silvermines, Rammelsberg, Mount Isa, McArthur River, Sullivan, and Tom (Large, 1980, Taylor, 1984, Andrew and Ashton, 1985). A similar lack of Pb/Zn ratio anomalies, coupled with intense areas of element concentration, is seen in the SWEX, where vertical fluid flow also dominates (compare Figure 2.6*e* and *j* with Figure 2.6 *f, g j* and *k*).

A situation involving primarily vertical flow still requires sufficient mixing with the sulfur-rich surface fluid to account for the dominance of bacteriogenic S in the deposit (Fallick et al., 2001). Furthermore, the complexity of texture in many zones within the main mine indicates repeated influx of metals with attendant overprinting (Andrew and Ashton, 1982), as might be expected in Irish ore environments that created economic ore deposits such as Navan (Barrie et al., 2009). These processes must have, to a greater or lesser extent, smoothed out some of the perhaps originally more coherent trends in the mine. That distinct, identifiable trends remain is a testament to the persistence and intensity of the metal discharge from the hydrothermal fluid.

2.6.2 Horizontal evolution of Pb/Zn

Not all areas of high metal concentration within the 5 Lens are overlain by high-grade material in overlying lenses and thus they do not always exhibit vertically stacked mineralization patterns. Furthermore, on a drift scale, the majority of mineralization is broadly bedding-parallel and often lies below marker horizons believed to have been aquitards at the time of ore deposition (Anderson et al., 1998, Andrew and Ashton, 1982,

Ashton et al., in press). This style of mineralization demands at least local lateral fluid flow. However, kilometer-scale lateral fluid flow, seen in other base metal deposits (Large, 1980) has never been demonstrated satisfactorily at Navan.

Our new data show, for the first time, that the 5 Lens has two distinct populations in Pb/Zn, best seen in Zn to Pb ratio space, and that these two populations are largely found in distinct geographic areas (Figure 2.5). The difference between these areas can be explained by variation either in the source fluid or in precipitation conditions. The mapped contact of the distinct ratio space is in contrast to the evidence for vertical flow discussed above. These populations show no alignment along major faults and do not define a sharp contact with each other. The lower Zn/Pb area in the western main mine 5 Lens (shown in red in Figure 2.5) shows a distinct km-scale progressive increase in Zn/Pb, and thus a decrease in Pb/Zn, to the northeast (Figures 2.3 and 2.4*m*). This could reasonably be the result of lateral movement of a fluid starting in the SW with a single composition and moving through the Pale Beds. The gradual nature of this change in metal ratio is more readily explained by changes in the thermodynamic regime during precipitation, rather than changes in the source fluid. Although changes due to thermodynamic conditions would be expected to produce only small differences in metal deposition (Reed and Palandri, 2006, Susak and Crerar, 1982), the changes seen are in fact small relative to other base metal deposits (Large, 1980).

The source of metals within the Irish ore field is most likely derived from the Lower Paleozoic basement, as indicated principally by Pb isotope analyses which show that sources vary across Ireland but each deposit has a single source (Everett et al., 2003, LeHuray et al., 1987, O'Keeffe, 1986, Walshaw et al., 2006). The large differences of Pb/Zn ratios from the southeast main mine could imply source fluids with two distinct initial metal ratios active in the deposit, with the southwest main mine being sourced from a more Pb-rich hydrothermal fluid compared with the remainder of the Navan deposit. This could explain the observed metal zoning patterns without the need for differing

precipitation mechanisms or thermodynamic properties. The basement rocks below the southern parts of the main mine and the SWEX are not constrained and could vary considerably, and thus this scenario cannot be excluded. However, without deeper drilling or isotopic work to distinguish the two areas, the idea that variable source fluids could explain the distinct Pb/Zn (Figure 2.5) ratios is speculative, especially given the marked homogeneity of Pb isotope ratios across all lenses noted in a study of main mine concentrates in Fallick et al. (2001).

The range of Pb/Zn values at Navan compared other Irish type deposits is relatively small (ca. 0.1 to 2 vs. 0.1 to 10, respectively) (Large, 1980, Taylor, 1984). A relatively ordered system thus must have been in place to create the patterns seen in the main mine 5 Lens, regardless of the observation that many pulses of mineralizing fluid created the deposit (Figure 2.4*m*). This consistency of geochemical parameters over time and space allowed for each pulse of fluid to precipitate a similar ratio of sulfides (galena: sphalerite) at a given location. During horizontal fluid migration up the slight dip of 5 Lens to the northeast, the Pb preferentially precipitated on contact with any sulfur provided by mixing with the surface fluid. This preferential precipitation slowly exhausted the Pb, driving the Pb/Zn of the fluid to lower values. Given the expectation for, and existence of, very little elemental variation indicates the presence of a non-chaotic system that was governed by the same flow style and thermodynamic constraints during the vast majority of ore genesis in this area.

2.6.3 The Erosion Surface and Conglomerate Group Ore mineralization – linkage of surface events to hydrothermal system evolution.

Conglomerate Group Ore generally resides in topographic lows, created by the erosion surface, above exposed Pale Beds and in areas not capped by Shaley Pales (Figure 2.10). The location of this high-grade mineralization can be understood, in simple hydrogeological terms, as the result of a vertically rising fluid following the path of least

resistance. The pressure in the pore space impeding the rising fluid is directly related to the water mass above it, equal here to depth below sea level. Subsiding basins with shale layers or other aquitard seals often become over-pressured, and the heat from hydrothermal fluids also contributes substantially to this effect (Bethke, 1986). The seal of the normal fault (A, C or E) on the west, and the cap of allochthonous Shaley Pales abutting it, could also have created restriction to flow and caused an over-pressuring in the porespace (Fyfe et al., 1978). The incisions through the upper stratigraphy of the Waulsortian Mudbank, Shaley Pales into the Pale Beds by the Boulder Conglomerate removed 100s of meters of semi-permeable to non-permeable lithology. This development of the erosion surface, especially at the lowest points in the erosion, would alter the hydrogeology dramatically, creating significant changes in the permeability, and thus pressure, especially when considering underlying hydrothermal fluids. This creation of permeable pathways would have allowed the rising fluids to escape and provided a mechanism for focusing flow (Giambalvo et al., 2000).

If the ore fluids were rising during active extension, as considered likely by many workers (Ashton et al., in press, Davidheiser-Kroll et al., 2014, Hitzman and Beaty, 1996, Russell et al., 1981), high-density brines could have been trapped in grabens. This would create ideal conditions for the mixing of hydrothermal fluids with bacteriogenic fluids trapped in these topographic lows. This is also consistent with the very light $\delta^{34}S$ values found within the Conglomerate Group Ore (Anderson et al., 1989, Boyce et al., 1983b, Ford, 1996). The possibility that this fluid existed in an anoxic state for an extended period of time would allow for the re-oxidation and reduction of sulfur as well as the heating and feeding of sulfate reducing bacteria from the hydrothermal fluid, in a way analogous to modern hydrothermal springs (Jørgensen et al., 1990, Weber and Jørgensen, 2002). The mixing of hydrothermal fluids with the brine could have allowed for sulfide saturation and precipitation of metal sulfides, similar to the formation of brine pool massive pyrite formation (Tornos et al., 2008). Admittedly these areas of Conglomerate Group Ore are

much smaller and it is likely that the surface was covered by loose recent slides of carbonate material of the type that would eventually form the Boulder Conglomerate. Nonetheless, the material within low-lying incisions would have had a higher preservation potential than material on the flanks due to the continued erosion and formation of the Boulder Conglomerate. The preserved material would be constrained to areas covered during periods when local subsidence was faster than erosion, as well as the end of extension and beginning of infilling by the less erosive Thinly Bedded Unit (Philcox, 1989). The presence of some stratiform Zn-Pb mineralization within the Thinly Bedded Unit (Ashton et al., 1992) and pyrite mineralization within the lower UDL implies that this mechanism likely existed for some time after extension slowed.

2.6.4 Argillaceous Bioclastic Limestone and 5 Lens mineralization – erosive removal and apparent influence on ore development

It has been previously noted that there is a sharp, aligned decrease in Zn grade within the southwestern main mine (Blakeman, 2002) (Figure 2.7*b* and 4*n*). This lineament of decrease in grade follows a NE trend that is coincident with the Caledonian basement fabric, inviting speculation that it was created by deep-seated sources. This grade decrease has significant economic implications as it defines the western edge of exploitable mineralization. However, it is also coincident with the extent of the overlying ABL (Figure 2.7*a* and *b*). The Erosion Surface has removed the ABL above the high-grade areas and some of the ABL over the lower grade areas. The ABL is argillaceous and has major thick shale units (Philcox, 1984) and thus would have likely presented a major impediment to fluid flow (Ashton et al., in press). The variation in ore grades can be explained if the impermeability of the ABL created a fluid pressure shadow that retarded vertical fluid flow of the hydrothermal fluids through the Pale Beds ca. 250 meters below. The impermeability of the ABL would have also created a barrier to downward flow of the sulfide-enriched brine towards the Pale Beds.

2.6.5 Using Pb/Zn to interrogate timing

Given that both mineralized clasts of Pale Beds and in situ mineralization are found within the Boulder Conglomerate, the timing of mineralization must have straddled the Chadian deposition of the Boulder Conglomerate (Andrew and Ashton, 1982). The control of the Erosion Surface on Pale Beds mineralization in the SWEX and southeast main mine, discussed above, implies that the majority of that mineralization must have occurred during or after the creation of a paleo-erosion surface. If we consider Pb/Zn patterns as a method of distinguishing between vertical and horizontal flow, and allow for vertical flow to be associated with the creation of the Erosion Surface, then we can use Pb/Zn as a speculative method for discerning timing. Areas that show long distance Pb/Zn variability (primarily horizontal flow) would be associated with the pre-Chadian erosional event, while areas of short distance Pb/Zn variation (primarily vertical flow) would have been created syn- or post-Chadian erosion. Given these assumptions the main mine west would have been created in the less tectonically active phase of Navan's history, and the east main mine and the SWEX would have been created during the active faulting and unroofing of the Chadian. This would suggest that the majority of mineralization at Navan occured relatively close to the Chadian event. If the high Pb values in the west mine represent a distinct source, this could be explained either by changes in the underlying convecting cell with time (Russell et al., 1981) or by open system Zn loss to the ocean and/or erosion. Later, a more massive, vertical flow overprinted the horizontal flow in the east main mine and created the SWEX. The higher tonnage of mineralization associated with the later vertical flow can be explained through active faulting and fracturing influencing hydrothermal activity in coincidence with the availability of seawater-hosted bacteriogenic sulfide (Andrew and Ashton, 1982, Boyce et al., 1983a).

2.7 Conclusions

Examination of the extensive lithogeochemical database at Navan, in 3D, has shed new light on the broad history of fluid flow responsible for this giant deposit. We are beginning to discern different styles of fluid ingress in the deposit, responding to the evolution of tectonics during the Lower Carboniferous. We also constrain the influence of the Erosion Surface, and attendant un-roofing of parts of the Carboniferous sequence during Chadian faulting, in directing fluid flow, mineral development, and metal zoning.

Fluid flow in the southern main mine was largely horizontal (moving up dip to the northeast), had an evolving Pb/Zn ratio, and was controlled by fault-related fractures. This Pb/Zn ratio is distinct from elsewhere in the deposit (Figure 2.5) and could imply a separate metal source, however if the area was an open system and large majority of the Zn did not precipitate it could have had the same initial Pb/Zn ratio as other areas of the mine. The low permeability of the Pale Beds suggests fluids migrated slowly. The movement of these fluids was highly controlled by the structure of the Pale Beds, overlying lithologies (e.g. the ABL, Figure 2.7), local dolomites, and local lithological permeability variations.

The northern main mine and the SWEX show localized vertical flow with vertical stacking and a constant Pb/Zn ratio, indicating an intense, relatively homogeneous hydrothermal metal fluid source. The controlling factors on the location and focusing of the vertical flow are the E Fault and C Fault, which added fractures, and the Shaley Pales Trough, which acted as an aquitard. The Erosion Surface seems to have strongly influenced pathways for fluid flow by relieving the overburden pressure while also creating pathways for the surface fluid to provide sulfide. The deepest incisions created by the Erosion Surface also created local ore zones within the Boulder Conglomerate (Figs. 8 and 10). The nature of the creation of the Erosion Surface means that only the last part of deposition is preserved and any earlier mineralization above the Pale Beds has been lost to erosion. The careful mapping and validation of erosional surfaces that control ore zones can help to predict locations of similar traps.

2.8 Acknowledgements

BD-K is fully funded by a Tara Mines New Boliden PhD award. AJB is funded by NERC support of the Isotope Community Support Facility at SUERC. Thanks to Mike Philcox and Dave Coller for discussions on Irish geology. Special thanks to Leah Morgan for ideas and support. Jim Geraghty, Jamie Wilkinson, Mike Russell, and Tony Fallick are thanked for many discussions on Navan and wider aspects of the Irish orefield.

2.9 Figures

Figure 2.1. Schematic map of the Navan ore body with satellite deposits. Note locations of faults, zones, and major ore groups. All faults in the main mine and SWEX are traced at their intersection with the 5 Lens and 1 Lens, respectively. Modified from Ashton et al. (in press).

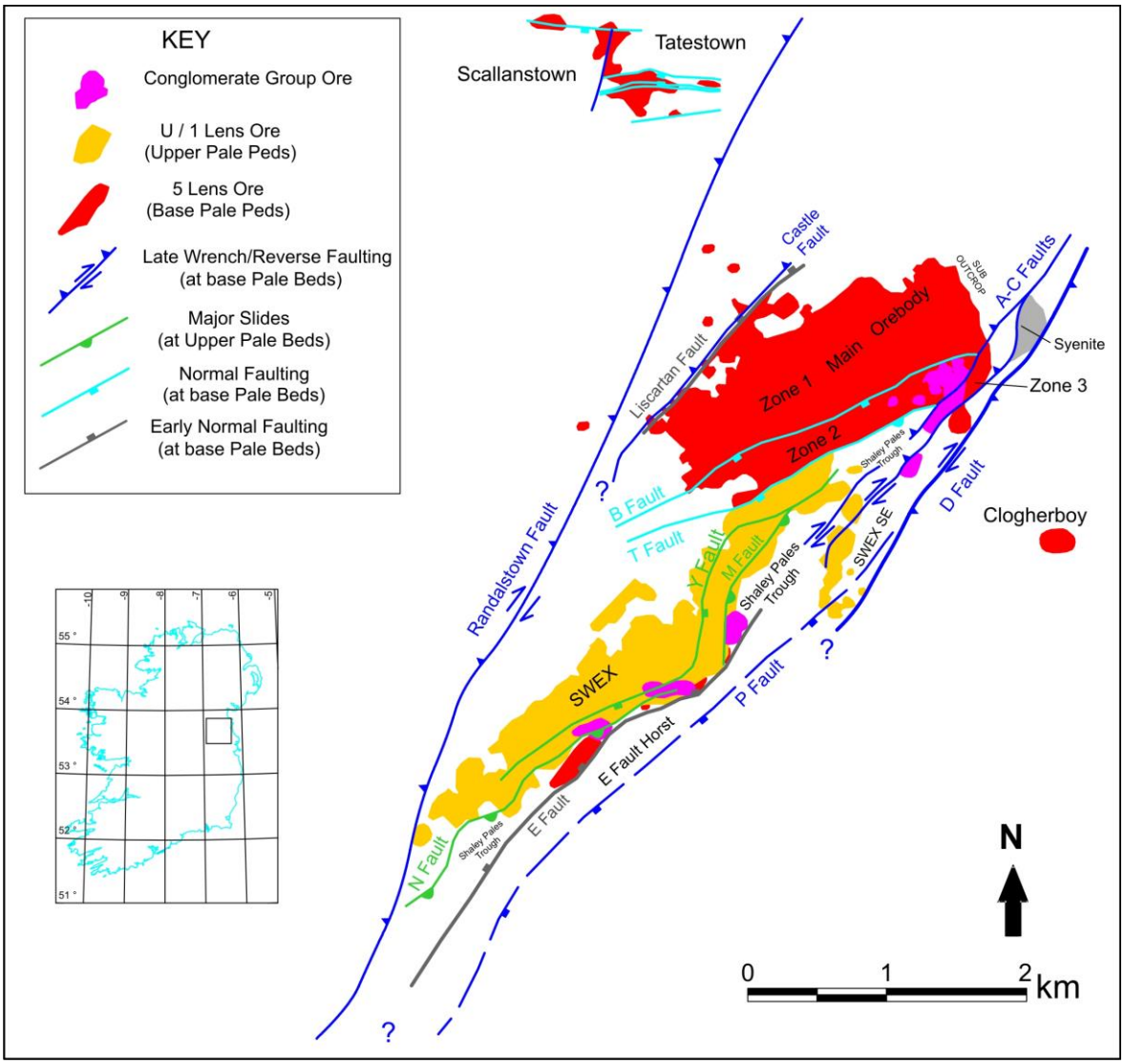

Figure 2.2. Cartoon of stratigraphic sequence with informal classifications. Ore lenses are shown in red, within the yellow Pale Beds. Note that the erosion surface (black dashed line) is dated to Chadian times and cuts deeper into the stratigraphy in the SE. The Boulder Conglomerate lies above the Erosion Surface. Modified from Ashton et al. (in press).

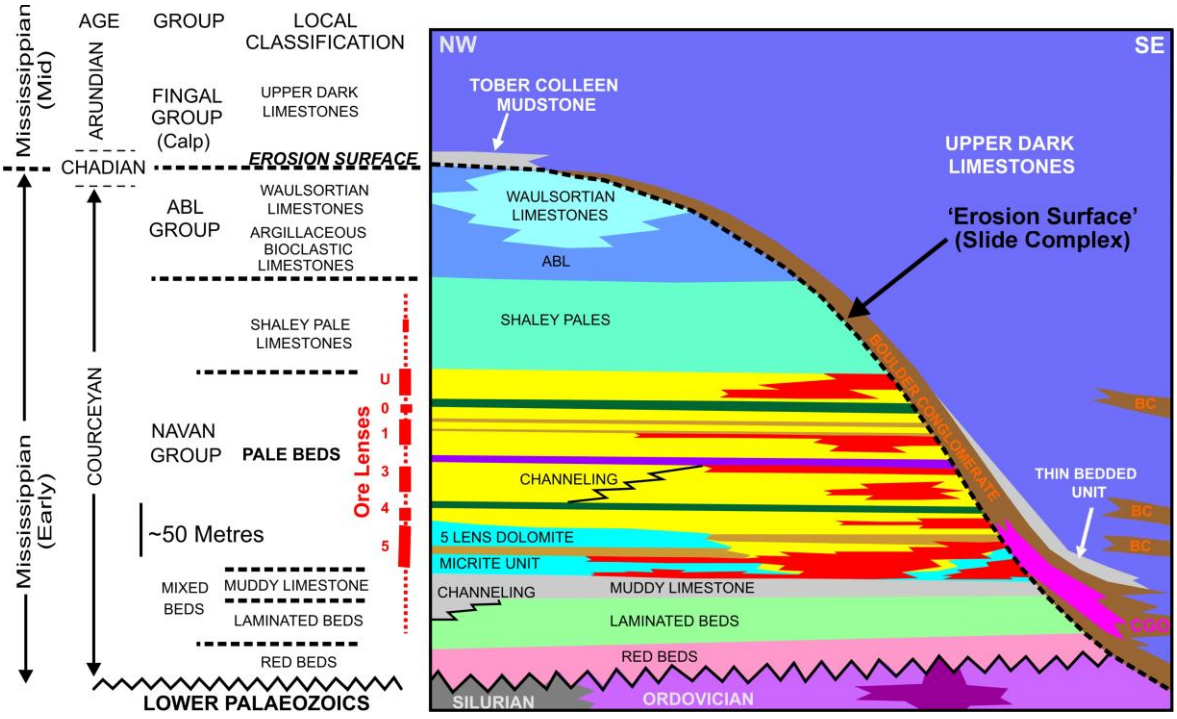

Figure 2.3. Pb/Zn ratios of the lowermost mineralized lens from all areas of the mine (main mine: 5 Lens, SWEX: 5 and 3-1 lenses). The variation of Pb/Zn ratios within the main mine is much more prominent than within the SWEX. The lenses shown are the most widely mineralized and represent the majority of ore found at Navan.

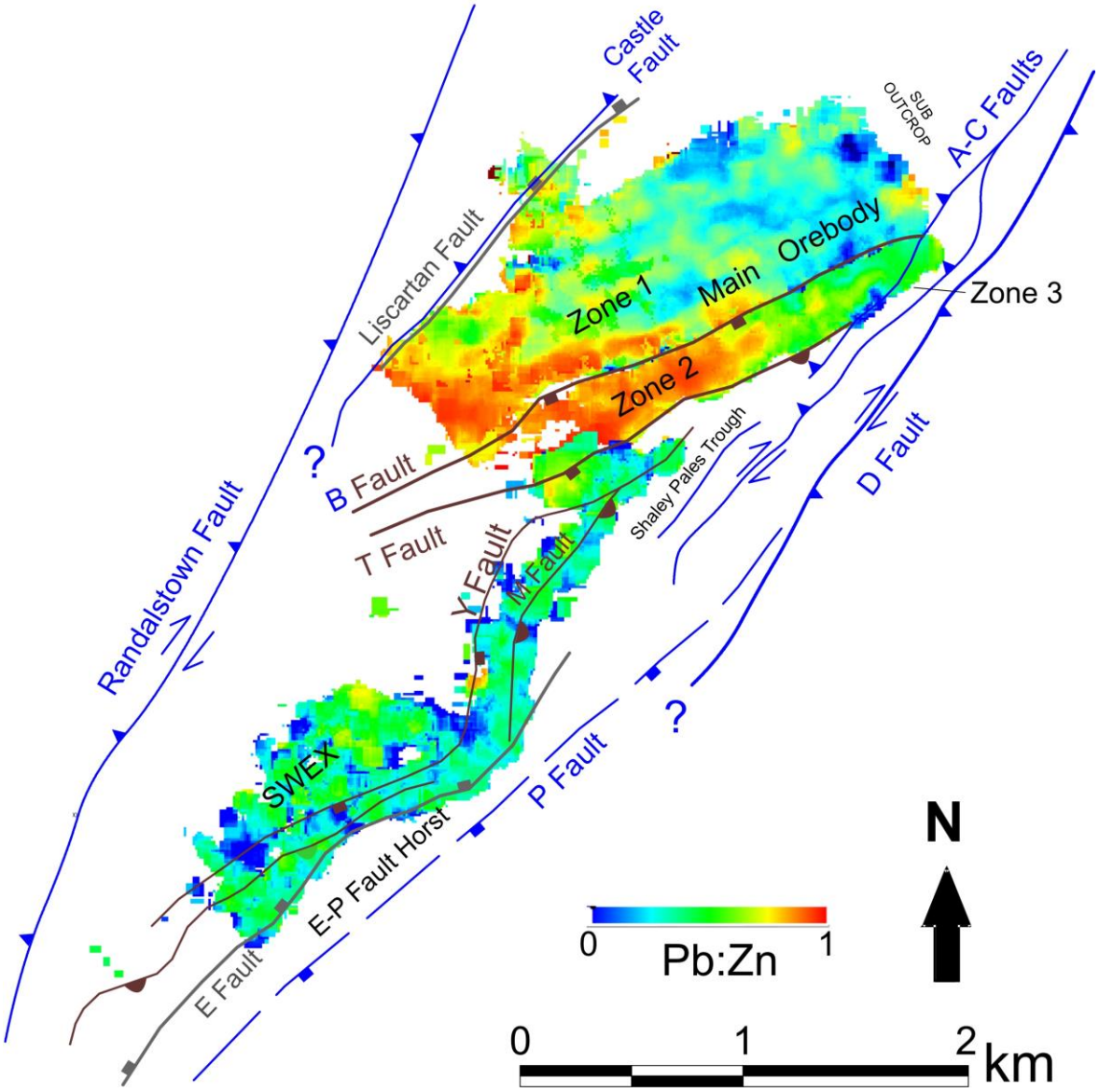

Figure 2.4. A two-page figure showing a grid of aggregated element maps and their respective histograms for the main mine. Columns contain maps that represent the element or ratio of interest, while rows contain maps representing the same stratigraphic layer. The 1 Lens row also shows an outline of the Main Ore body and faults traced at their intersection with the 5 Lens. Note that the eastern edge of the Pb and Zn maps shows the highest values, with over 10% Zn and 3% Pb seen in all lenses. The 1 Lens is only mineralized in the east section of the mine above the highest grade areas. The 5 Lens Zn map has a strong grade drop along a NNE line along the SW side of the deposit. It has been previously noted (CITE) that although the deposit is bound by major faults, the grade contours actually follow a more NNE direction along fracture networks. The Pb/Zn of the 5 Lens has a small absolute change (ca. 1) across the deposit. This variation is systematic with the highest ratios in the SW and the lowest in the NE. The ratios within other lenses are more homogeneous but generally reflect ratios in the 5 Lens.

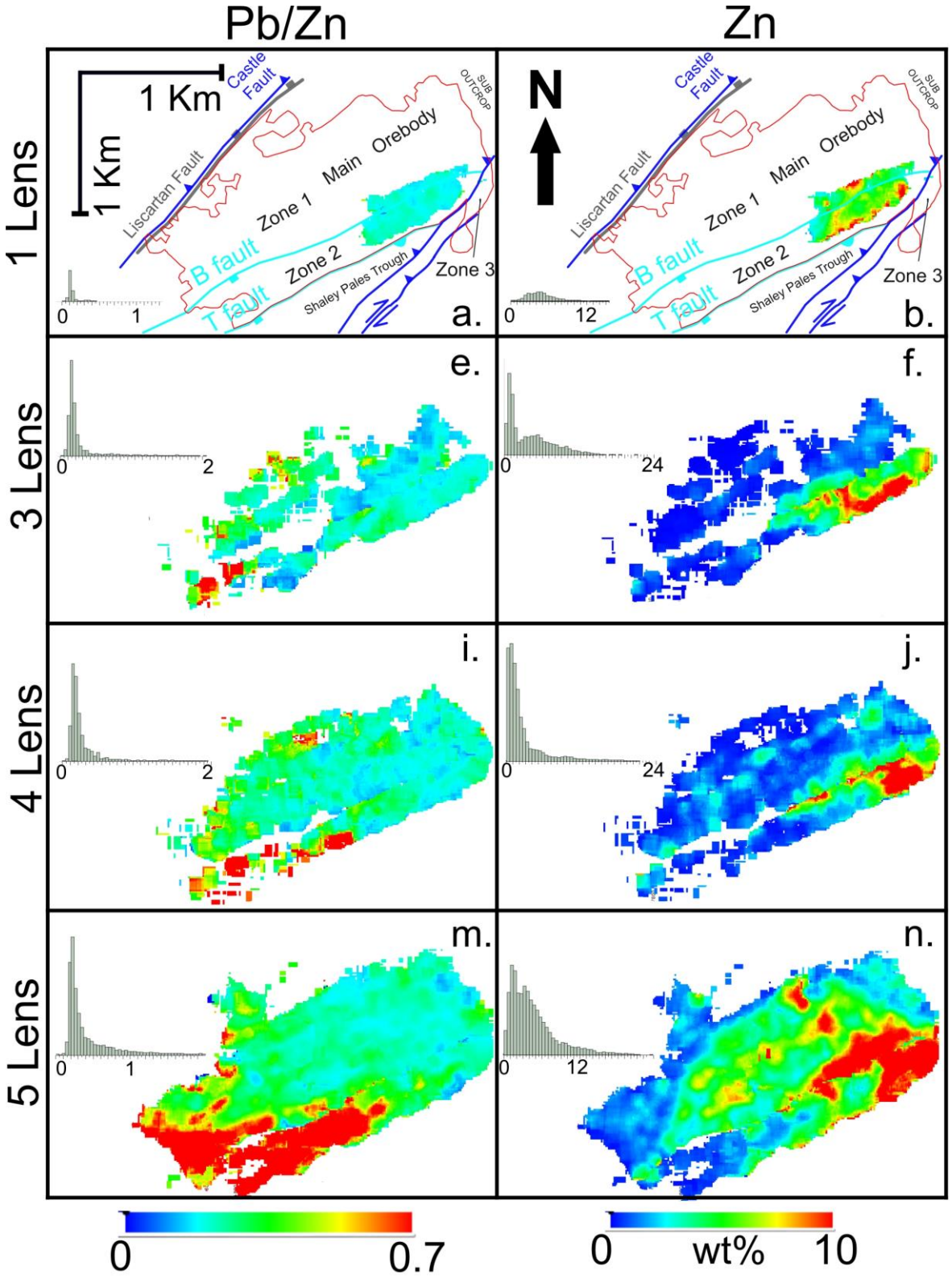
Pb/Zn
Zn
1 Lens
3 Lens
4 Lens
5 Lens
1 Km
1 Km
N
Castle Fault
Liscartan Fault
Main Orebody
Zone 1
Zone 2
Zone 3
B fault
T fault
Shaley Pales Trough
SUB OUTCROP
a.
b.
e.
f.
i.
j.
m.
n.
0
1
2
12
24
0
0.7
wt%
10

Figure 2.4, continued

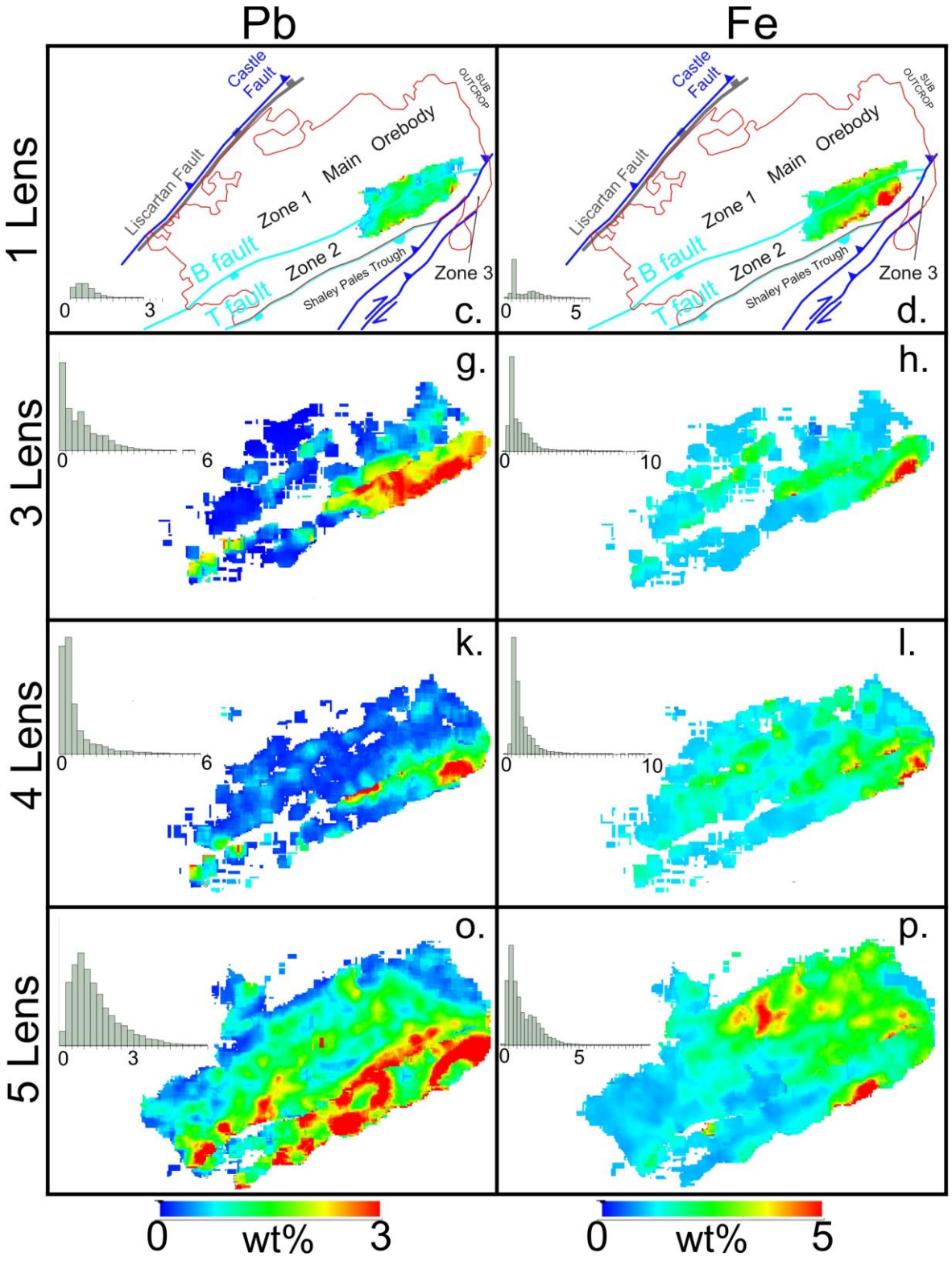

Figure 2.5. Map of Zn/Pb values (note inverse of typical Pb/Zn) for the main mine 5 Lens, with values < 2.75 shown in red and those > 2.75 in blue. The accompanying histogram yields a clearly bimodal distribution with the same color pattern, which shows how Zn/Pb ratios vary spatially. Values below 2.75 are largely from the SW, while those above 2.75 are from the NE.

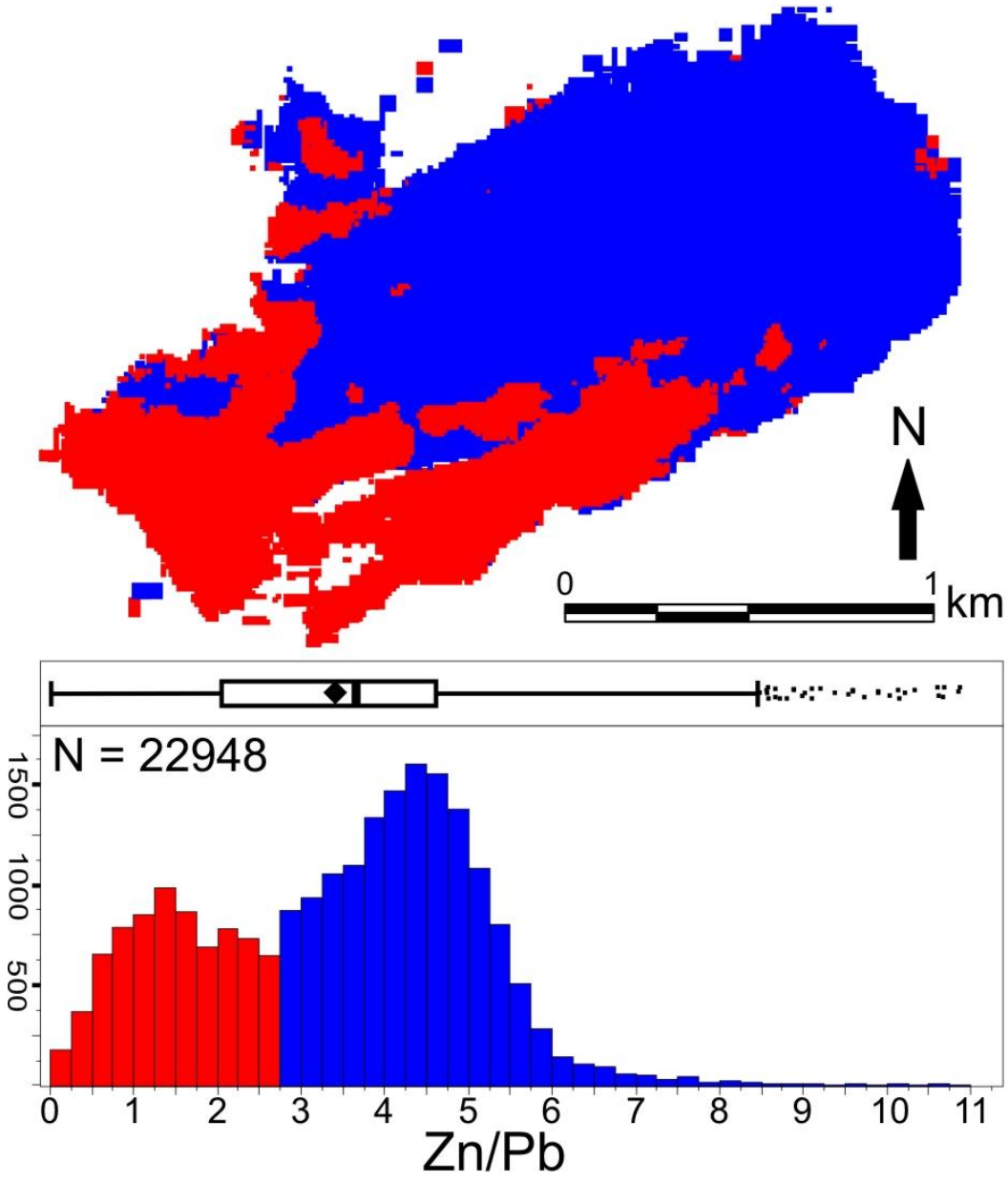

Figure 2.6. A two-page figure showing aggregated element maps and their respective histograms for the SWEX. Columns contain maps that represent the element or ratio of interest, while rows contain maps representing the same stratigraphic layer. The CGO row also shows an outline of the SWEX and faults traced at their intersection with the 1 Lens. The SWEX has a general trend of higher grades on the eastern edge and lower grades to the west. However there are three clear areas of higher enrichment in Zn and Pb, as the high grade areas in the 1 Lens are more elongated along the Shaley Pales Trough and the high grade areas in the U Lens are more spherical. Fe concentrations are much higher in the stratigraphically higher lenses. The Pb/Zn ratio is homogeneous across the entirety of the SWEX.

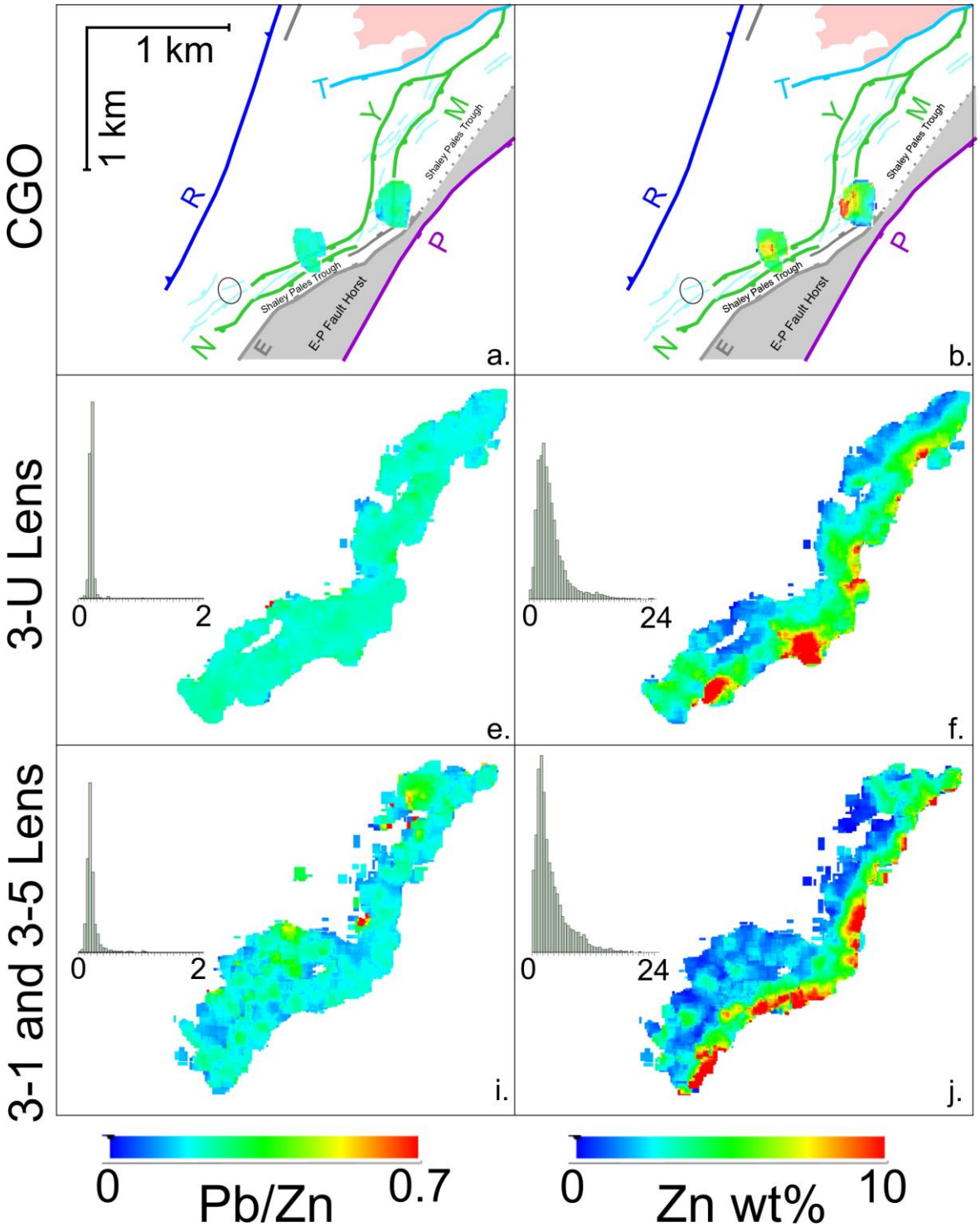

Figure 2.6, continued

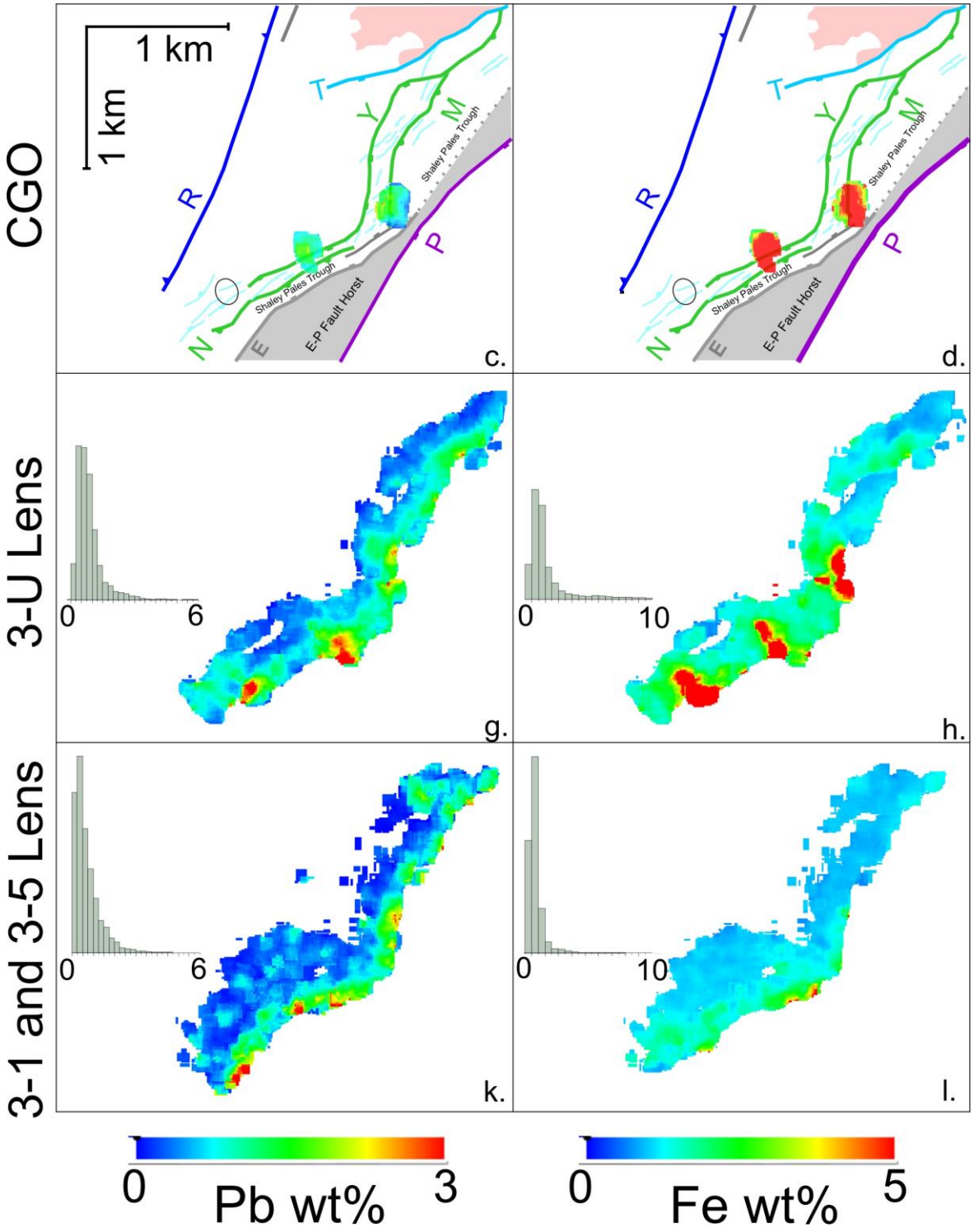

Figure 2.7. (top) Map of lithologies exposed at the Erosion Surface, extracted from Ashton et al. (in press) overlain by the outline of the Orebody in red. **(bottom)** Map of Zn concentrations for the lowermost mineralized lens of the Orebody, with the outline showing the extent of the presently existing ABL in black. Note that the ABL boundary within the Maine Mine coincides with an abrupt drop in grade (blue to green).

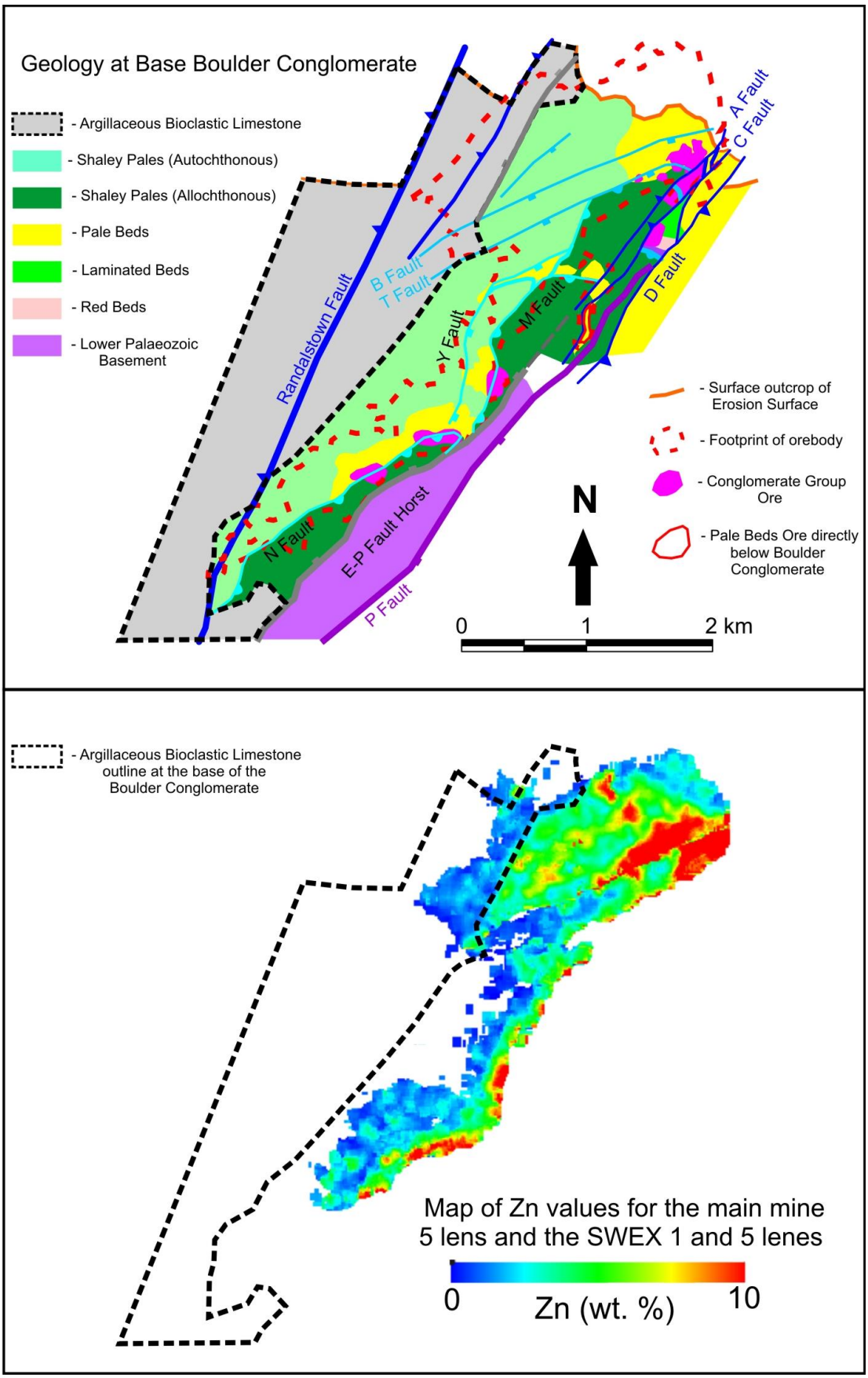

Figure 2.8. A geologic map, from Ashton et al. (in press), on the base of the erosion surface (ES) created by the boulder conglomerate, contoured to 20 meters; major faults are shown in black, and color represents the lithologies that are in contact with the ES. Elevations are shown to an arbitrary local mine zero. The ES cuts deeper into the stratigraphy to the south. On the eastern edge along the major normal faults a major allochthonous unit is present (Shaley Pales Trough). The location of exposed Pale Beds is quite varied but is generally concentrated to the eastern edge of the deposit along the Shaley Pales Trough. In the lower map the added areas in red represent all areas of diamond core drilling intersections of > 1% Zn and so includes all Conglomerate Group Ore. Areas a, b and c are all above Pale Beds exposed within valleys or channels cut into the Navan Group. Area d is again above exposed Pale Beds but has far fewer incisions than the other areas. The northeastern area e has high metal concentrations but has been complicated by a large degree of reverse faulting during compression. However it is similar to the other areas in that it lies directly over exposed pale beds (Ashton et al., 1992), and in the seeming relationship with the lowest or most channeled areas; this implies it likely resembled the other areas before compression.

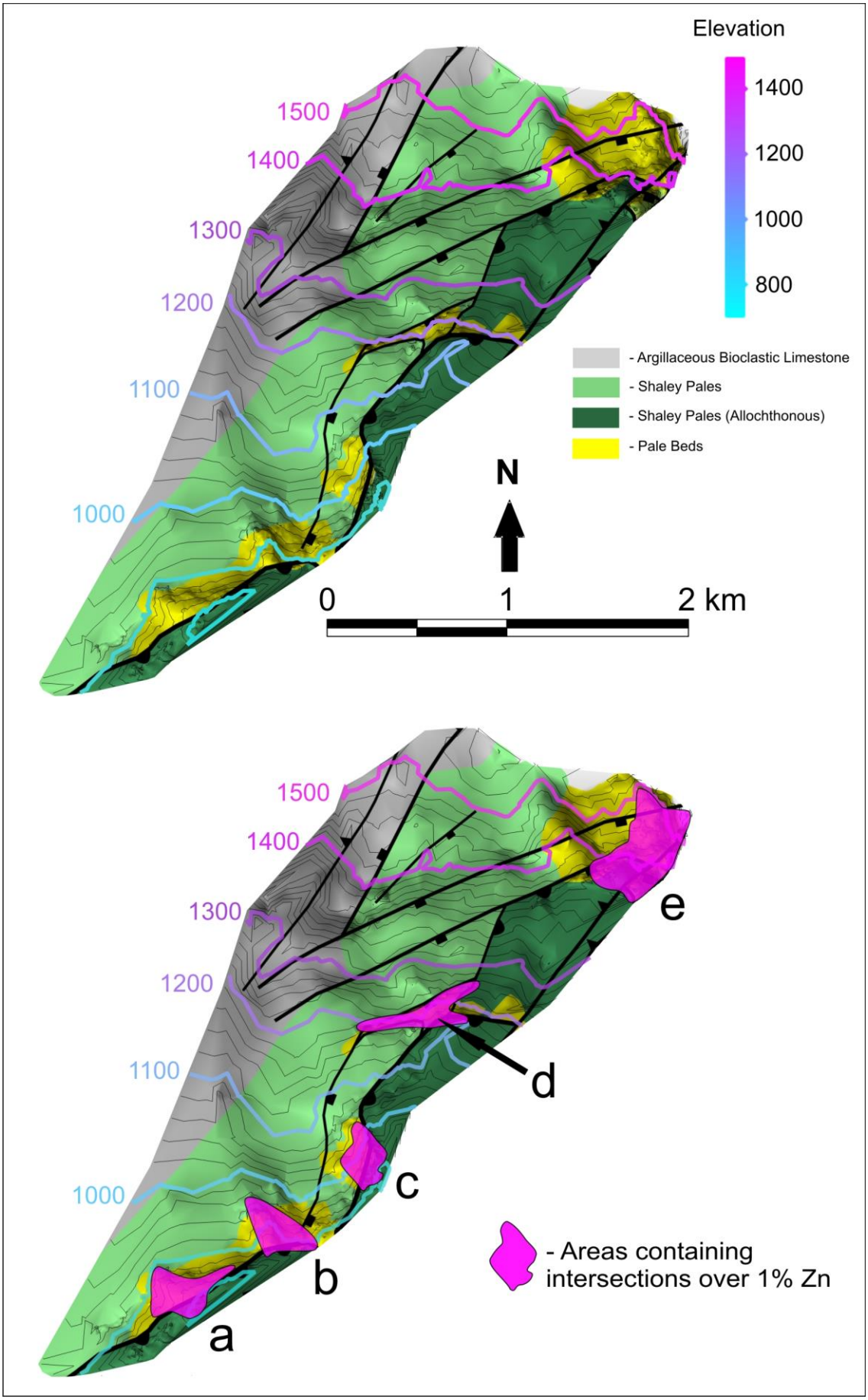
Elevation
1400
1200
1000
800
1500
1400
1300
1200
1100
1000
- Argillaceous Bioclastic Limestone
- Shaley Pales
- Shaley Pales (Allochthonous)
- Pale Beds
N
0
1
2 km
1500
1400
1300
1200
1100
1000
a
b
c
d
e
- Areas containing intersections over 1% Zn

Figure 2.9. Schematic diagram showing horizontal and vertical flow end members. For horizontal flow, the fluid moves vertically from a single basement source, is constrained by an impermeable layer, and moves horizontally over long distances. For vertical flow, the fluid has multiple source regions within the basement, so the flow is largely vertical and has only local horizontal movement.

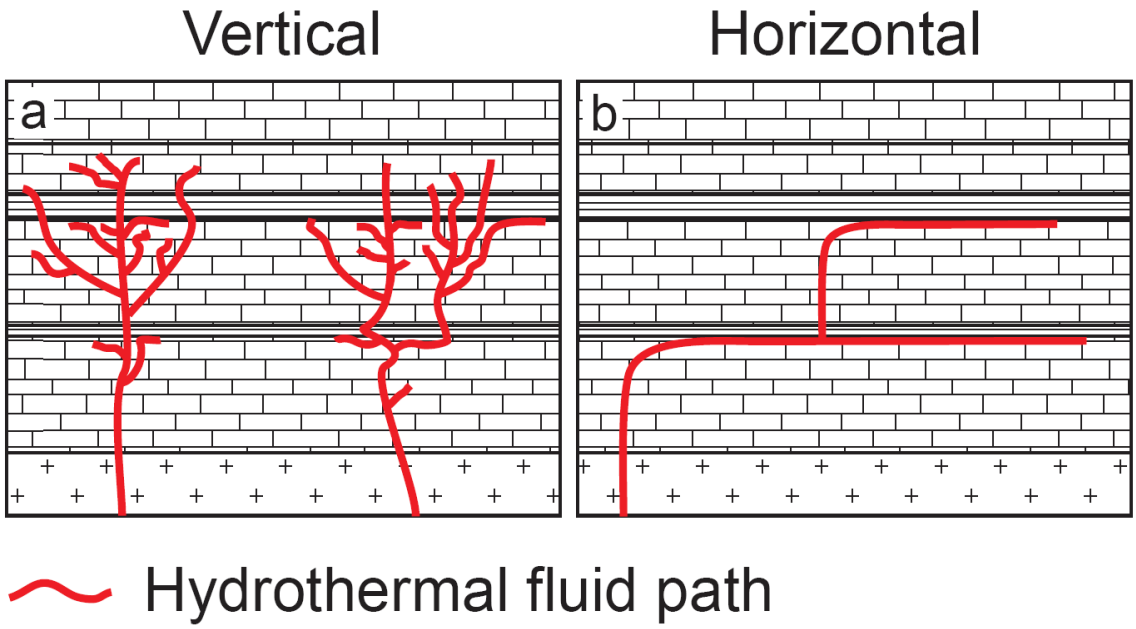

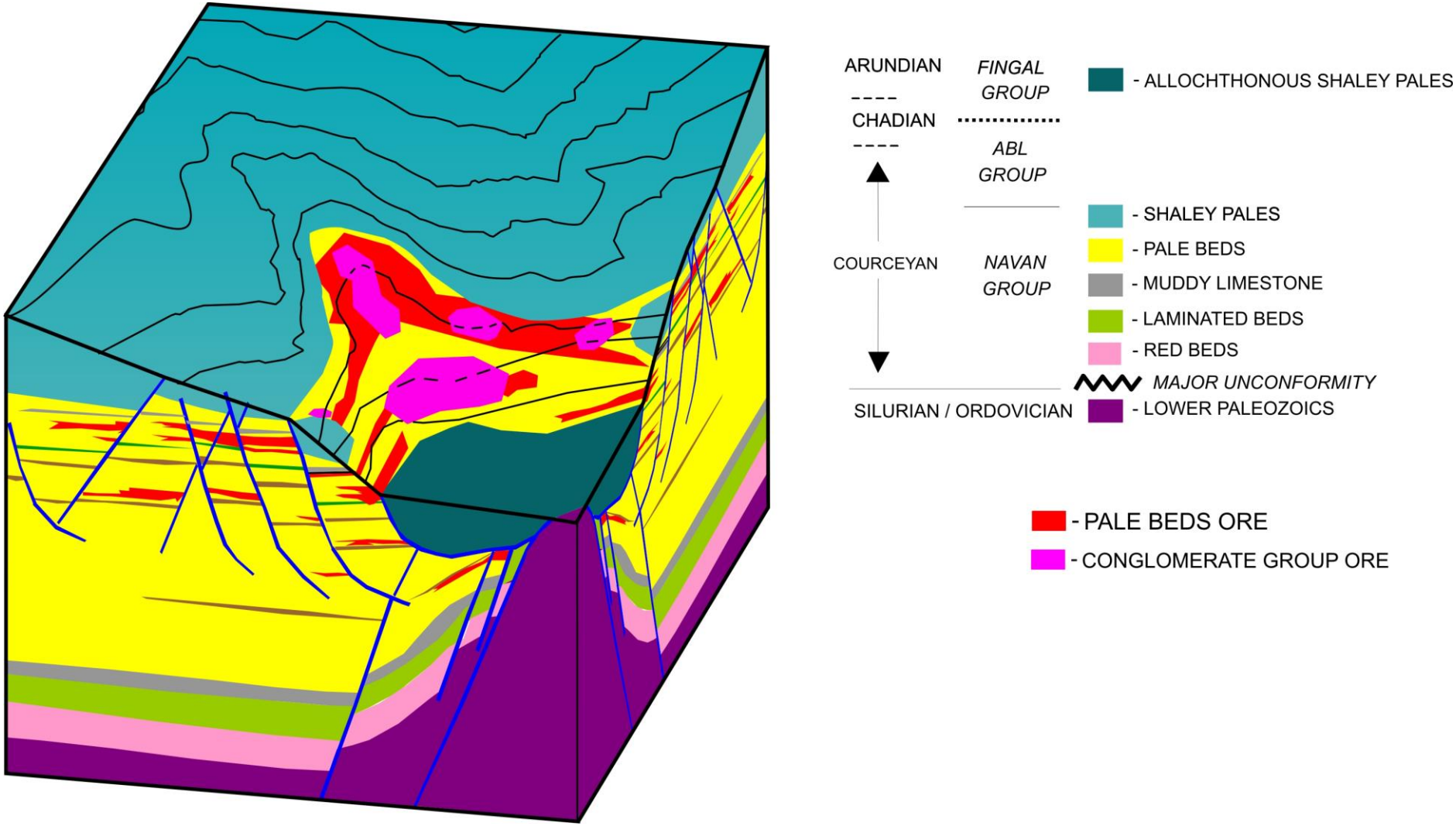

Figure 2.10. A schematic block model based on a region near area b of Figure 2.7. The contour lines show a channel cutting into the Pale Beds just to the NW of the allochthonous Shaley Pales that terminates along the E Fault. The areas where Conglomerate Group Ore is found above the Pale Beds have been added to show that the majority of ore is focused within the lowest points of the channel.

Table 2.1. Table of average metal concentration values used to create metal concentration maps.

Zone	Lens	n	avg Zn	std	avg Pb	std	avg Fe	std	avg Pb/Zn	std
Main	1 Lens	6278	2.25	2.65	0.44	0.52	1.71	1.08	0.22	0.10
Main	3 Lens	10945	2.11	2.87	0.44	0.60	1.45	0.78	0.25	0.18
Main	4 Lens	15810	2.25	2.93	0.53	0.69	1.56	0.68	0.30	0.34
Main	5 Lens	22978	3.56	3.51	1.17	0.98	1.40	0.94	0.46	0.50
SWEX	U lens	12513	3.88	2.59	0.82	0.56	2.17	2.00	0.21	0.04
SWEX	1 Lens	12712	3.24	2.58	0.63	0.51	1.21	0.43	0.20	0.08
SWEX	5 Lens	1549	4.59	4.22	0.92	0.91	1.49	0.70	0.20	0.08

Chapter 3

Mantle heat drives hydrothermal fluids responsible for carbonate-hosted base metal deposits: Evidence from $^{3}He/^{4}He$ of ore fluids in the Irish Pb-Zn ore district

B. Davidheiser-Kroll, F.M. Stuart & A.J. Boyce

Isotope Geosciences Unit, Scottish Universities Environmental Research Centre, Rankine Avenue, East Kilbride, G75 0QF, UK

Published in Mineralium Deposita, v. 49, no. 5, pp. 547-553

- F.M. Stuart provided guidance with respect to ideas, isotope analysis, and editing
- A.J. Boyce provided supervision and editorial guidance

3.1 Abstract

There is little consensus on whether carbonate-hosted base metal deposits, such as the world-class Irish Zn+Pb ore field, formed in collisional or extensional tectonic settings. Helium isotopes have been analyzed in ore fluids trapped in sulfide samples from the major base metal deposits of the Irish Zn-Pb ore field in order to quantify the involvement of mantle-derived volatiles, that require melting to be realised, as well as test prevailing models for the genesis of the ore fields. $^{3}He/^{4}He$ ratios range up to 0.2 R_a, indicating that a small but clear mantle helium contribution is present in the mineralising fluids trapped in galena and marcasite. Sulfides from ore deposits with the highest fluid inclusion temperatures (~200°C) also have the highest $^{3}He/^{4}He$ (> 0.15 R_a). Similar $^{3}He/^{4}He$ are recorded in fluids from modern continental regions that are undergoing active extension. By analogy we consider that the hydrothermal fluids responsible for the carbonate-hosted Irish base metal mineralization circulated in thinned continental crust undergoing extension and demonstrate that enhanced mantle heat flow is ultimately responsible for driving fluid convection.

3.2 Introduction

Carbonate-hosted base metal deposits are a major source of the world's Zn, Pb and Ag. The ores hosted in the Carboniferous carbonates in the Irish Midlands constitute the highest known concentration of Zn per square kilometer on the planet (Singer, 1995), and the province includes the giant Navan deposit (Ashton et al., in press). Despite extensive research, there remains no consensus on the tectonic setting and driving mechanism for their genesis (Leach et al., 2005, Russell, 1978, Wilkinson and Hitzman, in press). Difficulty in interpreting the origin of the Irish mineralization arises partly from the coincidence of both extensional and compressional features within the deposits. For example, extensional features typically appear to have formed early, e.g., syndepositional faulting; submarine debris flow breccias (Anderson et al., 1998, Ashton et al., in press,

Boyce et al., 1983a, Taylor, 1984), whereas compressional features are common later in the geological history of the deposits, e.g. reverse and thrust faulting; Variscan shortening (Hitzman and Beaty, 1996, Johnston et al., 1996, Leach et al., 2010). There are no absolute age determinations for ore deposition, however, controversial paleomagnetic data support ore deposition at 350-269 Ma (Johnston et al., 2013, Pannalal et al., 2008b, Pannalal et al., 2008a, Symons et al., 2007, Symons et al., 2002).

One view is that the ore deposits developed in compressional tectonic regimes, where crustal thickening was caused by thrust belt loading, leading to extension and the hydrological conditions necessary for topographically driven fluid flow. This is linked to Variscan compression arising from the collision of Gondwana and Laurussia (Figure 2.1; Garven et al., 1999, Hitzman, 1999, Leach et al., 2005, McCann et al., 2006, Pannalal et al., 2008b). In this case, mineralization must be substantially younger (310 Ma) than the age of the host rocks (~350 Ma). In the alternative view mineralization is intimately related to thinning and extension of the crust and lithosphere during the Mississippian in response to upwelling of the asthenosphere (figure 1b Russell, 1978). This increased heat flow in the crust and stimulated convection of surface fluids into basement where interaction resulted in the generation metal-rich acidic fluids (Everett et al., 1999, Everett et al., 2003, LeHuray et al., 1987, Russell, 1978, Walshaw et al., 2006). In this case, the ore deposition occurred during extension around the time of host rock deposition, and substantially earlier than the age favored by the compressional model.

The current upper mantle is characterized by $^{3}He/^{4}He$ of 6 – 9 R_a (where R_a is the atmospheric value; 1.39×10^{-6}) whereas helium in the continental crust is largely derived from the radioactive decay of U and Th resulting in $^{3}He/^{4}He < 0.01\ R_a$ (Ozima and Podosek, 2002). Waters and gases sampled from regions of active rifting have $^{3}He/^{4}He > 0.04\ R_a$ indicating that volatiles are exsolved from mantle melts and have advected into the shallow crust (Oxburgh et al., 1986). Helium isotopes of ancient hydrothermal fluids are trapped and preserved in ore minerals and can be used to trace the contribution of mantle

volatiles and heat sources in a variety of ore "deposit–types" (e.g. Burnard and Polya, 2004, Stuart et al., 1995).

Here we report the helium isotope composition of ore fluids in sulfides from the main Pb-Zn mines in Ireland. All contain a small but genetically significant component of mantle-derived He. This indicates that heat advected from the mantle, most likely during a period of crustal thinning and extension, was the driver of fluid convection that led to the development of this ore field.

3.3 Samples and methods

Helium isotopes are reported from 20 samples of sulfide (galena and marcasite) sourced from the five main economic Irish type deposits: Navan, Silvermines, Lisheen, Galmoy and Tynagh. The samples selected are from areas in or close to putative feeder faults, with the exception of the Tynagh samples, which are from museum collections, and thus only the general area of origin is known.

Specimens were gently crushed, sieved and 0.5–2 mm sulfide grains were handpicked under a binocular microscope then washed in analar grade acetone. Helium was extracted from fluid inclusions by *in vacuo* crushing of approximately ~1 g of each sample in a multi-sample hydraulic crusher. The gas was purified prior to analysis with a MAP 215-50 mass spectrometer following procedures similar to those of Stuart et al. (2000). After crushing samples were sieved and the crushed material (<100 μm) was weighed to allow determination of He concentrations (Table 3.1).

Sulfur isotopes were measured on 5-10 mg of the powdered sample that remained after crushing for helium extraction. The sulfides were converted to SO_2 and analyzed on a VG SIRA 2 mass spectrometer by standard techniques (Robinson and Kusakabe, 1975).

3.4 Results

Atmosphere-corrected $^{3}He/^{4}He$ ratios range from 0.03 to 0.21 R_a (Table 3.1). There is no correlation between the ^{4}He concentration and $^{3}He/^{4}He$, indicating that no significant lattice-hosted radiogenic ^{4}He was released by crushing (Kendrick et al., 2002, Stuart et al., 1994). This is consistent with the extremely low U and Th content of the minerals analyzed here (see appendix) and with previous studies using this apparatus (e.g. Stuart et al., 2003).

$^{3}He/^{4}He$ in excess of ~0.04 R_a in crustal fluids typically requires a contribution of mantle-derived He (Oxburgh et al. 1986). Before making a similar interpretation for ancient hydrothermal fluids it is necessary to rule out the generation of nucleogenic ^{3}He by bombardment on ^{6}Li by thermal neutrons (Andrews and Kay, 1982). Using the neutron flux calculated from the composition of the ore minerals we calculate that the radiogenic ^{3}He produced in the trapped fluids is 5 orders of magnitude less than measured in these samples (see Appendix 3.1). This rules out *in situ* production as an explanation for the elevated $^{3}He/^{4}He$ in the inclusion fluids, and strongly implies that the helium isotope ratio can be used to faithfully trace the source of volatiles in the ore fluids.

Sulfide $\delta^{34}S$ values range from +15.9 to -16.1 ‰ (Table 3.1), which fall well within the range recorded for each deposit (e.g. Anderson et al., 1998, Barrie et al., 2009, Boast et al., 1981, Boyce et al., 1983a, Wilkinson et al., 2005b).

3.5 Discussion

3.5.1 Mantle He in Irish Pb-Zn deposits – extension and deep faulting

Each mine displays a range of $^{3}He/^{4}He$ (Table 3.1) that can most simply be interpreted as a binary mixture of crustal radiogenic He ($^{3}He/^{4}He$ ~ 0.01 R_a) and mantle-derived He ($^{3}He/^{4}He$ > 6 R_a). Assuming that the Carboniferous modern sub-continental lithosphere mantle had a $^{3}He/^{4}He$ of 10 R_a, the highest $^{3}He/^{4}He$ (0.15 to 0.2 R_a) values are consistent with ~2 % of the He in the ore fluids being derived from the upper mantle.

Previous studies have shown that there is a similar mantle He contribution to crustal fluids in regions of active extension (e.g. Ballentine et al., 2002, Oxburgh et al., 1986). Mantle helium is typically absent in aqueous fluids in basins that formed through tectonic loading of the crust during compression, where crustal radiogenic helium dominates (Oxburgh et al., 1986). Furthermore, the flux of mantle-derived ^{3}He into the continental crust is strongly coupled to mantle heat flow and both are elevated in extensional settings, even where volcanic activity is not manifest at the surface (Marty et al., 1992, Oxburgh et al., 1986).

Deep faults likely act as conduits for the migration of mantle-derived volatiles into the shallow crust (e.g. Kennedy et al., 1997). All of the studied deposits are located in areas with evidence of significant, fault-related subsidence during the Lower Carboniferous (Boyce et al., 1983a, Strogen, 1988). Across Ireland the structural grain is strongly influenced by the preceding Caledonian Orogeny, most manifest in the occurrence of the broad Iapetus Suture Zone (Figure 2.1 Phillips et al., 1976) There is general acceptance that the controlling faults associated with the deposits are re-activated Caledonian structures (Johnston et al., 1996, Phillips et al., 1976) which have certainly penetrated to the underlying Lower Palaeozoic Caledonian basement (e.g. Dixon et al., 1990, Everett et al., 2003), and possibly deeper (Mills et al., 1987). It is these faults that controlled the input of hydrothermal fluids to the deposits, and it is also likely that these fundamental features also facilitated the tapping of mantle-derived volatiles into the crust. Upon reaching the crust, the volatiles were diluted by the principal ore fluid of the Irish deposits, which is considered to be dominated by Mississippian evaporated seawater that had strongly interacted with the Lower Paleozic basement lithologies (Banks et al., 2002, Bischoff et al., 1981, Wilkinson, 2010).

Fluid inclusion trapping temperatures have not been determined on the samples analyzed for He isotopes, but, there is an abundance of fluid inclusion data (Ashton et al., in press, Banks and Russell, 1992, Samson and Russell, 1987, Wilkinson et al., 2005b), which

facilitate comparison of 'temperature' and the concentration of mantle-derived ^{3}He in the ore-forming fluids. We note a tendency for the mineral deposits hosted by Waulsortian Limestone formation in the central southern part of the orefield (Figure 3.1) to be generally associated with the highest $^{3}He/^{4}He$ and the highest fluid inclusion temperatures in the metal bearing ore fluid (Figure 3.2). In contrast, the Navan deposit is hosted largely by the contemporaneous Navan Group (Andrew, 1986), has the lowest published fluid inclusion temperatures in the metal bearing ore fluid, and consistently displays lower $^{3}He/^{4}He$.

The deposits with highest $^{3}He/^{4}He$ and fluid inclusion temperatures (Silvermines, Galmoy, Lisheen) are located within the central southern part of the Irish Lower Carboniferous in and around the Shannon Trough. There is abundant evidence that these areas have undergone the greatest subsidence, with the development of synsedimentary breccias, and cross-fault thickening of sequences during late Tournaisian (Andrew, 1986, Ashton et al., in press, Boyce et al., 1983a, Hitzman, 1999, Shearley et al., 1995, Wilkinson et al., 2011). The greatest subsidence at Navan occurred later, during Chadian times resulting in submarine debris flows, although tectonism is seen in the upper parts of the Navan Group prior to this. Thus, it appears that the deposits around the Shannon Trough and southern Ireland, which have a distinct character compared to Navan, show the highest temperatures of mineralization as well as the most influence of mantle ^{3}He. It is thus perhaps not surprising new discoveries of Irish type Zn+Pb ores have been identified, associated with contemporaneous Carboniferous basaltic diatremes and pyroclastic deposits, in the Limerick Basin (Figure 3.1 Elliot et al., 2013, McCusker and Reed, 2013). This association between diatremes from low degree partial melts, extensional faults, and SEDEX deposits has been documented in the Selwyn Basin, Yukon (Goodfellow et al., 1995).

The occurrence of the mantle He component demands a high heat flow in the crust during mineralization, and also provides a strong genetic link to crustal extension. This extension is reflected in differential subsidence across Ireland during the Lower Carboniferous, linked to reactivation of deep-lying, inherited fault systems. These faults facilitated the

movement of mantle volatiles into the crust where they mixed with and were diluted by the hydrothermal fluids which carried the ore metals.

3.5.2 Significance for carbonate-hosted mineralization

Despite the evident relationship between mantle He, tectonism, heat and ore-bearing hydrothermal fluids, the greatest concentration of base metals, at Navan, does not correlate with the most intense heat flow and strongest mantle He isotope signature. Indeed, Navan is 4 to 5 times larger than any of the central, southern deposits but has the lowest contribution of mantle ^{3}He in our study. Thus, whilst the mantle influence is felt, and is genetically significant in terms of its association with extension, the influence of mantle volatiles, and fluid heat, was not the major influence on ore deposit size. It appears rather to be the efficiency of precipitation of ore metals that is key to ability to develop economic levels of accumulation; in particular the dominance of bacteriogenic sulfide (Fallick et al., 2001).

This importance of bacteriogenic sulfide is echoed in the absence of correlation between helium and sulfur isotope data. Sulfide ore deposition in all economic Irish type Pb-Zn deposits was a result of mixing of a hot, hydrothermal fluid with a cool, surface fluid. In practice, the hydrothermal metal-bearing fluid had a limited reduced sulfide component, that was likely derived from the underlying Lower Paleozoic basement (Blakeman et al., 2002) $\delta^{34}S$ range from 0 to +15‰. In contrast, the surface fluid was essentially seawater containing bacteriogenic sulfide, with a typical ore-stage $\delta^{34}S = -15 \pm 10$ ‰. Thus, it might be anticipated that sulfides with a dominantly hydrothermal $\delta^{34}S$ signature would have higher $^{3}He/^{4}He$ than those dominated by seawater-derived sulfur. The absence of such a correlation between S and He isotopes between or within the deposits (Figure 3.3) highlights the importance of mixing with surface/shallow crustal fluids in the genesis of these deposits, but underlines that ore forming processes are not reliant simply on heat. The seawater-derived fluid, with its associated bacteriogenic sulfide, overwhelms the

sulfur budget in all producing Irish type deposits (Anderson et al., 1998, Blakeman et al., 2002, Boyce et al., 1983b, Fallick et al., 2001).

3.6 Conclusions

Helium isotopes have been measured in sulfides from every producing Irish mine. All contain a component of mantle-derived He indicating that at least some heat from the mantle during a period of crustal attenuation was involved in the fluid convection which led to the development of this ore field (Figure 3.4). The mantle heat may be important in initiating or driving localized hydrothermal cells but its existence is an indication of the tectonic setting and thermal regime of Irish ore field genesis.

3.7 Acknowledgements

BD-K is fully funded by a Tara Mines New Boliden PhD award. AJB is funded by NERC support of the Isotope Community Support Facility at SUERC. Thanks to the Geological Survey of Ireland and Gerry Stanley, and to the Hunterian Museum and John Faithfull for allowing access to samples from older deposits. We also acknowledge Paul McDermott from Galmoy and Roy Coates from Lisheen for sending samples as well as John Ashton and Rob Blakeman of Tara Mines, Navan. Special thanks to Matthijs van Soest and Leah Morgan for their ideas and support. We would like to thank Wayne Goodfellow for a helpful and informative review.

3.8 Figures

Figure 3.1. Simplified geological map of Ireland, showing location of those Mississippian carbonate-hosted Irish type deposits that have produced substantial ore; all have been analyzed in this study (adapted from hand out map Minerals Ireland Exploration & Mining Division). The approximate trace of the inferred Iapetus Suture is shown in purple after Phillips et al. (1976).

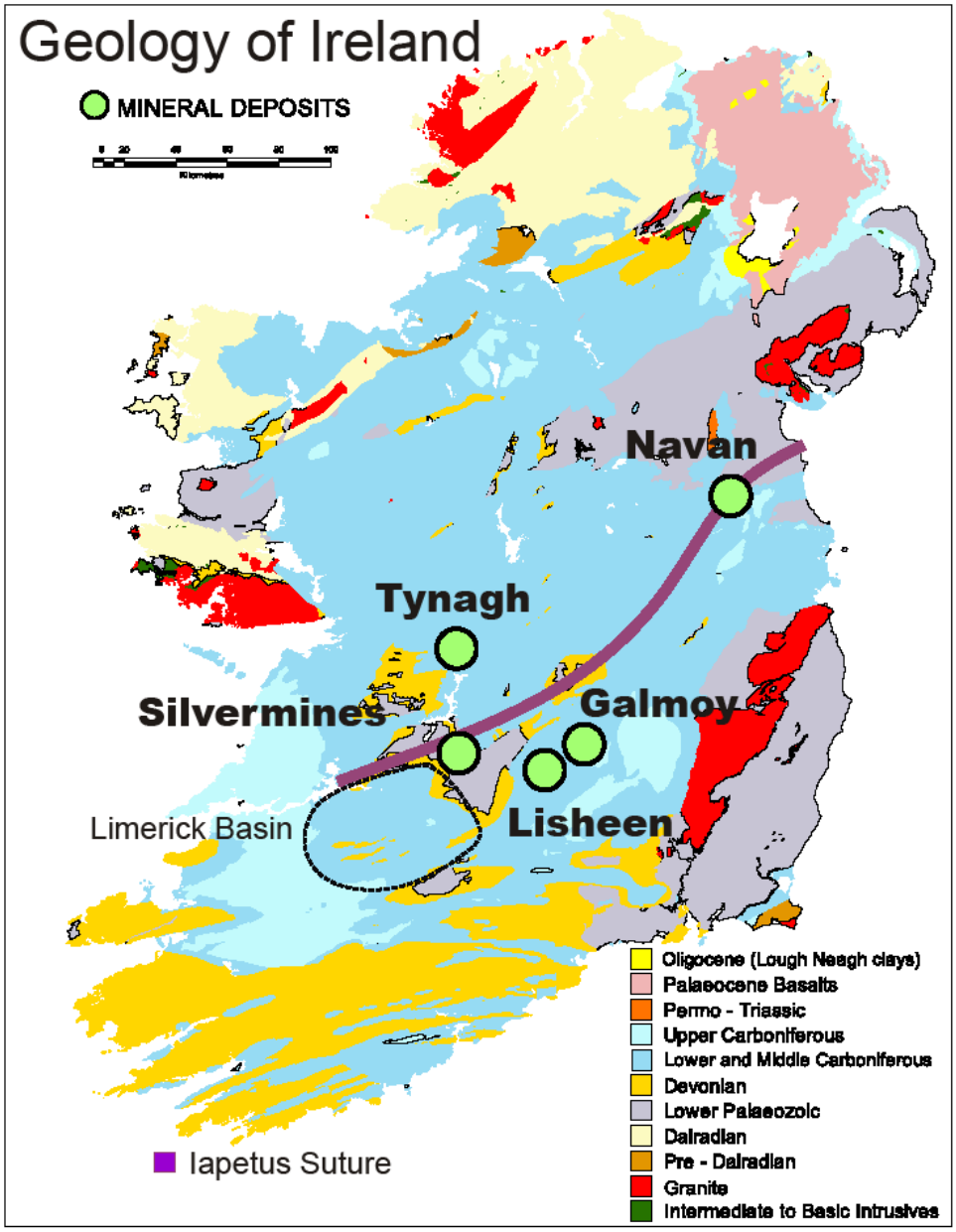

Figure 3.2. Maximum fluid inclusion temperatures of sphalerite for all ore Irish deposits shown against $^{3}He/^{4}He$ values of ore fluids. All deposits are dominated $^{3}He/^{4}He$ ratios that are above crustal radiogenic values, demanding a contribution of mantle-derived volatiles. The mines with the highest maximum fluid temperatures have the largest contribution of mantle-derived He in fluids. Inset figure shows measured $^{3}He/^{4}He$ relative to modern mantle values. Fluid inclusion temperature data from Wilkinson (2010).

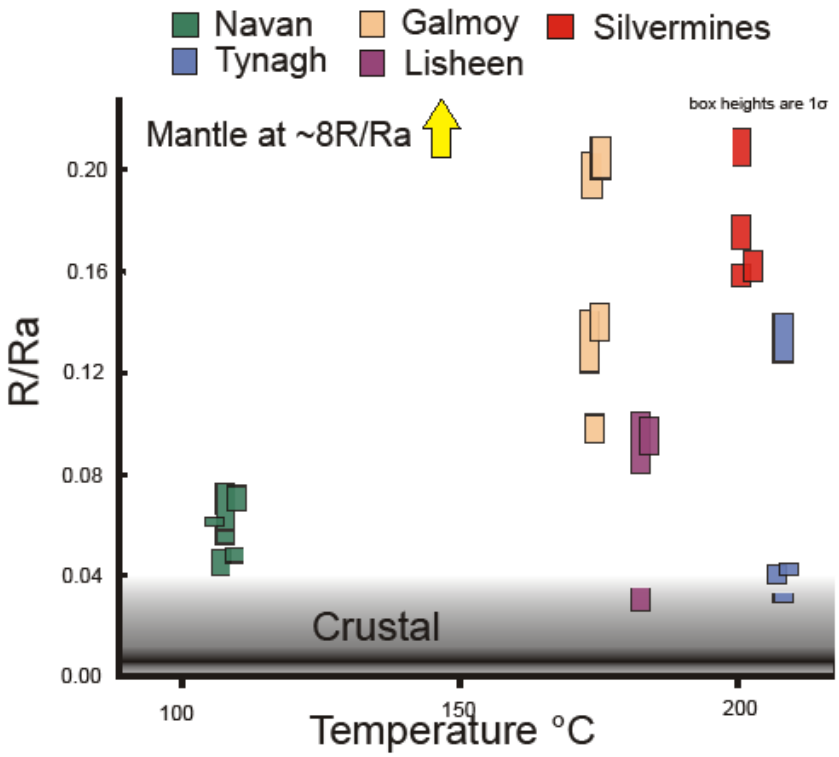

Figure 3.3. $\delta^{34}S$ vs. $^{3}He/^{4}He$ for samples from the Irish Pb-Zn province. There is no statistically significant correlation between $\delta^{34}S$ and $^{3}He/^{4}He$. It should also be noted that even in in isotopically light sulfides, generated from bacteriogenic sulfide, there is still a clear mantle signature implying that even further mixing with a fluid containing bacteriogenic sulfur at the site of deposition did not mask the mantle $^{3}He/^{4}He$ signature.

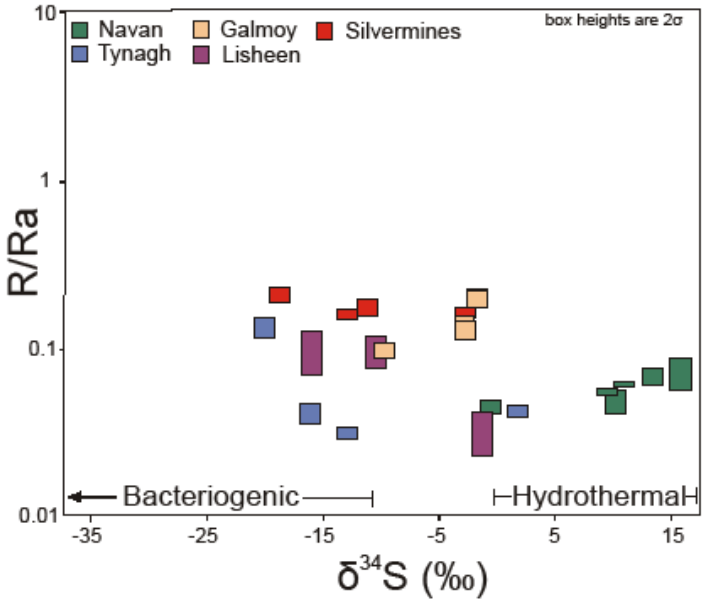

Figure 3.4. Schematic section of the rifting crust with some degree of mantle melting (modified from Latin et al., 1990). The red arrow indicates release of mantle helium from a location of partial melting under the extended crust. This volatile helium then mixes with and is diluted by the ore fluids in the basement beneath the deposits. Mines with the largest mantle ^{3}He component have been diluted the least by crustal fluids and are therefore potentially closer to rift axis, and areas of mantle melting.

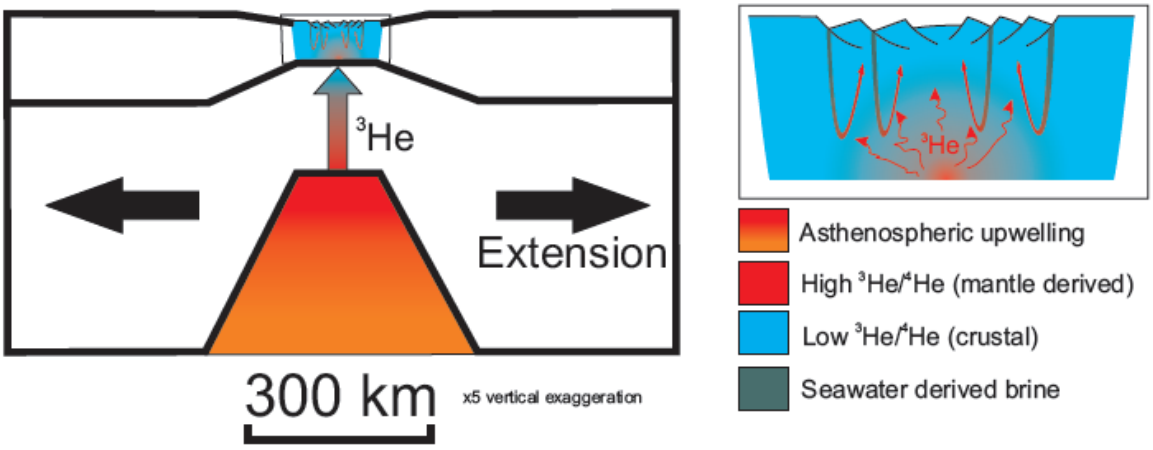

Table 3.1. $^{3}He/^{4}He$ and $\delta^{34}S$ of sulfides from the Irish Pb-Zn ore field.

Sample	Mineral	Source	Loction and or sample number	$\delta^{34}S$	4He (10-6 cc/g)†	$^{3}He/^{4}He$ (R/Ra)	σR/Ra	$^{4}He/^{20}Ne$	20Ne
Navan									
IRHe-1	gal	H	2-1 Lens	10.9	10.4	0.062	0.001	11194	0.001
IRHe-2	gal	H	2-2 Lens box 2.1 3 w245	9.5	7.2	0.055	0.001	7964	0.001
IRHe-3	gal	H	2-5 Lens box 2.1 17	-0.5	2.2	0.045	0.002	11467	0.000
IRHe-6	mar	I	3-1 lens	15.9	0.57	0.071	0.008	n.d.	n.d.
IRHe-25	mar	I	N01358, D19313 Blakeman	10.2	0.8	0.048	0.004	34	0.025
IRHe-26	mar	I	DDH U24309	13.4	0.7	0.068	0.004	759	0.001
Lisheen									
IRHe-7	gal	P	loc MN17054	-15.9	0.1	0.095	0.014	n.d.	n.d.
IRHe-8	gal	P	loc MW 50D02	-10.3	0.1	0.096	0.007	n.d.	n.d.
IRHe-9	gal	P	loc MN 2X60	-1.2	0.2	0.031	0.005	n.d.	n.d.
Galmoy									
IRHe-10	gal	R	RE1a - R Orebody G Fault	-1.7	1.7	0.199	0.008	170496	0.000
IRHe-10*	gal	R	"	-1.7	0.9	0.206	0.008	4532	0.000
IRHe-11	gal	R	RB2a - R Orebody NW	-2.8	0.2	0.140	0.007	355	0.001
IRHe-11*	gal	R	"	-2.8	0.2	0.133	0.011	266	0.001
IRHe-12	gal	R	GNE - G Orebody NW Feeder	-9.71	0.1	0.099	0.004	n.d.	n.d.
Tynagh									
IRHe-13	gal	GSI	box 1780	-20	7.4	0.135	0.008	64406	0.000
IRHe-14	gal	GSI	box 1781	-12.8	2.3	0.032	0.001	n.d.	n.d.
IRHe-15	gal	GSI	box 1777	1.8	2.3	0.042	0.002	n.d.	n.d.
IRHe-21	gal	GSI	box 1776	-16.1	2.3	0.041	0.003	45	0.052
Silvermines									
IRHe-4	gal	GSI	452-2 Mogul	-12.9	6.1	0.159	0.004	n.d.	n.d.
IRHe-5	gal	GSI	B45-2 Mogal Slivermine	-18.7	1.8	0.210	0.006	4745	0.000
IRHe-19	gal	GSI	B zone feeder 4500	-11	9.1	0.177	0.006	603	0.015
IRHe-23	gal	I		-2.7	5.2	0.163	0.005	2289	0.002

*gal = galena, mar = marcasite, * recrush of same sample, †uncertainty in measured ^{4}He is governed by reproducibility of standard ^{4}H*

H = Hunterian Museum, I = Internal SUERC samples, P = Paul Mc Dermott from Galmoy

R = Roy Coates from Lisheen, GSI = Geological Survey of Irish

3.9 Appendix 3.1

^{4}He is produced in crustal rocks by the α decay of ^{238}U, ^{235}U, and ^{232}Th. The ejection of α particles into surrounding rock induces (α,n) reactions that generate a background neutron flux that creates ^{3}He from the reaction ^{6}Li (n,α) ^{3}H (β) ^{3}He (Andrews, 1985). *In situ* production of ^{3}He in the inclusion fluids is dependent on the magnitude of the neutron flux and Li concentration in the fluids. The neutron flux is governed by the concentration of U and Th, and the major neutron absorbers (Na, Mg, Al, Ca, Fe, Zn, Co, Mn, Sm and Gd), in the local rock. Due to a lack of published U and Th data from the Irish ore field we measured two samples for U, Th as well as trace elements by quadrupole ICP-MS (Table 3.A1). Using the rock compositions of Navan, Galmoy and Lisheen (Wilkinson et al., 2011, table 1) and the equations from Andrews (1985) we calculate a neutron flux of 0.023 neutrons per year. For an average Li concentration of fluid inclusions in ore-stage sphalerite at Galmoy and Lisheen (400 ppm: Banks et al. (2002)), we calculate the fluids should contribute $<5x10^{-18}$ cc ^{3}He (assuming that fluid inclusions comprise up to 1% of the volume of the sample). This is 5 orders of magnitude lower than measured value and can be completely ruled out as a source of 3He in the Irish ore mineral.

Assuming from Banks et al. (2002) and the two samples measured here (Table 3.A1) the concentration of neutron absorbers in the fluids, the ^{3}He/^{4}He of the fluid inclusions is ~0.002R_a. This is lower than that of crustal He and has effectively *decreased* the ^{3}He/^{4}He of samples reported here.

Table 3.A1

	U		Th		La		Ce		Pr		Nd		Sm		Eu	
Samples names	ppm	RSD%	ppm	RSD%	ppm	RSD%	ppm	RSD%	ppm	RSD%	ppm	RSD%	ppm	RSD%	ppm	RSD%
IRHe3	0.08	1.49	0.01	4	1.39	1.39	4.18	0.69	0.58	0.94	2.42	1.31	0.64	2.89	1.26	1.86
IRHe4	0.02	5.11	0.02	1.14	3.76	0.43	9.62	0.46	1.27	1.08	5.14	0.89	1.12	2.07	0.97	0.71

	Gd		Tb		Dy		Ho		Er		Tm		Yb		Lu	
Samples names	ppm	RSD%	ppm	RSD%	ppm	RSD%	ppm	RSD%	ppm	RSD%	ppm	RSD%	ppm	RSD%	ppm	RSD%
IRHe3	0.59	2.91	0.08	2.98	0.44	2.11	0.09	2.04	0.25	1.65	0.03	5.14	0.28	2.43	0.04	1.09
IRHe4	0.98	2.98	0.14	1.48	0.79	2.12	0.16	1.64	0.46	0.39	0.07	3.37	0.5	2.49	0.07	1.79

3.10 Potential mixing with air-saturated seawater (ASSW)

It is well established that sulfur isotopes in Irish ore deposits record mixing between shallow seawater (Fluid 2, light at -40 to -20‰ $\delta^{34}S$, indicating bacteriogenically-derived sulfide) and the hydrothermal ore-bearing fluid (Fluid 1, heavy at 0 to +15‰ $\delta^{34}S$). One might expect that contamination of Fluid 2 with air-saturated seawater (ASSW) could yield similar mixing patterns in He isotopes, if they are not corrected for atmospheric He. Probing for these mixing relationships requires data that are not corrected for atmospheric contaminations using neon measurements. A thorough analysis of data from Irish base metal mines does not reveal a general correlation between $\delta^{34}S$ and $^{3}He/^{4}He$, suggesting these systems are at least somewhat decoupled.

However one can attempt, as shown in Figure 3.A1, to identify and interpret these types of mixing trends within individual mines in R/Ra - $\delta^{34}S$ space. The model is envisioned to involve two mixing events, each between two endmembers. The first mixing event involves the crustally-equilibrated Fluid 1 with a mantle melt-influenced fluid. This mixture is fixed in $\delta^{34}S$ space at the hydrothermal composition of the basement at each mine, but can result in changes in He R/Ra space by the mixing of crustal and mantle fluids. This can result in a R/Ra between crustal and mantle values. This mixing theoretically occurs deep in the crust prior to Fluid 1 entering the orebody.

The second mixing event is envisioned to occur between the resulting fluid from the first mixing event, and bacteriogenic Fluid 2. According to our model, Fluid 2 should have a light $\delta^{34}S$ bacteriogenic signature, but could have R/Ra values at or between air-saturated seawater (ASSW), which should have R/Ra values close to atmosphere, and a crustally-equilibrated fluid with low R/Ra crustal values. The R/Ra value of Fluid 2 could also vary between mines. When the two fluids mixed within the orebody during the second mixing event, and were trapped within primary sulfide minerals, preserving their R/Ra and $\delta^{34}S$ values until the present, they record this history of fluid interactions.

Although each individual mine yields a suggestion of a trend, the relatively small number of samples analyzed ($9 > n > 2$), does not constrain the slopes in R/Ra - $\delta^{34}S$ space . Samples within the hydrothermal field, or with only small degrees of mixing in $\delta^{34}S$ space, show a horizontal or a slightly positive slope. This implies initial mixing with a sulfur-bearing fluid that is devoid in helium and thus moves horizontally (e.g. Silvermines and Tynagh). The continued mixing of Fluid 1 (sulfur-poor) with Fluid 2 (sulfur-rich) drives samples closer to the atmospheric saturated seawater (ASSW) endmember. The trend towards ASSW with respect to $^{3}He/^{4}He$ values suggests that this later mixing may be with a Fluid 2 that contains ASSW R/Ra values.

The strongest indication of a crustal component is shown by the positive slope for the Navan samples. This implies mixing with a fluid containing a crustal $^{3}He/^{4}He$ ratio as seen in Figure 3.A1, however the bacteriogenic end member is not constrained for Navan due to sample selection. Lisheen is the only mine to show only an increasing R/Ra, represented by three samples yielding a negative slope (Fig 3.A1). It difficult to determine whether the Lisheen samples represent a true mixing line as the slope is largely controlled by single sample. It should be noted that if Fluid 2 is devoid in helium from any source or if helium does not effectivly mix before the fluid incluion is captured, the R/Ra ratio will reflect only the crustal-mantle mixing event 1.

The Irish deposits indicating tentative mixing with ASSW show that the sulfide-rich fluid creating the precipitation event is not crustally-equilibrated. Samples from Navan sugest that its sulfide-rich fluid was equilbrated with crustal fluids. This would suggest a fundamental difference in the preparation or storage of the sulfide-rich fluid between Navan and other orebodies. To adress this question more thoroughly, a sample suite covering the full range of fluid mixing, as recorded by $\delta^{34}S$, would need to be analyzed. The analyses should include helium, neon and argon isotopes. Analyzing this broad range of samples and elements would yield improved understanding of the atmospheric

component ($^{40}Ar/^{36}Ar$), as well as the mantle signature, and circumvent the possibility of elemental fractionation between neon and helium.

3.10.1 Figures:

Fig 3.A1. $\delta^{34}S$ vs. non-air-corrected $^{3}He/^{4}He$ divded by the $^{3}He/^{4}He$ of the atmosphere. All He data is reported to 1σ while the $\delta^{34}S$ data is shown at 2σ to increase visibility of the datapoints. Navan yields a negative slope, where samples with heavier $\delta^{34}S$ values have higher (mantle-like) R/Ra values, while samples with lighter $\delta^{34}S$ have more crustal He values. In other mines, samples with light $\delta^{34}S$ have higher R/Ra, suggesting that Fluid 2 could have contained an atmospheric-like R/Ra value.

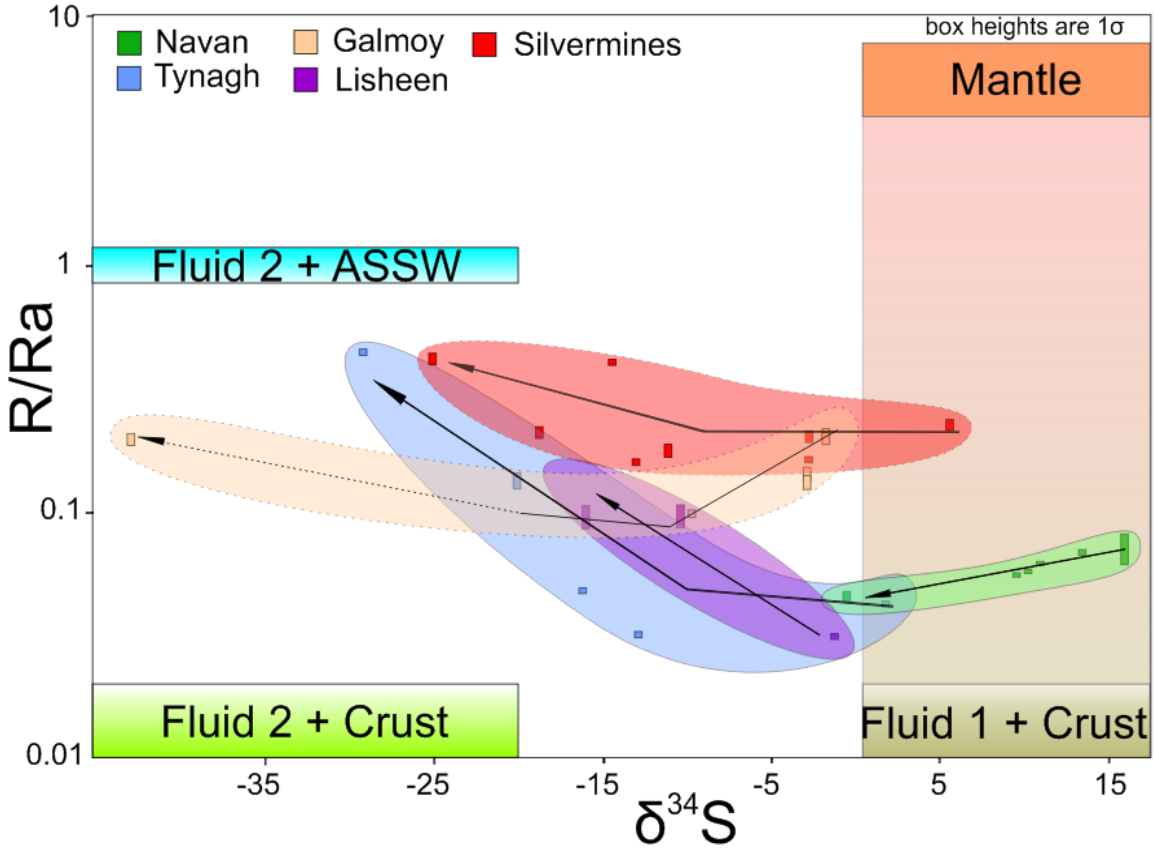

Table 3-A2.

Sample #	Mineral	Mine	Sample location	Sample size mm	grams start	g finish	>150µm	crushed	δ34S	R/Ra Corrected	σR/Ra Corrected	Temp Max	Min °C
IRHe-1	galena	Navan	2-1 Lens Kerr	<.5	0.4862	0.7156	0.5855	0.1301	10.9	0.06	0	175	90
IRHe-2	galena	Navan	2-2 Lens Kerr	~0.5	0.4791	0.7352	0.5886	0.1466	9.5	0.06	0	175	90
IRHe-3	galena	Navan	2-5 Lens Kerr	~0.75	0.7256	2.9573	2.6782	0.2791	-0.5	0.05	0	175	90
IRHe-4	galena	Silver M	452-2 Mogal Slivermine	<.75	0.7776	8.7785	8.1420	0.6365	-12.9	0.16	0	280	190
IRHe-5	galena	Silver M	B45-2 Mogal Slivermine			0.8964	0.7191	0.1773	-18.7	0.21	0.01	175	90
IRHe-6	marcasite	Navan		~0.75	0.8673				15.9	0.07	0.01	280	190
IRHe-7	galena	Lisheen	Sample 1 loc MN17054	1<2 cm	1.525	1.488	1.387	0.1015	-15.9	0.1	0.01	260	145
IRHe-8	galena	Lisheen	Sample 3 loc MW 50D02	1<2 cm	0.770	0.745	0.632	0.1131	-10.3	0.1	0.01	260	145
IRHe-9	galena	Lisheen	Sample 3 loc MN 2X60	1<2 cm	1.162	1.146	1.004	0.1414	-1.2	0.03	0	260	145
IRHe-10	galena	Galmoy	RE1a	1<2 cm	1.457	1.402	1.188	0.2147	-1.7	0.2	0.01	228	111
	re-crush	Galmoy							-1.7	0.21	0.01	228	111
IRHe-11	galena	Galmoy	RB2a bench	1<2 cm	1.524	1.506	1.309	0.1969	-2.8	0.14	0.01	228	111
	re-crush	Galmoy							-2.8	0.13	0.01	228	111
IRHe-12	galena	Galmoy	GNE GE6P3(7)	1<2 cm	1.717	1.688	1.490	0.1984	-9.71	0.1	0	228	111
IRHe-13	galena	Tynagh	K Zone Lower Ore	1<2 cm	1.507	1.492	1.347	0.1450	-20	0.13	0.01	280	80
IRHe-13 a	Py	Tynagh	K Zone Lower Ore		0.559	0.233		0.2329	-29.1	0.44	0.01	280	80
IRHe-14	galena	Tynagh	?	1<2 cm	1.888	1.862	1.642	0.2209	-12.8	0.03	0	280	80
IRHe-15	galena	Tynagh	?	1<2 cm	1.790	1.149	0.986	0.1628	1.8	0.04	0	280	80
IRHe-16	galena	Keel	?	1<2 cm		2.125	1.907	0.2176	-3.8	0.39	0.27	190	120
	re-crush	Keel	?						-3.8	0.15	0.03	190	120
IRHe-17	galena	Silver M	44769	1<2 cm		1.111	0.985	0.1256	5.6	0.15	0.02	280	190
IRHe-18	marcasite	Silver M	7/6 DDH 136 860 ft	1<2 cm	0.9223	1.440	1.263	0.1771	-14.3	0.4	0.01	280	190
IRHe-19	galena	Silver M	B zone feeder 4520	1<2 cm		1.839	1.664	0.1748	-11	0.18	0.01	280	190
IRHe-20	galena	Silver M	g zone M py	1<2 cm		1.855	1.673	0.1820	-24.9	0.07	0.12	280	190
IRHe-21	galena	Tynagh	78 0356	1<2 cm		1.876	1.677	0.1991	-16.1	0.04	0	280	80
IRHe-22	Py+Ga	Galmoy	G fault G Acces Vent 4 Pillar	1<2 cm		0.666	0.404	0.2613	-42.8	0.18	0.01	228	111
IRHe-23	Ga-Tra	Silver M				0.827	0.640	0.1874	-2.7	0.16	0	280	190
	re-crush	Silver M							-2.7	0.18	0.01		
IRHe-24	galena	Keel	?			1.329	1.198	0.1313	-1.1	0.17	0.15	190	120
IRHe-25	marcasite	East of E fault	East of E falt 445 NW N01358 606.6m			0.796	0.609	0.1869	10.2	0.05	0	175	90
IRHe-26	marcasite	between n and t 3-1	Between n and t fault 3-1 U24309 10.5m			1.053	0.807	0.2457	13.4	0.07	0	175	90

Temp °C	+-	Date	Run	4HeFP	d	atoms	3He atoms	g/cc 3He	3HeMP	d	20Ne	d	4He/20Ne	arbitrary σ	4He BlkCorr	d	%
132.5	42.5	6/29/12	BT008	10.4	0.003	368794.4	3.09787296	1.15654E-19	291	5	0.00093	0.00001	11194	1119	10.3546	0.00285	0.00%
132.5	42.5	6/29/12	BT006	7.2	0.004	255319.2	2.14468128	8.00681E-20	181	5	0.0009	0.00001	7964	796	7.1673	0.00386	0.10%
132.5	42.5	6/28/12	BT004	2.2	0.001	78014.2	0.5460994	2.03877E-20	47	2	0.0002	0.00001	11467	1147	2.2476	0.0015	0.10%
235	45	6/28/12	BT003	6.1	0.004	216312.1	4.84539104	1.80895E-19	439	10			9000	900	6.0716	0.00394	0.10%
132.5	42.5	7/2/12	BT010	1.8	0.001	63829.8	1.87659612	7.00596E-20	171	5	0.00038	0.00005	4745	474	1.7839	0.00074	0.00%
235	45	6/28/12	BT002	0.57	0.0004	20212.77	0.198085146	7.39518E-21	19	2			9000	4500	0.5715	0.00053	0.10%
202.5	57.5	2/5/13	BV093	0.1	0	3546.1	0.0496454	1.85343E-21	6	1			8000	800	0.0773	0.00028	0.40%
202.5	57.5	2/5/13	BV096	0.1	0	3546.1	0.0496454	1.85343E-21	11	1			8000	800	0.1328	0.0003	0.20%
202.5	57.5	2/5/13	BV097	0.2	0	7092.2	0.02978724	1.11206E-21	6	1			8000	800	0.2097	0.0003	0.10%
169.5	58.5	2/6/13	BV101	1.7	0.001	60283.7	1.6879436	6.30166E-20	275.7	8	0	0.00004	8000	800	1.7047	0.00082	0.00%
169.5	58.5	2/7/13	BV113	0.9	0.001	31914.9	0.93829806	3.50298E-20	158	3	0.00021	0.00003	4532	453	0.9426	0.00075	0.10%
169.5	58.5	2/6/13	BV104	0.2	0	7092.2	0.13900712	5.1896E-21	21	1	0.00052	0.00057	355	35	0.1827	0.00031	0.20%
169.5	58.5	2/7/13	BV112	0.2	0	7092.2	0.12907804	4.81891E-21	21	2	0.00072	0.00002	266	27	0.1917	0.00031	0.20%
169.5	58.5	2/6/13	BV105	0.1	0	3546.1	0.0496454	1.85343E-21	8	0			8000	800	0.0966	0.00027	0.30%
180	100	2/6/13	BV106	1.3	0.001	46099.3	0.83900726	3.13229E-20	141	8	0.00002	0.00005	64406	6441	1.2881	0.00102	0.10%
180	100	2/11/13	BV119	7.4	0.003	262411.4	16.16454224	6.03476E-19	2659	26			8000	800	7.3911	0.00274	0.00%
180	100	2/6/13	BV107	2.3	0.003	81560.3	0.34255326	1.27887E-20	60	2			8000	800	2.3168	0.00253	0.10%
180	100	2/11/13	BV120	2.3	0.001	81560.3	0.45673768	1.70515E-20	80	1			8000	800	2.301	0.00148	0.10%
155	35	2/11/13	BV123	0.2	0	7092.2	0.38723412	1.44567E-20	157	2	0.49924	0.00003	0.5	0	0.2401	0.00036	0.10%
155	35	2/13/13	BV135	0.1	0	3546.1	0.0744681	2.78014E-21	9	0	0.00074	0.00002	87	9	0.064	0.00029	0.50%
235	45	2/13/13	BV136	1.6	0	56737.6	1.1914896	4.44823E-20	295	6	0.42331	0.00135	4	0	1.6032	0.00047	0.00%
235	45	2/11/13	BV121	0.9	0	31914.9	1.7872344	6.67234E-20	281	4			8000	800	0.8534	0.00057	0.10%
235	45	2/12/13	BV129	9.1	0.004	322695.1	8.13191652	3.03592E-19	1307	20	0.01504	0.00001	603	60	9.0723	0.00359	0.00%
235	45	2/12/13	BV130	1.6	0	56737.6	0.55602848	2.07584E-20	551	13	1.91351	0.00523	0.8	0	1.6241	0.00051	0.00%
180	100	2/14/13	BV147	2.3	0.002	81560.3	0.45673768	1.70515E-20	93	3	0.05197	0.00004	45	5	2.3477	0.00154	0.10%
169.5	58.5	2/11/13	BV122	2.1	0.002	74468.1	1.87659612	7.00596E-20	342	5	0.1132	0.00017	19	2	2.1349	0.00225	0.10%
235	45	2/13/13	BV 137	5.2	0.005	184397.2	4.13049728	1.54205E-19	692	4	0.00228	0.00001	2289	229	5.217	0.00463	0.10%
		2/14/13	BV 140	4.1	0.002	145390.1	3.66383052	1.36783E-19	674	3	0.39586	0.00015	10	1	4.1074	0.00225	0.10%
155	35	2/14/13	BV141	0.2	0	7092.2	0.16879436	6.30166E-21	96	2	0.30231	0.00025	1	0	0.2161	0.00037	0.20%
132.5	42.5	2/14/13	BV144andBV142	0.8	0.001	28368.8	0.1985816	7.41371E-21	41	1	0.02492	0.00001	34	3	0.8444	0.00131	0.20%
132.5	42.5	2/14/13	BV146andBV145	0.7	0.001	24822.7	0.24326246	9.0818E-21	39	1	0.00089	0.00002	759	76	0.6745	0.00061	0.10%

3He BlkCorr	d	%	3He/4He regressed	d3/4 regressed	3He/4He ratio-ed	d3/4 ratio-ed	3/4cal	d3/4cal	R/Ra	dR/Ra	R/Ra ratio-ed	dR/Ra ratio-ed	Corrected R/Ra	Corrected σR/Ra	∂Corrected R/Ra d(R/Ra)	∂ d(4He/20Ne)	∂Corrected R/Ra d(4He/20Ne)
290.4	5	1.7%	28	1	28	0	9,260	51	0.06	0	0.061789	0.001	0.06	0	1.000028409	-8.38E-05	2.38E-09
180.3	4.5	2.5%			25	1	9,260	51			0.055431	0.001	0.06	0	1.000039933	-0.000118619	4.74E-09
46.4	2	4.3%	22	1	21	1	9,260	51	0.05	0	0.045485	0.002	0.05	0	1.000027732	-8.32E-05	2.31E-09
438.4	10	2.3%			72	2	9,260	51			0.159078	0.004	0.16	0	1.000035335	-9.34E-05	3.30E-09
170.2	4.9	2.9%	102	2	95	3	9,260	51	0.23	0	0.210209	0.01	0.21	0.01	1.000067029	-0.000166486	1.12E-08
18.4	2	10.9%	35	3	32	4	9,260	51	0.08	0	0.070944	0.01	0.07	0.01	1.000035335	-0.000103236	3.65E-09
6	0.8	14.0%	83	11	78	11	16,585	484	0.1	0	0.095466	0.01	0.1	0.01	1.000039752	-0.000113076	4.49E-09
10.4	0.7	7.0%	81	5	78	5	16,585	484	0.1	0	0.096464	0.01	0.1	0.01	1.000039752	-0.000112951	4.49E-09
5.3	0.8	14.4%	27	0	26	4	16,585	484	0.03	0	0.031369	0	0.03	0	1.000039752	-0.000121089	4.81E-09
275.2	8	2.9%	164	5	161	5	16,585	484	0.2	0	0.198549	0.01	0.2	0.01	1.000039752	-0.000100189	3.98E-09
157.9	3.4	2.2%	171	0	167	4	16,585	484	0.21	0	0.206013	0.01	0.21	0.01	1.000070174	-0.000175224	1.23E-08
21	0.8	3.7%	121	5	115	4	16,585	484	0.15	0	0.141115	0.01	0.14	0.01	1.00089731	-0.002425716	2.17E-06
20.9	1.7	7.9%	111	9	109	9	16,585	484	0.14	0	0.133951	0.01	0.13	0.01	1.001198951	-0.003269167	3.91E-06
7.8	0.3	3.3%	85	8	80	3	16,585	484	0.1	0	0.09867	0	0.1	0	1.000039752	-0.000112675	4.48E-09
140.9	7.9	5.6%	139	4	109	6	16,585	484	0.17	0	0.134586	0.01	0.13	0.01	1.000004937	-1.34E-05	6.63E-11
2657.4	25.7	1.0%	361	4	360	3	16,585	484	0.44	0	0.442251	0.01	0.44	0.01	1.000039752	-6.97E-05	2.77E-09
59.7	1.5	2.6%	26	1	26	1	16,585	484	0.03	0	0.031722	0	0.03	0	1.000039752	-0.000121044	4.81E-09
78.9	1.8	2.3%	36	1	34	1	16,585	484	0.04	0	0.042181	0	0.04	0	1.000039752	-0.000119737	4.76E-09
155.2	2.9	1.9%	667	15	646	12	16,585	484	0.82	0	0.794959	0.03	0.39	0.27	2.951565865	-3.714057308	2.455722756
7.9	1.5	19.2%	141	9	124	24	16,585	484	0.17	0	0.151944	0.03	0.15	0.03	1.003687752	-0.009870925	3.63E-05
293.3	6.4	2.2%	186	4	183	4	16,585	484	0.23	0	0.225052	0.01	0.15	0.02	1.091660943	-0.243846934	0.020474526
279.8	4	1.4%	328	5	328	5	16,585	484	0.4	0	0.403321	0.01	0.4	0.01	1.000039752	-7.46E-05	2.96E-09
1305.8	20.5	1.6%	323	14	144	2	16,585	484	0.4	0	0.177044	0.01	0.18	0.01	1.000527597	-0.001366095	7.20E-07
549.5	12.7	2.3%	343	8	338	8	16,585	484	0.42	0	0.416191	0.02	0.07	0.12	1.599169381	-1.759088397	0.659087098
91.4	3.4	3.7%	40	1	39	1	16,585	484	0.05	0	0.047888	0	0.04	0	1.00708901	-0.021375411	0.000150464
341.1	5.6	1.6%	165	1	160	3	16,585	484	0.2	0	0.196508	0.01	0.18	0.01	1.017151377	-0.044079745	0.00074328
690.7	4.3	0.6%	133	1	132	1	16,585	484	0.16	0	0.162841	0	0.16	0	1.000138934	-0.000365805	5.08E-08
672.3	3.2	0.5%	168	0	164	1	16,585	484	0.21	0	0.201339	0.01	0.18	0.01	1.031616498	-0.081915778	0.002510516
94.7	2.4	2.6%	439	22.54531	438	11	16,585	484	0.54	0	0.53914	0.02	0.17	0.15	1.801340968	-2.09196814	0.930628795
39.3	1.8	4.7%	48	1	47	2	16,585	484	0.06	0	0.057222	0	0.05	0	1.009474892	-0.028356471	0.000266153
37.6	1.8	4.7%	57	4	56	3	16,585	484	0.07	0	0.068504	0	0.07	0	1.000419285	-0.001228699	5.15E-07

Chapter 4

The timing of Variscan Compression in central Ireland: constraints from $^{40}Ar/^{39}Ar$ dating of altered K-feldspar

Davidheiser-Kroll, B[1], Mark, D. F.[1], Morgan, L. E.[1], and Boyce A. J.[1]

[1] Isotope Geosciences Unit, Scottish Universities Environmental Research Centre, Rankine Avenue, East Kilbride, G75 0QF Scotland, UK

In review in the Journal of the Geological Society

- D.F. Mark provided guidance with respect to ideas, isotope analysis, figure production, and editing
- L.E. Morgan provided guidance with respect to ideas, isotope analysis, figure production, and editing
- A.J. Boyce provided supervision and editorial guidance

4.1 Abstract

To constrain the age of compression and inversion in Central Ireland, on the northern foreland of the Variscan orogen, we have studied altered K-feldspar in a Caledonian syenite intrusion adjacent to a major Lower Carboniferous base-metal orebody at Navan. The K-feldspar displays patch perthite textures indicative of post-magmatic fluid-rock interaction. The altering water was hydrothermal, with fluid δD of -60 to -50‰ and $\delta^{18}O$ around 2.7‰, consistent with a crustally-equilibrated origin. $^{40}Ar/^{39}Ar$ dating of K-feldspar grains completely reset by Variscan compression constrains the timing of the most recent high temperature (~300 °C) fluid event to 293 ± 3 Ma (2σ). As expected, the $^{40}Ar/^{39}Ar$ system in some K-feldspar grains was not completely reset, and hence some age spectra display complex patterns and record ages that are older than the timing of Variscan compression. Numerical modeling of Ar diffusion using DIFFARG indicates that these apparent ages represent a hybrid $^{40}Ar/^{39}Ar$ age that is a function of the intrusion age, Variscan fluid flow, grain size and Ar loss. Our data provide the only geological constraint for the end of Variscan compression in the Irish midlands, and indicate a more protracted Variscan deformation event than previously considered.

4.2 Introduction

The Variscan Orogeny was created by the complex obduction-collision of Gondwana and Laurussia (Laurentia, Baltica and Avalonia) to form the supercontinent Pangea (Warr, 2012). The sutures and large-scale deformation run from present-day Eastern Europe to the Gulf of Mexico in a general east-west trend. E-W striking compressional deformation is seen in S Ireland in the latest, Asturian phase of the Variscan Orogeny, around late Westphalian to Stephanian time, with deformation lessening in intensity to the north, and tending to occur as thrust movement on earlier Caledonian structures, rather than as distinct Variscan fault systems (Figure 4.1). These basin-inverting, reverse movements have dissected base-metal deposits, most notably at the world-class Navan Zn+Pb deposit

(Anderson et al., 1998), and whilst these are presumed to be broadly 'late Variscan' in age (Johnston et al., 1996), no absolute age constraints are available for the Asturian events in Ireland (Warr, 2012). Partly, this is due to the diversity of the geological events spanning this period, which has recorded several distinct episodes, among them; deformation and metamorphism; extensional basin diagenesis; major hydrothermal activity associated with crustal thinning; and crustal heating and fluid movement related to the late Variscan activity.

To help unravel these events, we ran a series of step-heating $^{40}Ar/^{39}Ar$ experiments on potassium (K-) feldspar crystals from a small Caledonian syenite intrusion, which was likely emplaced in, or prior to, early Devonian times. The stock occurs just north of the Navan deposit close to a major reverse fault that is thought to have been active during basin inversion (Figure 1.7) (Anderson et al., 1998). The intrusion has also been proposed as a vertical conduit for fluid flow from the basement (Andrew and Ashton, 1982). We have applied the finite element diffusion model DIFFARG (Wheeler, 1996), to interrogate the complex age spectra retrieved from the step-heating experiments. We conclude that the maximum age for Asturian phase of the Variscan Orogeny (passing through a phase of heating to ca. 300 °C) in this area was 293 ± 3 Ma[1], coincident the earliest emplacement of the Cornubian batholith (Chen et al., 1993, Chesley et al., 1993).

4.3 Geologic Setting

The collision of Laurentia and Avalonia created modern-day Ireland with the closure of the Iapetus Ocean (Woodcock, 2012a). The suture is difficult to trace but in eastern Ireland it is believed to run between the Longford-Down inliers to the north and Grangegeeth and Bellewstown inliers to the south (Figure 4.1). Many small volume melts can be found along the proposed suture, including several syenites just to the northeast of Navan

[1] Note all $^{40}Ar/^{39}Ar$ ages are reported at the 2σ confidence level relative to the optimization model of Renne et al. (2011). Unless otherwise stated the $^{40}Ar/^{39}Ar$ ages include all sources of uncertainty including the decay constant uncertainty, allowing for direct comparison of the $^{40}Ar/^{39}Ar$ ages with other radioisotopic ages (e.g., U-Pb ages).

(Vaughan and Johnston, 1992). The Navan syenite was emplaced before the unconformable transgressive Carboniferous sedimentary sequence (Andrew and Ashton, 1982). It is also believed to be temporally coeval with the emplacement of lamprophyres found today across Ireland and Scotland (Vaughan, 1996). There are no available radioisotopic ages for the alkaline intrusions found throughout Ireland, however several ^{40}K-^{40}Ar ages of ca. 400 to 418 Ma do exist for Scottish lamprophyres (Rock et al., 1986), and for calc-alkaline granites spanning the Iapetus Suture, whose ages are coincident with the lamprophyres and postdate Iapetus Ocean subduction (Miles et al., 2013). It has been reasonably assumed that the Irish intrusions were emplaced in the same tectonic setting as the Scottish counterparts and are thus temporally coeval (Vaughan and Johnston, 1992).

Also postdating Iapetus closure are the Tournaisan fluvial to shallow marine conglomerates and sandstones known as Old Red Sandstones. As the precursor to the Dublin Basin began to fill, it developed a transgressive (from the south) sequence of muddy limestone, micrites, oolitic carbonates, and sandy bioclastic limestone in the Carboniferous (Courceyan ca. 363Ma), called the Navan Group. With continued deepening, the limestone transitioned to shaley argillaceous limestones known as the Argillaceous Bioclastic Limestone (ABL) Group. Above the shaley units is the Waulsortian limestone, a series of deep carbonate mudmound reefs (Monty et al., 1995). Beginning in the Chadian (ca. 350 Ma) major tectonic extension began creating large fault blocks, listric faults and a submarine erosion surface at Navan covered by poorly sorted sand- to large boulder-sized clasts termed the Boulder Conglomerate (Boyce et al., 1983b). The hydrothermal ore genesis event that created the world-class 110mMt @ 10% Zn+Pb deposit is believed to have been created during this extensional period (Anderson et al., 1998, Andrew and Ashton, 1982, Davidheiser-Kroll et al., 2014). The high-energy Boulder Conglomerate deposit is covered by deep water turbidites interbedded with shales, the Fingal Group, which continue into the Arundian. There are no preserved lithologies after the Arundian. Many of the normal faults have been inverted with reverse movements of at

least of 200m, and wrench movements up to 500m, at a hitherto unconstrained time period (Anderson et al., 1998, Coller et al., 2005). These reactivated faults are believed to control the extent of basin inversion and play a major role in our understanding of the Carboniferous structure and stratigraphy, and thus the exploration and targeting of base metals.

4.4 Sample

The samples of K-feldspar analyzed here were harvested from a core that cut through the syenite intrusion at 42.5 m depth in the N00130 NQ drill hole, provided by Boliden Tara Mines Limited. The syenite shows moderate calcite veining and alteration. The sample was selected as it displayed evidence for fluid interaction but was not altered so extensively that the K-feldspar grains had become structurally unstable or altered to clay (and hence unsuitable for $^{40}Ar/^{39}Ar$ dating). Thus it was believed that K-feldspar from this sample would most likely record the passage of post-intrusion hydrothermal activity, be that the mineralizing event (thought to be Chadian Anderson et al., 1998) or a subsequent Variscan heating event, or both.

4.5 Analytical techniques

4.5.1 Petrography

The sample was cut for a thin section, and the offcut and remaining core were jaw crushed, washed, sieved, and magnetically separated, followed by handpicking of K-feldspars. The K-feldspars were divided into several aliquots for various methods of investigation (detailed below).

4.5.2 SEM

Selected grains of K-feldspar were mounted on conductive sticky pads and analyzed under low vacuum mode in a Philips/FEI XL30 ESEM SEM to examine both the K-feldspar

micro-texture and the nature and composition of mineral inclusions. The elemental composition of the inclusions and feldspar were measured semi-quantitatively with an EDS detector.

4.5.3 Oxygen isotopes

Separates of K-feldspar were analyzed for O isotopes using a laser fluorination procedure, involving total sample reaction with excess ClF_3 using a CO_2 laser as a heat source (in excess of 1500°C; following Sharp, 1990). All fluorinations resulted in 100% release of O_2 from the silica lattice. This O_2 was then converted to CO_2 by reaction with hot graphite, and analyzed by a VG SIRA 10 spectrometer. Standards were run intermittently as well as pre- and post-unknown analyses. Reproducibility was better than ± 0.3‰ (1σ), based on repeat analyses of UWG2 (5.8‰) and SUERC internal standards: GP147 (7.2‰) and SES 2 (10.2‰). Results are reported in standard notation ($\delta^{18}O$) as per mil (‰) deviations from the Vienna Standard Mean Ocean Water (V-SMOW) standard.

4.5.4 Hydrogen isotopes

For H isotope analysis of fluid inclusion water, pure K-feldspar samples (between 0.3g for chalcedonic samples, and around 1g for others), were loaded into thoroughly outgassed Pt crucibles and heated to 110°C overnight under high vacuum to release surface volatiles. Samples were then step-heated in a radiofrequency induction furnace to temperatures around 1200°C (measured using an optical pyrometer). The released water at each step was reduced to H_2 in a chromium furnace at 800°C (Donnelly et al., 2001), with the evolved gas measured quantitatively in a Hg manometer, then collected using a Toepler pump. The gas was subsequently analyzed on a VG Optima mass spectrometer. Replicate analyses of water standards (international standards V-SMOW and GISP, and internal standard Lt Std) gave a reproducibility of ± 2‰. Replicate analyses of international mineral standard NBS-30 (biotite) also gave reproducibility around ± 2‰. A more conservative uncertainty estimate of ca. ± 5‰ is typically used for fluid inclusion samples (Gleeson et al., 2008).

4.5.5 $^{40}Ar/^{39}Ar$ geochronology

Approximately 50 handpicked K-feldspar grains were washed in analar-grade acetone, packaged in a Cu packet and put in an Al holder for irradiation at the CLICIT facility of the OSU TRIGA reactor for 80 hours for $^{40}Ar/^{39}Ar$ analysis. The neutron fluence was monitored using biotite standard GA1550 (99.738 ± 0.0104 Ma; Renne et al., 2011); the calculated J value is $1.972x10^{-02} \pm 4.860x10^{-05}$. The decay constants of Renne et al. (2011) and atmospheric $^{40}Ar/^{36}Ar$ of Lee et al. (2006) which has been independently verified by (Mark et al., 2011) were used. Single grains (n=18) were incrementally heated with a CO_2 laser in a stainless steel laser pan. The resulting gas was cleaned with SAES GP 50 hot and cold getters in vacuum and then analyzed on a MAP 215-50 noble gas mass spectrometer with a Balzers SEV-217 electron multiplier (system fully described in Mark et al., 2014). The extraction line and MAP 215-50 were fully automated and controlled by MassSpec software. Blanks were monitored between every two runs and air shots were measured (to monitor mass discrimination) after every four runs. Data were reduced and displayed using MassSpec software. All Ar isotope evolutions were viewed for every blank, sample step, monitor step, and air shot to select the best fit. Isotope data were corrected for radioactive decay, interference reactions, blank, and mass discrimination. Plateau ages were defined as including ≥ 50% of the total ^{39}Ar released and ≥ 3 contiguous steps that overlap at 2σ analytical uncertainty. Owing to the highly radiogenic nature of the bulk ^{40}Ar (radiogenic, excess, atmospheric) the isochron approach is not useful due to data clustering on one axis and hence they are not shown. The raw data for all runs, blanks, irradiation monitors and air calibrations can be found in the supplementary information (Table. 4.2).

4.6 Results

4.6.1 SEM

The feldspar grains analyzed by SEM with EDS were consistent with the bulk chemistry of orthoclase. The backscatter images show subtle density variations and a dominant patch

perthite texture (Figure 4.2 a-d) (Worden et al., 1990). Patch perthite microtextures result from the interaction of alkali feldspar with fluids, and are characterized by the presence of micropores and mosaics of misaligned submicron to micron-scale incoherent subgrains with abundant dislocations along their boundaries (Foland, 1994, Parsons and Lee, 2005, Walker et al., 1995). Studies have shown that patch perthite textures enhance Ar loss from alkali feldspar by shortening the effective diffusion dimension of grains (Burgess et al., 1992, Lee and Parsons, 2003, Mark et al., 2008, Mark et al., 2007, Mark et al., 2011, Parsons, 1978, Worden et al., 1990). The majority of our alkali feldspar grains show areas altered to patch perthite of around 200 µm diameters evident on the grain surface (Figure 4.2 a, b), while other grains show finer patch perthite alteration with zoning on the scale of <50 µm (Figures 4-2 c, d). The patch perthite shows where a fluid front has infiltrated the alkali feldspar grain with the alkali feldspar recrystallizing as the fluid penetrates deeper into the crystal lattice. The SEM images (Figure 4.2) show that the micron-scale incoherent subgrains have shortened the effective diffusion dimension of the alkali feldspar grain and will promote Ar loss from the crystal at lower ambient temperatures as a consequence (Lee, 1995). The patch perthite textures also contain many different mineral inclusions of varying phases and sizes. Apatite is the most abundant mineral inclusion, comprising nearly 5% of the total volume (Figure 4.2 e) and ranging from very large (ca. 300 µm) to small (ca. 10 µm). Minor amounts of chalcopyrite are present, as small blocky ca. 50 µm inclusions. Trace quantities of small 10 to 20 µm zircon inclusions were identified, although a mineral separation effort to locate larger grains, potentially dateable by U-Pb, was unsuccessful.

4.6.2 Stable isotopes

The oxygen isotope data for the three aliquots of feldspar yielded a mean $\delta^{18}O$ = 8.2 ± 0.2‰; full results are reported in Table 4.1. The hydrogen isotope composition of included fluids within a large aliquot of the feldspar yielded a bulk δD value of -48‰, from six steps that were measured along the step-heated profile at increasing temperatures (Figure

4.3). The initial release of hydrogen was detected at over 300°C, with progressively more gas being released at higher temperatures (Figure 4.3 a). The peak release of hydrogen was between 580 and 650°C, which recovered approximately 100µmol. Hydrogen was still being recovered in the final step between 875 and 1200°C. The comparison of δD to temperature yields an apparent parabolic function that becomes heavier with increasing temperature (Figure 4.3 b). The continuous release of hydrogen does not mimic typical release from decrepitation of fluid inclusions, for example, in quartz, whose release is more typified by sudden rupture and almost instantaneous release, typically between 200-300°C (Barker and Robinson, 1984). The other three aliquots of feldspar run for bulk hydrogen isotopes yielded slightly lower values, resulting in an overall mean of -56 ± 5‰ (see Table 4.1). The total water content of the grains is measured at 1.0 to 1.1 wt.%, which, again, is not consistent with typical water concentrations from fluid inclusions (which are usually substantially less, ≤0.2 wt %; Gleeson et al., 2008).

4.6.3 $^{40}Ar/^{39}Ar$ geochronology

The majority of the $^{40}Ar/^{39}Ar$ data show complicated step heating profiles with isotope ratios indicative of intermittent multiphase gas release (e.g., VanLaningham and Mark, 2011). Fine control of the laser power was required to create equal release of gas in subsequent steps, and it was thus necessary during the experimental run to replace the digital laser controller with an analog controller to obtain higher precision (i.e., smaller step size) control over the laser power. The first five grains (Figures 4.4 a,b,c; 4.6 c,d) were run with the digital controller and thus have age spectra that include some undesirably large steps. With both laser controllers, the first few steps (at the lowest laser power) of some grains yield relatively old ages and have slightly elevated K/Ca. However, the K/Ca does also vary drastically (>8000) between steps in other portions of the age spectrum with no clear pattern or correlation with apparent age. The apparent age of the middle portion of the age spectra generally trends toward progressively older ages with increasing power (Figure. 4.4 b,c,d,e; Figure 4.5 c,d,e; Figure 4.6 c,d). Seven of the nine

plateau ages defined by MassSpec software include the last, highest power steps, and define an age that is older than the integrated age (Figure 4.4 b and Figure 4.6 a,b,c,d,e)). Integrated ages (the mean age weighted by inverse variance, with uncertainties of standard error of the mean, multiplied by sqrt(MSWD) if MSWD>1) for all grains vary from 289 to 321 Ma, with the exception of a single grain with a calculated age of 356 ± 4 Ma (Figure 4.5 c); full results are reported in supplementary information (Table. 4.2). The plateau ages range from 293 to 321 Ma with an average total uncertainty of ± 3 Ma. The youngest plateau age yields no apparent variability in age after the initial decrease in age seen in the first two steps (Figure 4.4 e).

4.7 Discussion

Patch perthite textures result from the separation of a solid solution phase into its end-member constituents albite and anorthite in interwoven tube structures (Lee and Parsons, 2003). The observation of these textures within feldspar grains is consistent with post-magmatic alteration (Worden et al., 1990). In many cases, this alteration is likely related to deuteric alteration in the immediate post-magmatic phase of intrusion, but, in reality, the alteration could occur any time following initial magmatic cooling when a hot fluid passes through the feldspar. The alteration of the likely parent material, orthoclase, has significant implications for Ar diffusion and the closure temperature of the $^{40}Ar/^{39}Ar$ system due to the change in effective diffusion dimension (i.e., a grain size reduction) (Parsons et al., 1999). The diffusion of Ar within a crystal that is composed of a single diffusion domain with effective diffusion dimension equivalent to the radius of the crystal is governed by Fickian volume diffusion (McDougall and Harrison, 1999). In non-ideal crystals, inclusions and some defects can create fast diffusion pathways along which Ar can escape (Lee, 1995). For feldspars analyzed here, this fast diffusion would be prevalent along the boundaries of the sub-grains created by the patch perthite (e.g., Mark et al., 2008), as well as along the boundaries of other inclusions such as apatite (Figure 4.2) (assuming the patch

perthite microtexture is both micro-porous and micro-permeable). As a result, the reduction in diffusion domain size by patch perthite alteration means that Ar diffusion in this sample should be considered to be controlled by the size of sub grains, rather than total crystal size (Cassata and Renne, 2013, Parsons et al., 1999).

As discussed above, the formation of patch perthite textures is indicative of fluid-rock interaction. The fluid released from the patch perthite has an H isotope composition around -56‰. The evolution of these step-heated grains suggests that H may be lattice-bound, perhaps as OH groups, and that it is not H_2O trapped in fluid inclusions (Figure 4.3). Four repeat O isotope analyses of the silicate give a small $\delta^{18}O$ range from 8 to 8.4‰. The $\delta^{18}O$ value will have been imparted by the most recent fluid to recrystallize the feldspar. The $^{40}Ar/^{39}Ar$ data indicate that these feldspars have been heated to temperatures in excess of 280°C, which is in agreement with the regional thermal state during the Variscan Orogeny (Jones, 1992). If we assume that this heating event was related to the same fluid which produced the perthite texture, then the fluid in isotopic equilibrium with the measured "K-feldspar" values has a range of $\delta^{18}O$ from 1.9 to 2.3‰ (using the equation of O'Neil and Taylor, 1967); 3.2 to 3.6‰ is using the equation of Zheng, (1993). If end-member compositions of the patch perthite are used (albite and anorthite), then the range of calculated fluid $\delta^{18}O$, in equilibrium with these minerals at 280°C, ranges from 2.7 to 6.3‰ (using equations of Matsuhisa et al., 1979, Zheng, 1993). Whatever calculated fluid composition used, the character of the fluid is typical of crustally-equilibrated fluids (Sheppard, 1986) and consistent with fluids of a metamorphic character, with the implication that they were active during the Variscan Orogeny.

4.7.1 Geological significance of $^{40}Ar/^{39}Ar$ ages

Of the 19 grains analyzed by $^{40}Ar/^{39}Ar$ incremental heating, 18 yield ages between ca. 293 and 321 Ma. The single remaining grain, dated to ca. 356 Ma, indicates a potential for older ages to be retained within the feldspars. The disruption in the $^{40}Ar/^{39}Ar$ system is clearly evident in the complex incremental heating profiles observed in most grains

(Figures 4.4, 4.5, 4.6). Given the likelihood that the patch perthite subgrain radii control the diffusion of argon in these grains (see above), we used DIFFARG modeling (Wheeler, 1996) to interrogate the $^{40}Ar/^{39}Ar$ data with respect to the range in effective diffusion dimension (estimated from petrographical analysis) produced by the patch perthite alteration and the likely regional thermal history (reconstructed from various lines of geological evidence, discussed below).

4.7.2 DIFFARG Modeling

The finite element diffusion model DIFFARG (Wheeler, 1996) was employed to elucidate the interplay between grain/domain size and thermal history. This program forward models the ingrowth of Ar with time, allowing for Ar loss to be modeled from variable-sized effective diffusion domains using a single thermal history. In addition to determining apparent bulk age, the program also calculates the apparent age at different distances from the grain edge (i.e., produces a sub-grain profile). Modeling was performed using a range of effective diffusion domain sizes to test the sensitivity of Ar diffusion in feldspars that have undergone alteration. An approximation of the range of effective diffusion domain sizes were selected from observations of the patch perthite variability seen in SEM images (Figure 4.2). Within the DIFFARG program, the spherical feldspar geometry was selected, with the Crank-Nicolson option (giving more iterations) set to 10.

Thermal histories were set using the piecewise linear option in DIFFARG and constrained by known geological factors of the syenite history. From the contact of the syenite and the Red Beds it can be determined that the intrusive syenite was erosively exhumed at the time of deposition of the Red Beds (Andrew and Ashton, 1982, Vaughan, 1996). At this point the feldspars were at near surface temperatures, and for simplicity this is accepted as the starting point for the model even though some in-growth of Ar certainly occurred before this. The deposition of the Navan and ABL Groups would have buried the feldspars to at least 350m depth over the Courceyan (ca. 100 Ma) and raised temperatures slightly, to ca. 70°C. The next portion of the thermal model represents the ore genesis event that created

the Navan Pb-Zn deposit. There is considerable debate concerning the timing and duration of ore genesis, nonetheless the temperature of the fluid at Navan is believed to be less than 200°C from fluid inclusion analyses (see review Wilkinson, 2010). Many durations of ore genesis (from 1 to 20 Ma) were modeled using a temperature of 200°C; these yield similar patterns and thus only the 10 Ma duration is presented here. Following the ore genesis event, the model has a 30 Ma period of heating to 150°C, expressing the rapid subsidence and deposition of the Fingal Group as the Dublin Basin is created. This is followed by the compressional tectonic event that is represented here at 300 Ma (model time) and is associated with hot fluids that are modeled here at 300 °C. After this event a slow exhumation is modeled to present surface conditions. This thermal mode is schematically developed in time-temperature space in Figure 4.7A.

4.7.3 DIFFARG Modeling Results

Using the event history developed above, modeling shows (Figure 4.7 B) that heating feldspars to 200°C causes only trivial Ar loss (<0.1%), and thus does not affect $^{40}Ar/^{39}Ar$ ages (with respect to the reported age uncertainties), in all but the smallest diffusion domains (ca. 25µm) where a small (ca. 5%) loss is indicated. Less significant heating (<100 °C) yields no Ar loss, regardless of domain size. A ca. 300°C heating event releases all of the Ar held in small diffusion domains (<90 µm), thus resetting the $^{40}Ar/^{39}Ar$ chronometer, and also significantly effects larger domains with varying partial loss of Ar (Figure 4.7 B). The Ar that is lost from a sub-grain is preferentially lost from the outer portion of the sub-grain as the diffusion pathways are shorter (see Figure 4.8). This would create an apparent age profile across the effective radius of each of the feldspars subgrains (see Figure 4.7 C). If a diffusion domain was completely reset, Ar ingrown after the heating event will produce a flat apparent age spectrum across the grain radius (Figure 4.7 C). If diffusion domains of various sizes exist within a sample, some grains with small diffusion domains can be completely reset while others with larger domains retain evidence for complex thermal histories.

The model reasonably indicates that if the diffusion domains are small enough (ca. <90μm), the temperature high enough (>300 °C), or the heating event is long enough (>10Ma), all grains could be completely reset.

4.7.4 $^{40}Ar/^{39}Ar$ data interpretation with respect to modeling results

The nine plateau ages span the range of integrated ages, 293 to 321 Ma, with plateaux consisting of at least 3 contiguous steps, >50% of total ^{39}Ar, and a probability cutoff of 95%. The numerical modeling and petrographic information described above are critical in interpreting these $^{40}Ar/^{39}Ar$ data. The loss of Ar by diffusion due to heating in geological settings is analogous to the diffusion induced by laser incremental heating analysis (although there is a considerable difference in rates between laboratory and natural heating). With each progressive heating step, Ar gas diffuses from more centrally located sites within each diffusion domain (i.e., subgrain). The increase in age congruent with increased laser power, evident in a majority of the data, indicates that the edge of the diffusion domain has a relatively young apparent age, with older apparent ages towards the center of each domain, see Figure 4.4 b,c,d,e; Figure 4.5 a,c,e,f and Figure 4.6 c,d. This type of profile can be seen in the DIFFARG model from a grain that has undergone partial thermal resetting, (ca. 200 μm radius, Figure 4.7 C). This is analogous to measurements of Pb diffusion within apatite grains, where the grain represents a single diffusion domain (Cochrane et al., 2014, see figures 3b and 4). If the domain is large enough (e.g. radii of 400 μm), it is possible that the magmatic age could be retained within most retentive sites (Figure 4.7 C). The age of the Navan syenite is known to be older than the erosion surface, which the Red Beds overlie. It is believed to be Devonian in age (see above), and no apparent ages for any step of the experiments obtained herein approach this age (ca. 400 to 418 Ma). This is likely due to the lack of sufficiently large diffusion domains to retain Ar ages from this event. It should also be noted that the model indicates that the metal-bearing ore fluid, thought to be ≤200 °C, could not have fully reset any modeled diffusion domain, and thus should not have significantly affected ages presented here.

More generally, many age spectra yield plateau ages, which are typically interpreted to represent the age of a specific geological event. However care should be taken as DIFFARG modeling indicates that a diffusion domain size that is just large enough to avoid complete resetting will result in a nearly flat age profile relative to diffusion domain radius of a geologically meaningless age, (e.g. 100 μm radius Figure 4.7 C). Such apparent plateau ages in this study are masked by the several Ma analytical uncertainty for each individual step. Grains 2, 6, 8, 9 and 10 are believed to be represented by this apparently flat but actually variable profile. The second youngest plateau age, grain 6, yields a pattern similar to the ideally reset spectrum, although the last step (Figure 4.6 c step J) may be slightly older (but is within analytical uncertainty). The numerical model does indicate that if the diffusion domain is sufficiently small, the anticipated heating event can reset the diffusion domain completely (Figure 4.7 b 25μm). This completely reset diffusion domain faithfully records the last time it was at this high temperature, and yields a flat apparent age relative to domain radius (e.g. 25 μm radius, Figure. 4.7 c). Thus the youngest grain or grains that do not yield increasing ages with increased laser power in an incremental heating experiment should represent the most recent heating event. The effect of combining various subgrain sizes on apparent Ar ages is illustrated in Figure 4.8. Grain 29 (Figure. 4.6 e) fits these criteria, as it yields an apparently flat age spectrum (after the first two steps) with the youngest age seen in this study at 293 ±3Ma. This grain is interpreted to have small diffusion domains that have been completely reset.

We show that the majority of grains analyzed here yield age spectra that are indicative of partial thermal resetting from a moderately hot fluid (ca. 300°C) and degassing of varying sub-grain sizes with differing diffusion domain sizes (Figure 4.8). Many grains clearly record a rising age spectrum that can be interpreted to represent the partial retention of Ar and can thus only indicate that thermal disturbance is younger than the apparent age. The thermal modeling shows that no other geological event in this region was likely to be faithfully recorded in the grains. The complications of micro textures on Ar systematics

and step heating analyses have been investigated by others, with doubt being cast on the ability to extract multiple ages and create a detailed thermal history from a single grain (Parsons et al., 1999). Note that here we attempt only to use the youngest age to constrain the timing of the most recent heating event, and make no attempt to construct more detailed thermal histories. Other grains that appear to yield flat profiles (Figure 4.4 b Figure 4.5 b and Figure 4.6 a,b,c,) likely actually have unresolvably rising profiles. The youngest and completely flat plateau age recorded in grain Grain 29 (Figure 4.6 e) likely represents a grain with small patch perthite textures that have been completely reset and thus record a thermal event (Figure 4.7 b), as modeled in the 25 μm radius diffusion domain.

4.7.5 The Variscan Orogeny in the Irish Midlands

This new maximum age of 293 ± 3Ma is Lower Permian, as opposed to the late Carboniferous ages previously considered likely (Warr, 2012). This age, regionally coincident with the earliest development of the Cornubian batholith (Chen et al., 1993, Chesley et al., 1993), provides an absolute maximum age constraint for the end of Variscan (Asturian) compression in the Irish midlands, and thus indicates a more protracted Variscan deformation event than previously considered.

4.8 Conclusions

The new data presented here on the Navan syenite near the giant Navan Zn+Pb deposit records the mobilization of fluids created during the basin inversion event in both stable isotope composition and $^{40}Ar/^{39}Ar$ systematics. This fluid flowed along the 'Caledonian' trending major reverse faults and invaded the readily altered syenite. The fluid was sufficiently hot to disturb $^{40}Ar/^{39}Ar$ ages of feldspar grains, but only reset grains with fine-scale patch perthite textures and thus small diffusion domains. Due to the varying sizes of domains, and complex Ar diffusion within the sample, only completely reset grains can yield geologically significant ages. The youngest and most coherent grain indicates that the

last hot fluid (>280 °C) to pass though the Navan syenite is constrained to no later than 293 ±3 Ma. This constrains the absolute timing of the northernmost end-Variscan (Asturian) compression in Ireland to the Cisuralian, coincident regionally with the earliest emplacement of the Cornubian batholith (Chen et al., 1993, Chesley et al., 1993).

4.9 Acknowledgements

BD-K is fully funded by a Tara Mines New Boliden PhD award. AJB is funded by NERC support of the Isotope Community Support Facility at SUERC. DFM is funded by NERC support of the NERC Argon Isotope Facility at SUERC. Thanks to John Ashton and Rob Blakeman of Tara Mines, Navan for help collecting samples, ideas and their support. Thanks to Mike Philcox and Dave Coller for discussions on Irish geology. Thanks to Tony Fallick for thoughtful discussions on the stable isotopes presented here, and Martin Lee for the use of the SEM and his insights on patch perthite. We sourced O isotope fractionation equations from comprehensive University of Laval Community Website: http://www2.ggl.ulaval.ca/cgi-bin/alphadelta/alphadelta.cgi.

4.10 Figures

Figure 4.1. A schematic map of Britain and Ireland showing Variscan age faulting in dashed brown lines, the Iapetus Suture in sold blue, and the northernmost extent of strong Variscan deformation in green. Reproduced by permission of the British Geological Survey. © NERC. All rights reserved. CP14/059.

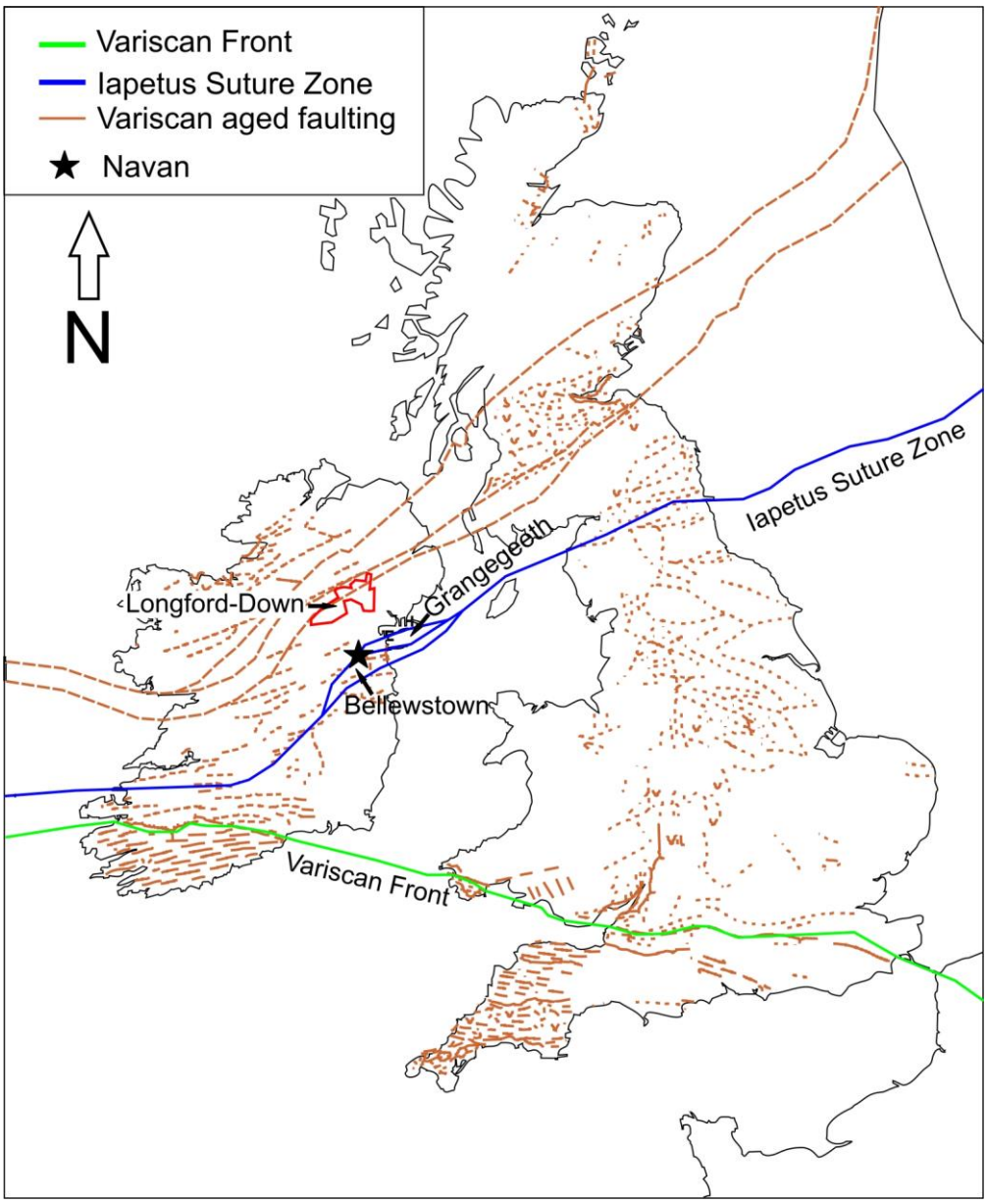

Figure 4.2. Low-vacuum SEM backscatter images of grains of patch perthite, with line drawings shown to the right of each. The light and dark domains within the feldspar grains represent the end members anorthite and albite, respectively. Several of the domains are labeled with Ab for albite and An for anorthite. (a) Domains are small, ca. 20 µm. (b) Domains are much larger, up to ca. 100 µm. Many inclusions can be seen within the grains, including chalcopyrite (Cu in (a)) and apatite (Ap): (b) contains apatite, and (c) contains a large, ca. 200 µm, apatite inclusion.

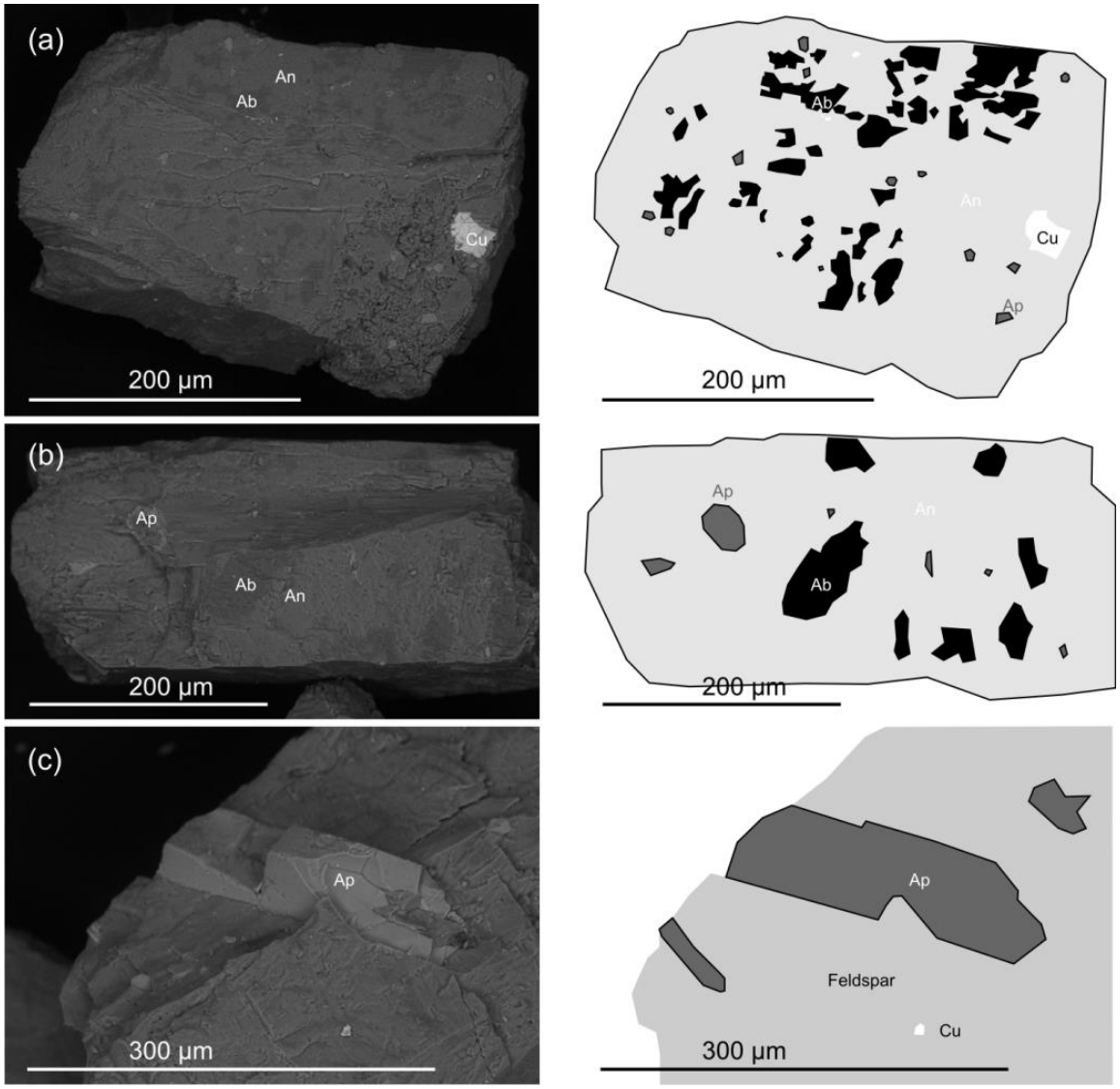

Figure 4.3. (a) Quantity of H_2O (in micromoles) resulting from each temperature step. It is important to note that very little hydrogen is recovered below 300°C, with increasing yields of hydrogen recovered up to the maximum at 600°C, although considerable quantities did remain through to 1200°C. Fluid inclusion-bound water is generally released at low temperatures (ca. 200 C), with highly variable yields, in contrast to the data presented here. **(b)** Hydrogen isotopic data from the incremental heating of the large aliquot (988mg) of feldspar are graphed against the highest temperature seen by the feldspars during analysis. The first step yields the heaviest value, and each subsequent step yields a consecutively lighter value. The data fit well to a parabolic curve, suggesting that the δD is consistently fractionating from the feldspar.

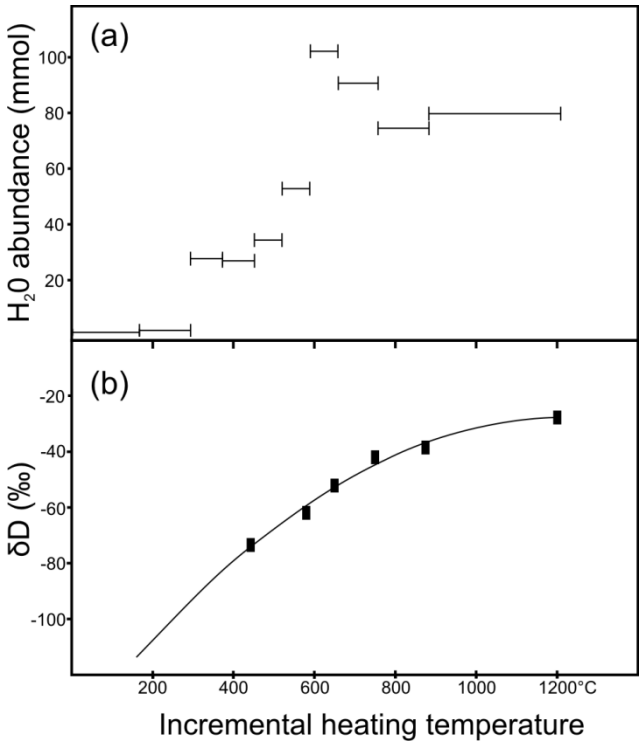

Figure 4.4. Argon release spectra and apparent K/Ca ratios for Navan syenite patch perthite samples calculated with biotite standard GA1550 (99.738 ± 0.0104 Ma; Renne et al., 2011) and decay constant of Renne et al. 2011. Box heights are ±2σ. Plateau ages are shown with arrows to indicate the included steps. Figure 4.4 (a-e) (grains 1, 2, 4, 21, 24) show rising ages, which represent the incomplete resetting of the domains, and the retention of older radiogenic argon within larger domains. Grain 27 (Figure 4.4(f)) yields a disturbed age with a plateau that is dominated by a single large gas release step.

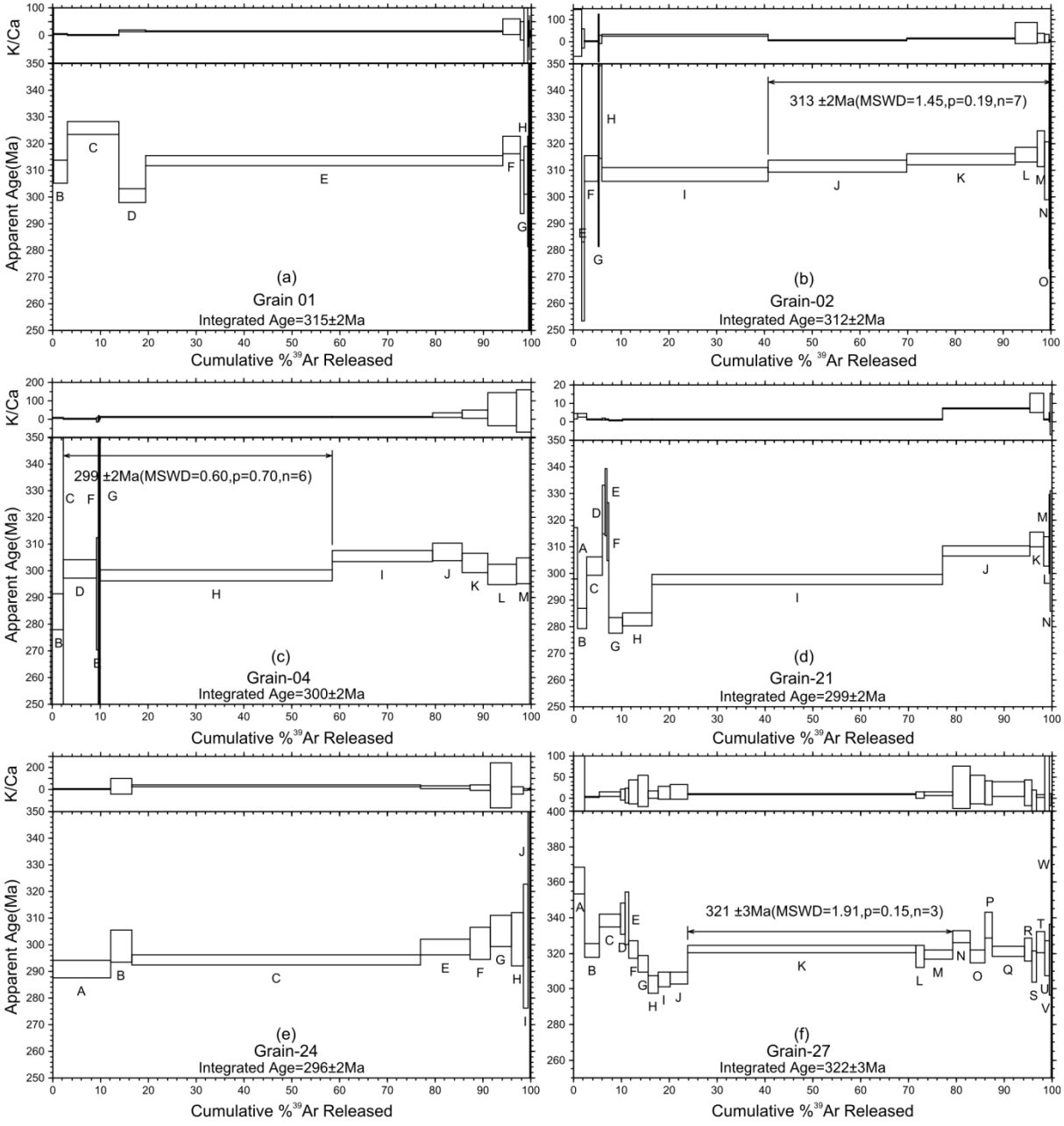

Figure 4.5. Argon release spectra and apparent K/Ca ratios for Navan syenite patch perthite samples calculated with biotite standard GA1550 (99.738 ± 0.0104 Ma; Renne et al., 2011) and decay constant of Renne et al. 2011. Box heights are ±2σ. Plateau ages are shown with arrows to indicate the included steps. The grains presented here (Figure 4.5 (a-f), grains 28, 10, 7, 23, 26, 25) all show a rising age pattern with the higher power laser steps yielding older ages. This represents the incomplete resetting of the domains and the retention of older radiogenic argon within larger domains.

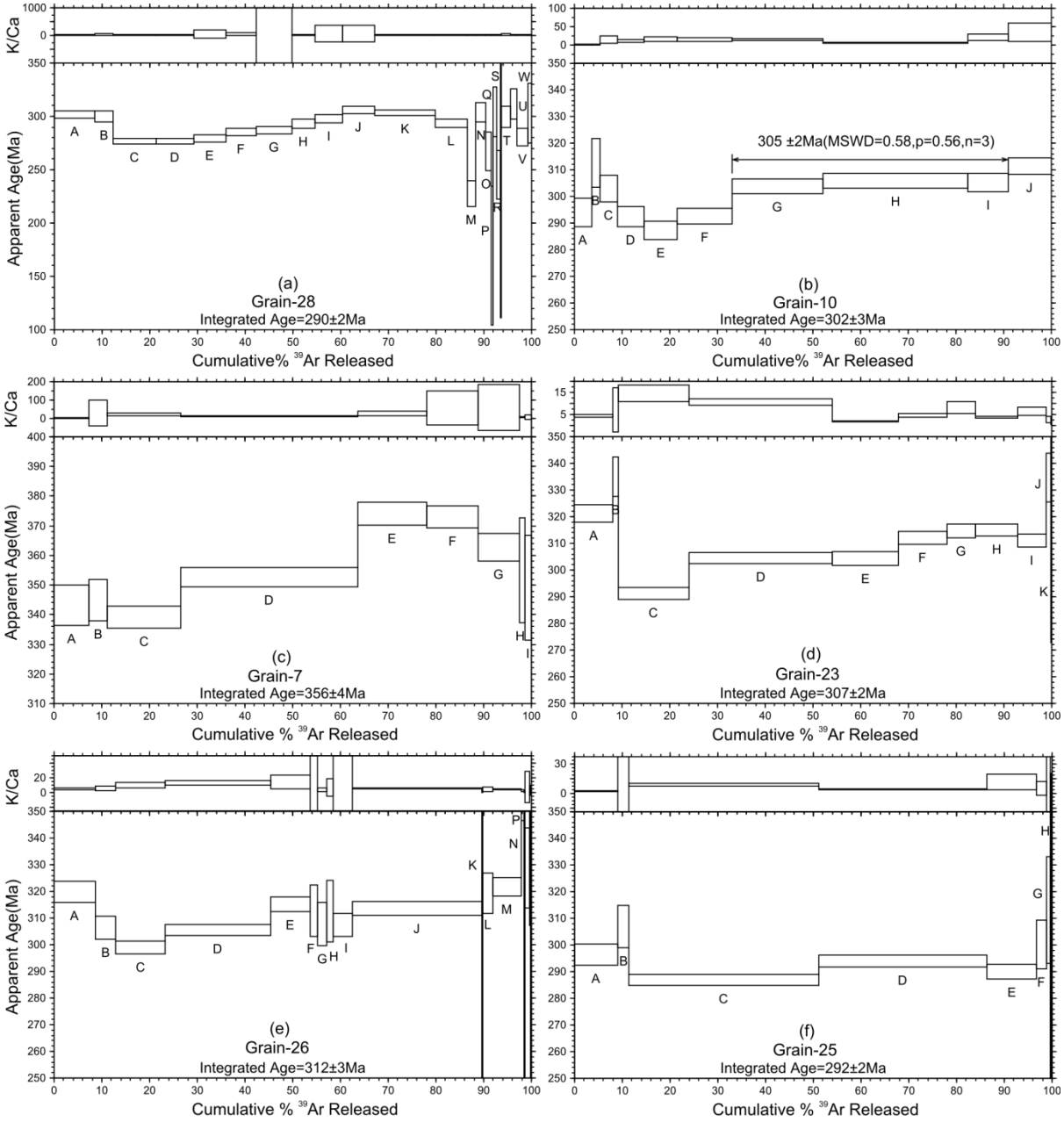

Figure 4.6. Argon release spectra and apparent K/Ca ratios for Navan syenite patch perthite samples calculated with biotite standard GA1550 (99.738 ± 0.0104 Ma; Renne et al., 2011) and decay constant of Renne et al. 2011. Box heights are ±2σ. Plateau ages are shown with arrows to indicate the included steps. The grains presented here show the youngest ages with all except (Figure. 4.6 (f), grain 30) yielding plateau ages that include the last laser steps. From the relatively large uncertainties for each step, grains 9, 8, and 6 (Figure 4.6 (a-c)) could represent incompletely reset grains with nearly flat apparent age vs. domain size, thus yielding ages older than the fluid resetting age. Grain 3 (Figure 4.6(d)) was run with less precise laser control but does yield a relatively young age; this could still contain a rising profile masked by the large step H. Grain 29 (Figure 4.6 (e)) yields a profile with minimal to no rise in age with heating step and has the youngest plateau age for any grain; this grain was likely completely reset by a 293±3 Ma heating event.

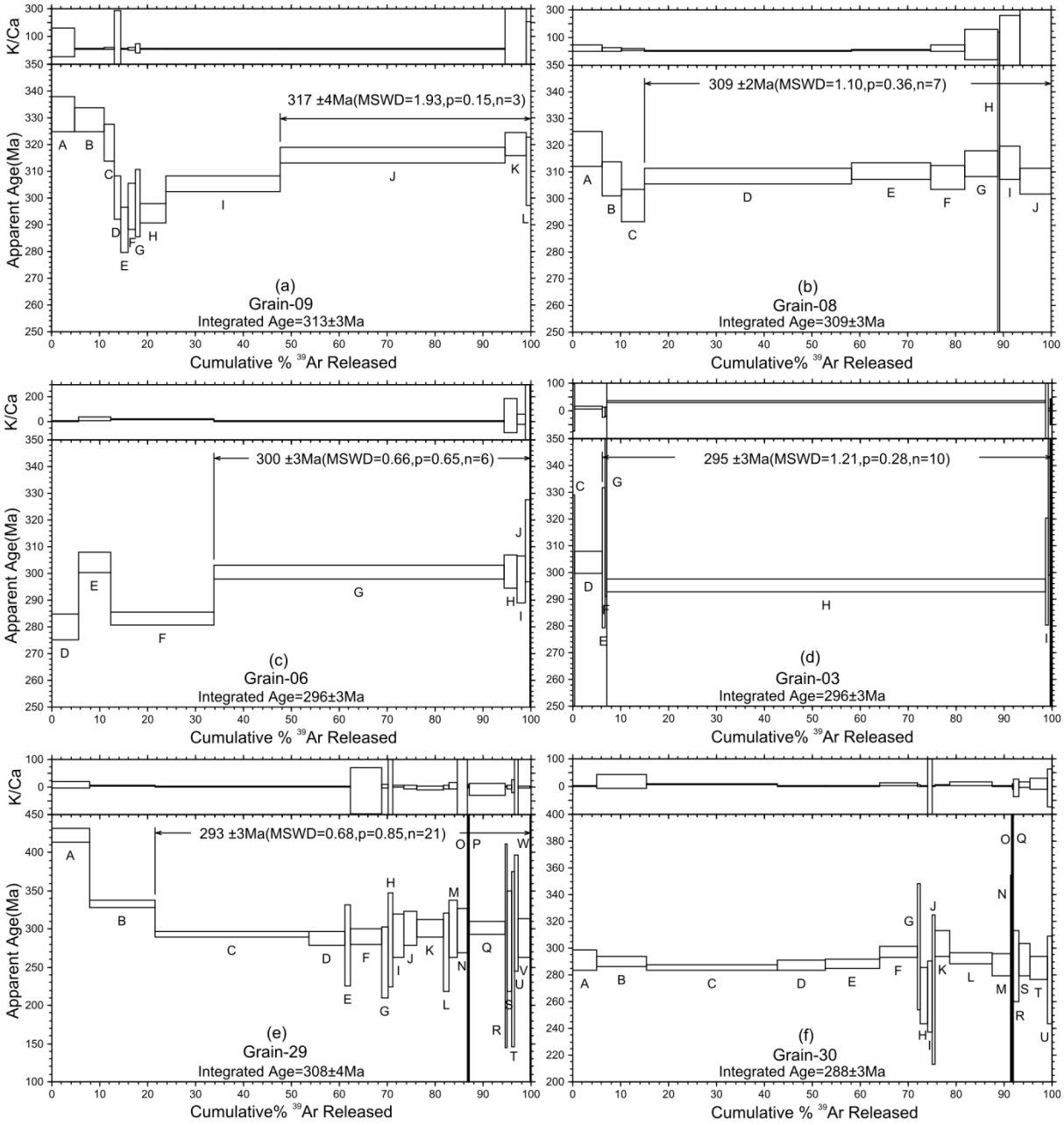

Figure 4.7. (A) Modeled temperature of the grain over time. Step (a) depicts the emplacement age of the syenite at the surface at time 0, followed by gradual heating related to burial. Step (b) represents the thermal event associated with ore fluids and is modeled with a duration of 10Ma. Step (c) represents the further burial of the syenite as the basin subsided and was filled. Step (d) represents a 300°C thermal heating event, evidenced by $\delta^{16}O$ and δD results, lasting 10Ma. Step (e) shows the gradual cooling related to exhumation to the surface. **(B)** Apparent bulk age of different sized feldspar mineral grains (or domains) modeled against time. All grains retain argon over the first 100Ma after emplacement. Some argon is lost during the 200°C heating event at 100-110 Ma in model time. This argon loss is evident in bulk ages for the smallest grains (<100 μm), while the effect on larger grains is negligible. During the 300°C heating event modeled at 140-150 Ma, all modeled grain sizes experience sufficient argon loss to effect their apparent bulk age. The apparent ages of grains <90 μm are effectively completely reset by this thermal event and thus will record its timing. Larger grains appear to partially retain argon and will have a bulk age that does not directly correlate to a geological event. **(C)** Apparent age of different sized grains relative to position in the grain. Smaller grains (e.g. 25μm) that are completely reset (Figure 4.4 C) show flat apparent age profiles across grain radii. Larger grains have more sloped age profiles, with older ages in the center of the grain and younger ages on the edges. This is due to the incomplete resetting during thermal events and the retention of argon within the center of the grains. Note that the center of the grain has a significantly older age then the bulk age for a comparable grain size.

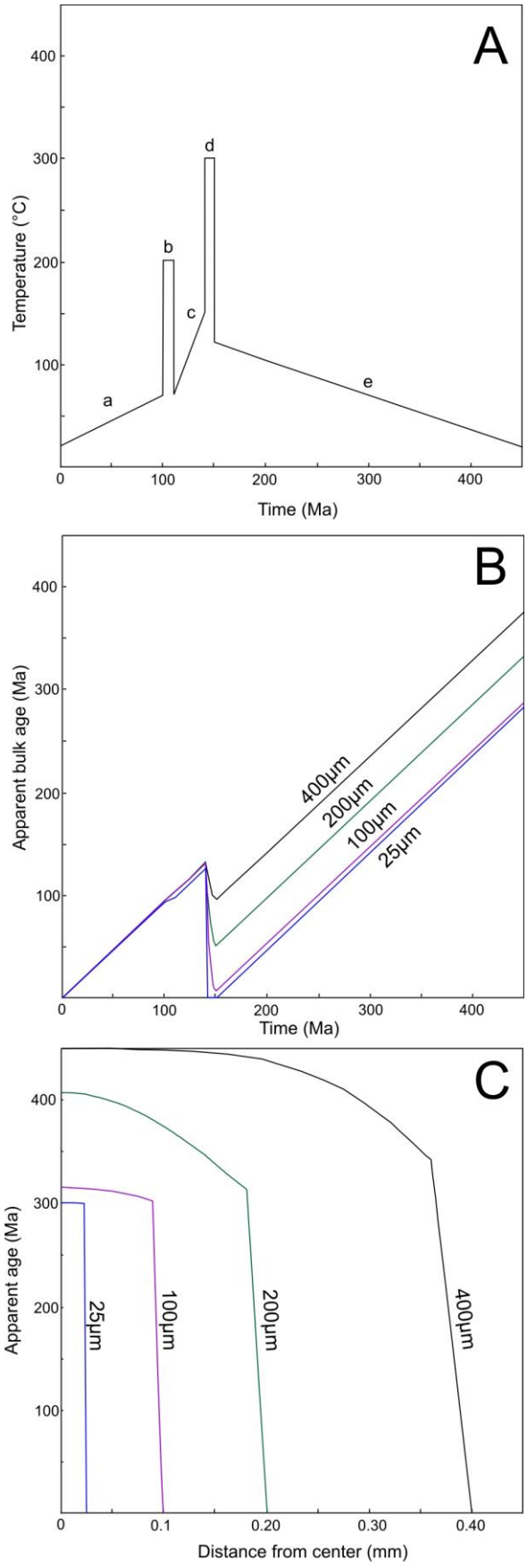

Figure 4.8. A cartoon (based on Mark et al., 2008) representing feldspars with varying grain sizes and thus diffusion radii. The shading represents the amount of radiogenic Ar that is held with in a sub grain after a heating event. The large patch perthite subgrains are sufficiently large to retain radiogenic Ar. The uniformly small patch perthite microtexture have sufficiently small diffusion radii to quantitatively lose radiogenic argon during heating events. The mixed microtexture samples have the ability to retain radiogenic Ar within some portions while losing Ar in other areas. The mixed patch perthite sample is thought to most closely represent the Navan syenite microtexture. When the sample is crushed, different portions of the feldspar will contain large microtextures (see (a) below) while other sections will have small microtextures (see (c) below). The differences in microtextures mean that different effective age vs. grain size will be contained within each fragment and thus the bulk age retained in the aggregate feldspar grain will vary. The youngest sample is thought to represent a fragment containing only small microtextures, as in fragment (c).

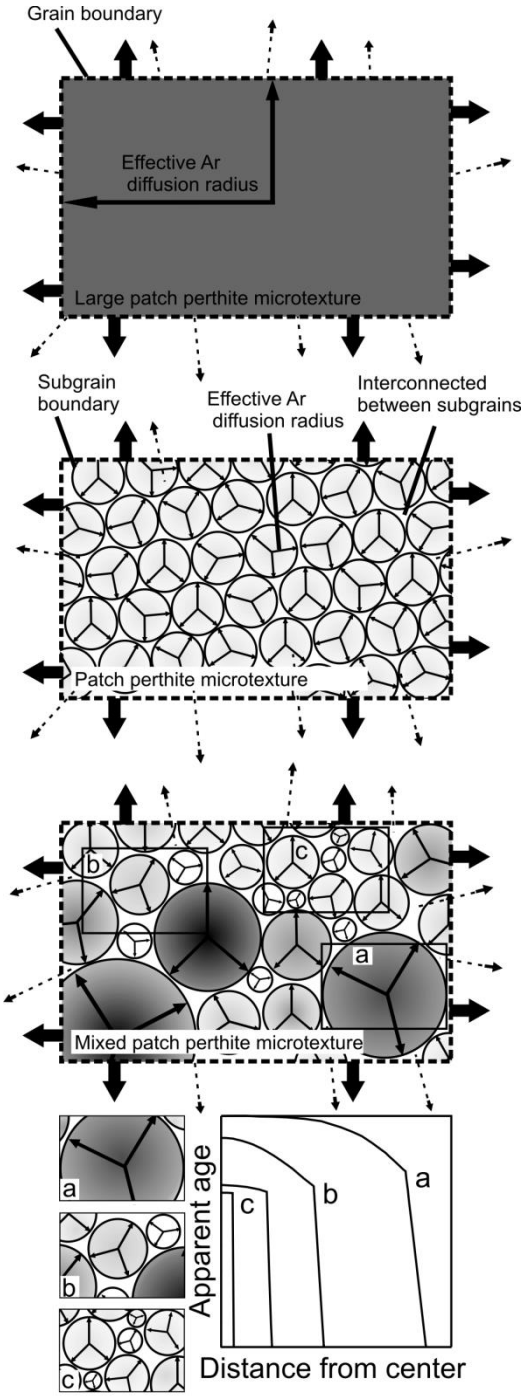

Figure 4.9. A stratigraphic column with ages from *The Geologic Time Scale* 2012 (Gradstein et al., 2012). The Ar/Ar ages are shown in age order for both integrated ages and defined plateau ages, with box height representing 2σ uncertainty. The far right column shows the timing of relevant events in the Navan area. The timing of Variscan Compression is adapted from (Hitzman, 1999). The best constraint on the end of fluid flow on reverse faults at Navan is 293 ± 3 Ma.

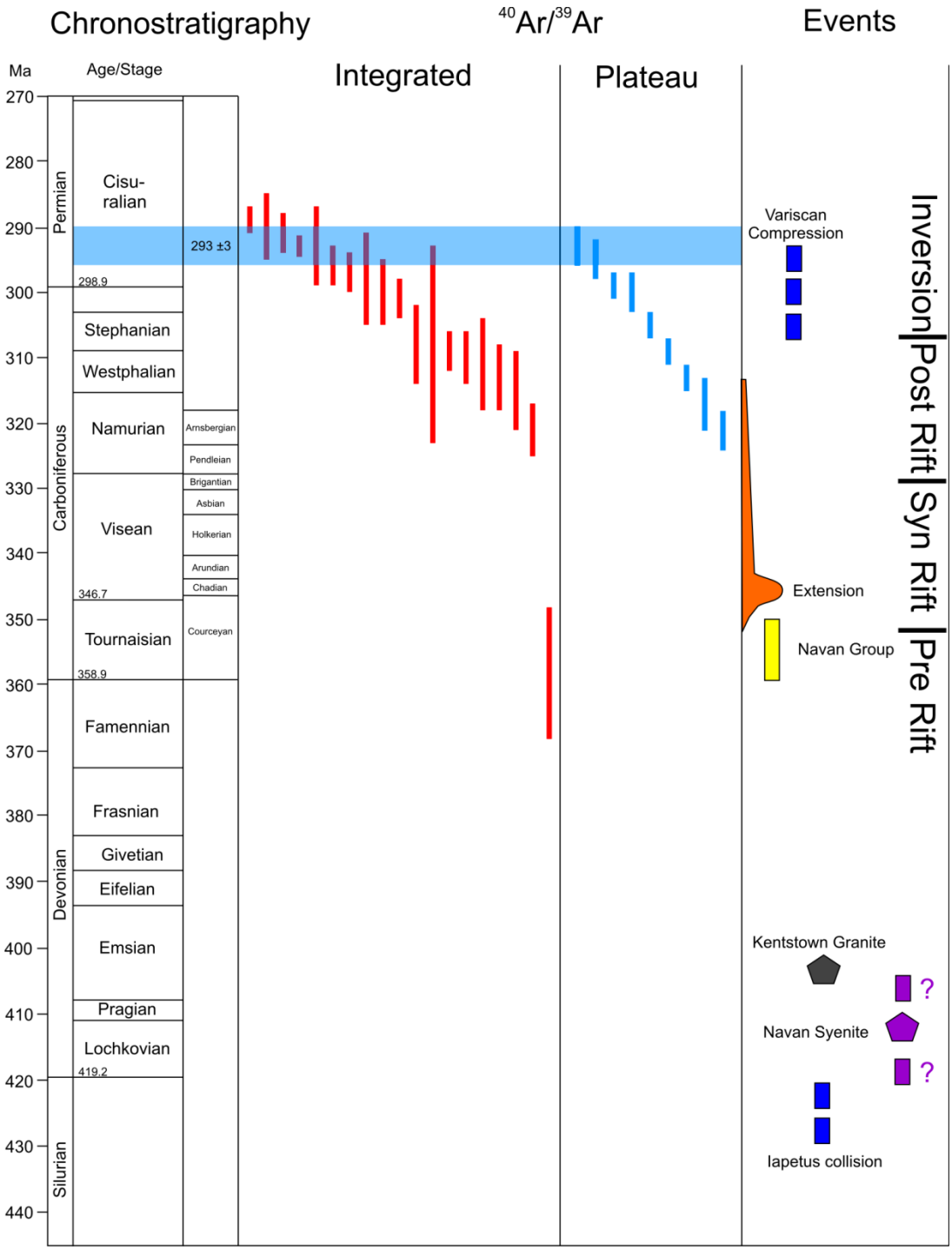

Table 4.1. Summary of stable isotope data. Data include step heating δD data for a single large aliquot of feldspar (data used to create Figure 4.3), three additional aliquots run as total fusion analyses, and $\delta^{18}O$ values for silica-bound O.

Step-heating δD			**Total fusion δD**				**Total fusion $\delta^{18}O$**		
T °C	**% H_2O**	**δD (‰)**							
<443	**0.10**	**-73.3**	**aliquot**	**mass (mg)**	**% H_2O**	**δD (‰)**	**aliquot**	**mass (mg)**	**$\delta^{18}O$ (‰)**
443-580	**0.16**	**-62**	**1**	90.6	1.1	-63.8	**1**	10.0	8.4
580-650	**0.19**	**-52.1**	**2**	89.9	1.0	-58.6	**2**	9.9	8.0
650-750	**0.16**	**-42**	**3**	105.6	1.0	-53.5	**3**	9.8	8.3
750-875	**0.14**	**-38.5**	**4**	988.0	0.9	-48.4			
875-1200	**0.15**	**-27.6**	**mean**			**-56.1**	**mean**		**8.2**
Total H_20 content	**0.89**								
Theoretical composite δD		**-48.4**							

Table 4.2. Full raw argon data, discrimination and background values, and standard analyses.

Run_ID	Plateau Steps	Laser Power	^{40}Ar	$\pm^{40}Ar$ (1σ)	^{39}Ar	$\pm^{39}Ar$ (1σ)	^{38}Ar	$\pm^{38}Ar$ (1σ)	^{37}Ar	$\pm^{37}Ar$ (1σ)	^{36}Ar	$\pm^{36}Ar$ (1σ)	% 39Ar
Grain-01	**Integrated age 315 ± 6 Ma No plateau age**						**J**	0.0201003	**± J (1σ)**	0.0000693			
90529-01A		1.9	0.3563287	0.0018709	0.0072557	0.0000520	0.0003101	0.0000326	0.0000082	0.0000300	0.0006697	0.0000101	0.35
90529-01B		2	0.6469817	0.0009657	0.0563879	0.0001315	0.0007891	0.0000376	0.0004304	0.0000347	0.0003759	0.0000091	2.74
90529-01C		2.1	2.4275960	0.0020640	0.2245221	0.0003106	0.0030372	0.0000564	0.0036187	0.0000572	0.0005975	0.0000103	10.93
90529-01D		2.2	1.0726340	0.0013039	0.1113679	0.0001910	0.0014217	0.0000484	0.0002366	0.0000316	0.0001645	0.0000098	5.42
90529-01E		2.3	15.3988300	0.0051254	1.5347490	0.0027001	0.0189707	0.0001322	0.0033768	0.0000728	0.0020936	0.0000219	74.69
90529-01F		2.4	0.7544984	0.0011225	0.0733889	0.0001612	0.0009053	0.0000400	0.0000699	0.0000316	0.0001106	0.0000092	3.57
90529-01G		2.5	0.1561002	0.0006868	0.0159848	0.0000690	0.0002095	0.0000332	0.0000308	0.0000316	0.0000248	0.0000081	0.78
90529-01H		2.6	0.1544882	0.0006301	0.0156512	0.0000632	0.0001600	0.0000283	-0.0000094	0.0000311	0.0000188	0.0000071	0.76
90529-01I		2.7	0.0649227	0.0005968	0.0065975	0.0000474	0.0000913	0.0000283	0.0000723	0.0000300	0.0000135	0.0000071	0.32
90529-01J		2.8	0.0124594	0.0005442	0.0012714	0.0000328	-0.0000031	0.0000347	0.0000070	0.0000295	-0.0000011	0.0000079	0.06
90529-01K		2.9	0.0338640	0.0005725	0.0032568	0.0000336	0.0000703	0.0000294	-0.0000085	0.0000300	-0.0000038	0.0000070	0.16
90529-01L		3	0.0073127	0.0005408	0.0007576	0.0000283	-0.0000173	0.0000283	0.0000252	0.0000328	-0.0000028	0.0000068	0.04
90529-01M		3.1	0.0281072	0.0005595	0.0028136	0.0000336	0.0000982	0.0000294	0.0000204	0.0000322	0.0000058	0.0000077	0.14
90529-01N		3.2	0.0004382	0.0005263	0.0000137	0.0000283	-0.0000553	0.0000319	-0.0000020	0.0000316	-0.0000023	0.0000076	0.00
90529-01O		3.3	0.0003679	0.0005239	0.0000493	0.0000239	-0.0000084	0.0000278	-0.0000314	0.0000291	-0.0000162	0.0000077	0.00
90529-01P		3.4	0.0002337	0.0005239	0.0000701	0.0000239	-0.0000059	0.0000278	0.0000052	0.0000305	0.0000011	0.0000070	0.00
90529-01Q		3.5	0.0025306	0.0005289	0.0002747	0.0000244	0.0000191	0.0000278	-0.0000254	0.0000295	-0.0000033	0.0000069	0.01
90529-01R		3.6	0.0003462	0.0005345	0.0000047	0.0000344	0.0000000	0.0000294	-0.0000440	0.0000305	-0.0000024	0.0000071	0.00
90529-01S		3.7	0.0001223	0.0005239	0.0000353	0.0000290	0.0000178	0.0000288	0.0000177	0.0000295	-0.0000076	0.0000078	0.00
90529-01T		3.8	0.0001363	0.0005239	0.0000762	0.0000228	0.0000215	0.0000273	0.0000386	0.0000300	0.0000036	0.0000068	0.00
90529-01U		3.9	0.0006849	0.0005345	0.0000244	0.0000320	0.0000049	0.0000283	-0.0000188	0.0000286	0.0000002	0.0000077	0.00
90529-01V		4	0.0001958	0.0005289	0.0000478	0.0000228	-0.0000194	0.0000268	0.0000192	0.0000322	-0.0000016	0.0000076	0.00
90529-01W		4.2	0.0001223	0.0005263	0.0000443	0.0000228	0.0000017	0.0000273	-0.0000025	0.0000311	0.0000026	0.0000069	0.00
90529-01X		4.5	0.0028292	0.0005289	0.0001668	0.0000312	0.0000176	0.0000268	0.0000278	0.0000311	-0.0000058	0.0000075	0.01
Grain-02	**Int. age 313 ± 5 Ma plat. age 313 ± 2 Ma**												
90529-02A		1.2	0.0000192	0.0005348	0.0000428	0.0000562	-0.0000106	0.0000489	0.0000330	0.0000288	-0.0000011	0.0000072	0.00
90529-02B		1.4	-0.0003874	0.0005357	0.0000247	0.0000538	0.0000120	0.0000421	0.0000237	0.0000283	0.0000097	0.0000061	0.00
90529-02C		1.6	-0.0006946	0.0005227	0.0001040	0.0000483	-0.0000033	0.0000407	-0.0000200	0.0000300	0.0000107	0.0000062	0.01
90529-02D		1.8	0.4676257	0.0010111	0.0257412	0.0001011	0.0005545	0.0000476	0.0000203	0.0000288	0.0005630	0.0000094	1.74
90529-02E		1.9	0.0786526	0.0005806	0.0088449	0.0000720	0.0001240	0.0000403	0.0000193	0.0000306	0.0000226	0.0000065	0.60
90529-02F		2	0.4514832	0.0009820	0.0427488	0.0001185	0.0005885	0.0000411	0.0003549	0.0000326	0.0001492	0.0000093	2.89
90529-02G		2	0.0397248	0.0005232	0.0040379	0.0000595	0.0000780	0.0000416	0.0000082	0.0000300	0.0000018	0.0000074	0.27
90529-02H		2	0.0767719	0.0005676	0.0072348	0.0000689	0.0001059	0.0000421	0.0000257	0.0000283	0.0000089	0.0000063	0.49
90529-02I		2.1	5.1363650	0.0049222	0.5142770	0.0014007	0.0063088	0.0000964	0.0005627	0.0000339	0.0009201	0.0000169	34.83
90529-02J	x	2.1	4.2906520	0.0049220	0.4280564	0.0007812	0.0053141	0.0000801	0.0028875	0.0000582	0.0006724	0.0000098	28.99

Run_ID	^{39}Ar moles	^{40}Ar moles	^{40}Ar*/^{39}Ar	± ^{40}Ar*/^{39}Ar (1σ)	%^{40}Ar*	Age	± Age (1σ)	± Age (1σ, w/J)	^{36}Ar/^{40}Ar	±^{36}Ar/^{40}Ar (%, 1s)	^{39}Ar/^{40}Ar	±^{39}Ar/^{40}Ar (%, 1s)
Grain-01												
90529-01A	8.20E-16	2.11E-16	21.533300	0.616037	43.8916	648.832	15.591	15.704	0.0018793	1.8830610	0.0203831	0.9797992
90529-01B	6.37E-15	1.09E-16	9.484481	0.070556	82.7441	314.796	2.149	2.368	0.0005780	2.6148010	0.0872416	0.3826558
90529-01C	2.54E-14	2.33E-16	10.030810	0.039008	92.8550	331.359	1.177	1.573	0.0002393	2.0223360	0.0925698	0.2984617
90529-01D	1.26E-14	1.47E-16	9.183591	0.042835	95.4519	305.609	1.311	1.631	0.0001523	6.0757770	0.1039374	0.3309543
90529-01E	1.73E-13	5.79E-16	9.618925	0.033163	95.9705	318.886	1.008	1.425	0.0001350	1.4362450	0.0997726	0.3086070
90529-01F	8.29E-15	1.27E-16	9.821478	0.054704	95.6350	325.030	1.657	1.948	0.0001462	8.3973160	0.0973733	0.3733141
90529-01G	1.81E-15	7.76E-17	9.295793	0.166092	95.2915	309.040	5.075	5.168	0.0001577	32.9526400	0.1025104	0.7037891
90529-01H	1.77E-15	7.12E-17	9.500821	0.150461	96.3584	315.293	4.581	4.689	0.0001220	37.7706900	0.1014212	0.6615930
90529-01I	7.46E-16	6.74E-17	9.237686	0.344653	93.9637	307.264	10.541	10.586	0.0002022	54.2168100	0.1017178	1.2768960
90529-01J	1.44E-16	6.15E-17	10.063560	1.921545	102.7987	332.347	57.956	57.966	-0.0000937	-673.1739000	0.1021495	5.4677780
90529-01K	3.68E-16	6.47E-17	10.728780	0.677482	103.2964	352.300	20.209	20.239	-0.0001104	-186.6974000	0.0962797	2.1455690
90529-01L	8.56E-17	6.11E-17	10.771330	2.826199	111.6765	353.569	84.245	84.252	-0.0003911	-238.5318000	0.1036794	8.9337570
90529-01M	3.18E-16	6.32E-17	9.378732	0.851592	93.9763	311.572	25.983	26.001	0.0002018	135.5705000	0.1002015	2.5108410
90529-01N	1.55E-18	5.95E-17	82.118830	247.381900	257.1976	1758.595	3384.377	3384.380	-0.0052652	-353.0709000	0.0313202	254.5778000
90529-01O	5.57E-18	5.92E-17	103.532300	70.971240	1400.6350	2030.060	835.303	835.313	-0.0435636	-161.4217000	0.1352849	162.3208000
90529-01P	7.92E-18	5.92E-17	-1.128597	30.796590	-33.8757	-41.397	1142.680	1142.680	0.0044840	709.0184000	0.3001580	245.3128000
90529-01Q	3.10E-17	5.98E-17	12.617380	7.854587	137.2428	407.774	227.204	227.208	-0.0012474	-219.6401000	0.1087728	24.5000700
90529-01R	5.27E-19	6.04E-17	194.176100	1426.366000	292.0062	2868.203	10549.370	10549.370	-0.0064311	-358.7187000	0.0150382	721.5280000
90529-01S	3.99E-18	5.92E-17	68.776350	91.037100	1977.5860	1566.151	1385.659	1385.664	-0.0628881	-474.7736000	0.2875386	472.0059000
90529-01T	8.61E-18	5.92E-17	-11.504360	27.981880	-639.7516	-474.431	1319.906	1319.907	0.0247773	461.9525000	0.5560948	417.2554000
90529-01U	2.76E-18	6.04E-17	24.073510	101.579600	86.6596	712.002	2482.350	2482.351	0.0004468	2513.1380000	0.0359979	161.7297000
90529-01V	5.40E-18	5.98E-17	14.471070	49.829240	352.2496	460.614	1399.773	1399.774	-0.0084489	-546.0221000	0.2434163	296.6687000
90529-01W	5.01E-18	5.95E-17	-15.004270	48.525980	-545.2921	-647.571	2519.534	2519.535	0.0216135	533.3372000	0.3634246	469.1164000
90529-01X	1.88E-17	5.98E-17	27.669560	14.958550	162.9353	797.807	348.570	348.578	-0.0021080	-127.6877000	0.0588861	28.3885100
Grain-02												
90529-02A	4.84E-18	6.04E-17	9.552459	54.344450	2113.4890	316.865	1653.229	1653.230	-0.0674401	-3071.3220000	2.2125080	3023.3610000
90529-02B	2.79E-18	6.05E-17	-133.264100	321.153200	841.0954	#NAME?	-6937.627	-6937.635	-0.0248223	-162.4791000	-0.0631149	-277.5419000
90529-02C	1.18E-17	5.91E-17	-37.614720	26.192890	564.7991	-2545.290	3893.734	3893.782	-0.0155680	-99.5324800	-0.1501537	-95.1195200
90529-02D	2.91E-15	1.14E-16	11.625870	0.156518	64.0641	378.863	4.601	4.749	0.0012036	1.9515600	0.0551048	0.5361051
90529-02E	9.99E-16	6.56E-17	8.124839	0.243088	91.4673	272.904	7.577	7.628	0.0002858	29.0507100	0.1125774	1.2014020
90529-02F	4.83E-15	1.11E-16	9.521206	0.082207	90.2412	315.914	2.502	2.694	0.0003269	6.4148570	0.0947792	0.4482844
90529-02G	4.56E-16	5.91E-17	9.700111	0.581854	98.7038	321.351	17.657	17.686	0.0000434	426.6023000	0.1017553	2.1288490
90529-02H	8.18E-16	6.41E-17	10.237310	0.293483	96.5755	337.580	8.826	8.890	0.0001147	71.5448600	0.0943368	1.3113890
90529-02I	5.81E-14	5.56E-16	9.444604	0.041705	94.6666	313.581	1.271	1.613	0.0001786	2.0814430	0.1002335	0.3916135
90529-02J	4.84E-14	5.56E-16	9.554355	0.036219	95.4159	316.923	1.102	1.489	0.0001535	1.7907310	0.0998663	0.3346577

Run_ID	±^{39}Ar/^{36}Ar (%, 1s)	ρ ^{40}Ar/^{39}Ar	ρ ^{36}Ar/^{39}Ar
Grain-01			
90529-01A	1.8404830	0.6364146	0.4599580
90529-01B	2.5412620	0.8678836	0.3199488
90529-01C	1.9199030	0.7839903	0.4112936
90529-01D	6.0428830	0.9761758	0.1393601
90529-01E	1.2968720	0.5651315	0.5634429
90529-01F	8.3743160	0.9873260	0.1008550
90529-01G	32.9460400	0.9990135	0.0276562
90529-01H	37.7650100	0.9992694	0.0238752
90529-01I	54.2090800	0.9994424	0.0213630
90529-01J	-673.1631000	0.9999652	0.0062028
90529-01K	-186.6908000	0.9999103	0.0095416
90529-01L	-238.4308000	0.9992839	0.0302668
90529-01M	135.5574000	0.9997837	0.0150330
90529-01N	-394.6151000	0.7735558	0.1879498
90529-01O	-69.9640100	0.2037407	0.9066370
90529-01P	667.1760000	0.9382362	0.3384992
90529-01Q	-218.6776000	0.9937434	0.0951215
90529-01R	-770.4272000	0.3646429	0.1078292
90529-01S	-134.1143000	0.1618068	0.9598962
90529-01T	203.3257000	0.4292473	0.8979395
90529-01U	2515.4750000	0.9979314	0.0175505
90529-01V	-464.0255000	0.8395701	0.5273686
90529-01W	265.1928000	0.4761865	0.8676881
90529-01X	-127.6420000	0.9752239	0.1130676
Grain-02			
90529-02A	-576.2613000	0.1764006	0.9822455
90529-02B	242.1930000	0.1019640	0.4964169
90529-02C	75.4961700	0.4362843	0.6999982
90529-02D	1.8744530	0.7448263	0.4193065
90529-02E	29.0453100	0.9981691	0.0341757
90529-02F	6.3848430	0.9775182	0.1330758
90529-02G	426.6021000	0.9999830	0.0029599
90529-02H	71.5444800	0.9996711	0.0133108
90529-02I	1.9977550	0.7905064	0.3930915
90529-02J	1.6771360	0.7199822	0.4618350

Run_ID	Plateau Steps	Laser Power	^{40}Ar	±^{40}Ar (1σ)	^{39}Ar	±^{39}Ar (1σ)	^{38}Ar	±^{38}Ar (1σ)	^{37}Ar	±^{37}Ar (1σ)	^{36}Ar	±^{36}Ar (1σ)	% 39Ar
90529-02K	x	2.1	3.3875800	0.0023464	0.3349817	0.0005916	0.0041936	0.0000783	0.0007194	0.0000369	0.0005291	0.0000099	22.68
90529-02L	x	2.2	0.7125392	0.0010482	0.0705618	0.0001468	0.0008880	0.0000470	0.0000519	0.0000312	0.0000927	0.0000070	4.78
90529-02M	x	2.3	0.2330974	0.0007269	0.0228730	0.0000802	0.0001424	0.0000583	0.0000441	0.0000306	0.0000314	0.0000075	1.55
90529-02N	x	2.5	0.1307406	0.0006321	0.0131659	0.0000777	0.0000137	0.0000496	0.0000345	0.0000288	0.0000189	0.0000070	0.89
90529-02O	x	2.7	0.0309136	0.0005220	0.0031035	0.0000538	-0.0000343	0.0000441	0.0000424	0.0000278	0.0000027	0.0000071	0.21
90529-02P	x	3.5	0.0082800	0.0004877	0.0009138	0.0000496	0.0000218	0.0000411	-0.0000230	0.0000260	0.0000024	0.0000060	0.06
Grain-03	**Int. age 297 ± 3 Ma plat. age 295 ± 3 Ma**												
90529-03A		1.6	-0.0004511	0.0004875	-0.0000947	0.0000492	-0.0000137	0.0000399	-0.0000562	0.0000283	-0.0000007	0.0000068	-0.01
90529-03B		1.8	0.0178216	0.0005045	0.0009792	0.0000496	-0.0000110	0.0000403	-0.0000361	0.0000283	0.0000143	0.0000068	0.11
90529-03C		1.9	0.0287689	0.0005129	0.0026661	0.0000522	0.0000574	0.0000421	0.0000073	0.0000294	0.0000209	0.0000070	0.31
90529-03D		2	0.5150312	0.0008930	0.0507390	0.0001278	0.0007256	0.0000447	0.0001435	0.0000332	0.0001455	0.0000091	5.86
90529-03E	x	2	0.0457608	0.0005224	0.0046449	0.0000629	0.0000465	0.0000407	-0.0000201	0.0000288	0.0000075	0.0000062	0.54
90529-03F	x	2	0.0268658	0.0005319	0.0026488	0.0000533	0.0000497	0.0000399	-0.0000169	0.0000306	-0.0000031	0.0000067	0.31
90529-03G	x	2	0.0108489	0.0005032	0.0010399	0.0000608	-0.0000280	0.0000464	0.0000030	0.0000288	-0.0000007	0.0000063	0.12
90529-03H	x	2.1	7.4129330	0.0083133	0.7916434	0.0021005	0.0098775	0.0000881	0.0007196	0.0000369	0.0009290	0.0000159	91.47
90529-03I	x	2.1	0.0608472	0.0005524	0.0061757	0.0000588	0.0000810	0.0000530	0.0000071	0.0000300	0.0000138	0.0000062	0.71
90529-03J	x	2.1	0.0261435	0.0005422	0.0026169	0.0000501	0.0000392	0.0000411	0.0000309	0.0000283	-0.0000066	0.0000066	0.30
90529-03K		2.1	0.0124903	0.0005109	0.0013481	0.0000496	0.0000256	0.0000399	-0.0000069	0.0000288	0.0000029	0.0000061	0.16
90529-03L		2.2	0.0009464	0.0004904	0.0001980	0.0000462	-0.0000268	0.0000392	-0.0000326	0.0000283	-0.0000039	0.0000061	0.02
90529-03M		2.3	0.0039221	0.0004930	0.0004116	0.0000462	0.0000011	0.0000458	0.0000351	0.0000294	0.0000086	0.0000061	0.05
90529-03N		2.7	0.0043687	0.0004899	0.0004417	0.0000522	-0.0000085	0.0000392	-0.0000047	0.0000319	0.0000021	0.0000061	0.05
Grain-04	**Int. age 301 ± 3 Ma plat. age 299 ± 2 Ma**												
90529-04A		1.6	-0.0004330	0.0004813	-0.0000172	0.0000451	0.0000041	0.0000392	-0.0000037	0.0000294	-0.0000010	0.0000059	0.00
90529-04B		1.8	0.3085461	0.0007678	0.0263452	0.0001074	0.0004532	0.0000421	0.0001170	0.0000319	0.0002690	0.0000078	2.50
90529-04C	x	1.9	-0.0004952	0.0004846	-0.0000304	0.0000488	-0.0000611	0.0000447	-0.0000610	0.0000273	-0.0000032	0.0000060	0.00
90529-04D	x	1.95	0.7317336	0.0013818	0.0713160	0.0001756	0.0009067	0.0000470	0.0007483	0.0000312	0.0002569	0.0000079	6.77
90529-04E	x	2	0.0550172	0.0005735	0.0057248	0.0000608	0.0001246	0.0000399	-0.0000256	0.0000273	0.0000137	0.0000060	0.54
90529-04F	x	2	0.0114194	0.0005076	0.0013027	0.0000483	0.0000226	0.0000403	0.0000116	0.0000283	-0.0000078	0.0000069	0.12
90529-04G	x	2.05	0.0061821	0.0004943	0.0007756	0.0000483	-0.0000107	0.0000399	-0.0000288	0.0000288	-0.0000019	0.0000061	0.07
90529-04H	x	2.1	4.8542390	0.0028401	0.5118381	0.0008611	0.0062172	0.0000688	0.0011711	0.0000416	0.0006330	0.0000150	48.56
90529-04I		2.1	2.1554170	0.0015745	0.2205981	0.0002834	0.0028286	0.0000671	0.0006180	0.0000392	0.0003098	0.0000111	20.93
90529-04J		2.1	0.6400474	0.0014816	0.0649500	0.0001563	0.0007496	0.0000447	0.0000924	0.0000283	0.0000967	0.0000067	6.16
90529-04K		2.2	0.5571301	0.0010234	0.0572748	0.0001468	0.0006976	0.0000411	0.0000673	0.0000306	0.0000870	0.0000079	5.43
90529-04L		2.3	0.5985337	0.0010172	0.0624665	0.0002637	0.0006490	0.0000502	0.0000334	0.0000278	0.0000941	0.0000069	5.93
90529-04M		2.7	0.3006897	0.0007976	0.0314095	0.0001185	0.0003813	0.0000430	0.0000204	0.0000273	0.0000415	0.0000062	2.98

Run_ID	^{39}Ar moles	^{40}Ar moles	^{40}Ar*/^{39}Ar	± ^{40}Ar*/^{39}Ar (1σ)	%^{40}Ar*	Age	± Age (1σ)	± Age (1σ, w/J)	^{36}Ar/^{40}Ar	±^{36}Ar/^{40}Ar (%, 1s)	^{39}Ar/^{40}Ar	±^{39}Ar/^{40}Ar (%, 1s)
90529-02K	3.79E-14	2.65E-16	9.633836	0.035274	95.3667	319.339	1.072	1.472	0.0001552	2.1271630	0.0989914	0.3159622
90529-02L	7.97E-15	1.18E-16	9.696296	0.048430	96.1259	321.235	1.470	1.786	0.0001298	7.6565310	0.0991367	0.3648739
90529-02M	2.58E-15	8.21E-17	9.773299	0.113256	96.0052	323.571	3.433	3.581	0.0001338	24.0613400	0.0982321	0.5578607
90529-02N	1.49E-15	7.14E-17	9.495420	0.179601	95.7238	315.129	5.469	5.559	0.0001432	37.5053400	0.1008105	0.8512372
90529-02O	3.51E-16	5.90E-17	9.714519	0.727704	97.6171	321.788	22.077	22.101	0.0000798	287.1961000	0.1004857	2.6047280
90529-02P	1.03E-16	5.51E-17	8.227056	2.108633	90.9255	276.087	65.614	65.620	0.0003039	240.2329000	0.1105201	8.5961360
Grain-03												
90529-03A	-1.07E-17	5.51E-17	3.524414	22.452160	73.5540	123.480	760.308	760.308	0.0008858	1712.7540000	0.2086984	129.4669000
90529-03B	1.11E-16	5.70E-17	13.759040	2.259383	75.7105	440.500	64.181	64.195	0.0008136	46.7652100	0.0550260	6.1933020
90529-03C	3.01E-16	5.80E-17	8.449995	0.832240	78.3920	283.011	25.797	25.813	0.0007237	33.7852500	0.0927716	2.8441880
90529-03D	5.73E-15	1.01E-16	9.288429	0.069248	91.6039	308.815	2.116	2.331	0.0002812	6.3638890	0.0986216	0.4071001
90529-03E	5.25E-16	5.90E-17	9.350662	0.437876	95.0224	310.716	13.366	13.402	0.0001667	81.1949200	0.1016210	1.9109490
90529-03F	2.99E-16	6.01E-17	10.476680	0.816762	103.4160	344.764	24.466	24.490	-0.0001144	-218.0854000	0.0987107	3.0329170
90529-03G	1.18E-16	5.69E-17	10.634500	1.993404	102.0478	349.486	59.555	59.565	-0.0000686	-846.5579000	0.0959591	7.9856490
90529-03H	8.95E-14	9.39E-16	9.004994	0.038037	96.2720	300.133	1.168	1.508	0.0001249	1.9788820	0.1069096	0.3912540
90529-03I	6.98E-16	6.24E-17	9.177205	0.331300	93.2454	305.413	10.143	10.189	0.0002262	45.3925500	0.1016054	1.4299420
90529-03J	2.96E-16	6.13E-17	10.746840	0.819439	107.6751	352.839	24.436	24.461	-0.0002571	-98.8633100	0.1001923	3.0375320
90529-03K	1.52E-16	5.77E-17	8.616776	1.448579	93.1126	288.173	44.774	44.784	0.0002307	211.4977000	0.1080597	5.9093700
90529-03L	2.24E-17	5.54E-17	10.443340	9.884615	219.1495	343.765	296.252	296.254	-0.0039908	-170.7940000	0.2098462	61.2768700
90529-03M	4.65E-17	5.57E-17	3.404234	4.623695	35.7267	119.406	156.928	156.929	0.0021528	73.4348400	0.1049478	18.0838800
90529-03N	4.99E-17	5.54E-17	8.428734	4.412575	85.3321	282.352	136.829	136.832	0.0004913	284.1436000	0.1012395	17.4405300
Grain-04												
90529-04A	-1.94E-18	5.44E-17	7.924214	109.085800	31.4995	266.639	3412.218	3412.218	0.0022944	606.5658000	0.0397510	303.3365000
90529-04B	2.98E-15	8.68E-17	8.660378	0.112820	74.0239	289.521	3.485	3.605	0.0008700	3.0709330	0.0854742	0.5646100
90529-04C	-3.44E-18	5.48E-17	-11.967300	66.609090	-71.7824	-496.401	3180.450	3180.450	0.0057537	237.0842000	0.0599821	203.9828000
90529-04D	8.06E-15	1.56E-16	9.191059	0.056247	89.6651	305.837	1.722	1.976	0.0003462	3.2590110	0.0975568	0.4112128
90529-04E	6.47E-16	6.48E-17	8.880086	0.346609	92.5099	296.294	10.665	10.707	0.0002509	43.4703600	0.1041768	1.6130990
90529-04F	1.47E-16	5.74E-17	10.545010	1.684950	120.4172	346.810	50.415	50.426	-0.0006839	-88.3747100	0.1141936	6.2204630
90529-04G	8.76E-17	5.59E-17	8.636607	2.524674	108.5248	288.786	78.009	78.014	-0.0002855	-348.0963000	0.1256567	10.8898500
90529-04H	5.78E-14	3.21E-16	9.108078	0.032204	96.1413	303.296	0.987	1.379	0.0001292	2.5784500	0.1055561	0.3081736
90529-04I	2.49E-14	1.78E-16	9.345511	0.034132	95.7506	310.558	1.042	1.433	0.0001423	3.7619130	0.1024562	0.2897053
90529-04J	7.34E-15	1.67E-16	9.401539	0.053567	95.5083	312.268	1.634	1.910	0.0001504	7.0333240	0.1015880	0.4324932
90529-04K	6.47E-15	1.16E-16	9.265479	0.058368	95.3569	308.114	1.784	2.034	0.0001555	9.1251310	0.1029163	0.4153504
90529-04L	7.06E-15	1.15E-16	9.122191	0.061369	95.3102	303.728	1.881	2.113	0.0001571	7.3956210	0.1044817	0.5417816
90529-04M	3.55E-15	9.01E-17	9.169474	0.079368	95.8887	305.176	2.430	2.616	0.0001377	15.1180300	0.1045739	0.5492234

Run_ID	±$^{39}Ar/^{36}Ar$ (%, 1s)	ρ $^{40}Ar/^{39}Ar$	ρ $^{36}Ar/^{39}Ar$
90529-02K	2.0346850	0.8046808	0.3890591
90529-02L	7.6309670	0.9848056	0.1107241
90529-02M	24.0532000	0.9983088	0.0362633
90529-02N	37.5013200	0.9991570	0.0239100
90529-02O	287.1952000	0.9999489	0.0053312
90529-02P	240.2157000	0.9993455	0.0199879
Grain-03			
90529-03A	1709.6480000	0.9971392	0.0616993
90529-03B	46.9683100	0.9909036	0.0354651
90529-03C	33.7874500	0.9957358	0.0458115
90529-03D	6.3340990	0.9775959	0.1330801
90529-03E	81.1954800	0.9995982	0.0140902
90529-03F	-218.0847000	0.9998860	0.0079329
90529-03G	-846.5665000	0.9999544	0.0038417
90529-03H	1.8884470	0.7678233	0.4141808
90529-03I	45.3884200	0.9991042	0.0237628
90529-03J	-98.8569900	0.9994437	0.0188478
90529-03K	211.4858000	0.9995912	0.0161877
90529-03L	-163.2081000	0.9336483	0.3005375
90529-03M	73.1359200	0.9694103	0.1397949
90529-03N	284.1571000	0.9981062	0.0298547
Grain-04			
90529-04A	656.4409000	0.8875910	0.0786616
90529-04B	3.0217680	0.8955770	0.2717052
90529-04C	274.5383000	0.6911722	0.2319386
90529-04D	3.1987910	0.9140482	0.2597277
90529-04E	43.4654200	0.9988757	0.0265554
90529-04F	-88.3298100	0.9974161	0.0431920
90529-04G	-348.0522000	0.9995038	0.0199019
90529-04H	2.5023250	0.8679523	0.3227311
90529-04I	3.7080470	0.9386029	0.2237445
90529-04J	7.0039770	0.9814416	0.1226416
90529-04K	9.1042820	0.9890691	0.0930813
90529-04L	7.3788480	0.9822638	0.1106018
90529-04M	15.1068600	0.9957368	0.0563542

Run_ID	Plateau Steps	Laser Power	^{40}Ar	$\pm^{40}Ar$ (1σ)	^{39}Ar	$\pm^{39}Ar$ (1σ)	^{38}Ar	$\pm^{38}Ar$ (1σ)	^{37}Ar	$\pm^{37}Ar$ (1σ)	^{36}Ar	$\pm^{36}Ar$ (1σ)	% 39Ar
Grain-06	**Int. age 293 ± 6 Ma plat. age 300 ± 3 Ma**												
90529-06A		5.5	-0.0003552	0.0004554	0.0000016	0.0000323	-0.0000305	0.0000342	0.0000013	0.0000297	-0.0000022	0.0000074	0.00
90529-06B		6	-0.0006307	0.0004522	0.0000058	0.0000323	0.0000204	0.0000372	0.0000204	0.0000277	0.0000022	0.0000073	0.00
90529-06C		6.2	-0.0002744	0.0004464	-0.0000250	0.0000345	0.0000156	0.0000338	-0.0000320	0.0000282	0.0000019	0.0000081	0.00
90529-06D		6.4	0.6195590	0.0009794	0.0614550	0.0002518	0.0009787	0.0000446	0.0004070	0.0000314	0.0003245	0.0000092	5.70
90529-06E		6.6	0.7094104	0.0011811	0.0714056	0.0001726	0.0009926	0.0000467	0.0000823	0.0000287	0.0001486	0.0000084	6.62
90529-06F		6.8	2.0667330	0.0015604	0.2328179	0.0003612	0.0028447	0.0000560	0.0003959	0.0000347	0.0002029	0.0000087	21.60
90529-06G	x	7	6.2182240	0.0030307	0.6538741	0.0009905	0.0079018	0.0000733	0.0028045	0.0000659	0.0007160	0.0000120	60.66
90529-06H	x	7.2	0.2766686	0.0008045	0.0288613	0.0001432	0.0003543	0.0000394	0.0000173	0.0000282	0.0000375	0.0000077	2.68
90529-06I	x	7.4	0.1715909	0.0005941	0.0178107	0.0000780	0.0002425	0.0000383	0.0000253	0.0000292	0.0000318	0.0000077	1.65
90529-06J	x	8	0.1013158	0.0005482	0.0103625	0.0000592	0.0001145	0.0000362	0.0000072	0.0000297	0.0000067	0.0000083	0.96
90529-06K		9	0.0103274	0.0004624	0.0010867	0.0000508	-0.0000694	0.0000439	0.0000511	0.0000302	-0.0000046	0.0000079	0.10
90529-06L		10	0.0027026	0.0004522	0.0003257	0.0000323	0.0000387	0.0000353	-0.0000280	0.0000287	-0.0000011	0.0000074	0.03
Grain-07	**Int. age 358 ± 10 Ma No plateau age**												
90529-7A		6.4	0.7689497	0.0011811	0.0557827	0.0001432	0.0009134	0.0000467	0.0004502	0.0000320	0.0005925	0.0000129	7.49
90529-7B		6.6	0.3081730	0.0007463	0.0276411	0.0001044	0.0003865	0.0000383	0.0000240	0.0000287	0.0000431	0.0000089	3.71
90529-7C		6.8	1.2558580	0.0012747	0.1143825	0.0003513	0.0014350	0.0000520	0.0001563	0.0000308	0.0001884	0.0000087	15.36
90529-7D		6.9	3.1738580	0.0020457	0.2769490	0.0005808	0.0035684	0.0000707	0.0006901	0.0000375	0.0004776	0.0000097	37.20
90529-7E		6.95	1.3069310	0.0015604	0.1078503	0.0002220	0.0012553	0.0000425	0.0001051	0.0000297	0.0001552	0.0000107	14.48
90529-7F		7	0.9626706	0.0011811	0.0800691	0.0001237	0.0009848	0.0000512	0.0000367	0.0000308	0.0001001	0.0000097	10.75
90529-7G		7.2	0.7626108	0.0011811	0.0646881	0.0002518	0.0008268	0.0000482	0.0000274	0.0000287	0.0001057	0.0000080	8.69
90529-7H		7.4	0.0963106	0.0005301	0.0080722	0.0000566	0.0001045	0.0000372	0.0000616	0.0000302	0.0000248	0.0000075	1.08
90529-7I		10	0.1078206	0.0005544	0.0091488	0.0000575	0.0001672	0.0000383	0.0000327	0.0000302	0.0000295	0.0000086	1.23
Grain-08	**Int. age 309 ± 3 Ma plat. age 309 ± 2 Ma**												
90529-08A		6.4	0.4735929	0.0012747	0.0412291	0.0001530	0.0007154	0.0000453	0.0000521	0.0000314	0.0002335	0.0000106	6.32
90529-08B		6.6	0.2586430	0.0006595	0.0256890	0.0000716	0.0003213	0.0000400	0.0000600	0.0000314	0.0000556	0.0000077	3.94
90529-08C		6.8	0.2903154	0.0007382	0.0310503	0.0001025	0.0004046	0.0000372	0.0000821	0.0000320	0.0000275	0.0000087	4.76
90529-08D	x	6.85	2.7878310	0.0017535	0.2830496	0.0006207	0.0035263	0.0000569	0.0012426	0.0000361	0.0003767	0.0000119	43.40
90529-08E	x	6.9	1.0624130	0.0012747	0.1077425	0.0001628	0.0013654	0.0000489	0.0002804	0.0000326	0.0001246	0.0000102	16.52
90529-08F	x	6.95	0.4521341	0.0008559	0.0455772	0.0000987	0.0005851	0.0000383	0.0000531	0.0000292	0.0000732	0.0000080	6.99
90529-08G	x	7	0.4598408	0.0009348	0.0459117	0.0001237	0.0005964	0.0000432	0.0000240	0.0000282	0.0000617	0.0000088	7.04
90529-08H	x	7.2	0.0225905	0.0004830	0.0022938	0.0000424	-0.0000047	0.0000394	-0.0000048	0.0000292	0.0000046	0.0000075	0.35
90529-08I	x	7.4	0.2768164	0.0007710	0.0276460	0.0000873	0.0003706	0.0000400	-0.0000116	0.0000308	0.0000360	0.0000078	4.24
90529-08J	x	10	0.4122668	0.0013693	0.0419371	0.0001140	0.0005531	0.0000367	0.0000118	0.0000297	0.0000613	0.0000079	6.43

Run_ID	^{39}Ar moles	^{40}Ar moles	^{40}Ar*/^{39}Ar	± ^{40}Ar*/^{39}Ar (1σ)	%^{40}Ar*	Age	± Age (1σ)	± Age (1σ, w/J)	^{36}Ar/^{40}Ar	±^{36}Ar/^{40}Ar (%, 1s)	^{39}Ar/^{40}Ar	±^{39}Ar/^{40}Ar (%, 1s)
Grain-06												
90529-06A	1.78E-19	5.15E-17	195.858500	4509.034000	-85.6817	2880.603	33120.290	33120.290	0.0062192	359.8022000	-0.0043747	-2184.4240000
90529-06B	6.51E-19	5.11E-17	-227.663400	1465.881000	197.7517	#NAME?	-14864.370	-14864.370	-0.0032741	-362.5152000	-0.0086861	-623.1171000
90529-06C	-2.83E-18	5.04E-17	35.882320	113.213400	321.7817	979.699	2385.130	2385.132	-0.0074284	-433.5057000	0.0896770	227.0342000
90529-06D	6.94E-15	1.11E-16	8.506760	0.081920	84.4688	284.770	2.537	2.695	0.0005202	3.2344730	0.0992961	0.5952155
90529-06E	8.07E-15	1.33E-16	9.305110	0.063708	93.7666	309.325	1.946	2.179	0.0002088	5.8604250	0.1007689	0.4871556
90529-06F	2.63E-14	1.76E-16	8.609746	0.041114	97.0990	287.956	1.271	1.568	0.0000972	4.6113320	0.1127780	0.4179662
90529-06G	7.39E-14	3.42E-16	9.179747	0.042655	96.6346	305.491	1.306	1.626	0.0001127	2.2874600	0.1052693	0.4119118
90529-06H	3.26E-15	9.09E-17	9.188844	0.105438	95.9651	305.769	3.227	3.370	0.0001351	20.6417400	0.1044365	0.7124267
90529-06I	2.01E-15	6.71E-17	9.092641	0.146257	94.4860	302.822	4.484	4.586	0.0001847	24.3367800	0.1039148	0.6985226
90529-06J	1.17E-15	6.19E-17	9.574465	0.254141	98.0389	317.534	7.728	7.793	0.0000657	124.2619000	0.1023962	0.9114978
90529-06K	1.23E-16	5.23E-17	10.835020	2.290252	114.0672	355.466	68.198	68.207	-0.0004712	-163.3156000	0.1052764	6.8438210
90529-06L	3.68E-17	5.11E-17	9.116207	6.985818	110.1325	303.545	214.093	214.095	-0.0003394	-806.4934000	0.1208096	20.6081800
Grain-07												
90529-7A	6.30E-15	1.33E-16	10.615910	0.117337	77.0904	348.930	3.507	3.673	0.0007673	2.6657170	0.0726178	0.4906705
90529-7B	3.12E-15	8.43E-17	10.673370	0.118895	95.8418	350.646	3.550	3.716	0.0001393	20.8848700	0.0897952	0.6039238
90529-7C	1.29E-14	1.44E-16	10.478160	0.063108	95.5418	344.809	1.890	2.178	0.0001493	4.8721750	0.0911818	0.5069218
90529-7D	3.13E-14	2.31E-16	10.937200	0.056014	95.5431	358.506	1.665	2.007	0.0001493	2.5425850	0.0873561	0.4413265
90529-7E	1.22E-14	1.76E-16	11.676850	0.065522	96.4681	380.361	1.924	2.259	0.0001183	7.1044540	0.0826149	0.4521734
90529-7F	9.05E-15	1.33E-16	11.637400	0.065927	96.9027	379.202	1.937	2.268	0.0001037	9.8200640	0.0832683	0.4301716
90529-7G	7.31E-15	1.33E-16	11.289280	0.079726	95.8696	368.942	2.356	2.622	0.0001383	7.7773160	0.0849210	0.5789664
90529-7H	9.12E-16	5.99E-17	11.016400	0.302695	92.4290	360.859	8.987	9.057	0.0002536	30.8253200	0.0839012	1.0120160
90529-7I	1.03E-15	6.26E-17	10.816310	0.300294	91.8786	354.909	8.945	9.013	0.0002720	29.2402100	0.0849445	0.9347571
Grain-08												
90529-08A	4.66E-15	1.44E-16	9.787292	0.110723	85.3003	323.995	3.355	3.507	0.0004924	4.7890060	0.0871542	0.6122427
90529-08B	2.90E-15	7.45E-17	9.415724	0.107796	93.6241	312.701	3.287	3.433	0.0002136	14.1043600	0.0994338	0.5482685
90529-08C	3.51E-15	8.34E-17	9.079218	0.100189	97.2146	302.411	3.072	3.219	0.0000933	32.1067500	0.1070737	0.5783802
90529-08D	3.20E-14	1.98E-16	9.448792	0.048917	96.0389	313.709	1.491	1.791	0.0001327	3.5633960	0.1016415	0.4461530
90529-08E	1.22E-14	1.44E-16	9.509058	0.053470	96.5422	315.544	1.628	1.909	0.0001158	8.4277160	0.1015265	0.4279681
90529-08F	5.15E-15	9.67E-17	9.432031	0.073845	95.1876	313.198	2.251	2.460	0.0001612	11.1474300	0.1009195	0.4835305
90529-08G	5.19E-15	1.06E-16	9.604568	0.079115	96.0047	318.450	2.405	2.607	0.0001338	14.4000700	0.0999573	0.5179132
90529-08H	2.59E-16	5.46E-17	9.232684	1.014219	93.8604	307.111	31.021	31.036	0.0002056	160.9530000	0.1016610	3.0113550
90529-08I	3.12E-15	8.71E-17	9.611974	0.103561	96.1075	318.675	3.147	3.305	0.0001304	21.6467000	0.0999873	0.5823035
90529-08J	4.74E-15	1.55E-16	9.383698	0.082602	95.5642	311.724	2.520	2.706	0.0001486	12.9770400	0.1018407	0.5897139

Run_ID	±$^{39}Ar/^{36}Ar$ (%, 1s)	ρ $^{40}Ar/^{39}Ar$	ρ $^{36}Ar/^{39}Ar$
Grain-06			
90529-06A	-2205.5450000	0.1396990	0.0236623
90529-06B	712.7065000	0.4860517	0.0257607
90529-06C	-423.7864000	0.8599491	0.3043384
90529-06D	3.1020810	0.7969712	0.3871910
90529-06E	5.7778620	0.9404993	0.2190716
90529-06F	4.5043700	0.9049886	0.2772040
90529-06G	2.0632020	0.5993714	0.5478026
90529-06H	20.6218400	0.9949125	0.0619619
90529-06I	24.3178300	0.9963567	0.0534693
90529-06J	124.2579000	0.9998492	0.0108110
90529-06K	-163.3176000	0.9990502	0.0217232
90529-06L	-806.3660000	0.9996705	0.0191328
Grain-07			
90529-7A	2.4814910	0.7050184	0.4729016
90529-7B	20.8631900	0.9951938	0.0615892
90529-7C	4.7786900	0.9133444	0.2603843
90529-7D	2.3480960	0.6782094	0.4935468
90529-7E	7.0363490	0.9599159	0.1806256
90529-7F	9.7698430	0.9791587	0.1312197
90529-7G	7.7221870	0.9655122	0.1631555
90529-7H	30.8122100	0.9974471	0.0428651
90529-7I	29.2253800	0.9972507	0.0452186
Grain-08			
90529-08A	4.6915020	0.9076583	0.2682145
90529-08B	14.0694400	0.9896164	0.0921180
90529-08C	32.0919000	0.9979813	0.0403200
90529-08D	3.4276100	0.8387722	0.3558823
90529-08E	8.3689480	0.9716898	0.1528198
90529-08F	11.1032500	0.9836367	0.1159872
90529-08G	14.3666700	0.9901178	0.0896656
90529-08H	160.9451000	0.9997511	0.0133939
90529-08I	21.6242400	0.9955535	0.0600912
90529-08J	12.9370100	0.9875906	0.1014713

Run_ID	Plateau Steps	Laser Power	^{40}Ar	$\pm^{40}Ar$ (1σ)	^{39}Ar	$\pm^{39}Ar$ (1σ)	^{38}Ar	$\pm^{38}Ar$ (1σ)	^{37}Ar	$\pm^{37}Ar$ (1σ)	^{36}Ar	$\pm^{36}Ar$ (1σ)	% 39Ar
Grain-09	**Int. age 311 ± 7 plat. age 317 ± 4 Ma**												
90529-09A		6.4	0.8512497	0.0011811	0.0632208	0.0002121	0.0010464	0.0000412	0.0000298	0.0000297	0.0006857	0.0000105	4.85
90529-09B		6.6	0.9234669	0.0018506	0.0804964	0.0001726	0.0011662	0.0000419	0.0002106	0.0000297	0.0003563	0.0000091	6.18
90529-09C		6.8	0.2758081	0.0007710	0.0274223	0.0001628	0.0002580	0.0000394	0.0000677	0.0000302	0.0000179	0.0000075	2.10
90529-09D		6.85	0.1778076	0.0006011	0.0189707	0.0000771	0.0002059	0.0000528	0.0000109	0.0000302	0.0000120	0.0000076	1.46
90529-09E		6.9	0.1811897	0.0005873	0.0198627	0.0001334	0.0003039	0.0000358	0.0000933	0.0000308	0.0000230	0.0000075	1.52
90529-09F		6.95	0.1777841	0.0005941	0.0192992	0.0000762	0.0002548	0.0000367	0.0000528	0.0000320	0.0000094	0.0000083	1.48
90529-09G		7	0.1100467	0.0005243	0.0117132	0.0000662	0.0001747	0.0000372	0.0000235	0.0000308	0.0000111	0.0000075	0.90
90529-09H		7.2	0.6685295	0.0010885	0.0723220	0.0001726	0.0009532	0.0000489	0.0001824	0.0000287	0.0000630	0.0000091	5.55
90529-09I		7.4	3.0155760	0.0020457	0.3094275	0.0006407	0.0040271	0.0000871	0.0006666	0.0000361	0.0004074	0.0000129	23.74
90529-09J	x	10	6.2629580	0.0052177	0.6122169	0.0010004	0.0075629	0.0000707	0.0021617	0.0000532	0.0010828	0.0000183	46.97
90529-09K	x	11	0.5844363	0.0009171	0.0570374	0.0001432	0.0006797	0.0000439	-0.0000054	0.0000308	0.0000759	0.0000093	4.38
90529-09L	x	12	0.1170749	0.0005360	0.0114682	0.0000653	0.0001799	0.0000362	0.0000102	0.0000326	0.0000269	0.0000075	0.88
Grain-10	**Int. age 300 ± 5 Ma plat. age 305 ± 2 Ma**												
90529-10A		6.4	0.4771368	0.0009884	0.0448979	0.0001140	0.0006991	0.0000453	0.0012869	0.0000438	0.0002562	0.0000086	3.72
90529-10B		6.6	0.2202221	0.0008045	0.0213739	0.0000930	0.0002863	0.0000388	0.0008052	0.0000455	0.0000556	0.0000095	1.77
90529-10C		6.8	0.4467162	0.0008472	0.0445523	0.0001140	0.0006099	0.0000383	0.0000809	0.0000302	0.0001129	0.0000093	3.69
90529-10D		6.85	0.6195590	0.0012747	0.0670948	0.0001237	0.0008198	0.0000394	0.0001662	0.0000314	0.0000702	0.0000093	5.56
90529-10E		6.9	0.7405733	0.0012747	0.0820045	0.0001628	0.0010600	0.0000383	0.0001349	0.0000297	0.0000775	0.0000095	6.80
90529-10F		6.95	1.2927000	0.0012747	0.1402357	0.0003413	0.0017318	0.0000497	0.0002480	0.0000347	0.0001367	0.0000085	11.62
90529-10G	x	7	2.2145600	0.0016568	0.2289585	0.0003513	0.0029153	0.0000654	0.0004367	0.0000398	0.0002871	0.0000110	18.98
90529-10H	x	7.2	3.5957920	0.0023399	0.3684902	0.0007106	0.0044025	0.0000707	0.0012924	0.0000354	0.0004860	0.0000100	30.54
90529-10I	x	7.4	0.9774544	0.0011811	0.1004510	0.0002121	0.0012961	0.0000467	0.0001238	0.0000292	0.0001287	0.0000096	8.32
90529-10J		10	1.0727190	0.0012747	0.1085615	0.0001628	0.0012970	0.0000419	0.0000797	0.0000302	0.0001195	0.0000100	9.00
Grain-21	**Int. age 298 ± 7 No plat. age**												
90529-21A		6.4	0.5693120	0.0006920	0.0324825	0.0001128	0.0007440	0.0000559	0.0000901	0.0000230	0.0008825	0.0000119	0.80
90529-21B		6.6	0.7255751	0.0007739	0.0751888	0.0001521	0.0009393	0.0000559	0.0001833	0.0000311	0.0002617	0.0000123	1.85
90529-21C		6.8	1.3599660	0.0015577	0.1242742	0.0001916	0.0019740	0.0000517	0.0008741	0.0000342	0.0007120	0.0000141	3.06
90529-21D		6.9	0.2374208	0.0005664	0.0227230	0.0000810	0.0003369	0.0000425	0.0001560	0.0000237	0.0000381	0.0000109	0.56
90529-21E		6.95	0.1669277	0.0005161	0.0158842	0.0000438	0.0001728	0.0000480	0.0001467	0.0000233	0.0000258	0.0000109	0.39
90529-21F		7	0.1917545	0.0005280	0.0187258	0.0000455	0.0003070	0.0000492	0.0001843	0.0000227	0.0000371	0.0000110	0.46
90529-21G		7.2	1.0464060	0.0014616	0.1113582	0.0001128	0.0016938	0.0000793	0.0018946	0.0000655	0.0003565	0.0000120	2.74
90529-21H		7.4	2.1850060	0.0018484	0.2398313	0.0004807	0.0032606	0.0000981	0.0015207	0.0000425	0.0004279	0.0000125	5.91
90529-21I		10	22.8162500	0.0051173	2.3615630	0.0022001	0.0312695	0.0002234	0.0159466	0.0001218	0.0046594	0.0000269	58.18

Run_ID	^{39}Ar moles	^{40}Ar moles	^{40}Ar*/^{39}Ar	± ^{40}Ar*/^{39}Ar (1σ)	%^{40}Ar*	Age	± Age (1σ)	± Age (1σ, w/J)	^{36}Ar/^{40}Ar	±^{36}Ar/^{40}Ar (%, 1s)	^{39}Ar/^{40}Ar	±^{39}Ar/^{40}Ar (%, 1s)
Grain-09												
90529-09A	7.14E-15	1.33E-16	10.215810	0.108347	75.9569	336.933	3.260	3.428	0.0008053	2.1536200	0.0743523	0.5358515
90529-09B	9.10E-15	2.09E-16	10.143700	0.074923	88.5184	334.762	2.257	2.491	0.0003846	2.9735950	0.0872644	0.4875659
90529-09C	3.10E-15	8.71E-17	9.856050	0.113732	98.1039	326.077	3.442	3.593	0.0000635	42.9482800	0.0995367	0.7854458
90529-09D	2.14E-15	6.79E-17	9.173336	0.134853	97.9854	305.295	4.129	4.241	0.0000675	63.0409300	0.1068154	0.6725177
90529-09E	2.24E-15	6.64E-17	8.774459	0.137839	96.2944	293.041	4.249	4.350	0.0001241	33.4678700	0.1097440	0.8693524
90529-09F	2.18E-15	6.71E-17	9.061278	0.141834	98.4747	301.860	4.351	4.455	0.0000511	91.0593800	0.1086764	0.6626231
90529-09G	1.32E-15	5.92E-17	9.104870	0.208074	97.0204	303.197	6.378	6.450	0.0000998	68.4749400	0.1065588	0.8654885
90529-09H	8.17E-15	1.23E-16	8.977770	0.059990	97.2318	299.297	1.843	2.074	0.0000927	14.8203200	0.1083029	0.4840821
90529-09I	3.50E-14	2.31E-16	9.345604	0.047981	96.0034	310.561	1.465	1.764	0.0001339	3.5427060	0.1027257	0.4405369
90529-09J	6.92E-14	5.90E-16	9.697009	0.049071	94.8952	321.257	1.489	1.802	0.0001710	2.2831480	0.0978603	0.4230431
90529-09K	6.45E-15	1.04E-16	9.837527	0.071854	96.1199	325.516	2.175	2.406	0.0001300	12.3018300	0.0977074	0.4887096
90529-09L	1.30E-15	6.06E-17	9.498080	0.214590	93.1463	315.210	6.534	6.610	0.0002296	28.0201500	0.0980685	0.8571769
Grain-10												
90529-10A	5.07E-15	1.12E-16	8.964916	0.088682	84.4207	298.902	2.725	2.886	0.0005218	3.7886510	0.0941679	0.5108594
90529-10B	2.42E-15	9.09E-17	9.583411	0.153305	93.0691	317.806	4.661	4.768	0.0002321	18.7494100	0.0971148	0.7073812
90529-10C	5.03E-15	9.57E-17	9.262891	0.084093	92.4862	308.034	2.571	2.750	0.0002517	8.4466200	0.0998459	0.5043699
90529-10D	7.58E-15	1.44E-16	8.915804	0.062161	96.6625	297.392	1.912	2.133	0.0001118	13.4753000	0.1084170	0.4764600
90529-10E	9.27E-15	1.44E-16	8.741371	0.056463	96.9051	292.020	1.741	1.974	0.0001037	12.5309600	0.1108580	0.4675381
90529-10F	1.58E-14	1.44E-16	8.919788	0.048750	96.8748	297.515	1.499	1.772	0.0001047	6.4637330	0.1086067	0.4667214
90529-10G	2.59E-14	1.87E-16	9.290569	0.046185	96.1624	308.880	1.411	1.717	0.0001285	4.1384550	0.1035053	0.4171165
90529-10H	4.16E-14	2.64E-16	9.359797	0.046463	96.0242	310.995	1.418	1.727	0.0001332	2.5877090	0.1025922	0.4329103
90529-10I	1.14E-14	1.33E-16	9.339528	0.055421	96.0905	310.376	1.692	1.957	0.0001309	7.6663130	0.1028858	0.4552829
90529-10J	1.23E-14	1.44E-16	9.542603	0.052935	96.6845	316.565	1.611	1.896	0.0001110	8.5124800	0.1013188	0.4271796
Grain-21												
90529-21A	3.67E-15	7.82E-17	9.416001	0.161580	53.7987	312.709	4.927	5.025	0.0015475	1.7294430	0.0571354	0.4637358
90529-21B	8.50E-15	8.75E-17	8.610302	0.063026	89.3547	287.973	1.948	2.154	0.0003566	4.8676690	0.1037765	0.3570390
90529-21C	1.40E-14	1.76E-16	9.256365	0.058047	84.6897	307.835	1.775	2.025	0.0005128	2.2936270	0.0914934	0.3335496
90529-21D	2.57E-15	6.40E-17	9.969728	0.153142	95.5369	329.514	4.626	4.741	0.0001495	30.7155000	0.0958270	0.5165989
90529-21E	1.79E-15	5.83E-17	10.058220	0.211651	95.8198	332.186	6.384	6.469	0.0001400	46.6246100	0.0952651	0.5047872
90529-21F	2.12E-15	5.97E-17	9.687106	0.182314	94.7052	320.957	5.534	5.626	0.0001773	32.4119700	0.0977642	0.4642711
90529-21G	1.26E-14	1.65E-16	8.519244	0.048543	90.7350	285.156	1.503	1.757	0.0003103	3.8687840	0.1065059	0.3221027
90529-21H	2.71E-14	2.09E-16	8.598618	0.037876	94.5014	287.612	1.171	1.487	0.0001842	3.2988590	0.1099030	0.3494856
90529-21I	2.67E-13	5.78E-16	9.094776	0.031959	94.2526	302.888	0.980	1.373	0.0001925	1.2524240	0.1036338	0.2860665

Run_ID	±$^{39}Ar/^{36}Ar$ (%, 1s)	ρ $^{40}Ar/^{39}Ar$	ρ $^{36}Ar/^{39}Ar$
Grain-09			
90529-09A	1.9356860	0.5369014	0.5746621
90529-09B	2.8024290	0.7642767	0.4288241
90529-09C	42.9400600	0.9987955	0.0293387
90529-09D	63.0334000	0.9994617	0.0206834
90529-09E	33.4584800	0.9979543	0.0374979
90529-09F	91.0540600	0.9997428	0.0143259
90529-09G	68.4682400	0.9995121	0.0192849
90529-09H	14.7877400	0.9907472	0.0869312
90529-09I	3.4055220	0.8371595	0.3580999
90529-09J	2.0588060	0.5976319	0.5487323
90529-09K	12.2631000	0.9865527	0.1045478
90529-09L	28.0044100	0.9970947	0.0468654
Grain-10			
90529-10A	3.6572600	0.8551836	0.3384042
90529-10B	18.7237000	0.9938384	0.0696799
90529-10C	8.3894220	0.9713222	0.1525626
90529-10D	13.4378900	0.9888251	0.0963400
90529-10E	12.4915700	0.9871028	0.1031248
90529-10F	6.3905030	0.9513755	0.1977076
90529-10G	4.0189040	0.8817658	0.3083793
90529-10H	2.3949400	0.6898309	0.4860141
90529-10I	7.6033350	0.9655694	0.1674298
90529-10J	8.4544510	0.9722617	0.1512894
Grain-21			
90529-21A	1.6112400	0.6397141	0.4977302
90529-21B	4.8184230	0.9579913	0.1823372
90529-21C	2.1824690	0.8072869	0.3871449
90529-21D	30.7081100	0.9988775	0.0290620
90529-21E	46.6185600	0.9995156	0.0198125
90529-21F	32.4034900	0.9990162	0.0283145
90529-21G	3.7995630	0.9337211	0.2325179
90529-21H	3.2252750	0.9078185	0.2682736
90529-21I	1.0311390	0.2873479	0.7006581

Run_ID	Plateau Steps	Laser Power	^{40}Ar	$\pm^{40}Ar$ (1σ)	^{39}Ar	$\pm^{39}Ar$ (1σ)	^{38}Ar	$\pm^{38}Ar$ (1σ)	^{37}Ar	$\pm^{37}Ar$ (1σ)	^{36}Ar	$\pm^{36}Ar$ (1σ)	% 39Ar
90529-21J		12	7.0130980	0.0034258	0.7089642	0.0005106	0.0087282	0.0000724	0.0008064	0.0000252	0.0010280	0.0000149	17.47
90529-21K		13	1.1349620	0.0013662	0.1139859	0.0001817	0.0014450	0.0000595	0.0000903	0.0000233	0.0001344	0.0000117	2.81
90529-21L		14	0.4014229	0.0006155	0.0403311	0.0000992	0.0005794	0.0000434	0.0002930	0.0000358	0.0000727	0.0000113	0.99
90529-22J		11	1.6622660	0.0010204	0.1722196	0.0001226	0.0055466	0.0000611	0.0194001	0.0001120	0.0027267	0.0000164	4.24
90529-21M		15	0.1288036	0.0004888	0.0130144	0.0000398	0.0000728	0.0000458	0.0000452	0.0000229	0.0000104	0.0000104	0.32
90529-22K		12	0.0001514	0.0004308	-0.0000315	0.0000282	-0.0000389	0.0000438	0.0000252	0.0000221	-0.0000137	0.0000106	0.00
90529-21N		16	0.0839549	0.0004741	0.0087083	0.0000368	0.0001320	0.0000422	0.0000168	0.0000226	0.0000055	0.0000108	0.21
Grain-23	**Int. age 308 ± 6 Ma No plat. age**												
90529-23A		6.4	2.1340580	0.0014616	0.1790397	0.0001521	0.0025902	0.0000699	0.0003528	0.0000242	0.0012261	0.0000130	8.13
90529-23B		6.6	0.2912409	0.0006155	0.0275856	0.0000550	0.0003543	0.0000430	0.0000320	0.0000227	0.0000196	0.0000108	1.25
90529-23C		6.8	3.0191940	0.0021416	0.3258494	0.0006805	0.0038089	0.0000908	0.0001806	0.0000233	0.0004117	0.0000129	14.80
90529-23D		6.9	6.4467470	0.0047187	0.6610886	0.0010003	0.0076810	0.0001073	0.0005008	0.0000342	0.0009359	0.0000164	30.03
90529-23E		7	3.0228880	0.0015577	0.3047640	0.0006705	0.0036367	0.0000819	0.0014660	0.0000290	0.0006327	0.0000149	13.84
90529-23F		7.2	2.2420790	0.0024365	0.2232339	0.0003708	0.0025618	0.0000836	0.0004017	0.0000311	0.0003548	0.0000131	10.14
90529-23G		7.4	1.3485300	0.0013662	0.1313242	0.0001324	0.0015830	0.0000845	0.0001327	0.0000237	0.0002654	0.0000120	5.96
90529-23H		8	1.9545990	0.0018484	0.1931131	0.0002512	0.0024753	0.0000511	0.0004257	0.0000311	0.0002917	0.0000124	8.77
90529-23I		9	1.3021000	0.0008509	0.1304438	0.0001226	0.0015965	0.0000691	0.0001671	0.0000242	0.0001928	0.0000118	5.92
90529-23J		12	0.2820170	0.0008683	0.0232075	0.0000791	0.0008297	0.0000458	0.0000764	0.0000227	0.0001425	0.0000107	1.05
90529-23K		14	0.0220616	0.0004427	0.0021130	0.0000383	0.0000465	0.0000498	0.0000646	0.0000270	-0.0000041	0.0000103	0.10
Grain-24	**Int. age 296 ± 3 Ma No plat. age**												
90529-24A		6.4	1.0514630	0.0010296	0.1039706	0.0001718	0.0015543	0.0000603	0.0001935	0.0000228	0.0004334	0.0000131	12.28
90529-24B		6.6	0.3432097	0.0006762	0.0367991	0.0001324	0.0003900	0.0000511	0.0000137	0.0000227	0.0000202	0.0000108	4.34
90529-24C		6.8	4.7704640	0.0043205	0.5121354	0.0005805	0.0063119	0.0000854	0.0001538	0.0000264	0.0005541	0.0000156	60.47
90529-24E		7	0.8309169	0.0007572	0.0868716	0.0000992	0.0009419	0.0000749	0.0000462	0.0000224	0.0001207	0.0000107	10.26
90529-24F		7.2	0.3454781	0.0005800	0.0365733	0.0001128	0.0003160	0.0000531	0.0000224	0.0000232	0.0000305	0.0000108	4.32
90529-24G		7.4	0.3539217	0.0009124	0.0370113	0.0000632	0.0004943	0.0000480	0.0000081	0.0000228	0.0000264	0.0000109	4.37
90529-24H		8	0.2027160	0.0007572	0.0213543	0.0001031	0.0002910	0.0000434	-0.0000150	0.0000230	0.0000173	0.0000110	2.52
90529-24I		9	0.0827016	0.0004652	0.0085097	0.0000368	0.0001242	0.0000469	-0.0000216	0.0000223	0.0000155	0.0000108	1.00
90529-24J		10	0.0263512	0.0004397	0.0025797	0.0000430	-0.0000541	0.0000463	-0.0000232	0.0000227	-0.0000116	0.0000107	0.30
90529-24K		12	0.0110463	0.0004397	0.0011490	0.0000340	-0.0000253	0.0000463	0.0000063	0.0000230	-0.0000101	0.0000106	0.14
Grain-25	**Int. age 291 ± 3 Ma No plat. age**												
90529-25A		6.4	1.1647170	0.0008947	0.1057006	0.0001817	0.0015319	0.0000650	0.0003043	0.0000247	0.0007000	0.0000149	9.17
90529-25B		6.6	0.2504158	0.0007406	0.0263135	0.0000886	0.0003451	0.0000552	0.0000058	0.0000226	0.0000094	0.0000109	2.28
90529-25C		6.8	4.2085540	0.0030293	0.4593132	0.0007804	0.0055041	0.0001167	0.0003053	0.0000237	0.0006514	0.0000137	39.85
90529-25D		6.9	3.8070610	0.0027325	0.4048011	0.0007804	0.0051238	0.0000749	0.0006305	0.0000383	0.0005825	0.0000138	35.12

Run_ID	^{39}Ar moles	^{40}Ar moles	^{40}Ar*/^{39}Ar	± ^{40}Ar*/^{39}Ar (1σ)	%^{40}Ar*	Age	± Age (1σ)	± Age (1σ, w/J)	^{36}Ar/^{40}Ar	±^{36}Ar/^{40}Ar (%, 1s)	^{39}Ar/^{40}Ar	±^{39}Ar/^{40}Ar (%, 1s)
90529-21J	8.01E-14	3.87E-16	9.450561	0.031821	95.6810	313.763	0.970	1.388	0.0001447	1.8204060	0.1012438	0.2832661
90529-21K	1.29E-14	1.54E-16	9.594426	0.047030	96.5049	318.141	1.430	1.748	0.0001171	8.8890350	0.1005844	0.3383995
90529-21L	4.56E-15	6.96E-17	9.440603	0.093480	94.9671	313.459	2.849	3.017	0.0001686	16.7197600	0.1005943	0.4013664
90529-22J	1.95E-14	1.15E-16	5.515321	0.068046	56.9447	189.670	2.221	2.306	0.0014421	1.3097080	0.1032482	0.2832402
90529-21M	1.47E-15	5.52E-17	9.660819	0.245436	97.7502	320.159	7.453	7.521	0.0000754	107.3701000	0.1011821	0.5702130
90529-22K	-3.56E-18	4.87E-17	-133.817300	153.543900	2886.8660	#NAME?	-3295.061	-3295.076	-0.0933437	-303.8002000	-0.2157318	-307.5145000
90529-21N	9.84E-16	5.36E-17	9.447002	0.379089	98.1346	313.654	11.553	11.595	0.0000625	206.9340000	0.1038791	0.7759166
Grain-23												
90529-23A	2.02E-14	1.65E-16	9.870431	0.054366	82.9300	326.512	1.645	1.941	0.0005717	1.5162870	0.0840186	0.2912583
90529-23B	3.12E-15	6.96E-17	10.336280	0.124303	98.0496	340.554	3.732	3.882	0.0000653	56.6642000	0.0948597	0.4024451
90529-23C	3.68E-14	2.42E-16	8.877473	0.036392	95.9585	296.213	1.120	1.463	0.0001354	3.3302030	0.1080921	0.3514846
90529-23D	7.47E-14	5.33E-16	9.318531	0.034520	95.7037	309.735	1.054	1.440	0.0001439	2.0725260	0.1027026	0.3194931
90529-23E	3.44E-14	1.76E-16	9.310743	0.040893	93.9960	309.497	1.249	1.588	0.0002011	2.6776530	0.1009544	0.3549690
90529-23F	2.52E-14	2.75E-16	9.563928	0.040518	95.3645	317.214	1.232	1.589	0.0001553	3.9090370	0.0997127	0.3375308
90529-23G	1.48E-14	1.54E-16	9.655736	0.044777	94.1728	320.004	1.360	1.694	0.0001952	4.6822540	0.0975305	0.3064605
90529-23H	2.18E-14	2.09E-16	9.667665	0.039684	95.6553	320.366	1.205	1.574	0.0001455	4.4907220	0.0989436	0.3156169
90529-23I	1.47E-14	9.62E-17	9.532923	0.042177	95.6439	316.271	1.284	1.627	0.0001459	6.3189480	0.1003301	0.2934160
90529-23J	2.62E-15	9.81E-17	10.323900	0.155183	85.0753	340.182	4.660	4.781	0.0004999	7.7021930	0.0824062	0.5440508
90529-23K	2.39E-16	5.00E-17	11.181340	1.489049	107.1090	365.749	44.088	44.103	-0.0002381	-196.4629000	0.0957927	2.8028830
Grain-24												
90529-24A	1.17E-14	1.16E-16	8.865191	0.055781	87.7901	295.835	1.717	1.958	0.0004090	3.2257100	0.0990279	0.3335386
90529-24B	4.16E-15	7.64E-17	9.150068	0.099104	98.2594	304.582	3.035	3.186	0.0000583	53.8828300	0.1073866	0.5001072
90529-24C	5.79E-14	4.88E-16	8.979362	0.032076	96.5481	299.346	0.985	1.369	0.0001156	3.0323090	0.1075222	0.3074900
90529-24E	9.82E-15	8.56E-17	9.138503	0.048759	95.6895	304.228	1.494	1.778	0.0001444	8.9605140	0.1047102	0.3079892
90529-24F	4.13E-15	6.55E-17	9.185545	0.098446	97.3906	305.668	3.014	3.166	0.0000874	35.9669500	0.1060259	0.4501220
90529-24G	4.18E-15	1.03E-16	9.336027	0.097069	97.7832	310.269	2.964	3.122	0.0000743	41.6216100	0.1047374	0.4172546
90529-24H	2.41E-15	8.56E-17	9.232834	0.167392	97.4151	307.115	5.120	5.212	0.0000866	63.0170600	0.1055094	0.6834141
90529-24I	9.62E-16	5.26E-17	9.145457	0.386432	94.2612	304.441	11.837	11.876	0.0001922	68.0526500	0.1030689	0.7798649
90529-24J	2.92E-16	4.97E-17	11.489600	1.264790	112.7010	374.853	37.259	37.278	-0.0004254	-95.5294300	0.0980897	2.4455820
90529-24K	1.30E-16	4.97E-17	12.234460	2.796902	127.4232	396.664	81.404	81.413	-0.0009185	-104.2763000	0.1041511	5.1244430
Grain-25												
90529-25A	1.19E-14	1.01E-16	9.043664	0.064445	82.1903	301.320	1.977	2.197	0.0005965	2.3977940	0.0908816	0.3311376
90529-25B	2.97E-15	8.37E-17	9.396766	0.133951	98.8944	312.122	4.086	4.203	0.0000370	117.9185000	0.1052431	0.5341667
90529-25C	5.19E-14	3.42E-16	8.729199	0.033755	95.4156	291.645	1.041	1.395	0.0001536	2.3738360	0.1093062	0.3289041
90529-25D	4.57E-14	3.09E-16	8.969774	0.035887	95.5177	299.051	1.103	1.455	0.0001501	2.6475920	0.1064884	0.3418719

Run_ID	±^{39}Ar/^{36}Ar (%, 1s)	ρ ^{40}Ar/^{39}Ar	ρ ^{36}Ar/^{39}Ar
90529-21J	1.6762020	0.6928148	0.4849272
90529-21K	8.8610770	0.9875417	0.1005594
90529-21L	16.7052600	0.9963991	0.0532631
90529-22J	1.0932770	0.3353415	0.6805488
90529-21M	107.3671000	0.9999056	0.0087915
90529-22K	115.9388000	0.1586424	0.9280511
90529-21N	206.9320000	0.9999714	0.0048748
Grain-23			
90529-23A	1.3399510	0.5446843	0.5793408
90529-23B	56.6595300	0.9996866	0.0159974
90529-23C	3.2594880	0.9098216	0.2648131
90529-23D	1.9511870	0.7639188	0.4256045
90529-23E	2.5897180	0.8589130	0.3282560
90529-23F	3.8456070	0.9350379	0.2277447
90529-23G	4.6277870	0.9553304	0.1909726
90529-23H	4.4345940	0.9512468	0.1986130
90529-23I	6.2790200	0.9756527	0.1411843
90529-23J	7.6703790	0.9818601	0.1186366
90529-23K	-196.4622000	0.9998742	0.0090701
Grain-24			
90529-24A	3.1491080	0.9042995	0.2752746
90529-24B	53.8788900	0.9996383	0.0163866
90529-24C	2.9485190	0.8923945	0.2935454
90529-24E	8.9324580	0.9878630	0.0997298
90529-24F	35.9607600	0.9992064	0.0246098
90529-24G	41.6149400	0.9994156	0.0221083
90529-24H	63.0136400	0.9997082	0.0144642
90529-24I	68.0474800	0.9997346	0.0147801
90529-24J	-95.5279700	0.9995709	0.0157878
90529-24K	-104.2402000	0.9987069	0.0329366
Grain-25			
90529-25A	2.2951080	0.8247658	0.3681790
90529-25B	117.9163000	0.9999232	0.0077284
90529-25C	2.2701130	0.8212937	0.3717343
90529-25D	2.5563880	0.8564513	0.3331531

Run_ID	Plateau Steps	Laser Power	^{40}Ar	$\pm^{40}Ar$ (1σ)	^{39}Ar	$\pm^{39}Ar$ (1σ)	^{38}Ar	$\pm^{38}Ar$ (1σ)	^{37}Ar	$\pm^{37}Ar$ (1σ)	^{36}Ar	$\pm^{36}Ar$ (1σ)	% 39Ar
90529-25E		7	1.1212580	0.0009302	0.1203977	0.0001916	0.0013963	0.0000682	0.0000639	0.0000230	0.0001876	0.0000117	10.45
90529-25F		7.2	0.2349837	0.0008422	0.0234156	0.0000532	0.0003070	0.0000517	0.0000297	0.0000226	0.0000675	0.0000111	2.03
90529-25G		7.4	0.0945573	0.0004610	0.0097461	0.0000604	0.0001012	0.0000492	-0.0000051	0.0000230	0.0000027	0.0000107	0.85
90529-25H		8	0.0269039	0.0004427	0.0024513	0.0000383	-0.0000252	0.0000463	-0.0000058	0.0000264	0.0000084	0.0000108	0.21
90529-25I		9	0.0049871	0.0004397	0.0003256	0.0000297	0.0000128	0.0000463	0.0000278	0.0000227	-0.0000001	0.0000105	0.03
90529-25J		10	0.0015271	0.0004291	0.0000871	0.0000297	-0.0000557	0.0000438	-0.0000254	0.0000264	-0.0000183	0.0000108	0.01
90529-25K		12	0.0001944	0.0004306	-0.0000105	0.0000282	0.0000330	0.0000443	-0.0000264	0.0000222	-0.0000067	0.0000106	0.00
Grain-26	**Int. age 310 ± 4 Ma No plat. age**												
90529-26A		6.4	1.4732930	0.0009751	0.1174632	0.0001226	0.0018301	0.0000498	0.0002155	0.0000233	0.0010655	0.0000125	8.78
90529-26B		6.7	0.5360063	0.0006530	0.0554917	0.0001324	0.0007074	0.0000463	0.0000858	0.0000242	0.0000512	0.0000112	4.15
90529-26C		6.75	1.3306370	0.0015577	0.1397204	0.0001226	0.0017158	0.0000492	0.0001130	0.0000237	0.0001778	0.0000117	10.44
90529-26D		6.8	2.8969120	0.0014616	0.2957727	0.0003609	0.0037020	0.0000603	0.0001881	0.0000230	0.0004322	0.0000129	22.10
90529-26E		6.825	1.1209690	0.0008596	0.1099267	0.0001031	0.0013666	0.0000674	0.0000642	0.0000223	0.0001896	0.0000117	8.22
90529-26F		6.85	0.2154771	0.0006841	0.0213968	0.0000848	0.0001545	0.0000552	0.0000052	0.0000233	0.0000333	0.0000108	1.60
90529-26G		6.875	0.2592879	0.0007992	0.0260784	0.0000497	0.0003689	0.0000595	0.0000584	0.0000230	0.0000452	0.0000110	1.95
90529-26H		6.9	0.1734516	0.0004888	0.0172825	0.0000472	0.0001874	0.0000438	0.0000227	0.0000232	0.0000256	0.0000108	1.29
90529-26I		6.95	0.5427227	0.0010754	0.0550926	0.0001226	0.0005093	0.0000566	0.0000142	0.0000230	0.0000782	0.0000110	4.12
90529-26J		7.05	3.6778240	0.0027325	0.3625513	0.0008404	0.0044307	0.0001018	0.0005185	0.0000264	0.0006283	0.0000136	27.10
90529-26K		7	0.0190005	0.0004397	0.0017325	0.0000383	-0.0000241	0.0000486	0.0000298	0.0000227	0.0000017	0.0000107	0.13
90529-26L		7.1	0.2884871	0.0008771	0.0281262	0.0000577	0.0002663	0.0000642	0.0000546	0.0000232	0.0000416	0.0000109	2.10
90529-26M		7.15	0.8173455	0.0011775	0.0794429	0.0001718	0.0010256	0.0000588	0.0001603	0.0000232	0.0001048	0.0000116	5.94
90529-26N		7.25	0.1341850	0.0004837	0.0086806	0.0000383	0.0006620	0.0000453	0.0000495	0.0000228	0.0001146	0.0000113	0.65
90529-26O		7.3	0.0001387	0.0004289	-0.0000082	0.0000282	-0.0000176	0.0000458	0.0000122	0.0000233	-0.0000114	0.0000107	0.00
90529-26P		7.4	0.0007306	0.0004368	0.0000181	0.0000297	-0.0000438	0.0000438	-0.0000234	0.0000228	-0.0000232	0.0000107	0.00
90529-26Q		7.6	0.0006974	0.0004291	0.0000480	0.0000282	-0.0000433	0.0000480	0.0000326	0.0000223	-0.0000096	0.0000107	0.00
90529-26R		8.1	0.0138602	0.0004368	0.0013238	0.0000354	0.0000103	0.0000403	0.0000269	0.0000233	0.0000008	0.0000107	0.10
90529-26S		9	0.1334099	0.0004789	0.0128981	0.0000406	0.0001235	0.0000422	0.0000145	0.0000226	0.0000087	0.0000107	0.96
90529-26T		10	0.0440839	0.0004569	0.0041296	0.0000320	0.0000487	0.0000411	0.0000157	0.0000270	-0.0000040	0.0000107	0.31
90529-26U		12	0.0106661	0.0004317	0.0008872	0.0000326	0.0000052	0.0000405	0.0000169	0.0000230	-0.0000032	0.0000107	0.07
Grain-27	**Int. age 321 ± 4 Ma plat. age 321 ± 3 Ma**												
90529-27A		6.4	0.9120580	0.0013662	0.0513906	0.0001226	0.0010509	0.0000573	-0.0000076	0.0000225	0.0011213	0.0000127	2.37
90529-27B		6.6	0.6907638	0.0007406	0.0664038	0.0001422	0.0007963	0.0000453	0.0002473	0.0000277	0.0001170	0.0000107	3.07
90529-27C		6.7	1.0853910	0.0013662	0.0953077	0.0001916	0.0012354	0.0000666	0.0000835	0.0000237	0.0002962	0.0000123	4.40
90529-27D		6.75	0.2499315	0.0007324	0.0235429	0.0000896	0.0003019	0.0000418	0.0000250	0.0000230	0.0000096	0.0000108	1.09
90529-27E		6.8	0.1399245	0.0005048	0.0132125	0.0000406	0.0001929	0.0000411	0.0000167	0.0000237	0.0000036	0.0000108	0.61

Run_ID	^{39}Ar moles	^{40}Ar moles	^{40}Ar*/^{39}Ar	± ^{40}Ar*/^{39}Ar (1σ)	%^{40}Ar*	Age	± Age (1σ)	± Age (1σ, w/J)	^{36}Ar/^{40}Ar	±^{36}Ar/^{40}Ar (%, 1s)	^{39}Ar/^{40}Ar	±^{39}Ar/^{40}Ar (%, 1s)
90529-25E	1.36E-14	1.05E-16	8.836637	0.044039	95.0323	294.956	1.356	1.649	0.0001664	6.3751790	0.1075435	0.3260098
90529-25F	2.65E-15	9.52E-17	9.167053	0.151530	91.4852	305.102	4.640	4.740	0.0002852	16.6035700	0.0997978	0.5140801
90529-25G	1.10E-15	5.21E-17	9.602718	0.336741	99.1332	318.393	10.235	10.285	0.0000290	388.7444000	0.1032345	0.8553214
90529-25H	2.77E-16	5.00E-17	9.920620	1.343501	90.5424	328.030	40.619	40.632	0.0003168	127.4154000	0.0912669	2.3545230
90529-25I	3.68E-17	4.97E-17	15.847100	9.875292	103.2095	498.860	271.592	271.596	-0.0001075	-1960.0780000	0.0651283	13.1007600
90529-25J	9.84E-18	4.85E-17	77.385090	45.481610	447.9989	1692.643	645.392	645.403	-0.0116559	-67.2012200	0.0578921	45.1484200
90529-25K	-1.19E-18	4.87E-17	-221.905500	773.865500	1058.8250	#NAME?	-8109.633	-8109.637	-0.0321149	-285.3615000	-0.0477151	-387.5320000
Grain-26												
90529-26A	1.33E-14	1.10E-16	9.829449	0.065286	78.4837	325.272	1.977	2.227	0.0007207	1.5969010	0.0798454	0.2972714
90529-26B	6.27E-15	7.38E-17	9.377548	0.071471	97.2295	311.536	2.181	2.393	0.0000928	22.6145600	0.1036833	0.3847790
90529-26C	1.58E-14	1.76E-16	9.133754	0.040539	96.0539	304.082	1.242	1.573	0.0001322	6.7531710	0.1051637	0.3082384
90529-26D	3.34E-14	1.65E-16	9.346951	0.034924	95.5787	310.602	1.066	1.451	0.0001481	3.2031370	0.1022566	0.3010484
90529-26E	1.24E-14	9.71E-17	9.670444	0.046414	94.9783	320.451	1.409	1.735	0.0001682	6.3099720	0.0982150	0.2962878
90529-26F	2.42E-15	7.73E-17	9.591906	0.162594	95.3955	318.065	4.943	5.044	0.0001542	32.6854900	0.0994542	0.5878062
90529-26G	2.95E-15	9.03E-17	9.423435	0.134739	94.9169	312.936	4.108	4.226	0.0001703	24.9805900	0.1007243	0.4607835
90529-26H	1.95E-15	5.52E-17	9.586889	0.193838	95.6668	317.912	5.893	5.978	0.0001451	43.1358800	0.0997892	0.4855621
90529-26I	6.23E-15	1.22E-16	9.413568	0.072891	95.7075	312.635	2.223	2.433	0.0001438	14.1604500	0.1016697	0.4079509
90529-26J	4.10E-14	3.09E-16	9.619844	0.041132	94.9727	318.914	1.250	1.606	0.0001684	2.4474420	0.0987258	0.3670322
90529-26K	1.96E-16	4.97E-17	10.756830	1.884767	98.1579	353.137	56.196	56.207	0.0000617	916.3787000	0.0912517	3.3109670
90529-26L	3.18E-15	9.91E-17	9.810319	0.125951	95.7875	324.693	3.815	3.950	0.0001411	26.8872800	0.0976396	0.4642889
90529-26M	8.98E-15	1.33E-16	9.890832	0.059682	96.2769	327.130	1.805	2.079	0.0001247	11.4525600	0.0973396	0.3790930
90529-26N	9.81E-16	5.47E-17	11.537380	0.403469	74.7326	376.260	11.877	11.934	0.0008463	10.0386300	0.0647743	0.6453484
90529-26O	-9.28E-19	4.85E-17	-408.717300	1396.802000	2588.4520	#NAME?	-7019.978	-7019.982	-0.0833485	-333.1354000	-0.0633311	-459.6682000
90529-26P	2.05E-18	4.94E-17	392.482200	647.402800	1029.7660	3941.572	2641.062	2641.068	-0.0311417	-77.7416500	0.0262373	170.8171000
90529-26Q	5.42E-18	4.85E-17	80.095650	85.387870	535.0004	1730.702	1186.375	1186.381	-0.0145700	-123.1190000	0.0667952	89.0236600
90529-26R	1.50E-16	4.94E-17	10.389590	2.446640	99.2953	342.154	73.394	73.402	0.0000236	3262.3480000	0.0955719	4.2711920
90529-26S	1.46E-15	5.41E-17	10.132470	0.253489	98.1097	334.424	7.637	7.709	0.0000633	126.3458000	0.0968270	0.5609658
90529-26T	4.67E-16	5.16E-17	10.967130	0.787102	102.8773	359.396	23.387	23.414	-0.0000964	-252.0931000	0.0938051	1.3627860
90529-26U	1.00E-16	4.88E-17	13.187000	3.682150	109.7657	424.177	105.547	105.555	-0.0003271	-307.9537000	0.0832378	5.6500270
Grain-27												
90529-27A	5.81E-15	1.54E-16	11.215560	0.130361	63.2927	366.762	3.858	4.024	0.0012295	1.5725120	0.0564330	0.3951866
90529-27B	7.50E-15	8.37E-17	9.882314	0.062807	95.1324	326.872	1.900	2.162	0.0001630	9.5727110	0.0962653	0.3644411
90529-27C	1.08E-14	1.54E-16	10.449240	0.060020	91.8942	343.942	1.799	2.098	0.0002715	4.3036400	0.0879434	0.3630018
90529-27D	2.66E-15	8.28E-17	10.483500	0.149471	98.9019	344.968	4.477	4.606	0.0000368	117.6775000	0.0943406	0.5626951
90529-27E	1.49E-15	5.70E-17	10.499630	0.251178	99.2935	345.452	7.521	7.599	0.0000237	326.7053000	0.0945685	0.5578321

Run_ID	±$^{39}Ar/^{36}Ar$ (%, 1s)	ρ $^{40}Ar/^{39}Ar$	ρ $^{36}Ar/^{39}Ar$
90529-25E	6.3368510	0.9758393	0.1395250
90529-25F	16.5856400	0.9961619	0.0569687
90529-25G	388.7435000	0.9999915	0.0023897
90529-25H	127.4100000	0.9997723	0.0119465
90529-25I	-1960.0910000	0.9999774	0.0032730
90529-25J	-69.7795700	0.7829698	0.2790917
90529-25K	355.4277000	0.2843061	0.4754320
Grain-26			
90529-26A	1.4320520	0.5927594	0.5502843
90529-26B	22.6041800	0.9980455	0.0392216
90529-26C	6.7150280	0.9785951	0.1328890
90529-26D	3.1251540	0.9039456	0.2769733
90529-26E	6.2699410	0.9755650	0.1415120
90529-26F	32.6784300	0.9989722	0.0277903
90529-26G	24.9689800	0.9983467	0.0373429
90529-26H	43.1296800	0.9994394	0.0212366
90529-26I	14.1428600	0.9949673	0.0636452
90529-26J	2.3522290	0.8300561	0.3585029
90529-26K	916.3758000	0.9999924	0.0021261
90529-26L	26.8766600	0.9985707	0.0345963
90529-26M	11.4314400	0.9923887	0.0779075
90529-26N	10.0162000	0.9887353	0.0910811
90529-26O	342.4686000	0.0746699	0.6690556
90529-26P	-166.0838000	0.1715280	0.2883905
90529-26Q	-122.4304000	0.7369037	0.3701063
90529-26R	3262.3440000	0.9999991	0.0008123
90529-26S	126.3434000	0.9999322	0.0074020
90529-26T	-252.0925000	0.9999708	0.0049217
90529-26U	-307.9524000	0.9998219	0.0104994
Grain-27			
90529-27A	1.4152370	0.5667480	0.5573779
90529-27B	9.5477810	0.9891585	0.0927167
90529-27C	4.2473920	0.9460525	0.2066871
90529-27D	117.6754000	0.9999218	0.0076780
90529-27E	326.7042000	0.9999899	0.0028678

Run_ID	Plateau Steps	Laser Power	^{40}Ar	±^{40}Ar (1σ)	^{39}Ar	±^{39}Ar (1σ)	^{38}Ar	±^{38}Ar (1σ)	^{37}Ar	±^{37}Ar (1σ)	^{36}Ar	±^{36}Ar (1σ)	% 39Ar
90529-27F		6.825	0.4432477	0.0006607	0.0438410	0.0000706	0.0004743	0.0000511	0.0000233	0.0000231	0.0000287	0.0000110	2.03
90529-27G		6.85	0.4597634	0.0010296	0.0465482	0.0000753	0.0006291	0.0000430	0.0000215	0.0000242	0.0000369	0.0000105	2.15
90529-27H		6.875	0.4156484	0.0006378	0.0430672	0.0001226	0.0005164	0.0000498	0.0000402	0.0000230	0.0000567	0.0000104	1.99
90529-27I		6.9	0.5252683	0.0006841	0.0542667	0.0000743	0.0007178	0.0000443	0.0000352	0.0000232	0.0000601	0.0000105	2.51
90529-27J		6.95	0.7929450	0.0007572	0.0815247	0.0001718	0.0009932	0.0000474	0.0000409	0.0000231	0.0000937	0.0000113	3.77
90529-27K	x	7.05	10.6578300	0.0045196	1.0303620	0.0013002	0.0127152	0.0000819	0.0008652	0.0000258	0.0014787	0.0000172	47.61
90529-27L	x	7	0.3831386	0.0010022	0.0375645	0.0001226	0.0004008	0.0000611	0.0000399	0.0000229	0.0000522	0.0000108	1.74
90529-27M	x	7.1	1.3237760	0.0013662	0.1290053	0.0002016	0.0016761	0.0000448	0.0000974	0.0000233	0.0001924	0.0000120	5.96
90529-27N		7.15	0.8502341	0.0013662	0.0802473	0.0001521	0.0009504	0.0000474	0.0000237	0.0000231	0.0001168	0.0000114	3.71
90529-27O		7.2	0.6937080	0.0008422	0.0678676	0.0000973	0.0007040	0.0000552	0.0000267	0.0000232	0.0000992	0.0000112	3.14
90529-27P		7.25	0.3188371	0.0006155	0.0298906	0.0001031	0.0003449	0.0000498	0.0000190	0.0000226	0.0000289	0.0000109	1.38
90529-27Q		7.3	1.5316430	0.0018484	0.1478847	0.0002314	0.0018242	0.0000674	0.0000540	0.0000230	0.0002352	0.0000111	6.83
90529-27R		7.4	0.3346843	0.0006229	0.0321158	0.0000541	0.0004543	0.0000504	0.0000189	0.0000223	0.0000545	0.0000105	1.48
90529-27S		7.6	0.2273804	0.0007000	0.0228572	0.0000810	0.0002229	0.0000469	-0.0000164	0.0000225	0.0000264	0.0000107	1.06
90529-27T		8.1	0.3719670	0.0006155	0.0353539	0.0000659	0.0004425	0.0000434	0.0000583	0.0000224	0.0000559	0.0000111	1.63
90529-27U		9	0.2095028	0.0007908	0.0204982	0.0000829	0.0002661	0.0000566	0.0000067	0.0000228	0.0000324	0.0000104	0.95
90529-27V		10	0.0978140	0.0004610	0.0097571	0.0000447	0.0000717	0.0000474	-0.0000157	0.0000229	0.0000096	0.0000107	0.45
90529-27W		12	0.0201957	0.0004427	0.0017765	0.0000383	0.0000128	0.0000469	0.0000165	0.0000226	0.0000061	0.0000105	0.08
Grain-28	**Int. age 290 ± 5 Ma No plat. age**												
90529-28A		6.4	0.9718639	0.0013662	0.0902217	0.0000953	0.0011745	0.0000603	0.0002837	0.0000237	0.0004735	0.0000117	8.53
90529-28B		6.6	0.3906425	0.0006378	0.0414543	0.0001324	0.0005758	0.0000517	0.0000240	0.0000229	0.0000338	0.0000104	3.92
90529-28C		6.7	0.8166935	0.0012714	0.0945166	0.0001619	0.0013080	0.0000699	0.0000621	0.0000225	0.0000756	0.0000113	8.94
90529-28D		6.75	0.7153495	0.0006841	0.0833498	0.0000848	0.0008030	0.0000642	0.0000588	0.0000224	0.0000504	0.0000111	7.88
90529-28E		6.8	0.6237830	0.0010846	0.0711329	0.0001521	0.0008477	0.0000448	0.0000133	0.0000233	0.0000693	0.0000107	6.72
90529-28F		6.825	0.5964114	0.0010479	0.0671682	0.0001521	0.0008375	0.0000448	0.0000211	0.0000224	0.0000441	0.0000111	6.35
90529-28G		6.85	0.7137019	0.0012714	0.0791658	0.0001422	0.0007947	0.0000552	-0.0000029	0.0000225	0.0000710	0.0000113	7.48
90529-28H		6.875	0.4661900	0.0009932	0.0506959	0.0001128	0.0006487	0.0000434	0.0000303	0.0000227	0.0000445	0.0000106	4.79
90529-28I		6.9	0.5753588	0.0010846	0.0614134	0.0000800	0.0008306	0.0000438	0.0000086	0.0000230	0.0000547	0.0000105	5.81
90529-28J		6.95	0.6964763	0.0010846	0.0717510	0.0000829	0.0009046	0.0000588	0.0000090	0.0000229	0.0000779	0.0000111	6.78
90529-28K		7	1.3017020	0.0014616	0.1340073	0.0002016	0.0016472	0.0000463	0.0002102	0.0000242	0.0001995	0.0000118	12.67
90529-28L		7.05	0.6896678	0.0008078	0.0709738	0.0001521	0.0010747	0.0000425	0.0009439	0.0000252	0.0002009	0.0000121	6.71
90529-28M		7.1	0.1866194	0.0005532	0.0191162	0.0000463	0.0005154	0.0000411	0.0015212	0.0000270	0.0002189	0.0000117	1.81
90529-28N		7.15	0.2255155	0.0007489	0.0226457	0.0000447	0.0002298	0.0000559	0.0003324	0.0000237	0.0000564	0.0000110	2.14
90529-28O		7.2	0.1060258	0.0004652	0.0113950	0.0000447	0.0002626	0.0000430	0.0002204	0.0000242	0.0000507	0.0000108	1.08
90529-28P		7.25	0.0340466	0.0004397	0.0033880	0.0000308	0.0000811	0.0000469	0.0004205	0.0000252	0.0000659	0.0000112	0.32
90529-28Q		7.3	0.0858694	0.0004610	0.0085189	0.0000368	0.0000706	0.0000492	0.0001456	0.0000226	0.0000247	0.0000108	0.81

Run_ID	^{39}Ar moles	^{40}Ar moles	^{40}Ar*/^{39}Ar	± ^{40}Ar*/^{39}Ar (1σ)	%^{40}Ar*	Age	± Age (1σ)	± Age (1σ, w/J)	^{36}Ar/^{40}Ar	±^{36}Ar/^{40}Ar (%, 1s)	^{39}Ar/^{40}Ar	±^{39}Ar/^{40}Ar (%, 1s)
90529-27F	4.95E-15	7.47E-17	9.902218	0.083088	98.0931	327.474	2.513	2.717	0.0000639	38.7831600	0.0990617	0.3511753
90529-27G	5.26E-15	1.16E-16	9.628126	0.078036	97.6304	319.165	2.371	2.577	0.0000794	28.7408600	0.1014012	0.3917786
90529-27H	4.87E-15	7.21E-17	9.249135	0.083907	95.9816	307.614	2.566	2.745	0.0001346	18.7111500	0.1037735	0.4275060
90529-27I	6.13E-15	7.73E-17	9.337629	0.067041	96.6185	310.318	2.047	2.271	0.0001133	17.6985000	0.1034722	0.3319014
90529-27J	9.21E-15	8.56E-17	9.371380	0.055107	96.4994	311.348	1.682	1.949	0.0001173	12.1810600	0.1029724	0.3588568
90529-27K	1.16E-13	5.11E-16	9.904534	0.034380	95.9005	327.544	1.040	1.465	0.0001373	1.5954520	0.0968248	0.3015289
90529-27L	4.24E-15	1.13E-16	9.775227	0.100977	95.9866	323.629	3.060	3.226	0.0001344	21.1067100	0.0981937	0.5076061
90529-27M	1.46E-14	1.54E-16	9.805023	0.045845	95.6995	324.532	1.389	1.725	0.0001440	6.3808870	0.0976025	0.3306672
90529-27N	9.07E-15	1.54E-16	10.146320	0.059315	95.9129	334.841	1.787	2.074	0.0001369	9.8734330	0.0945297	0.3710851
90529-27O	7.67E-15	9.52E-17	9.771630	0.061187	95.7478	323.520	1.855	2.117	0.0001424	11.3772800	0.0979855	0.3311365
90529-27P	3.38E-15	6.96E-17	10.365150	0.120679	97.3219	341.420	3.622	3.777	0.0000897	38.1080900	0.0938933	0.4872338
90529-27Q	1.67E-14	2.09E-16	9.868655	0.043833	95.4333	326.459	1.326	1.679	0.0001530	4.8789860	0.0967034	0.3370505
90529-27R	3.63E-15	7.04E-17	9.902594	0.106271	95.1707	327.485	3.214	3.376	0.0001618	19.4995700	0.0961069	0.3731593
90529-27S	2.58E-15	7.91E-17	9.583691	0.150721	96.4944	317.815	4.583	4.692	0.0001174	40.2533000	0.1006860	0.5530638
90529-27T	3.99E-15	6.96E-17	10.042720	0.102713	95.5947	331.718	3.099	3.270	0.0001476	20.3355700	0.0951881	0.3717206
90529-27U	2.32E-15	8.94E-17	9.735501	0.165214	95.4029	322.425	5.011	5.113	0.0001540	32.4148300	0.0979948	0.6300358
90529-27V	1.10E-15	5.21E-17	9.705824	0.334124	96.9778	321.525	10.138	10.189	0.0001012	107.7917000	0.0999171	0.7285772
90529-27W	2.01E-16	5.00E-17	10.385630	1.803362	91.4601	342.035	54.101	54.111	0.0002860	182.4710000	0.0880640	3.1810440
Grain-28												
90529-28A	1.02E-14	1.54E-16	9.208750	0.059570	85.6101	306.379	1.823	2.065	0.0004820	2.7186880	0.0929661	0.3242249
90529-28B	4.68E-15	7.21E-17	9.168725	0.086691	97.4484	305.153	2.654	2.825	0.0000855	31.2353700	0.1062834	0.4562726
90529-28C	1.07E-14	1.44E-16	8.392526	0.048133	97.2790	281.229	1.493	1.743	0.0000911	15.2566900	0.1159114	0.3593119
90529-28D	9.42E-15	7.73E-17	8.392388	0.048334	97.9373	281.224	1.500	1.748	0.0000691	22.5774500	0.1166978	0.3048265
90529-28E	8.04E-15	1.23E-16	8.466064	0.057238	96.6952	283.509	1.774	1.991	0.0001107	15.5459700	0.1142150	0.3908339
90529-28F	7.59E-15	1.18E-16	8.671525	0.061144	97.8130	289.865	1.888	2.102	0.0000733	25.4348900	0.1127980	0.3990975
90529-28G	8.95E-15	1.44E-16	8.733185	0.055210	97.0251	291.768	1.703	1.940	0.0000996	15.9647800	0.1110993	0.3744528
90529-28H	5.73E-15	1.12E-16	8.922849	0.073694	97.1831	297.609	2.266	2.455	0.0000944	24.1342700	0.1089148	0.4159239
90529-28I	6.94E-15	1.23E-16	9.089102	0.061747	97.1697	302.714	1.893	2.123	0.0000948	19.2444500	0.1069079	0.3580185
90529-28J	8.11E-15	1.23E-16	9.368423	0.057585	96.6659	311.258	1.757	2.015	0.0001117	14.3153200	0.1031827	0.3350511
90529-28K	1.51E-14	1.65E-16	9.263737	0.043517	95.5121	308.060	1.330	1.650	0.0001503	6.1155110	0.1031032	0.3309776
90529-28L	8.02E-15	9.13E-17	8.936213	0.064750	92.0500	298.020	1.990	2.204	0.0002663	6.7134390	0.1030079	0.3676318
90529-28M	2.16E-15	6.25E-17	6.793554	0.192996	69.4346	230.921	6.158	6.203	0.0010238	6.2187550	0.1022066	0.4770929
90529-28N	2.56E-15	8.46E-17	9.286468	0.153212	93.3346	308.755	4.682	4.783	0.0002233	21.8317100	0.1005060	0.4808151
90529-28O	1.29E-15	5.26E-17	8.084507	0.291426	86.9419	271.646	9.091	9.132	0.0004374	23.4454100	0.1075414	0.6635599
90529-28P	3.83E-16	4.97E-17	4.988496	1.003813	49.4069	172.390	33.083	33.088	0.0016946	19.4781800	0.0990418	1.6552660
90529-28Q	9.63E-16	5.21E-17	9.305011	0.386711	92.3806	309.322	11.814	11.854	0.0002552	49.3829500	0.0992805	0.7600625

Run_ID	±$^{39}Ar/^{36}Ar$ (%, 1s)	ρ $^{40}Ar/^{39}Ar$	ρ $^{36}Ar/^{39}Ar$
90529-27F	38.7765700	0.9993438	0.0231593
90529-27G	28.7314800	0.9987868	0.0317501
90529-27H	18.6990900	0.9970952	0.0473454
90529-27I	17.6841400	0.9968689	0.0506876
90529-27J	12.1617200	0.9933243	0.0727987
90529-27K	1.4330130	0.5915808	0.5494543
90529-27L	21.0954900	0.9976332	0.0427889
90529-27M	6.3421570	0.9758425	0.1397447
90529-27N	9.8482470	0.9897874	0.0908821
90529-27O	11.3552200	0.9924201	0.0786953
90529-27P	38.1024200	0.9992811	0.0232093
90529-27Q	4.8278840	0.9584800	0.1830410
90529-27R	19.4862600	0.9973826	0.0463574
90529-27S	40.2472400	0.9993346	0.0226636
90529-27T	20.3231400	0.9975947	0.0441924
90529-27U	32.4071000	0.9989304	0.0286184
90529-27V	107.7888000	0.9998975	0.0088741
90529-27W	182.4665000	0.9998202	0.0101159
Grain-28			
90529-28A	2.6219560	0.8645958	0.3295058
90529-28B	31.2283900	0.9989449	0.0282626
90529-28C	15.2401600	0.9957450	0.0588794
90529-28D	22.5661900	0.9980932	0.0396464
90529-28E	15.5301300	0.9958533	0.0577337
90529-28F	25.4252800	0.9984464	0.0352524
90529-28G	15.9489100	0.9960927	0.0564674
90529-28H	24.1237400	0.9982626	0.0374786
90529-28I	19.2307100	0.9973277	0.0471393
90529-28J	14.2971800	0.9952078	0.0630182
90529-28K	6.0746450	0.9736826	0.1460431
90529-28L	6.6771620	0.9778649	0.1323563
90529-28M	6.1736800	0.9728754	0.1483900
90529-28N	21.8177800	0.9978140	0.0430453
90529-28O	23.4329400	0.9979140	0.0406878
90529-28P	19.4398900	0.9939267	0.0723942
90529-28Q	49.3759500	0.9995018	0.0200960

Run_ID	Plateau Steps	Laser Power	^{40}Ar	±^{40}Ar (1σ)	^{39}Ar	±^{39}Ar (1σ)	^{38}Ar	±^{38}Ar (1σ)	^{37}Ar	±^{37}Ar (1σ)	^{36}Ar	±^{36}Ar (1σ)	% 39Ar
90529-28R		7.4	0.0866766	0.0004610	0.0089821	0.0000368	0.0001102	0.0000458	0.0002941	0.0000237	0.0000745	0.0000108	0.85
90529-28S		7.6	0.0171263	0.0004397	0.0016563	0.0000347	0.0000302	0.0000414	0.0000162	0.0000233	0.0000190	0.0000106	0.16
90529-28T		8.1	0.1914844	0.0005404	0.0201797	0.0000455	0.0002955	0.0000425	0.0000150	0.0000225	0.0000219	0.0000107	1.91
90529-28U		9	0.1427104	0.0004610	0.0140572	0.0000472	0.0001849	0.0000434	0.0000384	0.0000232	0.0000284	0.0000108	1.33
90529-28V		10	0.2444611	0.0007080	0.0251302	0.0000506	0.0004386	0.0000492	0.0005494	0.0000247	0.0001121	0.0000110	2.38
90529-28W		12	0.0668907	0.0004569	0.0068430	0.0000354	0.0000855	0.0000408	0.0000509	0.0000227	0.0000126	0.0000106	0.65
Grain-29	**Int. age 308 ± 15 Ma plat. age 293 ± 3 Ma**												
90529-29A		6.4	0.3905990	0.0009035	0.0254349	0.0000532	0.0003196	0.0000492	0.0000249	0.0000222	0.0001683	0.0000113	8.01
90529-29B		6.6	0.4618393	0.0006454	0.0430408	0.0000743	0.0004992	0.0000559	0.0000941	0.0000229	0.0000692	0.0000111	13.55
90529-29C	x	6.7	0.9936068	0.0015577	0.1025177	0.0001718	0.0015003	0.0000448	0.0008177	0.0000252	0.0002758	0.0000112	32.28
90529-29D	x	6.75	0.2282228	0.0007000	0.0236043	0.0000867	0.0003432	0.0000566	0.0003374	0.0000230	0.0000794	0.0000110	7.43
90529-29E	x	6.8	0.0364010	0.0004397	0.0037372	0.0000302	0.0000420	0.0000434	0.0000817	0.0000232	0.0000176	0.0000107	1.18
90529-29F	x	6.825	0.1926311	0.0005161	0.0205559	0.0000669	0.0002722	0.0000463	-0.0000089	0.0000229	0.0000363	0.0000107	6.47
90529-29G	x	6.85	0.0399413	0.0004460	0.0042871	0.0000314	0.0000611	0.0000443	0.0000143	0.0000233	0.0000229	0.0000107	1.35
90529-29H	x	6.875	0.0305218	0.0004427	0.0031877	0.0000383	0.0000085	0.0000414	-0.0000030	0.0000230	0.0000094	0.0000107	1.00
90529-29I	x	6.9	0.0686096	0.0004460	0.0070536	0.0000333	-0.0000178	0.0000438	0.0000284	0.0000237	0.0000207	0.0000108	2.22
90529-29J	x	6.95	0.0836206	0.0004741	0.0089357	0.0000586	0.0001010	0.0000458	-0.0000207	0.0000221	0.0000045	0.0000106	2.81
90529-29K	x	7.05	0.1674669	0.0004837	0.0174946	0.0000463	0.0002584	0.0000405	-0.0000286	0.0000226	0.0000219	0.0000108	5.51
90529-29L	x	7	0.0362282	0.0004460	0.0037457	0.0000430	-0.0000042	0.0000434	-0.0000133	0.0000228	0.0000187	0.0000103	1.18
90529-29M	x	7.1	0.0520443	0.0004427	0.0052880	0.0000354	0.0000306	0.0000448	0.0000118	0.0000228	0.0000120	0.0000107	1.67
90529-29N	x	7.15	0.0656861	0.0004610	0.0068741	0.0000524	0.0000543	0.0000443	-0.0000029	0.0000226	0.0000106	0.0000107	2.16
90529-29O	x	7.2	0.0043090	0.0004297	0.0004997	0.0000297	0.0000429	0.0000403	-0.0000102	0.0000229	0.0000100	0.0000105	0.16
90529-29P	x	7.25	0.0080642	0.0004317	0.0008119	0.0000308	-0.0000057	0.0000402	0.0000065	0.0000228	0.0000039	0.0000103	0.26
90529-29Q	x	7.3	0.2266798	0.0007908	0.0234738	0.0000876	0.0003299	0.0000498	-0.0000182	0.0000225	0.0000340	0.0000108	7.39
90529-29R	x	7.4	0.0138105	0.0004368	0.0014914	0.0000361	-0.0000318	0.0000504	-0.0000196	0.0000223	0.0000037	0.0000108	0.47
90529-29S	x	7.6	0.0285234	0.0004460	0.0029893	0.0000406	0.0000499	0.0000463	-0.0000130	0.0000229	0.0000087	0.0000107	0.94
90529-29T	x	8.1	0.0165405	0.0004342	0.0017273	0.0000354	0.0000014	0.0000403	0.0000049	0.0000230	0.0000100	0.0000107	0.54
90529-29U	x	9	0.0255792	0.0004427	0.0025276	0.0000383	0.0000543	0.0000443	-0.0000011	0.0000228	0.0000021	0.0000106	0.80
90529-29V	x	10	0.0775966	0.0004610	0.0079572	0.0000354	0.0000804	0.0000474	-0.0000340	0.0000230	0.0000252	0.0000109	2.51
90529-29W	x	12	0.0033423	0.0004287	0.0003383	0.0000302	-0.0000114	0.0000453	-0.0000198	0.0000224	0.0000019	0.0000105	0.11
Grain-30	**Int. age 289 ± 2 Ma No plat. age**												
90529-30A		6.4	0.4024081	0.0008509	0.0349522	0.0001128	0.0005486	0.0000438	0.0001927	0.0000247	0.0003118	0.0000124	5.04
90529-30B		6.6	0.6855221	0.0012714	0.0722456	0.0000810	0.0009187	0.0000474	0.0000295	0.0000229	0.0001564	0.0000106	10.42
90529-30C		6.7	1.7422310	0.0015577	0.1898944	0.0001422	0.0023865	0.0000511	0.0002081	0.0000233	0.0003099	0.0000120	27.40
90529-30D		6.75	0.6443223	0.0007655	0.0685399	0.0000829	0.0009836	0.0000453	0.0004720	0.0000252	0.0001585	0.0000117	9.89

Run_ID	^{39}Ar moles	^{40}Ar moles	^{40}Ar*/^{39}Ar	± ^{40}Ar*/^{39}Ar (1σ)	%^{40}Ar*	Age	± Age (1σ)	± Age (1σ, w/J)	^{36}Ar/^{40}Ar	±^{36}Ar/^{40}Ar (%, 1s)	^{39}Ar/^{40}Ar	±^{39}Ar/^{40}Ar (%, 1s)
90529-28R	1.01E-15	5.21E-17	7.364307	0.367667	76.3096	249.039	11.613	11.641	0.0007935	15.7790700	0.1036209	0.7431373
90529-28S	1.87E-16	4.97E-17	6.963113	1.942130	67.4134	236.322	61.780	61.784	0.0010915	56.9907700	0.0968150	3.4280910
90529-28T	2.28E-15	6.11E-17	9.155550	0.163908	96.6380	304.750	5.020	5.112	0.0001126	49.5122100	0.1055513	0.4594277
90529-28U	1.59E-15	5.21E-17	9.551907	0.237258	94.2260	316.848	7.218	7.287	0.0001934	39.3551900	0.0986462	0.5501248
90529-28V	2.84E-15	8.00E-17	8.519605	0.140448	87.6230	285.167	4.348	4.442	0.0004146	10.9749300	0.1028487	0.4523223
90529-28W	7.73E-16	5.16E-17	9.256912	0.470917	94.8150	307.852	14.398	14.431	0.0001737	91.3070000	0.1024262	0.9239208
Grain-29												
90529-29A	2.87E-15	1.02E-16	13.366640	0.151860	87.1739	429.319	4.341	4.536	0.0004296	6.8399270	0.0652175	0.4191510
90529-29B	4.86E-15	7.29E-17	10.247970	0.087145	95.6476	337.900	2.620	2.828	0.0001458	16.5920200	0.0933332	0.3529012
90529-29C	1.16E-14	1.76E-16	8.924775	0.050886	92.1941	297.668	1.565	1.828	0.0002615	4.4645050	0.1033013	0.3578448
90529-29D	2.67E-15	7.91E-17	8.740865	0.149676	90.4832	292.005	4.617	4.709	0.0003188	15.1324200	0.1035174	0.5612889
90529-29E	4.22E-16	4.97E-17	8.454620	0.864727	86.8435	283.154	26.802	26.818	0.0004407	66.5644500	0.1027173	1.5252410
90529-29F	2.32E-15	5.83E-17	8.827478	0.163363	94.3535	294.674	5.031	5.118	0.0001891	29.5138600	0.1068861	0.5104396
90529-29G	4.84E-16	5.04E-17	7.731787	0.753335	83.1080	260.610	23.643	23.658	0.0005658	47.2609400	0.1074887	1.4048880
90529-29H	3.60E-16	5.00E-17	8.674120	1.014630	90.7444	289.945	31.330	31.344	0.0003100	112.8219000	0.1046150	1.9612460
90529-29I	7.97E-16	5.04E-17	8.862348	0.465205	91.2397	295.748	14.319	14.350	0.0002934	53.7607000	0.1029521	0.8717400
90529-29J	1.01E-15	5.36E-17	9.179360	0.365340	98.2608	305.479	11.184	11.226	0.0000583	218.4032000	0.1070453	0.9325222
90529-29K	1.98E-15	5.47E-17	9.173240	0.191019	95.9921	305.292	5.848	5.928	0.0001342	48.3069000	0.1046436	0.4852908
90529-29L	4.23E-16	5.04E-17	8.145753	0.834867	84.3721	273.556	26.015	26.030	0.0005234	54.3172900	0.1035781	1.7563220
90529-29M	5.98E-16	5.00E-17	9.163132	0.616028	93.2416	304.982	18.864	18.889	0.0002264	91.2142700	0.1017573	1.1483490
90529-29N	7.77E-16	5.21E-17	9.076811	0.475791	95.1456	302.337	14.591	14.623	0.0001626	100.2768000	0.1048228	1.1004140
90529-29O	5.65E-17	4.86E-17	2.522295	6.346840	29.3277	89.221	219.046	219.047	0.0023671	103.8725000	0.1162737	11.9898500
90529-29P	9.17E-17	4.88E-17	8.536875	3.853888	86.0530	285.702	119.283	119.287	0.0004671	274.6447000	0.1008016	6.7801370
90529-29Q	2.65E-15	8.94E-17	9.204683	0.148552	95.4770	306.254	4.546	4.648	0.0001515	31.4154000	0.1037265	0.5911065
90529-29R	1.69E-16	4.94E-17	8.416383	2.184988	91.0961	281.969	67.768	67.774	0.0002982	261.7863000	0.1082367	4.1165500
90529-29S	3.38E-16	5.04E-17	8.629721	1.082573	90.6075	288.574	33.454	33.466	0.0003146	118.9677000	0.1049947	2.1529310
90529-29T	1.95E-16	4.91E-17	7.858253	1.868517	82.1810	264.575	58.514	58.521	0.0005968	108.1648000	0.1045792	3.4454320
90529-29U	2.86E-16	5.00E-17	9.854300	1.277462	97.5333	326.024	38.665	38.679	0.0000826	503.4606000	0.0989754	2.3873970
90529-29V	8.99E-16	5.21E-17	8.762432	0.415839	90.0208	292.670	12.821	12.855	0.0003342	42.0314700	0.1027350	0.8114052
90529-29W	3.82E-17	4.84E-17	7.785943	9.353362	79.1749	262.309	293.278	293.279	0.0006975	451.0495000	0.1016896	16.1256700
Grain-30												
90529-30A	3.95E-15	9.62E-17	8.870615	0.124084	77.1495	296.002	3.819	3.933	0.0007654	4.1714830	0.0869719	0.4793769
90529-30B	8.16E-15	1.44E-16	8.830592	0.057454	93.2123	294.770	1.769	2.002	0.0002273	6.9137170	0.1055561	0.3497167
90529-30C	2.15E-14	1.76E-16	8.680381	0.035822	94.7598	290.138	1.106	1.441	0.0001755	4.0683450	0.1091655	0.2944318
90529-30D	7.75E-15	8.65E-17	8.740434	0.061361	93.0937	291.992	1.893	2.109	0.0002313	7.9096420	0.1065092	0.3204028

Run_ID	±^{39}Ar/^{36}Ar (%, 1s)	ρ ^{40}Ar/^{39}Ar	ρ ^{36}Ar/^{39}Ar
90529-28R	15.7581400	0.9951645	0.0629702
90529-28S	56.9617700	0.9979050	0.0394796
90529-28T	49.5065200	0.9995795	0.0186161
90529-28U	39.3484400	0.9993048	0.0233742
90529-28V	10.9488500	0.9914453	0.0843626
90529-28W	91.3022400	0.9998378	0.0115745
Grain-29			
90529-29A	6.8018470	0.9782716	0.1329336
90529-29B	16.5768700	0.9964107	0.0539861
90529-29C	4.4068670	0.9498737	0.2010817
90529-29D	15.1164400	0.9952652	0.0601057
90529-29E	66.5526100	0.9995284	0.0205852
90529-29F	29.5056400	0.9987882	0.0306658
90529-29G	47.2462000	0.9991437	0.0278479
90529-29H	112.8148000	0.9997762	0.0129684
90529-29I	53.7531800	0.9995483	0.0194645
90529-29J	218.4018000	0.9999715	0.0043937
90529-29K	48.3012600	0.9995531	0.0190276
90529-29L	54.3090700	0.9991636	0.0237162
90529-29M	91.2088500	0.9998095	0.0123986
90529-29N	100.2739000	0.9998478	0.0100642
90529-29O	103.5250000	0.9932352	0.0860042
90529-29P	274.6090000	0.9996830	0.0168202
90529-29Q	31.4074200	0.9988854	0.0293693
90529-29R	261.7734000	0.9998629	0.0105341
90529-29S	118.9610000	0.9997709	0.0127318
90529-29T	108.1457000	0.9994135	0.0215127
90529-29U	503.4572000	0.9999851	0.0032149
90529-29V	42.0228300	0.9992900	0.0242779
90529-29W	450.9313000	0.9993562	0.0243189
Grain-30			
90529-30A	4.1176070	0.9397222	0.2132584
90529-30B	6.8752420	0.9792933	0.1311847
90529-30C	4.0051710	0.9408951	0.2196630
90529-30D	7.8769970	0.9843391	0.1133161

Run_ID	Plateau Steps	Laser Power	^{40}Ar	$\pm^{40}Ar$ (1σ)	^{39}Ar	$\pm^{39}Ar$ (1σ)	^{38}Ar	$\pm^{38}Ar$ (1σ)	^{37}Ar	$\pm^{37}Ar$ (1σ)	^{36}Ar	$\pm^{36}Ar$ (1σ)	% 39Ar
90529-30E		6.8	0.7358888	0.0010846	0.0784489	0.0000905	0.0010874	0.0000463	0.0003222	0.0000252	0.0001628	0.0000113	11.32
90529-30F		6.825	0.5327651	0.0006841	0.0552907	0.0000791	0.0007131	0.0000545	0.0000629	0.0000226	0.0001031	0.0000104	7.98
90529-30G		6.85	0.0377225	0.0004427	0.0040927	0.0000314	-0.0000218	0.0000463	0.0000179	0.0000231	0.0000005	0.0000106	0.59
90529-30H		6.875	0.0878875	0.0004652	0.0096657	0.0000375	0.0001405	0.0000486	0.0001497	0.0000237	0.0000384	0.0000109	1.39
90529-30I		6.9	0.0686531	0.0004652	0.0075338	0.0000354	0.0000269	0.0000458	0.0000020	0.0000227	0.0000284	0.0000107	1.09
90529-30J		6.95	0.0312887	0.0004460	0.0035215	0.0000314	-0.0000045	0.0000486	0.0000375	0.0000225	0.0000094	0.0000106	0.51
90529-30K		7	0.2031600	0.0006684	0.0209960	0.0000497	0.0002313	0.0000434	0.0000570	0.0000229	0.0000289	0.0000108	3.03
90529-30L		7.05	0.5797467	0.0011775	0.0623247	0.0000791	0.0006426	0.0000603	0.0000570	0.0000233	0.0000798	0.0000111	8.99
90529-30M		7.1	0.2399749	0.0007324	0.0256365	0.0000944	0.0003720	0.0000498	0.0001498	0.0000230	0.0000542	0.0000108	3.70
90529-30N		7.15	0.0215628	0.0004427	0.0023066	0.0000354	-0.0000129	0.0000463	0.0000256	0.0000228	0.0000098	0.0000107	0.33
90529-30O		7.2	0.0030645	0.0004317	0.0003729	0.0000292	0.0000388	0.0000408	0.0000306	0.0000228	0.0000025	0.0000106	0.05
90529-30P		7.25	0.0104865	0.0004342	0.0011371	0.0000326	0.0000040	0.0000453	-0.0000206	0.0000224	0.0000036	0.0000106	0.16
90529-30Q		7.3	0.0097826	0.0004308	0.0010651	0.0000326	0.0000121	0.0000448	-0.0000053	0.0000220	0.0000059	0.0000105	0.15
90529-30R		7.4	0.0689067	0.0004569	0.0074159	0.0000532	0.0001256	0.0000425	-0.0000085	0.0000230	0.0000137	0.0000106	1.07
90529-30S		8.1	0.1588742	0.0004888	0.0167409	0.0000414	0.0002129	0.0000463	0.0000229	0.0000226	0.0000338	0.0000108	2.42
90529-30T		10	0.2302253	0.0006607	0.0248354	0.0000848	0.0003407	0.0000538	0.0000202	0.0000227	0.0000492	0.0000108	3.58
90529-30U		12	0.0556508	0.0004610	0.0060220	0.0000347	0.0000881	0.0000469	-0.0000052	0.0000233	0.0000169	0.0000106	0.87

Run_ID	^{39}Ar moles	^{40}Ar moles	^{40}Ar*/^{39}Ar	± ^{40}Ar*/^{39}Ar (1σ)	%^{40}Ar*	Age	± Age (1σ)	± Age (1σ, w/J)	^{36}Ar/^{40}Ar	±^{36}Ar/^{40}Ar (%, 1s)	^{39}Ar/^{40}Ar	±^{39}Ar/^{40}Ar (%, 1s)
90529-30E	8.86E-15	1.23E-16	8.773289	0.055392	93.6585	293.005	1.708	1.946	0.0002124	7.3316030	0.1067541	0.3308688
90529-30F	6.25E-15	7.73E-17	9.071634	0.066595	94.2928	302.178	2.042	2.257	0.0001912	10.3200300	0.1039425	0.3337913
90529-30G	4.62E-16	5.00E-17	9.191209	0.786985	99.8593	305.842	24.088	24.107	0.0000047	5984.3340000	0.1086465	1.4726560
90529-30H	1.09E-15	5.26E-17	7.991883	0.343170	87.9647	268.754	10.722	10.756	0.0004031	30.7837000	0.1100676	0.7289429
90529-30I	8.51E-16	5.26E-17	7.976419	0.432964	87.6719	268.271	13.531	13.558	0.0004129	37.9255600	0.1099138	0.8923268
90529-30J	3.98E-16	5.04E-17	8.138997	0.908697	91.7015	273.345	28.319	28.332	0.0002779	121.5965000	0.1126693	1.7572370
90529-30K	2.37E-15	7.55E-17	9.267007	0.160892	95.9134	308.160	4.918	5.014	0.0001369	38.7893800	0.1034999	0.4972973
90529-30L	7.04E-15	1.33E-16	8.911189	0.064197	95.9492	297.251	1.974	2.189	0.0001357	14.1592200	0.1076727	0.3651827
90529-30M	2.90E-15	8.28E-17	8.752613	0.136371	93.6272	292.367	4.205	4.307	0.0002135	21.0799800	0.1069706	0.5610074
90529-30N	2.61E-16	5.00E-17	8.132242	1.400913	87.0805	273.134	43.663	43.672	0.0004327	114.4225000	0.1070806	2.6584940
90529-30O	4.21E-17	4.88E-17	6.723080	8.618371	81.5806	228.671	275.318	275.319	0.0006169	561.2098000	0.1213441	16.6658300
90529-30P	1.28E-16	4.91E-17	8.153783	2.816344	88.6417	273.806	87.746	87.751	0.0003804	265.8938000	0.1087124	5.2069010
90529-30Q	1.20E-16	4.87E-17	7.480451	2.988539	81.6019	252.704	94.207	94.210	0.0006162	174.9283000	0.1090869	5.5453300
90529-30R	8.38E-16	5.16E-17	8.720239	0.438157	94.0075	291.369	13.519	13.551	0.0002007	76.9432600	0.1078038	1.0421980
90529-30S	1.89E-15	5.52E-17	8.881846	0.198001	93.7349	296.348	6.092	6.165	0.0002098	32.3595100	0.1055354	0.4879208
90529-30T	2.81E-15	7.47E-17	8.670087	0.139368	93.6761	289.820	4.304	4.402	0.0002118	22.2150100	0.1080451	0.5321274
90529-30U	6.80E-16	5.21E-17	8.382254	0.535867	90.8565	280.910	16.630	16.654	0.0003063	62.4475600	0.1083915	1.0753640

Run_ID	±$^{39}Ar/^{36}Ar$ (%, 1s)	ρ $^{40}Ar/^{39}Ar$	ρ $^{36}Ar/^{39}Ar$
90529-30E	7.2959470	0.9817048	0.1228165
90529-30F	10.2955200	0.9907759	0.0868433
90529-30G	5984.3330000	0.9999999	0.0002262
90529-30H	30.7724400	0.9987423	0.0323692
90529-30I	37.9147800	0.9990798	0.0280385
90529-30J	121.5874000	0.9998330	0.0126362
90529-30K	38.7818000	0.9993028	0.0241007
90529-30L	14.1402600	0.9950483	0.0642862
90529-30M	21.0685900	0.9975623	0.0431260
90529-30N	114.4091000	0.9996593	0.0168394
90529-30O	561.0635000	0.9995560	0.0227922
90529-30P	265.8701000	0.9997952	0.0136995
90529-30Q	174.8911000	0.9994672	0.0220443
90529-30R	76.9397000	0.9997520	0.0129634
90529-30S	32.3507900	0.9990026	0.0286421
90529-30T	22.2041600	0.9978377	0.0408711
90529-30U	62.4395000	0.9996145	0.0182225

Run_ID	Plateau Steps	Laser Power	^{40}Ar	±^{40}Ar (1σ)	^{39}Ar	±^{39}Ar (1σ)	^{38}Ar	±^{38}Ar (1σ)	^{37}Ar	±^{37}Ar (1σ)	^{36}Ar	±^{36}Ar (1σ)	% 39Ar	^{39}Ar moles
Standard analyses														
90528-01A		3.75	16.0895100	0.0160007	4.9888370	0.0064000	0.0800529	0.0005201	0.0040370	0.0000614	0.0057375	0.0000361	100	5.64E-13
90528-02A		3.75	12.9803800	0.0120022	4.1452720	0.0055001	0.0661914	0.0002021	0.0008062	0.0000338	0.0033176	0.0000273	100	4.68E-13
90530-01A		3.75	21.5712800	0.0160048	5.8545180	0.0060002	0.0946102	0.0002739	0.0009398	0.0000328	0.0159082	0.0000395	100	6.62E-13
90530-02A		3.75	10.0513300	0.0050211	2.0542400	0.0024009	0.0334248	0.0001876	0.0000859	0.0000262	0.0134774	0.0000367	100	2.32E-13

Run_ID	^{40}Ar moles	^{40}Ar*/^{39}Ar	± ^{40}Ar*/^{39}Ar (1σ)	%^{40}Ar*	Age	± Age (1σ)	± Age (1σ, w/J)	^{36}Ar/^{40}Ar	±^{36}Ar/^{40}Ar (%, 1s)	^{39}Ar/^{40}Ar	±^{39}Ar/^{40}Ar (%, 1s)	±^{39}Ar/^{36}Ar (%, 1s)	ρ ^{40}Ar/^{39}Ar	ρ ^{36}Ar/^{39}Ar
Standard analyses														
90528-01A	1.81E-15	2.8794810	0.0117762	89.394	101.507	0.404	0.528	0.0003552	1.1651960	0.3104521	0.2987244	0.9749273	0.3214319	0.6892272
90528-02A	1.36E-15	2.8892750	0.0108382	92.385	101.843	0.371	0.505	0.0002551	1.2780430	0.3197499	0.2982633	1.1087410	0.4443216	0.6330133
90530-01A	1.81E-15	2.8701020	0.0155948	77.991	101.185	0.535	0.633	0.0007372	1.0068570	0.2717347	0.2781959	0.7780511	0.0694563	0.7823395
90530-02A	5.67E-16	2.9307130	0.0270636	59.967	103.262	0.927	0.989	0.0013409	1.0112420	0.2046147	0.2782348	0.7882429	0.0821291	0.7769144

Run ID	Discrim.	Discrim. (1σ)	^{40}Ar bkgd	±^{40}Ar bkgd (1σ)	^{39}Ar bkgd	±^{39}Ar bkgd (1σ)	^{38}Ar bkgd	±^{38}Ar bkgd (1σ)	^{37}Ar bkgd	±^{37}Ar bkgd (1σ)	^{36}Ar bkgd	±^{36}Ar bkgd (1σ)
Grain-01 Int. age 315 ± 6 Ma No plat. age	1.019905	0.002479	0.0040710	0.0005100	0.0001158	0.0000200	0.0000428	0.0000240	0.0002894	0.0000260	0.0000168	0.0000063
Grain-02 Int. age 313 ± 5 Ma plat. age 313 ± 2 Ma	1.019905	0.002479	0.0055763	0.0004959	0.0001358	0.0000440	0.0000458	0.0000370	0.0002967	0.0000240	0.0000162	0.0000053
Grain-03 Int. age 297 ± 3 Ma plat. age 295 ± 3 Ma	1.019905	0.002479	0.0043099	0.0004670	0.0001358	0.0000440	0.0000458	0.0000370	0.0002967	0.0000240	0.0000162	0.0000053
Grain-04 Int. age 301 ± 3 Ma plat. age 299 ± 2 Ma	1.019905	0.002479	0.0040982	0.0004661	0.0001358	0.0000440	0.0000458	0.0000370	0.0002967	0.0000240	0.0000162	0.0000053
Grain-06 Int. age 293 ± 6 Ma plat. age 300 ± 3 Ma	1.015550	0.003824	0.0043090	0.0004300	0.0001398	0.0000300	0.0000388	0.0000320	0.0002961	0.0000250	0.0000327	0.0000068
Grain-07 Int. age 358 ± 10 Ma No plateau age	1.015550	0.003824	0.0043090	0.0004300	0.0001398	0.0000300	0.0000388	0.0000320	0.0002961	0.0000250	0.0000327	0.0000068
Grain-08 Int. age 309 ± 3 Ma plat. age 309 ± 2 Ma	1.015550	0.003824	0.0043090	0.0004300	0.0001398	0.0000300	0.0000388	0.0000320	0.0002961	0.0000250	0.0000327	0.0000068
Grain-09 Int. age 311 ± 7 plat. age 317 ± 4 Ma	1.015550	0.003824	0.0043090	0.0004300	0.0001398	0.0000300	0.0000388	0.0000320	0.0002961	0.0000250	0.0000327	0.0000068
Grain-10 Int. age 300 ± 5 Ma plat. age 305 ± 2 Ma	1.015550	0.003824	0.0043090	0.0004300	0.0001398	0.0000300	0.0000388	0.0000320	0.0002961	0.0000250	0.0000327	0.0000068
Grain-21 Int. age 298 ± 7 No plat. age	1.008620	0.002711	0.0042850	0.0004200	0.0001203	0.0000250	0.0000384	0.0000390	0.0002676	0.0000210	0.0000228	0.0000100
Grain-23 Int. age 308 ± 6 Ma No plat. age	1.008620	0.002711	0.0042850	0.0004200	0.0001203	0.0000250	0.0000384	0.0000390	0.0002676	0.0000210	0.0000228	0.0000100
Grain-24 Int. age 296 ± 3 Ma No plat. age	1.008620	0.002711	0.0042850	0.0004200	0.0001203	0.0000250	0.0000384	0.0000390	0.0002676	0.0000210	0.0000228	0.0000100
Grain-25 Int. age 291 ± 3 Ma No plat. age	1.008620	0.002711	0.0042850	0.0004200	0.0001203	0.0000250	0.0000384	0.0000390	0.0002676	0.0000210	0.0000228	0.0000100
Grain-26 Int. age 310 ± 4 Ma No plat. age	1.008620	0.002711	0.0042850	0.0004200	0.0001203	0.0000250	0.0000384	0.0000390	0.0002676	0.0000210	0.0000228	0.0000100
Grain-27 Int. age 321 ± 4 Ma plat. age 321 ± 3 Ma	1.008620	0.002711	0.0042850	0.0004200	0.0001203	0.0000250	0.0000384	0.0000390	0.0002676	0.0000210	0.0000228	0.0000100
Grain-28 Int. age 290 ± 5 Ma No plat. age	1.008620	0.002711	0.0042850	0.0004200	0.0001203	0.0000250	0.0000384	0.0000390	0.0002676	0.0000210	0.0000228	0.0000100
Grain-29 Int. age 308 ± 15 Ma plat. age 293 ± 3 Ma	1.008620	0.002711	0.0042850	0.0004200	0.0001203	0.0000250	0.0000384	0.0000390	0.0002676	0.0000210	0.0000228	0.0000100
Grain-30 Int. age 289 ± 2 Ma No plat. age	1.008620	0.002711	0.0042850	0.0004200	0.0001203	0.0000250	0.0000384	0.0000390	0.0002676	0.0000210	0.0000228	0.0000100
Standard analyses												
90528-01A	1.019905	0.002479	0.0044160	0.0001500	0.0001431	0.0000250	0.0000760	0.0000120	0.0003024	0.0000130	0.0000220	0.0000028
90528-02A	1.019905	0.002479	0.0062430	0.0002300	0.0001815	0.0000330	-0.0000120	0.0000290	0.0002839	0.0000190	0.0000249	0.0000037
90530-01A	1.019905	0.002479	0.0115090	0.0003900	0.0004569	0.0000490	0.0000830	0.0000460	0.0003027	0.0000170	0.0000293	0.0000063
90530-02A	1.019905	0.002479	0.0125210	0.0004600	0.0006166	0.0000660	0.0000981	0.0000530	0.0003287	0.0000190	0.0000262	0.0000071

Chapter 5

Initial interpretations of mineralization in the South-West Extension-South (SWEXS), Navan

5.1 Introduction

Exploration for further ore within economic distance of the existing infrastructure in Navan was prioritized in the late 1980s. The most important discovery of such ore was made in the early 1990s by drilling to the southwest of the main ore body. This discovery was named the South West Extension (SWEX), as documented by Ashton et al. (2003). The SWEX is estimated to contain 30 Mt of mineral resources, which is currently being extracted. Several smaller areas of interest have also been located in the Clogherboy and Tatestown/Scallanstown areas, but these are of insufficient grade and tonnage for exploitation.

Irish type base metal deposits are commonly found in the hanging wall of major structures (Ashton et al., in press), understanding the structures in the area surrounding Navan may lead to other potentially mineralized targets. Similar structural studies by the oil industry have demonstrated that seismic profiles can cost-effectively provide shallow and deep structural information over large distances. Thus an experimental seismic line was taken along a NW-SE strike just south of the ore deposit (Figure 5.1). Based on the high quality of the data, four additional lines covering ca 100 km were collected. Interpretation of the data identified several potential targets. One favored target, at ca. 1.5 km SW of the SWEX, appeared to be at 1100 m depth near a major basin-bounding fault identified from the seismic data. Drilling to 1560m resulted in the intersection of massive Zn+Pb mineralization in the basal 5 Lens horizon (33m @ 14% Zn+Pb). This new area was named SWEX-South (SWEXS).

This chapter summarizes my investigative methods, results, analyses, and conclusions related to data from the SWEXS area, along with suggestions for future research. As the area is further drilled and studied this understanding will no doubt become clearer.

5.1.1 Seismic lines

Seismic studies are a way of imaging deep into the earth. The method relies on the fact that sound waves propagate through different lithologies at different velocities. Further, as a sound wave moving through the subsurface reaches a change in lithology, and thus changes velocity, some of the energy of the sound wave is reflected. This reflection then travels up to the surface and can be detected. By placing many detectors, or geophones, in an area and measuring the difference in arrival time of the incoming wave, a pseudo-cross-section of distance along the surface to time (depth) of a particular reflective subsurface layer can be made. The raw data from a seismic profile require significant interpretation in order to provide an accurate representation of reflective surfaces in the subsurface. Different filters can be applied to select which detectors are used to receive each signal and can effectively filter out shallow or deep noise by focusing the profile for a specific depth. This interpretation can be complicated and imprecise, but if done carefully can yield important qualitative information.

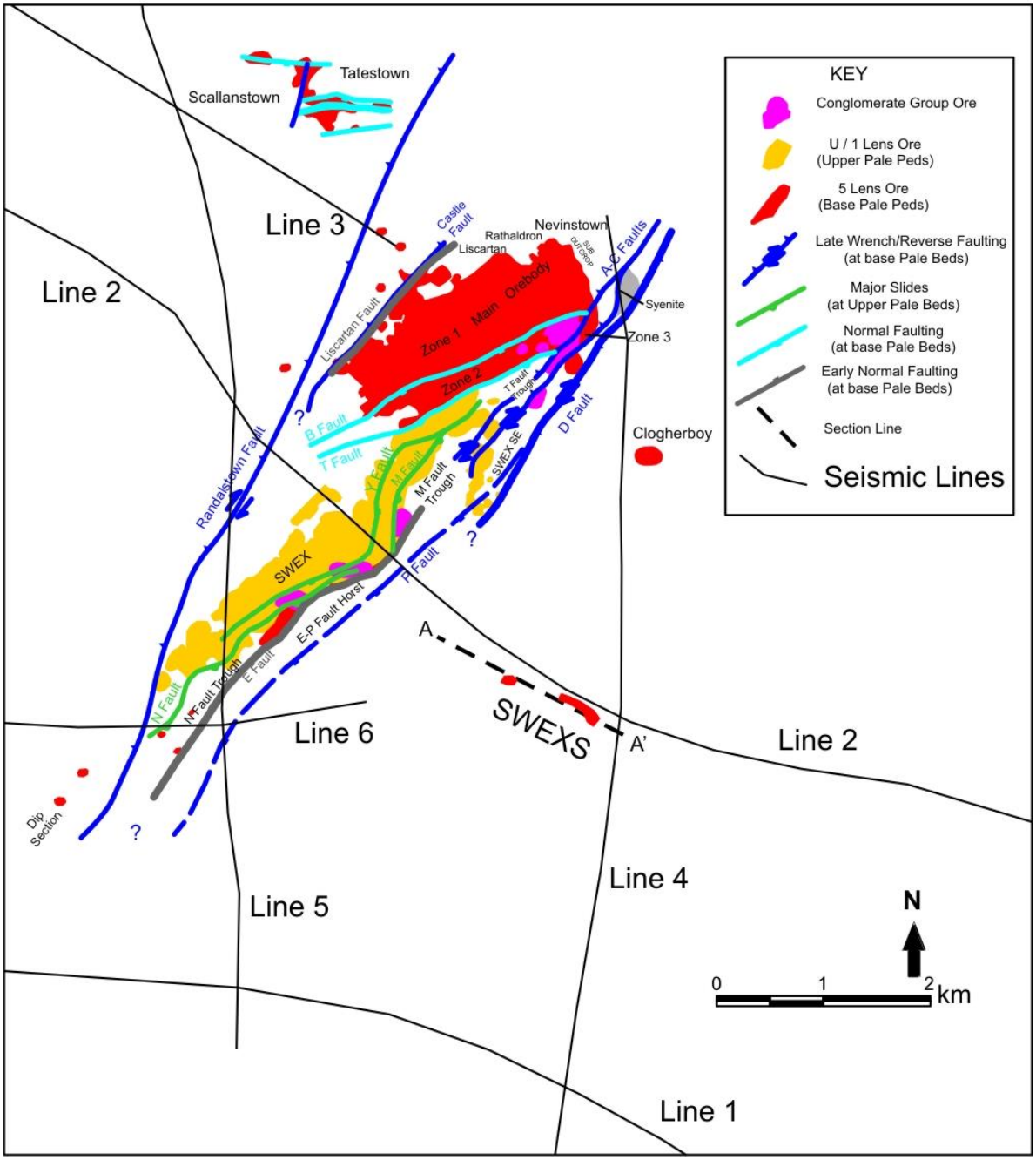

Figure 5.1. Map of the Navan area showing the known extent of mineralization. Note seismic lines shown in black, which continue off the map. The SWEXS contains 5 Lens mineralization. The section A - A’ is shown in Figures 5.2 and 5.6.

5.2 Methods

5.2.1 Drilling

In the SWEXS area there are 7 NQ (47.6mm core diameter) diamond drill holes that begin at the surface (mother holes) with an additional 13 angled navigational holes (navi holes) that diverge from the mother holes at depth (as of mid-2014). The drilling spans an area of ca. 2 x 1 km, with the majority of the holes located along the approximately NW- SE seismic profile. Approximately 27700m of drill core has been recovered from the SWEXS and logged by Tara exploration geologists and consultant researcher M. Philcox, for lithology, structure, alteration and mineralization. Drill holes are all down-hole surveyed to produce accurate depth and drill hole azimuth information. Core lengths with potential economic mineralization and exploration relevance have been assayed for Zn, Pb and Fe. The drill hole logs and element data have then been imported to Leapfrog™ for 3D visualization. I inspected the majority of SWEXS drill core for textures and sampling. The majority of samples were selected from quartered core, with sample name indicating the drill hole number and depth.

5.2.2 Petrography

Selected samples were cut and polished into thin sections, thick sections, or polished blocks. The samples were selected so as to maximize the number and type of textures. Four samples were taken from both N02176 and N02240. Thin sections were viewed under a petrographic microscope with transmitted and/or reflected light for textural, paragenesis, and mineralogical analyses. The polished samples were viewed both by reflected light microscopy as well as with the Hitachi Scanning Electron Microscope S-3700N (SEM) at SUERC. SEM analyses were made on unpolished samples in low-vacuum mode. The attached Energy Dispersive Spectroscopy (EDS) detector was used to obtain semi-

quantitative elemental data on individual ca. 50 µm spots. Samples of layered pyrite within the UDL were taken from several drill holes to maximize the area covered, see table 5.3.

5.2.3 Sulfur isotopes

Samples for sulfur isotope analysis were acquired from drill hole intersections. Sufficiently large or isolated sulfides were sub-sampled with a dentist drill. Resulting powders were mixed with Cu_2O in excess and combusted *in vacuo* at 1050 °C. The resulting SO_2 was separated from CO_2 and other non-condensable gases via a distillation step at -130 °C with a n-pentane-jacketed cold finger initially frozen by liquid N_2. The purified SO_2 was then analysed isotopically on either a Thermo Scientific MAT 253 or a VG Sira II duel-inlet gas source mass spectrometer. This conventional method followed Robinson and Kusakabe (1975).

Samples with finer textures were polished to thick sections and laser combusted *in situ* under an atmosphere of O_2. Resulting gas was then purified as above and concentrated directly to a VG Sira II as in Fallick et al. (1992) and Wagner et al. (2002). During laser combustion, soot can be deposited on the cover slip, obstructing the camera's view of the sample surface. This is particularly problematic for galena samples, although sphalerite can also be affected. Thus each laser burn path was inspected after analysis to ensure that only the phase of interest was combusted. Data collected from laser paths indicating a mixture of sulfide phases were discarded.

5.2.4 Seismic interpretations

The raw data from the Navan seismic lines were interpreted by expert consultants producing multiple distance vs. time pseudo-sections with a range of filters. These sections were integrated using Kingdom® software to select and link reflectors between overlapping cross-sections. Sections were then converted from time to depth profiles using the simplistic but reasonable assumption of a single seismic speed. The depth vs. time

profile was then either directly drawn on or exported to Leapfrog™ 3D visualization software.

5.3 Results

5.3.1 Lithological and Seismic Results

The drilling of the SWEXS can be divided into four areas along the NW-SE section. These areas are named here, from NW to SE, the Horst, the Pale Beds Trough, the Terrace, and the Basin Margin (Figure 5.2).

5.3.1.1 E-Fault Horst

The western-most area (SE flank of E-Fault Horst) is defined by three drill holes (N02207, N02214 and N02220) that have no pre-Chadian stratigraphy and enter directly into Lower Paleozoic (LP) basement rocks (Figure 5.2). The LP contact is either an erosional contact or a large low angle detachment fault, as hundreds of meters of section are missing. The LP that has been intersected here contains considerable disseminated pyrite. The BC present is very thin (< 12.5m) and is non-mineralized. The Upper Dark Limestone (UDL) contains considerable massive (meter-scale) to thin (mm-scale) bedding-parallel pyrite layers (Figure. 5.2). Seismic profiles show a strong shallowly dipping reflector here that coincides with the straight-line dip of the LP contact seen in drill holes. The depth of the reflector is coincident with the layered pyrite in the UDL and may represent the transition from upper UDL to the basal Thinly Bedded Unit (TBU) (Figure 1.5). Seismic results imply that no Pale Beds are preserved in the 740 m between N02207 and N01031 (on the E-Fault horst just to the east of the SWEX).

5.3.1.2 Pale Beds Trough

The Pale Beds Trough, includes the deepest Pale Beds drilled to date and is currently defined by five drill holes (N02181, N02176, N02195, N02198, and N02199) (Figure 5.3). This area is structurally complicated, with large parts of the lithological section missing in

each drill hole. Three drill holes intersect Pale Beds with varying thickness (52, 118, and 131 m) and all have missing section above and below the Pale Beds. The basal contact of the Navan Group appears to be fault-controlled while the top seems to be cut by the Erosion Surface (ES). Faulting in hole N02195 has created a repetition of the Muddy Limestone (ML) and Laminated Beds (LB). This can be somewhat constrained with faulting found in hole N02176, which has removed the Muddy Limestone and significantly thinned the Laminated Beds to 1.3 m from their usual ca. 40 m (Strogen et al., 1990). Typically missing and repeated sections are associated with normal and reverse faulting, respectively. However, due to the complex nature of this faulting, the limited drilling cannot constrain the type of faults responsible for this movement. The drill hole fan defining the Pale Beds Trough is 260m to the SW of the closest point on the seismic line. The seismic data in the area of the Pale Beds are weak as it is shadowed beneath strong reflectors within the TBU (Figure 5.2). Further, it is likely that the small-scale changes and 3D nature of the faulting evident in the drilling is below the resolution of the seismic data. An early interpretation of the seismic section by consultants suggested large SE-dipping reverse faults were controlling the area. Although this model is not consistent with small-scale drilling, it could still be true on a larger scale.

5.3.1.3 Terrace

The Terrace area is farther to the east and constrained by a fan of NE holes drilled off the mother hole, N02201 (Figure 5.4). There are a total of seven intersections with mineralized Pale Beds, with the grade and thickness of mineralization increasing to the east. The sequence in the Terrace holes is more complete and consistent than those in the Pale Beds Trough. The four western holes contain similar thicknesses of Pale Beds, Muddy Limestone, and Laminated Beds as well as containing some portion of the Red Beds. The next drill hole in the fan to the east of N02227 has more massive Boulder Conglomerate and intersects the PB deeper below the surface. It has similar thicknesses of PB and ML, but the base of the LB and the entirety of the RB are missing. The deepening trend

continues to the east, with N02240 and N02246 containing more Boulder Conglomerate and a deeper contact. Two of the eastern holes (N02227 and N02240) that intersect the Pale Beds also show a repetition of the ML and LB and a thin remnant of RB before intersecting the LP. The final hole that limits the edge of the Terrace is N02217, which does not intersect the Pale Beds. This hole intersects very high-energy BC with several clasts of Waulsortian Limestone that measure over 30m in diameter. This hole contains only the BC/TBU above the LP basement and defines the maximum Eastern extent of the Terrace. This drill hole fan defining the Terrace is drilled 20 m to the south of the seismic line. The seismic data here show strong horizontal reflectors that onlap over a low-reflectance zone (Figure 5.2). This shape is consistent with the strong reflector being either the BC or TBU, and the weaker reflector being the contact with the Pale Beds. An E-dipping fault can be seen on the seismic line between the two western holes that is not apparent from the drilling.

5.3.1.4 Basin Margin

There are 4 mother holes and 1 navi hole around the SWEXS that have been drilled into the Basin Margin. One of these mother holes and one navi hole can be seen in Figure 5.2, but the 3D structure of the Basin Margin is more evident in Figure 5.5. These holes are distinct in that although they are very deep, they end in Boulder Conglomerate or other allochthonous units and never reach the Pale Beds or the Lower Paleozoic basement. Some of these holes contain mineralized BC clasts and matrix. N02237, a navi from the Pale Beds Trough area, contains meter-sized clasts that are massively mineralized (>30 Zn+Pb wt.%). The two main seismic lines in the SWEXS area, lines 2 and 4, yield a horizon that can be interpreted as the LP contact. The extrapolation of these two lines into a 3D plane, combined with constraints from the drill holes, can be used to create a 3D mesh that defines the top of the LP with reasonable certainty. This contact deepens to the S and E to depths as great as 4 km (Figure 5.6). The Basin Margin represents the extent of cost-

effective exploration for exploitable base metal resources, as the costs of mining deeper into the basin are considered to be prohibitive.

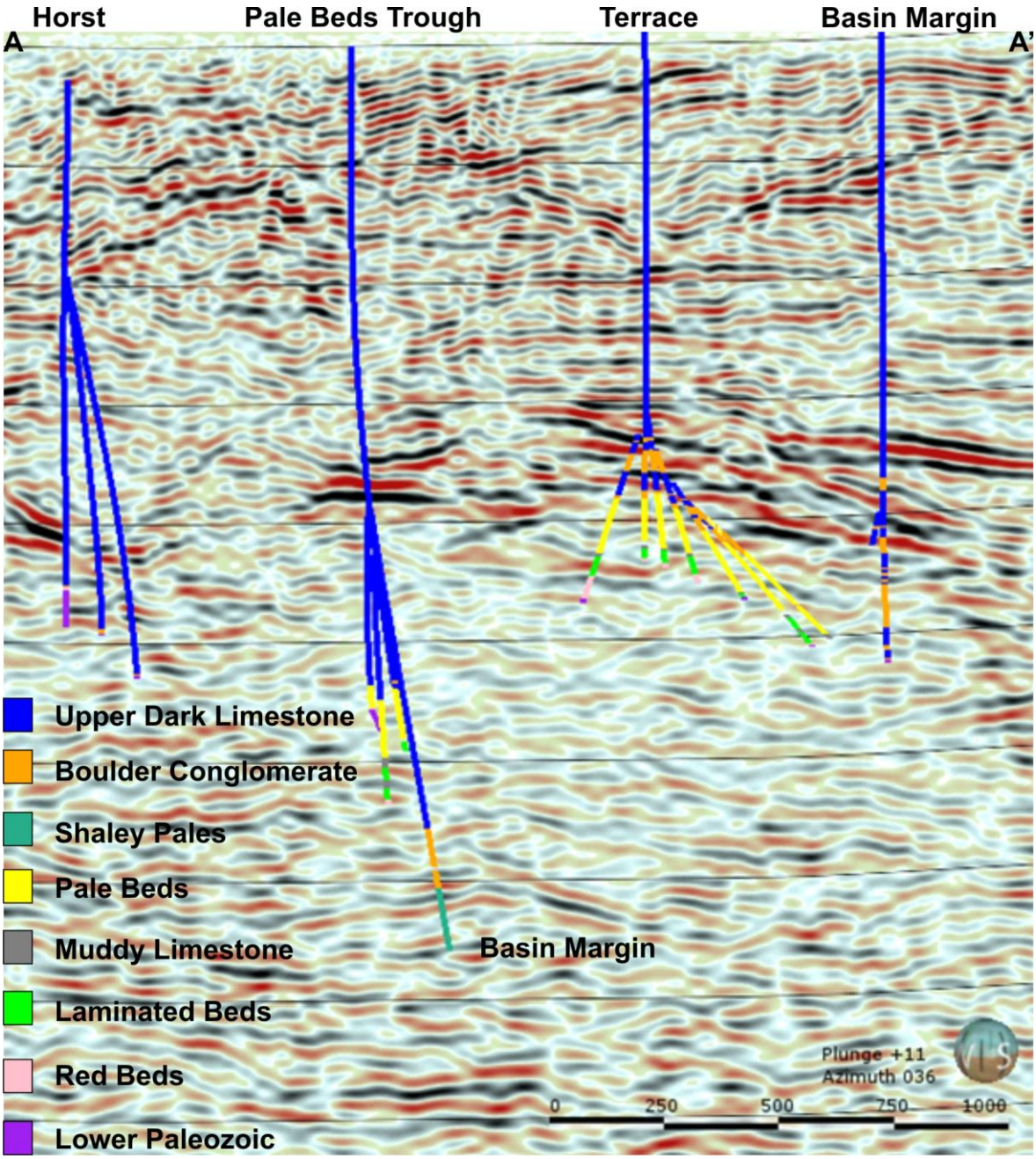

Figure 5.2. Drill holes in the SWEXS, shown on the NW-SE section A to A' (see Figure 5.1). This is overlain on the seismic profile taken along a nearby transect (line 2 on Figure 5.1). The four main areas in the SWEXS are shown at the top. Note that the Basin Margin area is represented not only in the SE-most drill hole, but also in a navi hole from the Pale Beds Trough region. This is due to the 3D relationships between holes and can be better viewed in Figure 5.3.

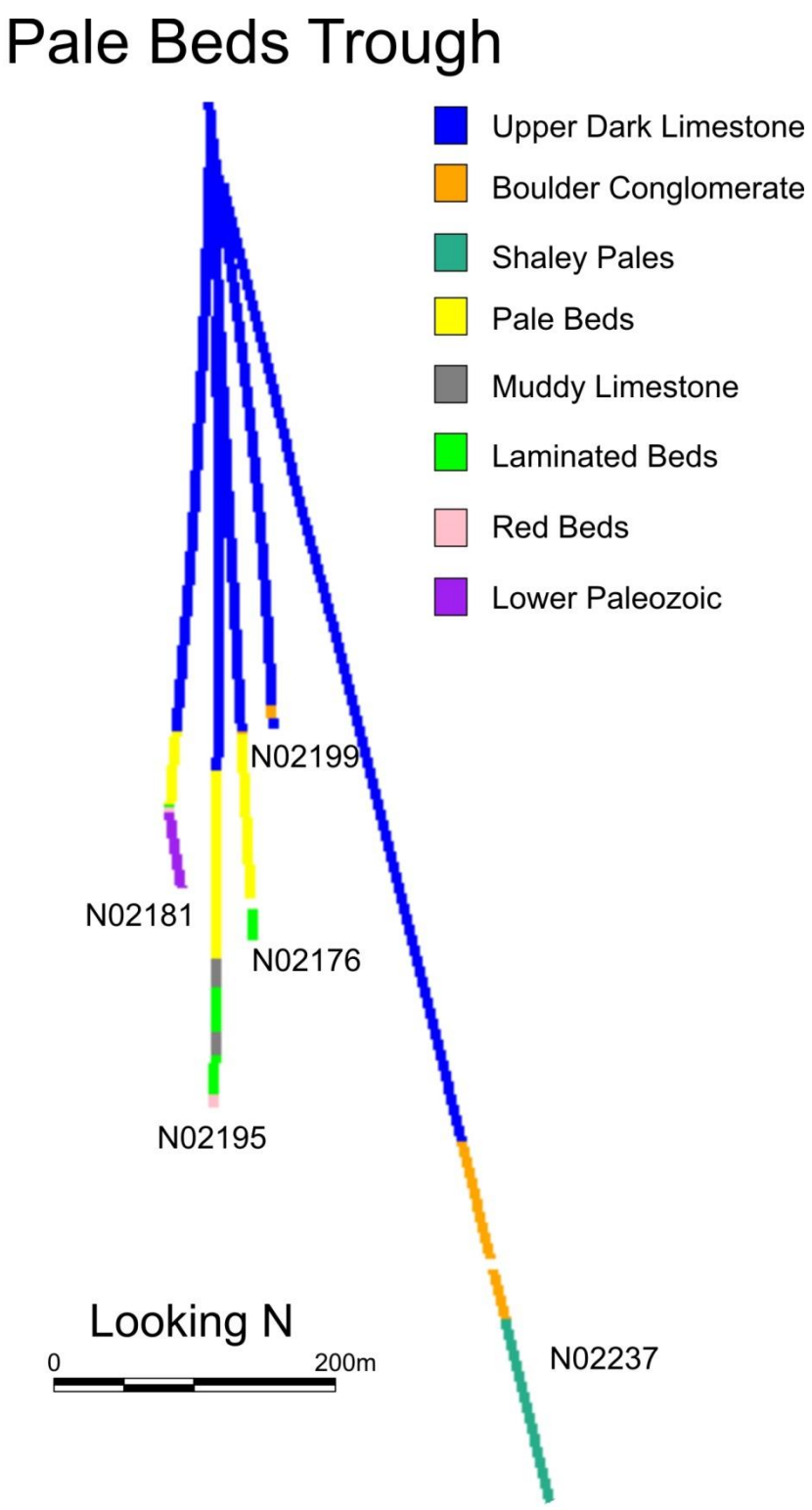

Figure 5.3. The mother hole (N02176) and associated navi holes. Four of the navi holes enter the Pale Beds Trough, while N02237 enters the Basin Margin area. The view differs from that in Figure 5.2. No clear stratigraphic correlations can be determined, indicating complex faulting.

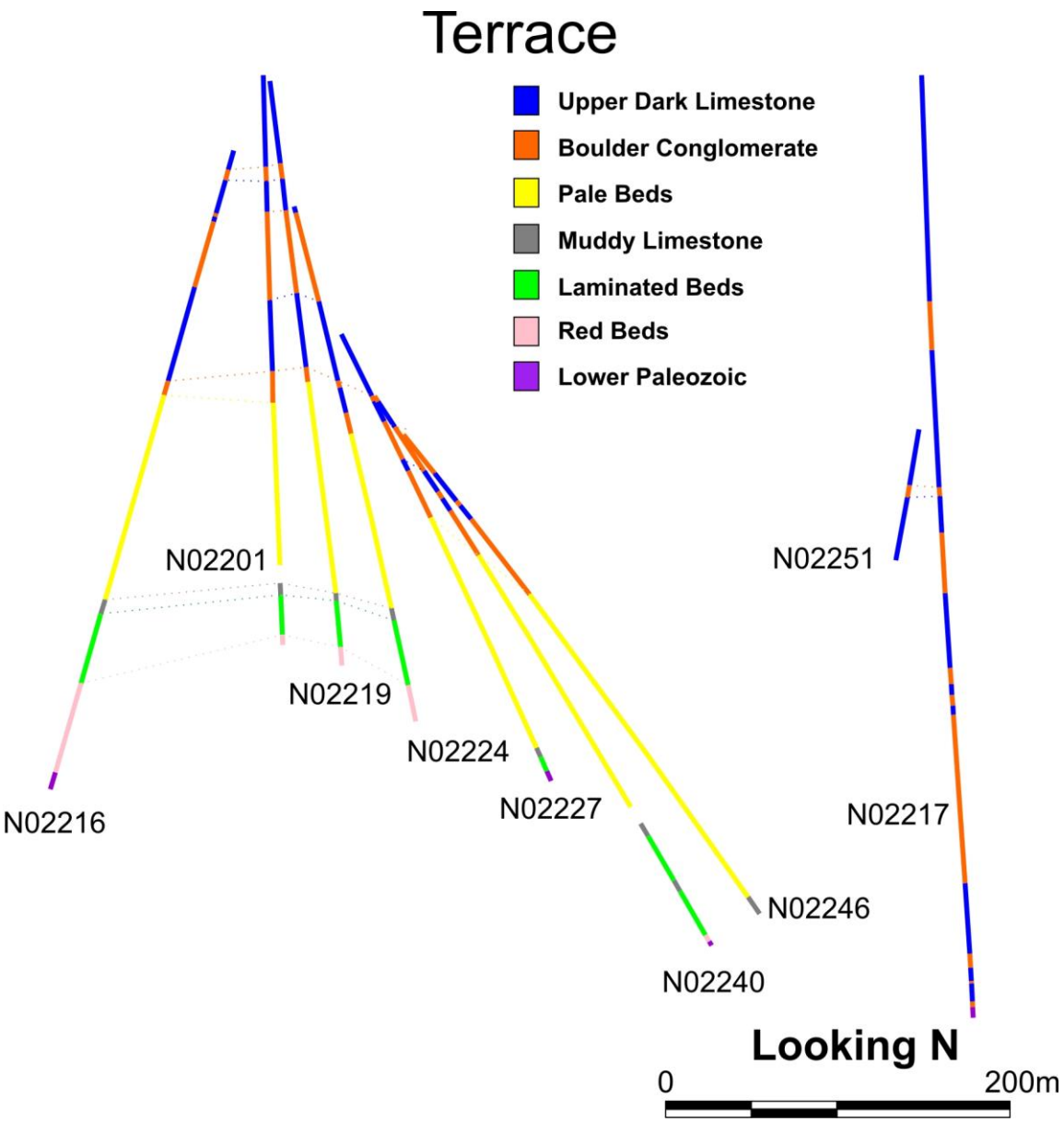

Figure 5.4. Drills holes associated with the Terrace area. Many of the holes on the western part of the fan are readily correlated stratigraphically. The eastern holes are not as easily correlatable. The upper contact of the Pale Beds begins to vary in the eastern holes and is completely removed by N02217. The Muddy Limestone, Laminated Beds, and Red Beds vary in thickness and show missing and/or repeated sections in the eastern holes.

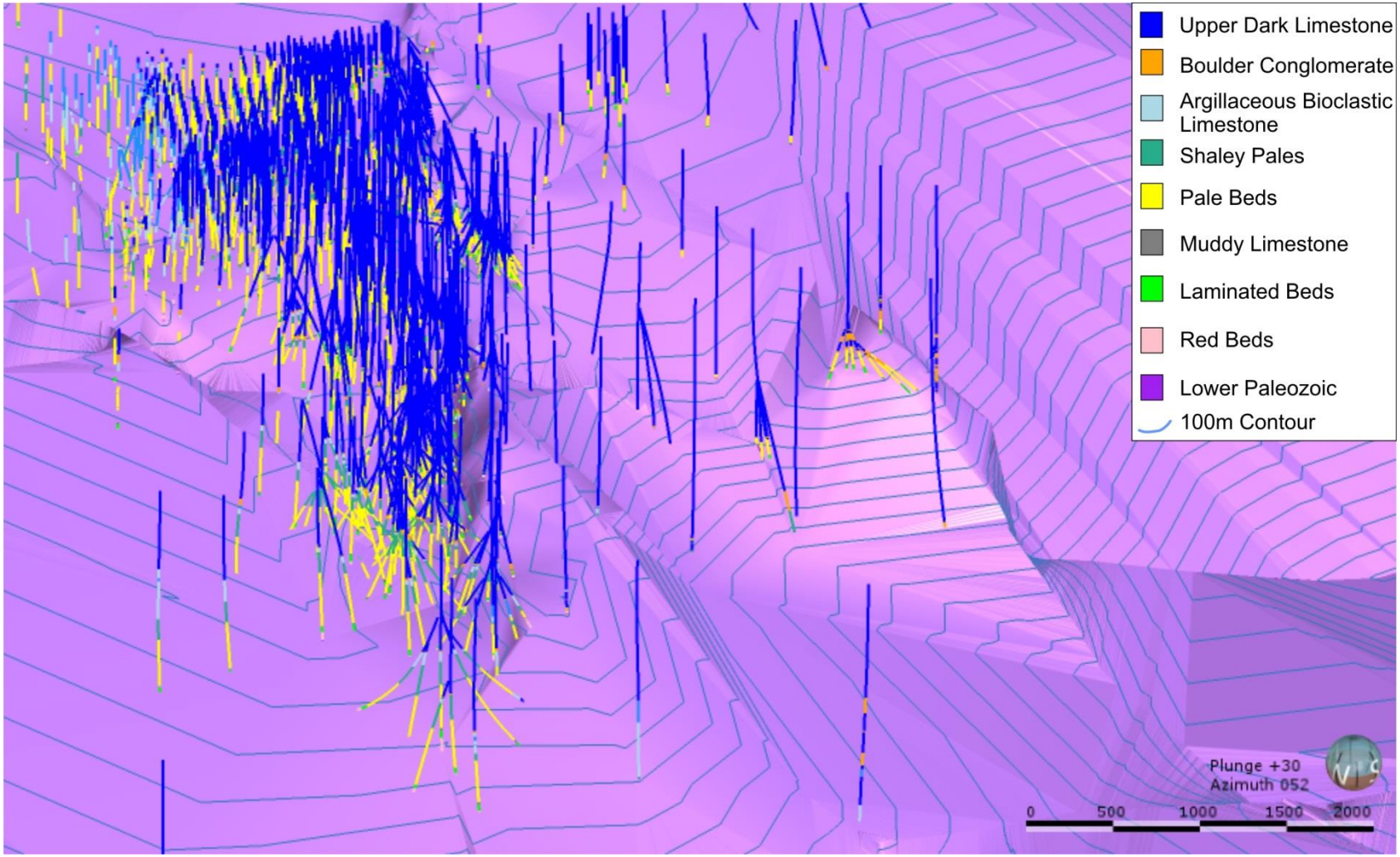

Figure 5.5. A perspective view of surface drill holes in the Navan area, facing NNE and dipping 30°. The purple contoured surface represents the upper contact of the Lower Paleozoic basements rocks. This surface was created from contacts found in drill holes as well as interpreted contacts from the seismic lines seen on Figure 5.1. Note that the basin deepens to the E and SE.

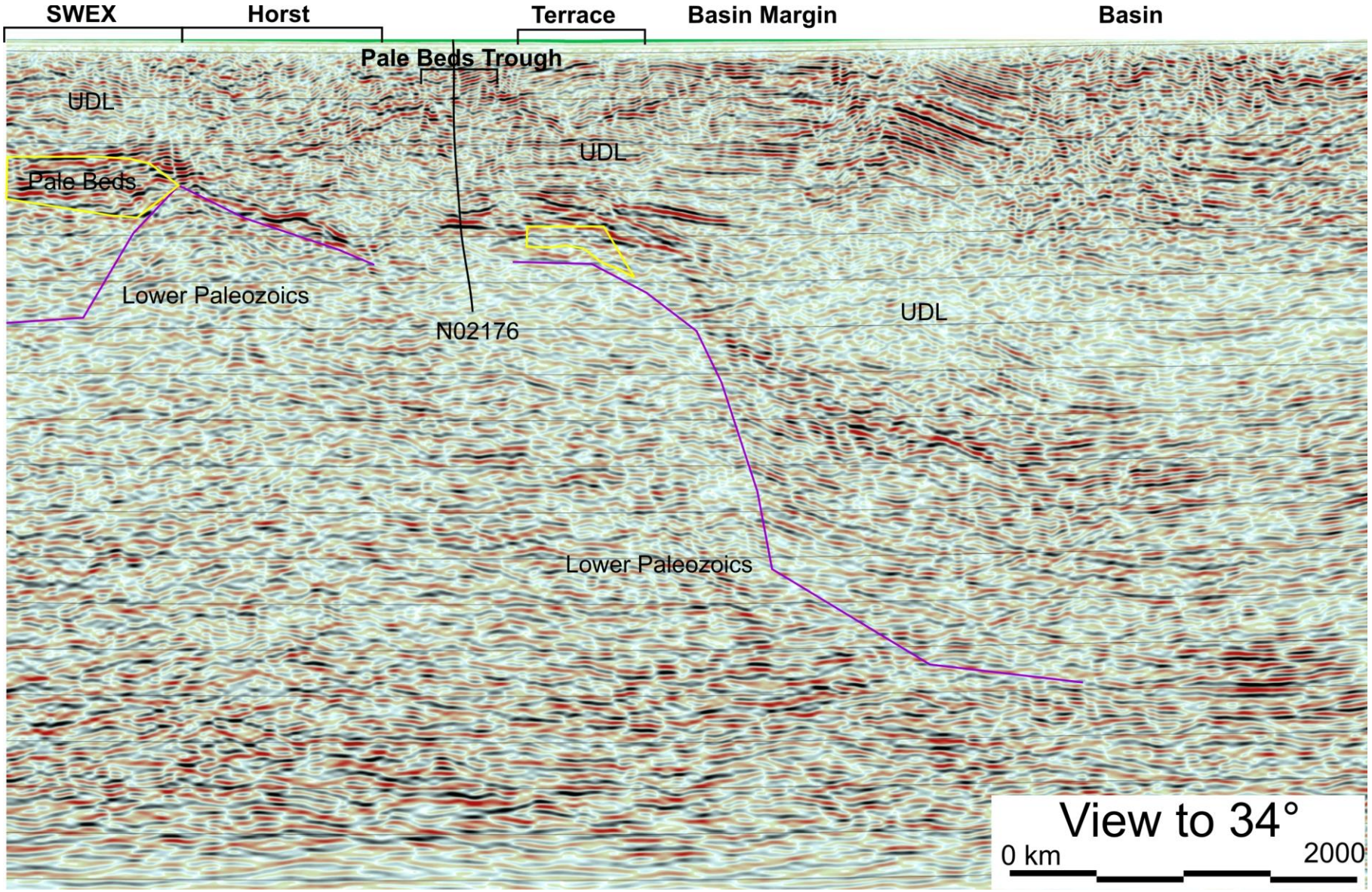

Figure 5.6. Seismic Line 2 (Figure 5.1). Upper contact of Lower Paleozoics is shown in purple, and areas of known Pale Beds are outlined in yellow. Drill hole N02176 is shown for reference. No Pale Beds area is shown around N02176 due to the complex nature of faulting in this region (see Figure 5.3).

5.3.2 Petrography and lithogeochemistry

5.3.2.1 TBU

The Thinly Bedded Unit in the SWEXS contains abundant bedding-parallel layered pyrite on the mm-scale set in layered calcic turbidites, interbedded with shales (Philcox, 1984) (Figure 5.7). Some drill holes have layers of massive pyrite on the cm- to meter-scale. Hole N02234 contains a small section with several mm-scale layered sphalerite layers. These layers of pyrite in the TBU are very similar to those seen in the main mine and studied by other authors (Altinok, 2005, Andrew and Ashton, 1985, Andrew and Ashton, 1982, Ashton et al., in press). The highest occurrence of layered pyrite in the SWEXS area is similar between holes (within 100m vertical meters). The pyrite layers are composed of discrete grains of pyrite in the form of framboids, aggregates of framboids, equant grains, and more massive crystalline pyrite (Figure 5.7). Small grains of sphalerite are present within these layers as well. Whole rock geochemistry on layered pyrite sections of N02176 shows that high Zn and Pb values are associated with high Fe, while some high Fe values are independent of Zn or Pb (Figure 5.8).

Hole N02223 was drilled 1 km SSW of the Terrace area and intersects significant sections of siderite. The siderite is located near the bottom of the hole, below large sections of layered and massive pyrite (Figure 5.9). Thin sections of N02223 show that siderite is replacing bio-clastic carbonate. This fine-scale replacement preserves the bio-clasts. The use of XRD confirms that the tan-brown mineral is siderite rather than ankerite, and also indicates the presence of apatite (see Table 5.1). Five subsamples of siderite were run for $\delta^{13}C$ and $\delta^{18}O$, which yielded clusters of data ca. $\delta^{13}C$= -5.5 and $\delta^{18}O$= -4.5 (Figure 5.10 and Table 5.1). Hand-held XRF from the same fresh half-core (Figure 5.11) as the isotopic data and thin sections shows mostly Ca, Fe, and some Si. There are minor amounts of Al, K, and trace Zn that indicate detrital input. The Pb and Zn values (65 and 25 ppm respectively) are only

slightly above trace levels (Table 5.1). Drilling of this hole ended when it intersected methane gas. Another hole in the basin margin area that did not contain siderite also intersected methane.

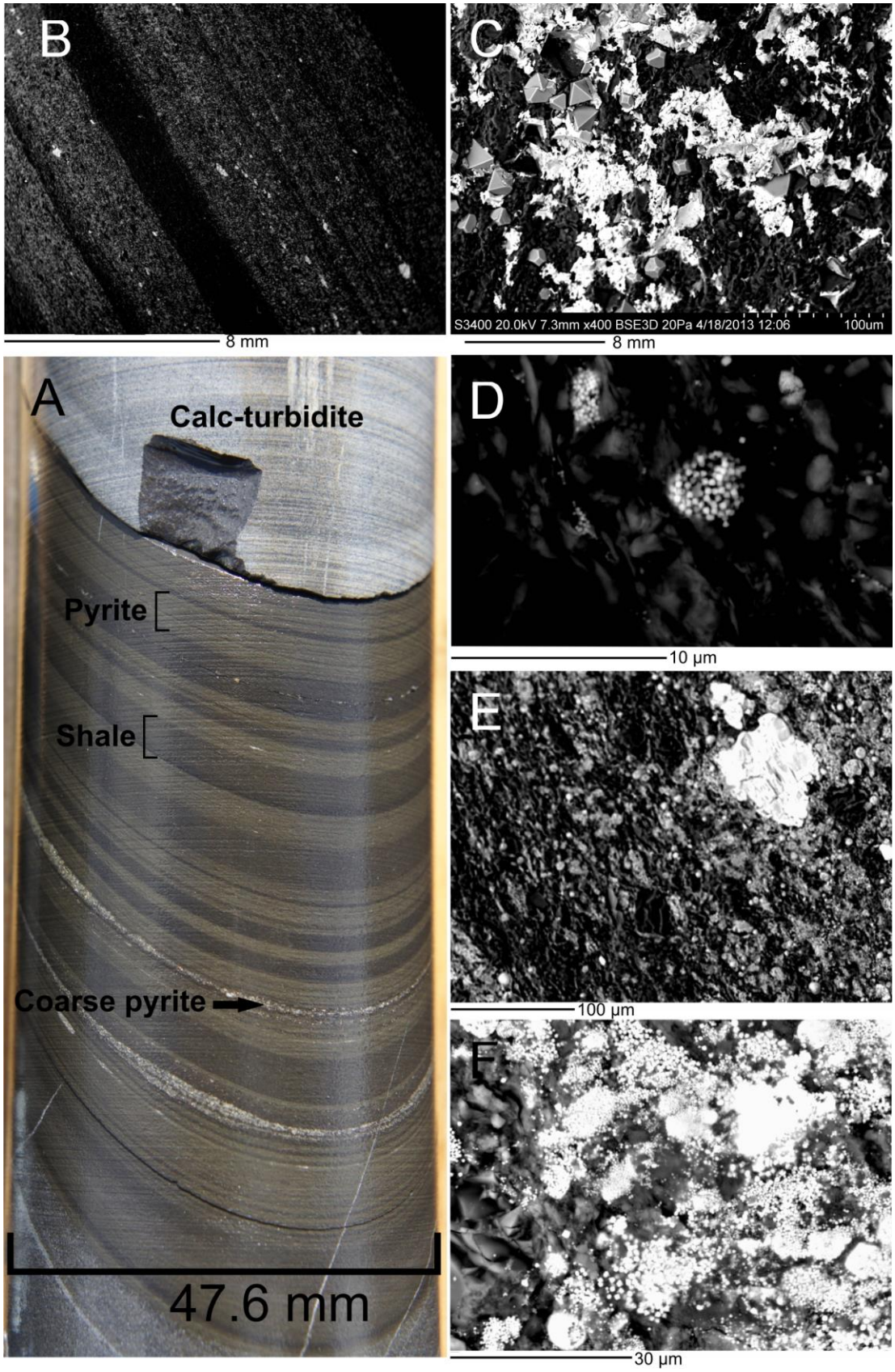

Figure 5.7. Layered pyrite from N02176. (A) Core photo of layered pyrite showing pyrite interbedded with black shale. Two bands of coarser, lighter colored, pyrite are visible. (B) SEM backscatter image of finely layered pyrite and black shale. (C) Equant grains of pyrite

surrounded by framboidal pyrite from a semi-massive pyrite band. (D) Solitary framboidal pyrite. (E) Large pyrite grain surrounded by framboidal pyrite grains in black shale. (F) Aggregate of framboidal pyrite.

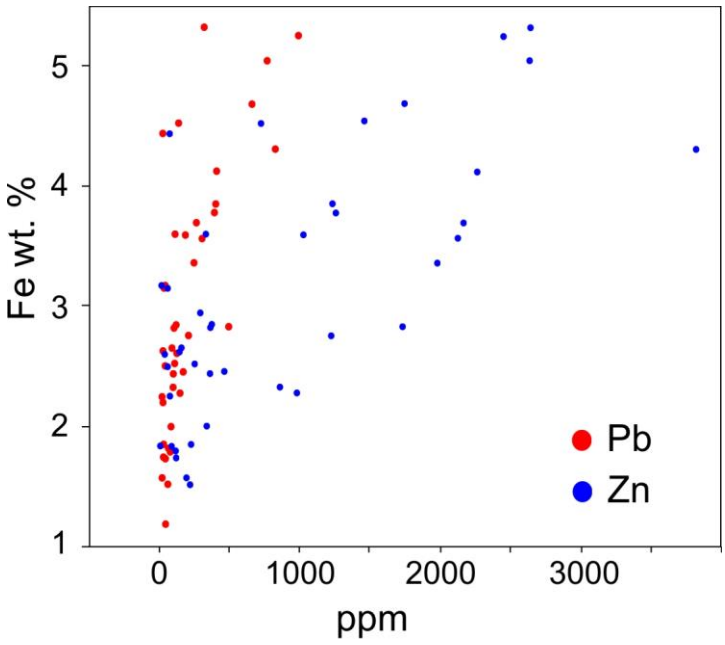

Figure 5.8. Zn (blue) and Pb (red) concentrations shown against wt.% Fe values for 1.5 m sections containing layered pyrite in N02176 from the SWEXS. Note that high Pb and Zn values are generally associated with high Fe values.

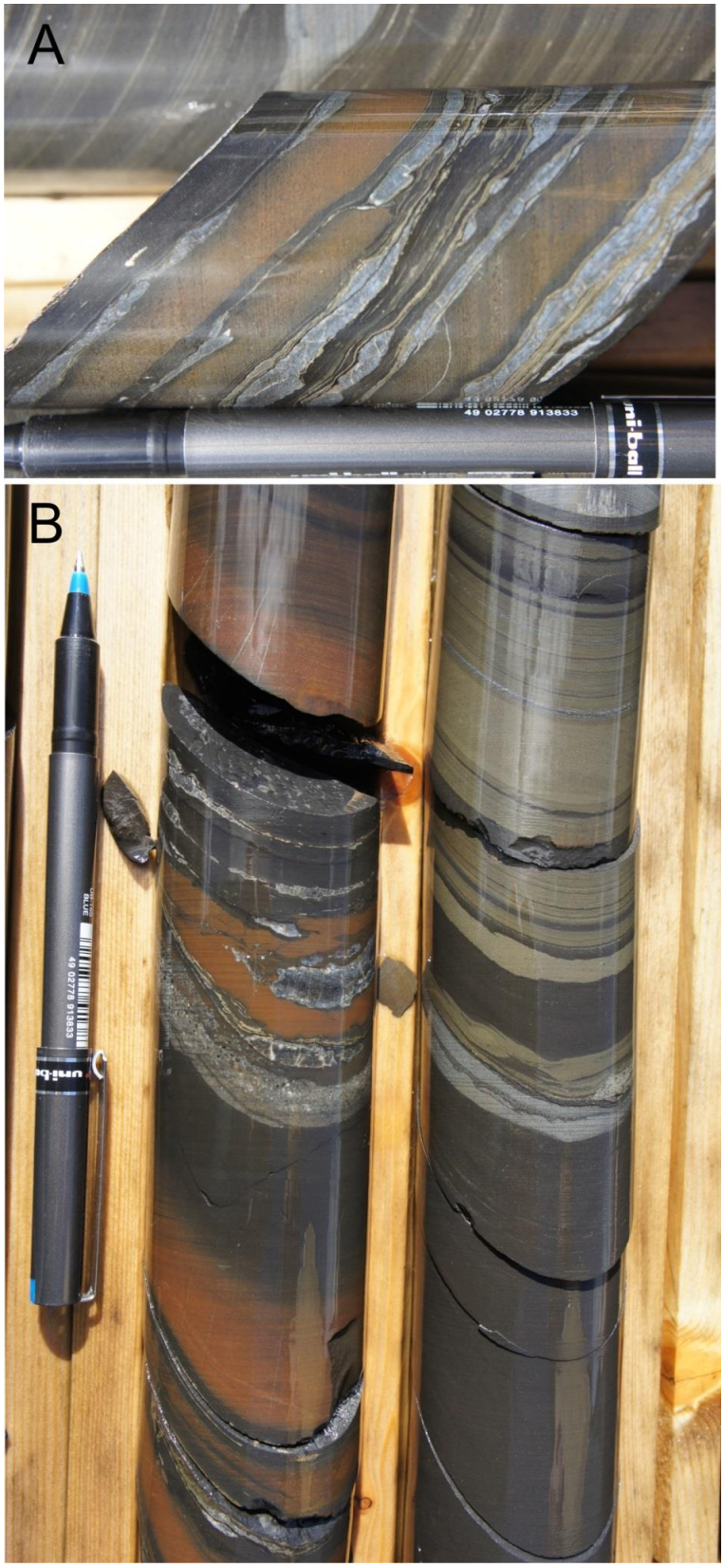

Figure 5.9. Core photos from hole N02223. (A) Interbedding of diffuse orange siderite-rich areas and thinly layered pyrite. (B) Siderite-rich layers on left, and pyrite-rich layers on right.

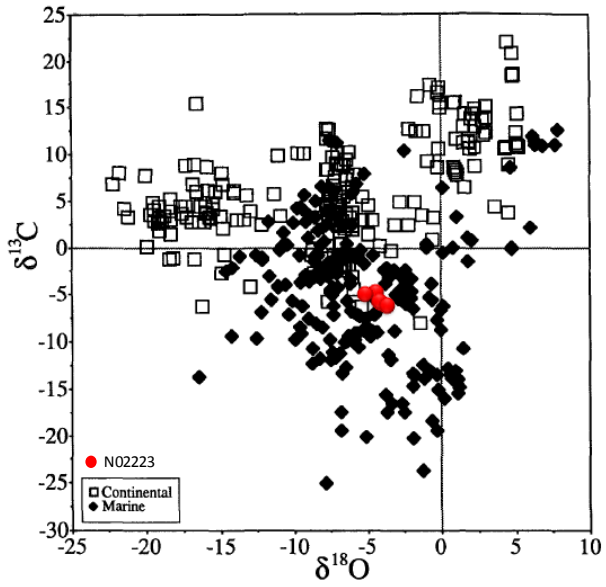

Figure 5.10. Plot of $\delta^{18}O$ against $\delta^{13}C$ for siderites from continental and marine environments. The red dots represent values for siderite from N02223. Modified from Mozley and Wersin (1992).

Figure 5.11. Photo of core with siderite from N02223. Locations of XRD, isotope, and XRF sampling are shown. Data are presented in Table 5.1 and Figure 5.10.

XRD Rietveld analysis	
mineral	modal %
Quartz	25%
Apatite	12%
Calcite	29%
Dolomite	3%
Siderite	31%

Isotope data			
Sample	$\delta^{13}C$	$\delta^{18}O_{PDB}$	± 1σ (all)
Siderite 1	-4.7	-4.4	0.2
Siderite 2	-5.9	-4.1	0.2
Siderite 3	-5.6	-4.2	0.2
Siderite 4	-4.8	-5.1	0.2
Siderite 5	-6.1	-3.6	0.2

Handheld XRF		± 1σ
Ca wt.%	31.47	0.57
Fe	22.29	0.17
Si	8.05	0.08
Al	0.89	0.11
K	0.30	0.02
P	0.11	2.87
Ag ppm	125	9
Pb	65	5
Co	50	3
Zr	32	5
Zn	25	3

Table 5.1. XRD, isotopic ($\delta^{18}O$ and $\delta^{13}C$), and XRF data from siderite from N02223, as shown in Figure 5.11. XRD data courtesy of N. Odling, University of Edinburgh. XRF data from an Olympus DELTA handheld XRF.

5.3.2.2 Boulder Conglomerate

The majority of the Boulder Conglomerate mineralization is contained within discrete clasts. These clasts range in size from small megacrysts (200 mm) to meter-sized boulders. The mineralization within the clasts includes disseminated, veins, massive layers, and podfill. One megacryst of galena has a rounded, oblong shape. The matrix of the Boulder Conglomerate also contains some sulfides. Some unmineralized clasts within the matrix are rimmed with sphalerite that decreases inwards over ca. 10 mm. The only major pyrite mineralization observed is a horizontally contiguous instance of several meters of massive pyrite sandwiched between large (ca. 15 m) boulders of Waulsortian reef. These intersections are within the BC in the eastern holes of the Terrace. This pyrite has not been investigated in detail but looks similar to the massive pyrite found within the TBU.

5.3.2.3 Pale Beds

Mineralization is dominated by sphalerite and galena with minor sulfosalts (boulangerite $Pb_5Sb_4S_{11}$), gangue minerals of pyrite, barite, and dolomite; tennantite-tetrahedrite have been reported in these ores by others (Treloar, 2014). Mineralization textures include massive (Figure 5.12 A, B, C and Figure 5.13 E) brecciated (Figure 5.12 E, Figure 5.13 A, B, C), vein-disseminated (Figure 5.12 D), layered (Figure 5.12 F), and small ramifying veinlets (Figure 5.13 D). The Pale Beds in the SWEXS are typified by chaotic broken mineralization textures that are hosted in brecciated regions surrounded by non-mineralized clasts. Each hole within the SWEXS contains different mineralization intensities and relative abundances of sulfide minerals. Navi holes share the same characteristics as companion holes from the same mother. The two most mineralized holes, N02176 from the Pale Beds Trough and N02240 from the Terrace, have some conspicuous differences in that N02176 contains more galena and darker, more layered sphalerite than N02240 (Figures 5.12 and 5.13). Notably, N02176 yields higher Pb/Zn ratios than N02240 (Table 5.2).

I have conducted detailed petrography on four samples from N02176. These samples are all limestones, with varying amounts of detrital minerals, replaced by hydrothermal minerals, including galena, sphalerite, pyrite, barite, dolomite, and calcite. Galena within the samples often forms coarse blebs or bands. The bands of galena have a number of sulfosalts (e.g. boulangerite, $Pb_5Sb_4S_{11}$) that are often strongly oriented along the length of the band (Figure 5.14). There are also areas within the bands that have more randomly oriented sulfosalts, as well as some that show elongation perpendicular to the vein growth (Figure 5.15). The sulfosalts grow in the same 3D orientation within small areas. There are areas where the galena bands have been broken apart and banded sphalerite has grown along cracks. There are also small (ca. 2µm) fluid inclusion trails within the galena. The small blebs of galena that are present are mantled by pyrite and are devoid of visible sulfosalts.

Sphalerite present in N02176 is varied in color and texture. The major texture in most samples is that of randomly oriented grains of sphalerite with zoned growth, seen as dark and light bands (Figure 5.16). These grains sometimes create aggregates with coherent zoning patterns (Figure 5.17). Some grains are nucleated around non-sphalerite grains. Many grains seem to follow a consistent growth pattern.

The layered sphalerite varies from pale brown to dark brown sphalerite, and is also associated with banded galena and barite. The sphalerite bands can often be followed across the entire section. In some areas the bands are broken apart by later barite, sphalerite, pyrite or calcite (Figure 5.17 , 5.18 and 5.21). It is usually evident how these broken bands can be reconstructed. Energy Dispersive Spectroscopy (EDS) analyses do not detect trace element variation between different sphalerite colors, although such variations have been found elsewhere in the Irish Orefield (Barrie et al., 2009).

Pyrite is present within all samples from N02176. The pyrite varies in texture, which includes small framboids, framboidal aggregates, colloform, mantles on other minerals, bands, and massive. Within the host rock, pyrite grains exhibit two textures: a ubiquitous framboidal (<2 μm) texture, and a more rare massive texture with irregular grain boundaries (~10 μm). Framboidal pyrite is often found within calcite grains and seems to predate them. Pyrite with massive texture is very rare in the sparsely mineralized areas, although it has the same texture there as in more strongly mineralized areas. Pyrite in mineralized zones generally mantles galena and sphalerite and does not exclusively replace it (Figure 5.18 A). SEM images indicate a slight density zonation in this pyrite, forming colloform textures over the sphalerite or galena grains (Figure 5.19). Regions with massive pyrite textures have very little to no calcite and slightly fewer detrital grains than the host rock. The majority of areas with pyrite have no other sulfides in them. The sphalerite that is associated with these areas is generally much larger (ca. 100-500 μm), with relatively few smaller grains (ca. 50 μm). In many cases, pyrite appears to replace the sphalerite. This is based on the lobate shape of the grain boundary seen in association with sphalerite and galena but not in the host rock or massive pyrite zones. The massive galena grains seem to be aggressively replaced by pyrite, more extensively so than the sphalerite. EDS analyses detected arsenic within the massive pyrite, but not within the disseminated framboidal pyrite.

In some areas rhombohedral dolomites replace sphalerite and galena (Figure 5.20). These dolomites are not found in the host rock. There are also areas of late calcite growth. Late stage calcite shows cross-cutting relationships and the dissolution of sphalerite, galena, and pyrite. The calcite also seems to rip apart grains in jigsaw patterns; it is sometimes possible to identify grain pieces that have been divided across a small gap (20 μm) (Figure 5.21).

Barite is very common within mineralized areas and varies in texture and association. Some barite grains are small (ca. 10-50 μm) and are orientated along the same bands as the galena

(Figure 5.22). This could be due to either a replacement of banded galena or a co-precipitation with galena. The bands are too fine for micro drilling for sulfur analyses. The barite in one sample forms fans that appear to overprint all other sulfide phases (Figure 5.23). There are a few locations where individual blades of barite can be seen growing within pyrite (Figure 5.24). The barite does not seem to replace dolomite, and the blades terminate at contact points. In some slides significant dissolution of sulfides has occurred (Figure 5.23).

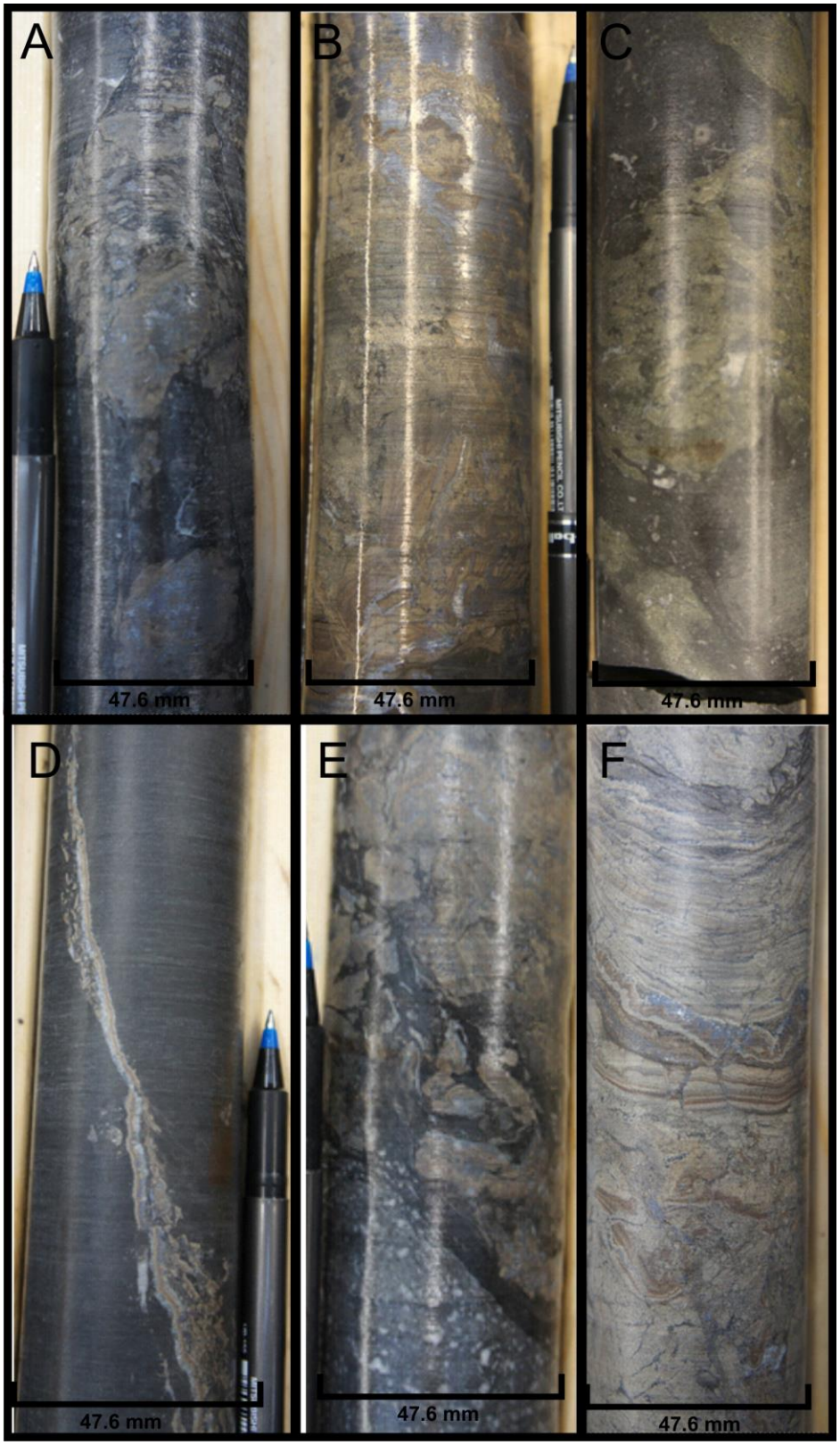

Figure 5.12. A range of mineralization textures from N02176 in the Pale Beds. (A) Massive Pb-Zn mineralization with pod-like textures surrounded by a black matrix. (B) Massive Pb-Zn mineralization. (C) Matrix-hosted massive Zn mineralization. (D) Ramifying vein of Pb and Zn cutting Pale Beds. (E) Massive Zn and Pb mineralization within a black matrix, showing disaggregation. (F) Massive layered Pb-Zn mineralization.

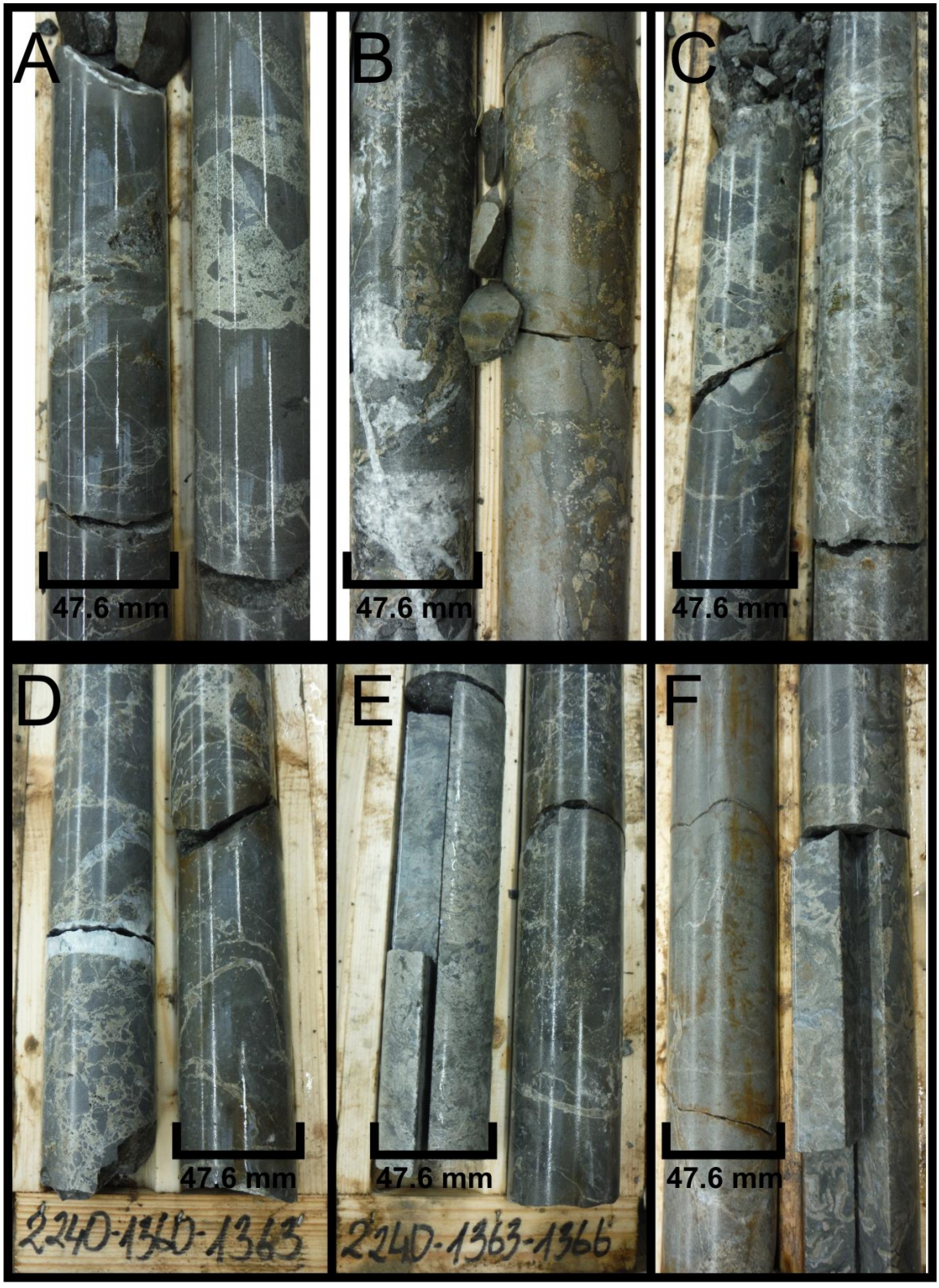

Figure 5.13. A range of mineralization textures from N02240 in the Pale Beds. (A) Brecciated Pale Beds with sphalerite in the matrix. (B) Pale Beds brecciated by black matrix, with sphalerite and pyrite in the matrix. (C) Brecciated Pale Beds with sphalerite and calcite. (D) Ramifying veinlets of sphalerite brecciating the Pale Beds. (E) Massive Pb-Zn mineralization. (F) Non-mineralized dolomite (left), and brecciated Pale Beds with sphalerite matrix (right).

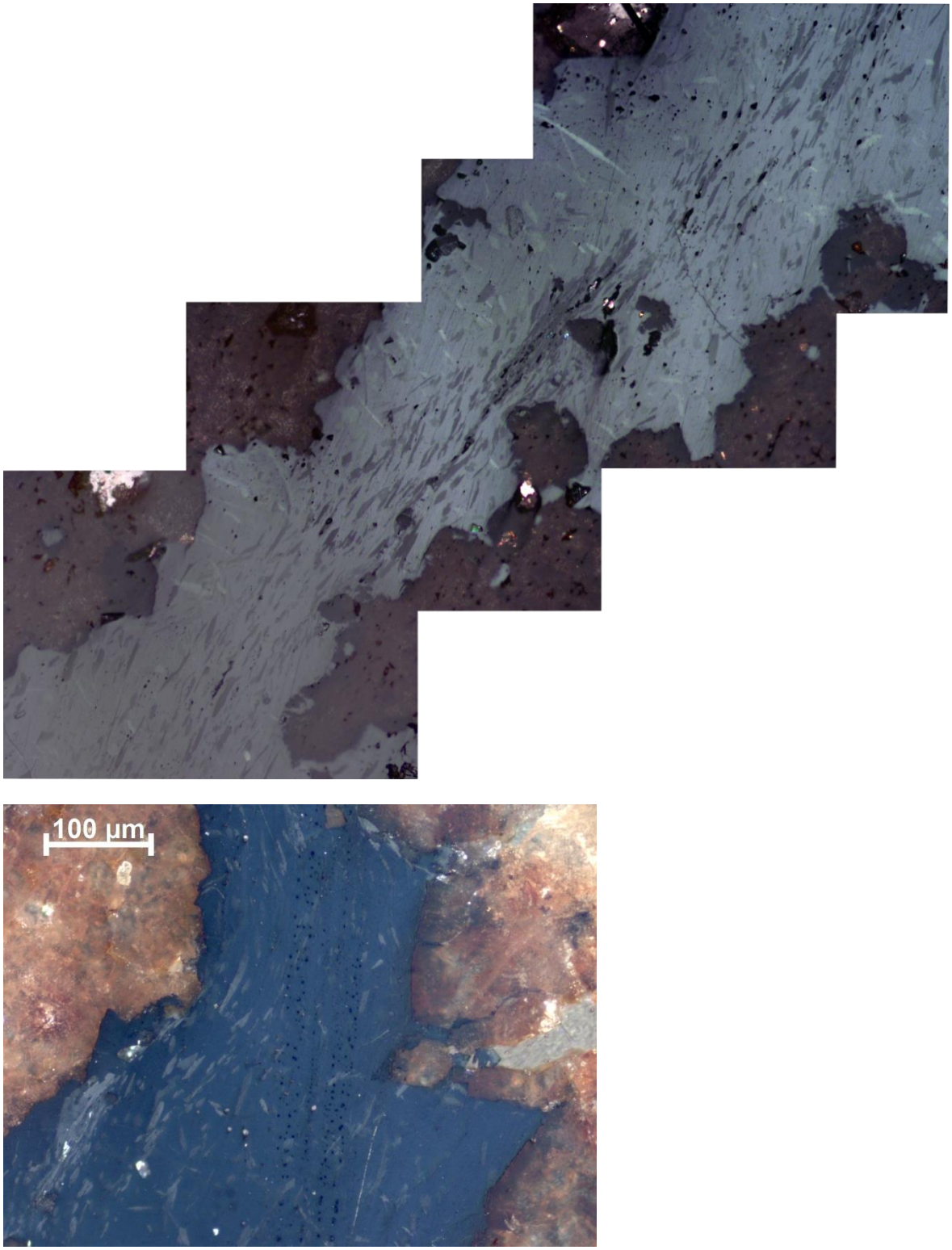

Figures 5.14. Top image shows an aggregated reflected light image of galena surrounded by sphalerite with aligned boulangerite inclusions. The lower figure shows a two-photon light image of galena with boulangerite inclusions and several fluid inclusion trails surrounded by sphalerite and barite.

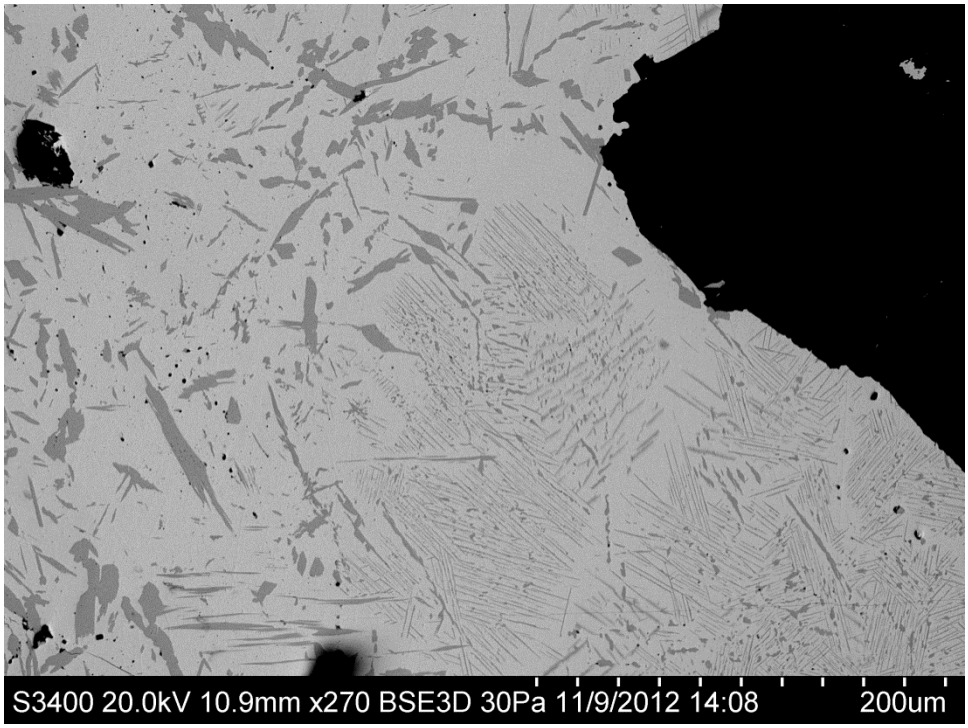

Figure 5.15. An SEM image showing galena with blades of boulangerite growing with preferred orientations in some areas (the lower right) and larger zones of boulangerite with no clear orientation in other areas (the upper left).

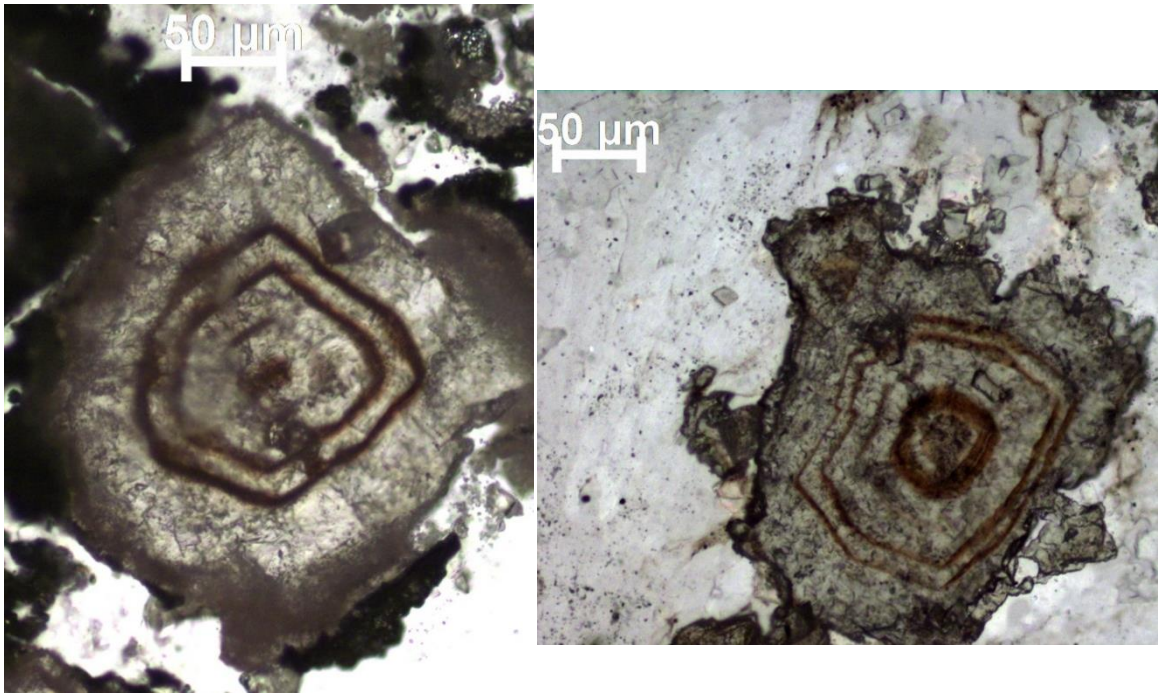

Figure 5.16. Sphalerite grains in transmitted and reflected light. Note similarities in the double dark band seen in the two distinct grains, found centimeters apart.

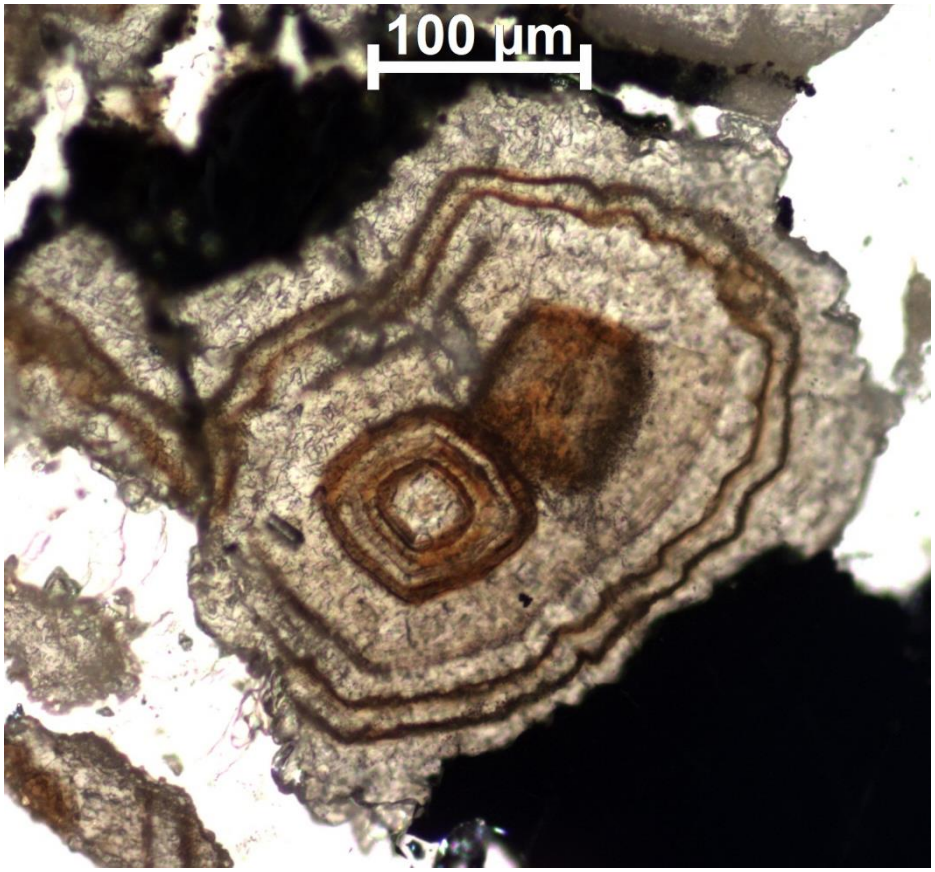

Figure 5.17. Two sphalerite grains growing into an aggregate grain. Note the left and right edges show calcite veining.

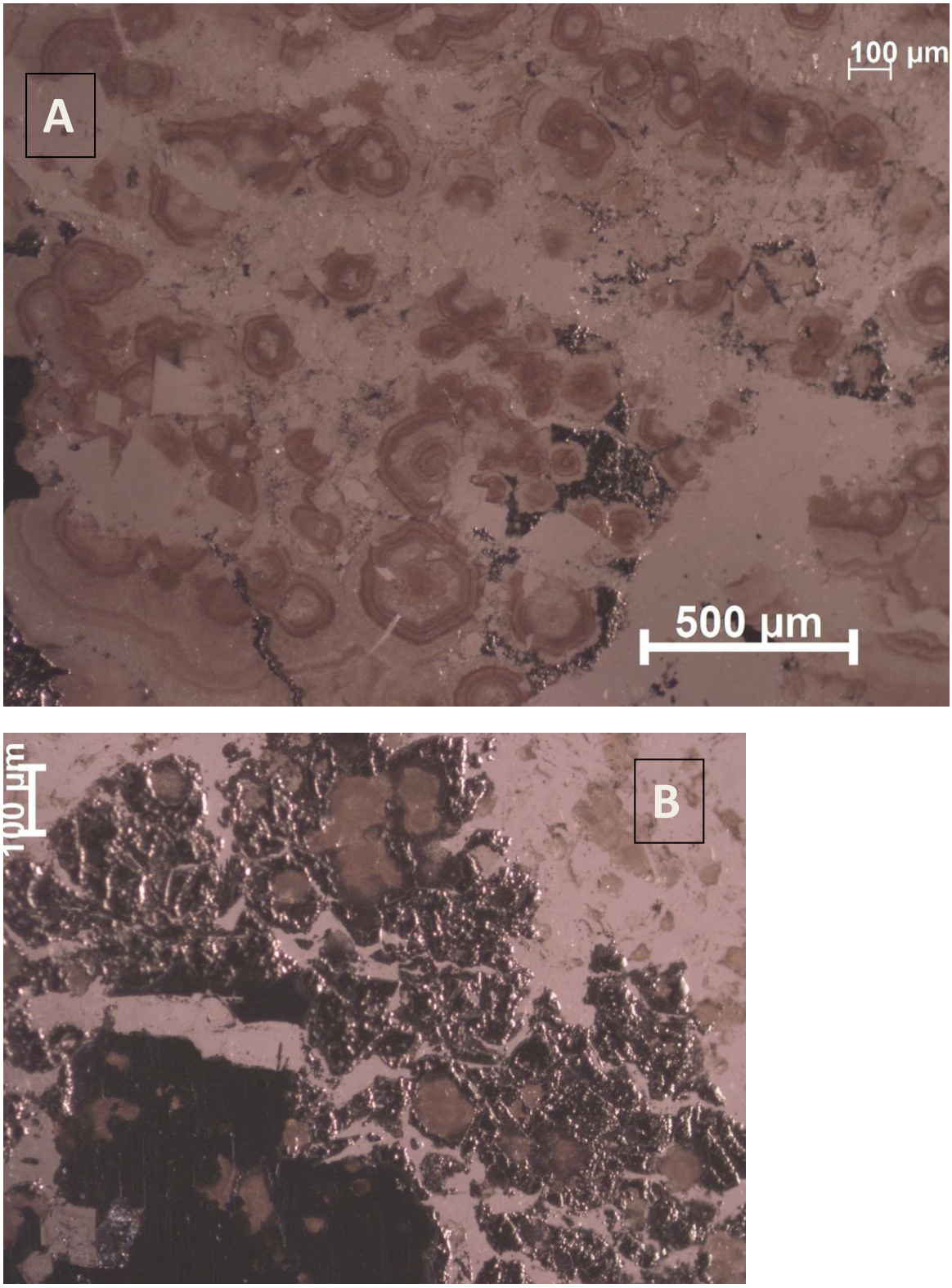

Figure 5.18. Reflected oblique lighting images, showing pyrite mantling galena and sphalerite. The sphalerite grains have similar color patterns and are being overgrown and replaced by calcite. The large dark galena grain at the bottom of B can be seen replacing sphalerite as well as being broken apart by calcite.

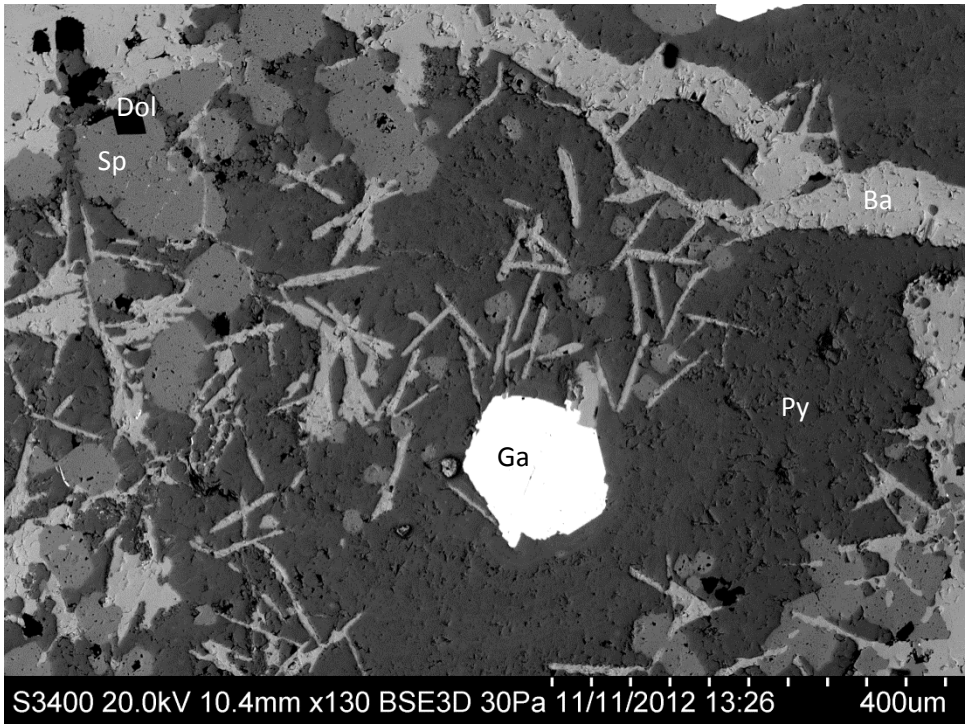

Figure 5.19. SEM image showing a galena grain surrounded by dark gray pyrite, with small lighter gray "balls" of sphalerite. The light gray blades are barite overgrowing pyrite and sphalerite, and the black masses are dolomite or silicates. There is subtle density zonation within the pyrite. Sp = sphalerite, Ga = galena, Py = pyrite, Ba = barite, Dol = dolomite.

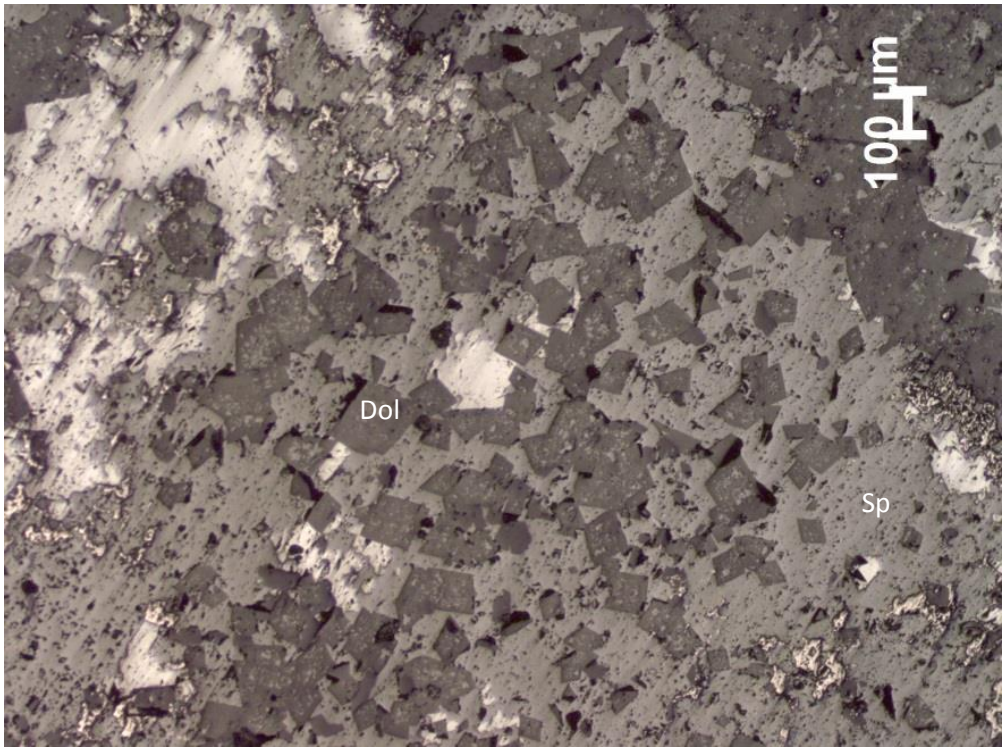

Figure 5.20. Dolomite crystals growing in replacement of sphalerite. Small inclusions of sphalerite remain within the dolomite. Dol=dolomite, Sp=sphalerite.

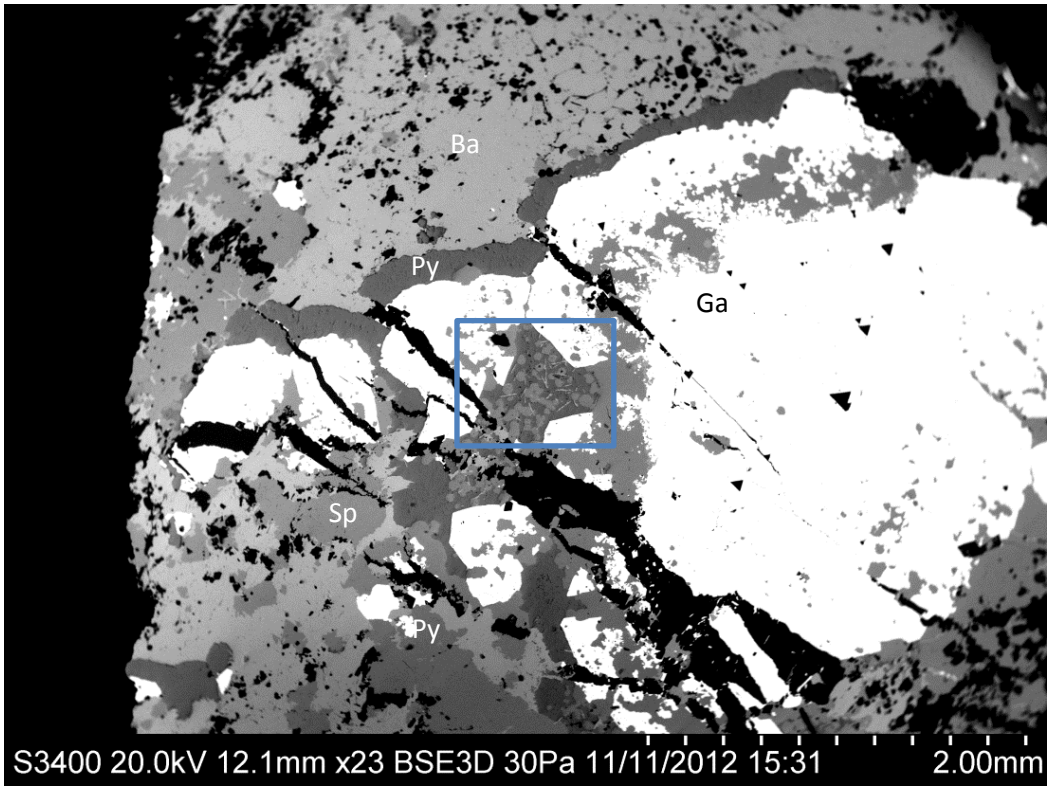

Figure 5.21. Large overview of a galena grain that is replacing sphalerite and being coated with pyrite and surrounded by barite. Note that the black calcite veins are later-stage but do not replace the barite. The blue box outlines the image shown in Figure 5.24. Py = pyrite, Ga = galena, Sp = sphalerite, Ba = barite.

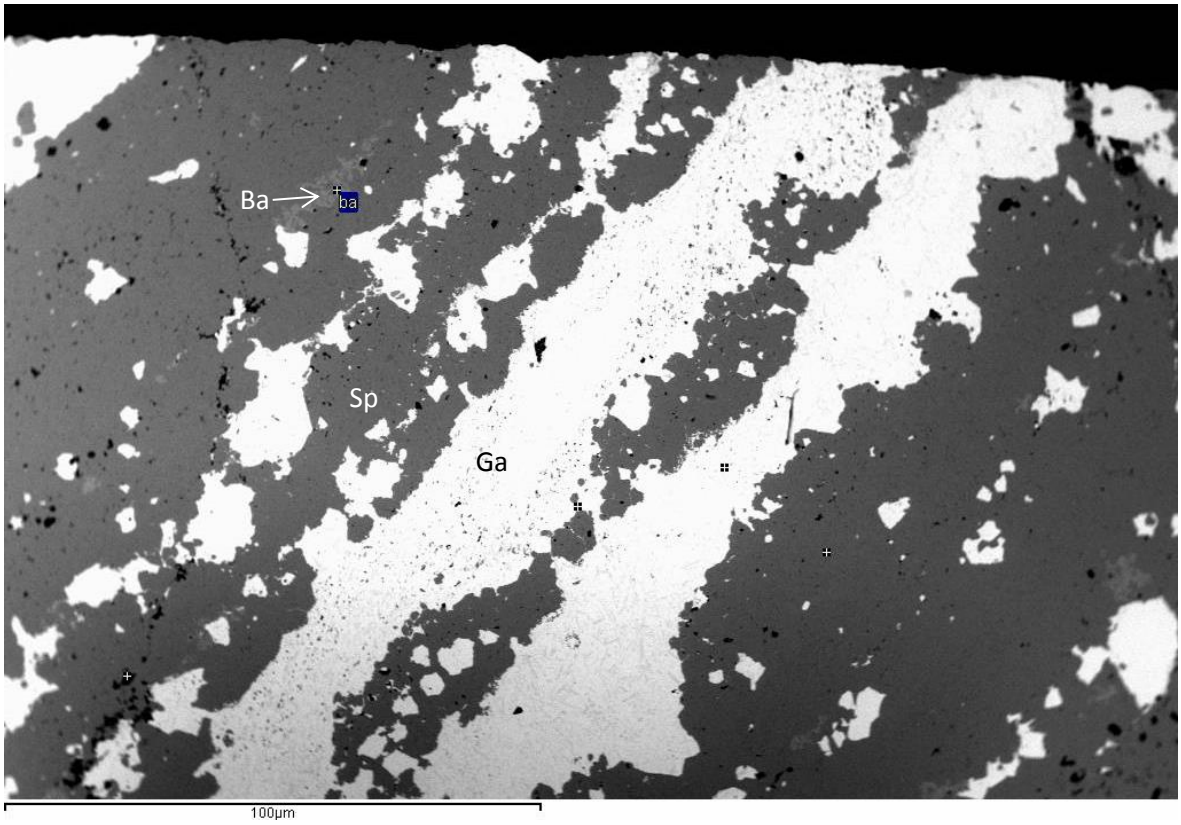

Figure 5.22. SEM image showing banded galena, sphalerite, and barite. Note the small barite bands that are oriented parallel to the larger bands of galena and sphalerite. Ba=barite, Sp=sphalerite, Ga=galena.

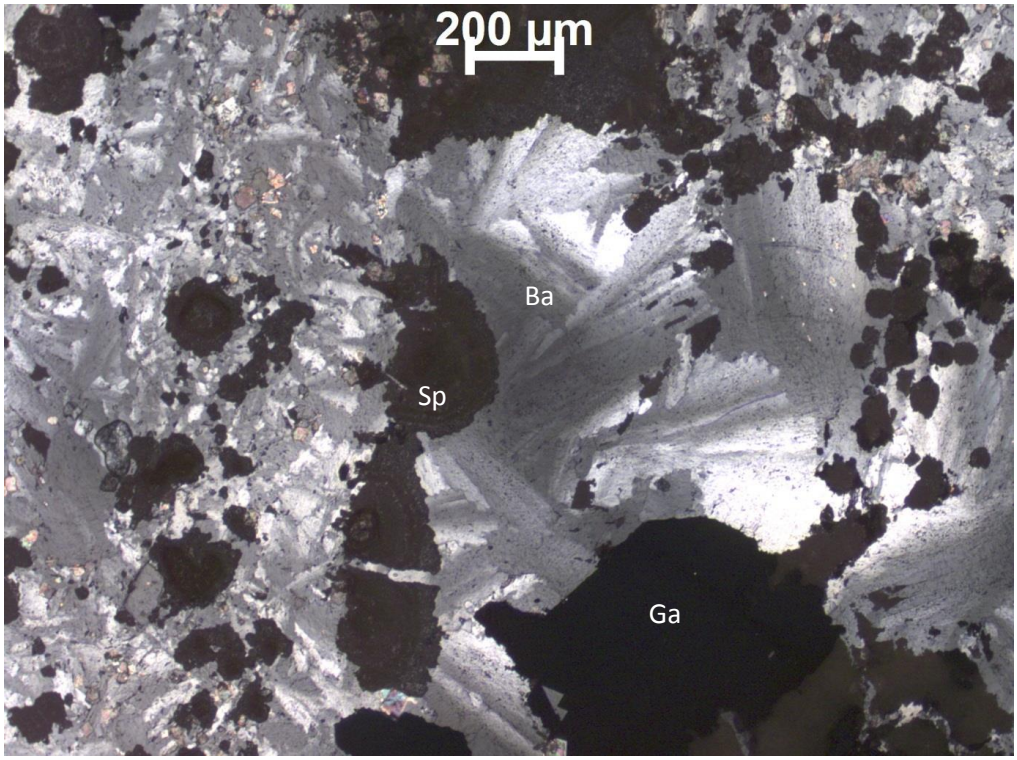

Figure 5.23. Barite shown in transmitted light growing over sphalerite and creating bladed aggregates. Note the large abundance of barite. Sp= sphalerite, Ga = galena, Ba = barite.

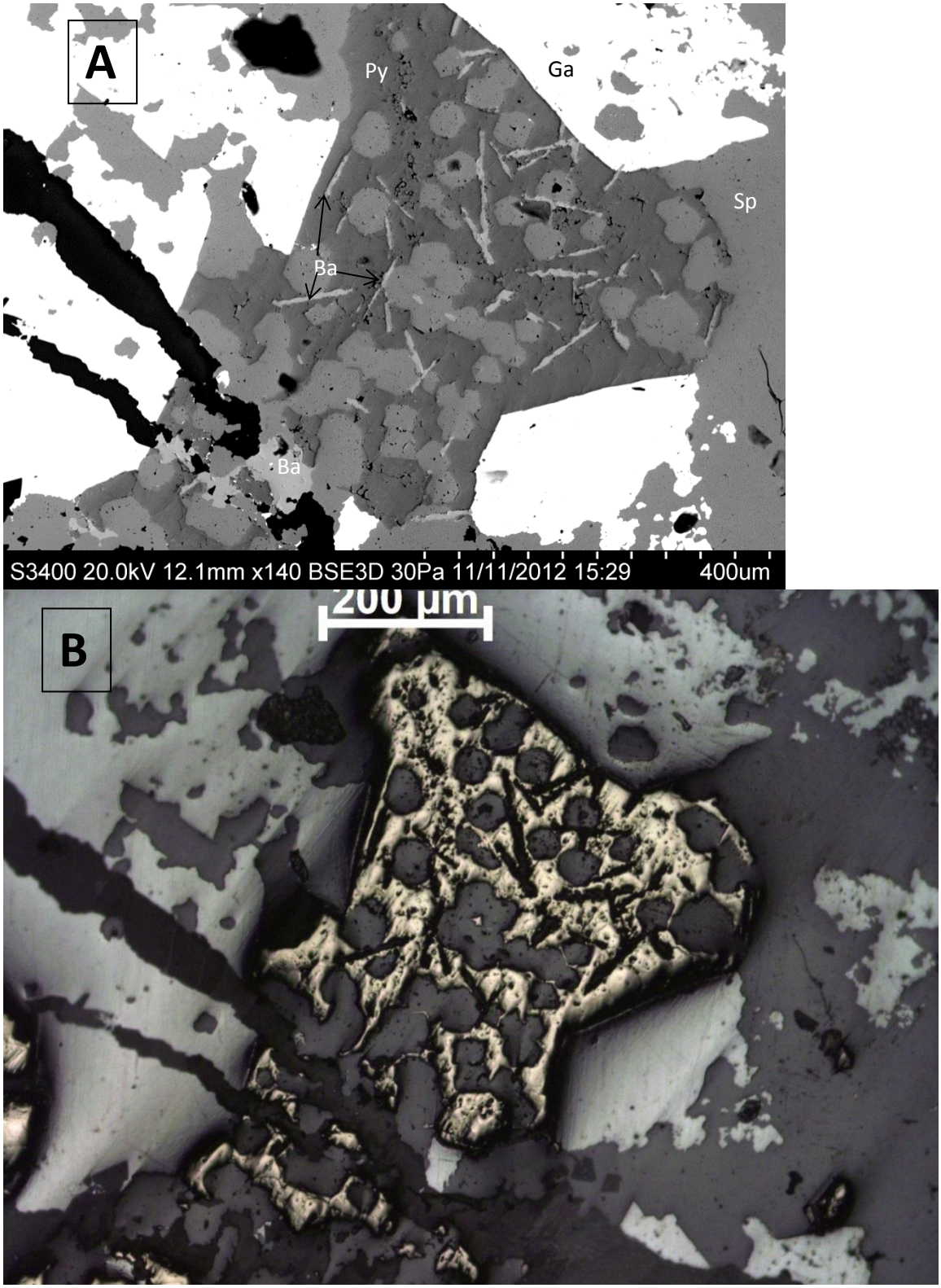

Figure 5.24. Enlarged images of the boxed area of Figure 5.21. (A) SEM image showing grains of sphalerite surrounded by pyrite and cut by blades of barite. Note that barite does not overprint sphalerite. (B) The equivalent reflected light image. Ba=barite, Sp=sphalerite, Py=pyrite, Ga=galena.

HoleID	N02240					HoleID	N02176				
Assay From	Assay To	wt. % Zn	wt. % Pb	wt. % Fe	Zn/Pb	Assay From	Assay To	wt. % Zn	wt. % Pb	wt. % Fe	Zn/Pb
1219.4m	1222.4	0.71	0.2	0.83	3.6	1286.6m	1288.1	0.21	0.03	3.57	0
1222.4	1225.4	0.77	0.08	0.37	0	1297.1	1298.6	0.09	0.01	2.33	0
1225.4	1228.4	0.4	0.05	0.1	0	1298.6	1299.9	0.23	0.04	4.13	0
1276.6	1279.6	0.12	0.05	1.11	0	1299.9	1301.6	0.38	0.08	4.32	0
1279.6	1282.6	0.46	0.05	0.79	0	1301.6	1304.3	0.15	0.03	4.55	0
1282.6	1285.6	0.17	0.05	0.85	0	1304.3	1306.1	0.17	0.07	4.69	0
1285.6	1288.6	0.16	0.05	0.95	0	1306.1	1307.3	0.12	0.02	2.76	0
1288.6	1291.6	0.21	0.05	1.03	0	1307.3	1309.1	0.26	0.08	5.05	0
1291.6	1294.6	0.27	0.05	1.06	0	1309.1	1310.7	0.26	0.03	5.33	0
1294.6	1297.7	0.35	0.05	0.88	0	1310.7	1312.1	0.25	0.1	5.26	2.5
1297.7	1300.7	0.35	0.05	0.82	0	1312.1	1313.6	0.02	0.01	2.53	0
1300.7	1303.7	0.23	0.05	1.12	0	1313.6	1315.1	0.12	0.04	3.86	0
1303.7	1306.7	0.57	0.05	1.32	0	1315.1	1316.6	0.13	0.04	3.79	0
1306.7	1309.7	0.23	0.05	0.85	0	1325.6	1327.1	0.22	0.03	3.7	0
1309.7	1312.7	0.25	0.05	1	0	1327.1	1328.6	0.17	0.05	2.84	0
1312.7	1315.7	0.44	0.05	0.83	0	1517.9	1519.4	0.11	0.05	1.09	0
1315.7	1318.7	1.06	0.2	1.47	5.3	1519.4	1520.9	0.05	0.05	0.74	0
1318.7	1321.7	1.43	0.19	1.07	7.5	1520.9	1521.9	0.05	0.05	1.08	0
1321.7	1324.7	4.51	1.23	3.49	3.7	1521.9	1523	0.09	0.05	1.01	0
1324.7	1327.8	6.25	1.72	3.31	3.6	1523	1524.5	4.45	1.52	1.3	2.9
1327.8	1329.3	5.99	1.19	4.54	5	1524.5	1526	3.65	0.79	0.91	4.6
1329.3	1330.8	7.36	1.08	7.15	6.8	1526	1527.6	1.3	0.3	0.66	4.3
1330.8	1332.3	7.2	1.89	10	3.8	1527.6	1529	6.62	4.12	1.69	1.6
1332.3	1333.8	4.75	1.41	6.31	3.4	1529	1530.6	10.74	3.91	1.85	2.7
1333.8	1335.3	8.78	2.37	6.78	3.7	1530.6	1532.1	1.88	1.4	1.12	1.3
1335.3	1336.8	4.52	1.16	3.39	3.9	1532.1	1533.6	1.75	0.63	1.3	2.8
1336.8	1338.3	2.82	0.95	2.84	3	1533.6	1534.9	0.5	0.05	1.26	0
1338.3	1339.8	8.55	0.6	3.58	14.3	1534.9	1535.9	8.19	2.12	1.63	3.9
1339.8	1341.3	5.57	2.41	4.51	2.3	1535.9	1537.4	11.11	5.12	1.65	2.2
1341.3	1342.8	7.24	1.32	6.07	5.5	1537.4	1539	33.52	4.44	1.11	7.5
1342.8	1344	2.74	0.52	3.64	5.3	1539	1540.5	39.98	9.41	0.79	4.2
1344	1345.8	10.28	2.21	9.5	4.7	1540.5	1542	30.02	12.83	1.31	2.3
1345.8	1348.8	5.38	0.96	3.58	5.6	1542	1543.5	0.69	0.05	0.73	0
1348.8	1350.3	3.67	0.76	1.25	4.8	1543.5	1545	2.72	1.03	1.19	2.6
1350.3	1352	16.73	1.12	2.59	14.9	1545	1546.5	3.73	0.07	1.07	0
1352	1354.8	9.47	1.65	5.6	5.7	1546.5	1548	0.59	0.05	0.77	0
1354.8	1356.3	9.61	2.08	3.53	4.6	1548	1549.5	3.34	0.27	1.21	12.4
1356.3	1357.8	13.3	1.58	5.33	8.4	1549.5	1551	10.37	2.09	2.13	5
1357.8	1359.3	9.02	0.88	2.84	10.3	1551	1552.5	19.94	3.46	5.45	5.8
1359.3	1360.9	12.46	2.85	5.46	4.4	1552.5	1554	8.09	0.89	4.25	9.1
1360.9	1362.4	26.36	6.39	4.73	4.1	1554	1555.5	10.07	3.63	5.46	2.8
1362.4	1363.9	5.2	0.75	1.04	6.9	1555.5	1557	2.72	0.62	2.08	4.4
1363.9	1365.4	4.89	1.19	2.66	4.1	1557	1558.5	1.15	0.05	1.44	0
1365.4	1366.9	5.66	2.54	4.9	2.2	1558.5	1559.5	1.57	0.05	1.51	0
1366.9	1368.4	4.04	0.68	2.45	5.9	1559.5	1560.5	1.07	0.42	1.07	2.5
1368.4	1369.9	4.07	1.1	3.65	3.7	1560.5	1562.4	0.11	0.05	1.09	0
1369.9	1371.4	6.22	1.59	2.51	3.9	1562.4	1563.3	0.13	0.05	1.09	0
1371.4	1372.9	15.28	2.42	8.23	6.3	1563.3	1564.6	0.5	0.05	0.89	0
1372.9	1374.4	9.97	1.69	6.33	5.9	1564.6	1566	0.05	0.05	1.77	0
1374.4	1375.9	5.84	1.73	9.16	3.4	1566	1567.5	0.14	0.05	1.28	0
1375.9	1377.4	9.55	2.44	11.4	3.9	1567.5	1569	0.31	0.05	1.24	0
1377.4	1378.9	7.59	1.77	8.54	4.3	1569	1570.5	0.05	0.05	1.53	0
1378.9	1380.4	17.64	2.69	5.4	6.6	1570.5	1571.6	0.05	0.05	1.71	0
1380.4	1381.9	12.14	2.86	8.86	4.2	1571.6	1572.8	1.47	0.5	3.04	2.9
1381.9	1383.4	6.25	1.94	7.32	3.2	1572.8	1574.1	0.32	0.05	1.84	0
1383.4	1384.9	6.11	1.21	5.66	5						
1384.9	1386.4	4.24	1.65	5.83	2.6						
1386.4	1387.9	5.41	1.9	6.2	2.8						
1387.9	1389.4	7.6	0.13	1.49	58.5						
1389.4	1390.9	3.03	0.33	1.19	9.2						
1390.9	1394	1.22	0.07	0.69	0						
1394	1397	0.67	0.05	0.72	0						
1397	1400	0.37	0.05	0.69	0						

Table 5.2. Assay data from N02240 and N02176. Note that N02176 contains significantly more Pb and has higher Pb/Zn values than N02240.

5.3.3 δ34S

Within the SWEXS, 51 samples from 8 separate holes were analyzed for $\delta^{34}S$ (Table 5.3). The data can be divided into three groups based on lithological units: the Thinly Bedded Unit (TBU), the Boulder Conglomerate (BC), and Pale Beds. Data are presented in Figure 5.25.

5.3.3.1 TBU

There are 13 TBU samples from six different holes (N02176, N02214, N02211, N02223, N02220 and N02234). The $\delta^{34}S$ data (Figure 5.25) ranged from -41.5 to -20.8‰, with one sample at 1.2‰.

5.3.3.2 BC

The four analyses of BC samples come from a single hole (N02237). The samples were drilled out of either mono-phase zones of mineralized clasts or areas of clasts with disseminated sulfides. The $\delta^{34}S$ values ranged from -9.7 to -0.4‰ (Figure 5.25). Two analyses come from two clasts < 5 mm apart. One clast contains disseminated sphalerite that decreases in abundance away from the contact with the black matrix. The second clast is composed of sphalerite floating in the black matrix. These two clasts yielded $\delta^{34}S$ values of -2.5‰ and -8.9‰, respectively.

5.3.3.3 Pale Beds

A large portion of data (n=22) comes from 4 thick sections from the highly mineralized N02176 Pale Beds mineralization. The other 11 Pale Beds analyses are from another 4 thick sections from the highly mineralized hole N02240. All Pale Beds samples except one (N02176, 1446m) were analyzed by laser combustion.

Iron sulfides yielded a large range in $\delta^{34}S$, from -7.7 to -23.7‰, with one sample at 21.7‰. The majority of data is very light and clusters around -20‰. The single sample of pyrite at -7.7‰ is from sample N02176, 1525.8m, and is within 2-3‰ of associated mono sulfides. The

isotopically heaviest sample, 21.7‰, comes from a vein of marcasite near the contact with the Boulder Conglomerate in N02176, 1446m.

Galena and sphalerite data from the Pale Beds yield the classic bimodal trend evident in the main Navan orebody (Anderson et al., 1998, Blakeman et al., 2002, Fallick et al., 2001). The mineralization in N02176 is relatively coarse-grained (20 mm), and there are more isotopically heavy analyses than elsewhere in the SWEXS. The few light analyses in N02176 are all from sample 1525.8m, which is from a less mineralized area with finer-grained textures. Analyses from N02240 also show lighter signatures.

Drill hole section	Sample type	Lithology	$\delta^{34}S$	Laser/Conventional	Comments
N02176 1540.6m	PbS	PB	15.8	L	Core large bleb
N02176 1540.6m	ZnS	PB	7.4	L	Sp in center of Ga bleb
N02176 1540.6m	ZnS	PB	15.4	L	Sp in banded layer
N02176 1572.1m	FeS2	PB	-16.7	L	Massive Py
N02176 1572.1m	FeS2	PB	-19.6	L	Diffuse Py
N02176 1540.6m	PbS	PB	6.3	L	Rim large bleb
N02176 1540.6m	PbS	PB	10.1	L	Banded Ga
N02176 1540.6m	ZnS	PB	9.9	L	Banded Sp
N02176 1540.6m	PbS	PB	14.2	L	Vein
N02176 1540.6m	PbS	PB	5.1	L	Blebs of Ga
N02176 1540.6m	ZnS	PB	13.7	L	Light colored Sp
N02176 1540.6m	ZnS	PB	13.9	L	Dark colored Sp
N02176 1540.6m	PbS	PB	4.4	L	Bleb of Ga
N02176 1540.6m	FeS2	PB	-23.7	L	
N02176 1555.4m	FeS2	PB	-17.0	L	
N02176 1555.4m	ZnS	PB	10.1	L	Bleb
N02176 1555.4m	ZnS	PB	12.1	L	Dark colored
N02176 1555.4m	ZnS	PB	9.0	L	
N02176 1572.1m	FeS2	PB	-17.6	L	Large Banded
N02176 1525.8	FeS2	PB	-7.7	L	
N02176 1525.8	PbS	PB	-9.3	L	Bleb of Ga
N02176 1525.8	ZnS	PB	-10.2	L	
N02176 1446m	FeS2	PB	21.7	C	Marcasite near UDL contact
N02240 1333.2m	FeS2	PB	-19.0	L	
N02240 1333.2m	PbS	PB	-11.8	L	
N02240 1333.2m	ZnS	PB	8.8	L	
N02240 1363.2m	FeS2	PB	-18.9	L	
N02240 1363.2m	PbS	PB	-14.3	L	
N02240 1363.2m	ZnS	PB	-9.8	L	
N02240 1374m	FeS2	PB	-18.1	L	
N02240 1374m	PbS	PB	3.9	L	
N02240 1374m	ZnS	PB	13.9	L	
N02240 1399.9m	PbS	PB	-11.6	L	
N02240 1399.9m	ZnS	PB	-16.6	L	
N02176	FeS2	TBU	-22.1	C	TBU band 1
N02176	FeS2	TBU	-20.8	C	TBU band 1 repeat
N02176	FeS2	TBU	-26.6	C	TBU band 2
N02214 1289.5 b1	FeS2	TBU	-42.1	C	
N02214 1289.5 t1	FeS2	TBU	-41.5	C	
N02214 1266	FeS2	TBU	-26.0	C	
N02214 1336	FeS2	TBU	-33.0	C	Whole rock Py
N02211 999	FeS2	TBU	-37.6	C	Whole rock Py
N02223 1619.1 #1	FeS2	TBU	1.2	C	Thicker (1mm) band of coarser Py 1mm TBU
N02223 1492.2 #1	FeS2	TBU	-31.1	C	Layered Py
N02223 1455.5	FeS2	TBU	-34.0	C	Thin Py layer (< mm) in TBU
N02234 1679 #1	FeS2	TBU	-24.6	C	Bedding parallel Sp in TBU
N02220 1439	FeS2	TBU	-28.4	C	Massive Py
N02234 1679 #1	ZnS	TBU	-24.6	C	Layered Sp
N02237 1766.9	ZnS	BC	-0.4	C	Small Sp clast in BM next to PB clasts in BC
N02237 1779.9 #1	ZnS	BC	-2.5	C	Disseminated Sp in rim of carb clast in BC
N02237 1779.9 #2	ZnS	BC	-8.9	C	Massive min in Sp clast in BC
N02237 1796.3	ZnS	BC	-9.7	C	Layered Sp in massive min clast in BC

Table 5.3. List of $\delta^{34}S$ analyses from SWEXS. Ga=galena, Sp=sphalerite, Py=pyrite, BC=Boulder Conglomerate, TBU=Thinly Bedded Unit, PB=Pale Beds, BM=black matrix, WR=whole rock, L=laser, C=conventional. All data are corrected to Canyon Diablo Troilite.

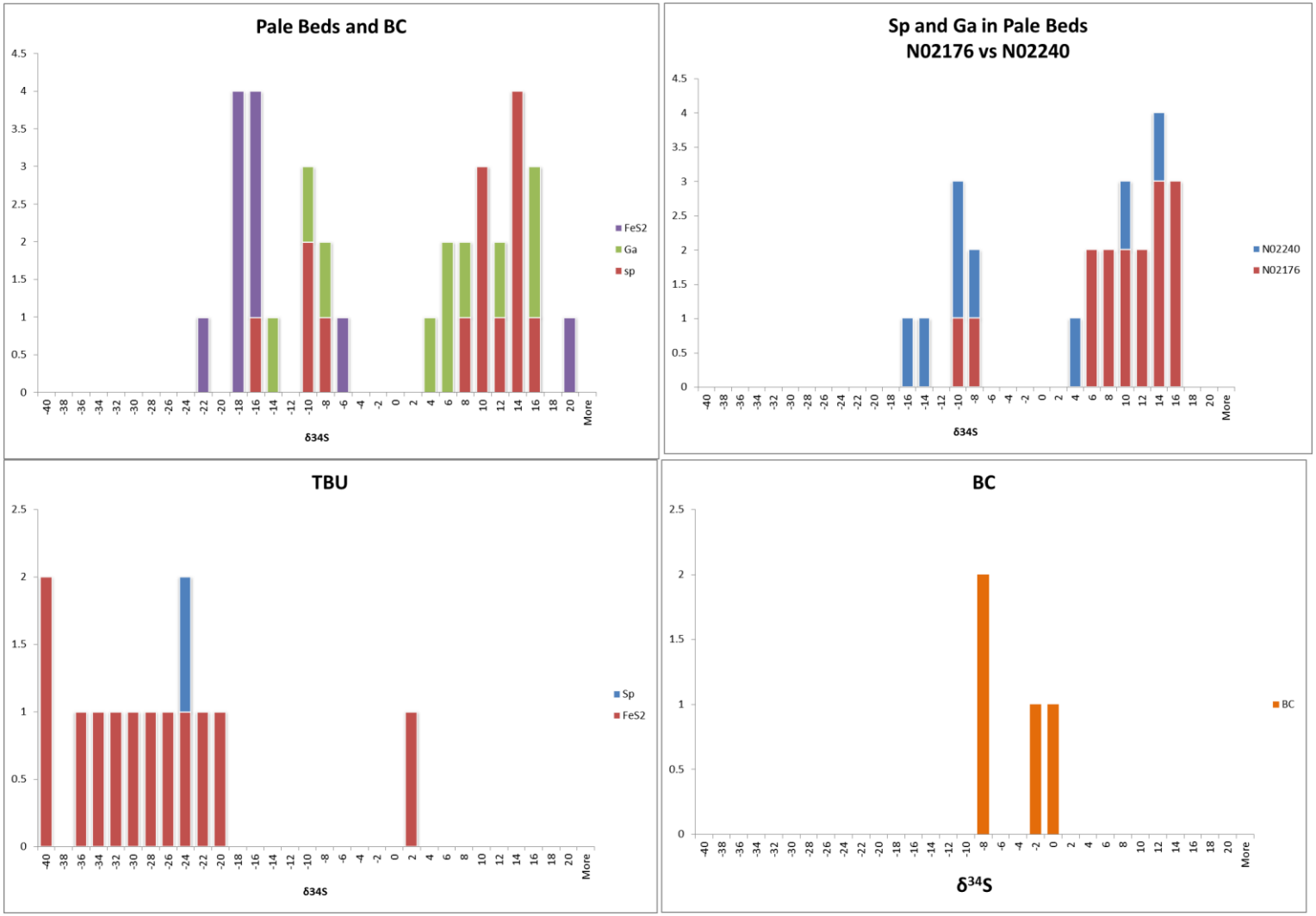

Figure 5.25. Histogram showing $\delta^{34}S$ for sulfides from each lithological group. The Pale Beds and BC histogram shows a bimodal distribution for galena and sphalerite. N02176 and N02240 show similar patterns, although N02176 is more dominated by heavy values. The TBU is dominated by light values that vary between -40 and -20‰. The single heavy value at 1‰ is from a sample with a distinctly coarse texture. The BC samples yield typically light values as seen in the main mine, as well as values of ca. 0‰ as noted by previous studies (Ford, 1996).

5.4 Discussion

5.4.1 Structure

The structural setting of the SWEXS area is only partly understood pending the completion of additional drilling. The seismic data coupled with the drilling in the E-Fault Horst area give a clear picture of the geometry between the UDL and the Lower Paleozoics (Figures 5.2 and 5.6). Determining the nature of this contact (e.g. erosional or faulted), however, is difficult. In the erosional model, the top of the horst would be deeply eroded, removing all of the Pale Beds and overlying stratigraphy, and the resulting contact would have UDL, BC or other allochthonous units above it. In the faulting model, a low angle listric fault would form the contact and have detached overlying lithologies. Results from current drilling cannot distinguish between these two models.

The Pale Beds Trough area is the most complicated area with respect to both drilling and seismic profiles. The variation of the removal of large portions of the Pale Beds stratigraphy within the area implies a complex mixture of normal or listric faulting that created drastic thickness changes in a small area (ca 200 X 200m). The repetition of the Muddy Limestone and Laminated Beds at the base of hole N02195 implies some degree of reverse faulting in order to repeat the stratigraphy (Figure 5.3). The change in the assumed Lower Paleozoic contact from south to north is very steep and difficult to explain. It is possible that this entire area is a rafted piece of Carboniferous section that is resting on the edge of the Basin Margin, analogous to the Shaley Pales in the Shaley Pales Trough (Chapter 2.3.3). This could explain the dramatic lithological variations seen in such a small area and would suggest that mineralization found in the area may not be laterally extensive.

The structure within the Terrace area is relatively simple. In the western part of the Terrace, the Upper Dark Limestone and Boulder Conglomerate can be matched from hole to hole while the Pale Beds, Muddy Limestone, and Lower Paleozoics show a continuous

thickness. This suggests that the Terrace area is a continuous unit and that the top of the carbonate lithology, down to the Pale Beds, has been removed by the Chadian erosional event with the basin filling conformably across it. The eastern end of the Terrace has a deeper Pale Beds contact, with thicker Boulder Conglomerate sections above (Figure 5.4). The similar thickness of Pale Beds, along with evident loss and doubling of the Muddy Limestone and Laminated Beds, suggests that the lower contact has been faulted. This faulting is likely listric in nature and caused by its proximity to the large fault that defines the Basin Margin.

The drill holes in the Basin Margin area have not penetrated though the basin fill and thus give a very incomplete and simplistic view of the area. They simply show the area as a deep basin that is filled by Upper Dark Limestone with inter-fingered Boulder Conglomerate and occasional Shaley Pales. The seismic data yield a larger-scale view of the area and suggest that the basin deepens quickly to the east and less quickly to the south (Figure 5.6).

5.4.2 Mineralization

5.4.2.1 Unit-Based Interpretation

The texture (framboidal) and bedding-parallel nature of the pyrite and sphalerite layers in the TBU suggest that they were synsedimentary (Figure 5.7). The coexistence and correlation of Zn and Pb within the pyrite layers strongly suggest that the base metals precipitated together. For the pyrite and associated sphalerite and galena, this is commonly viewed as indicative of a SEDEX model for its generation. The light $\delta^{34}S$ values in the TBU for all but the coarse recrystallized sulfides suggest that the exhaling fluids mixed with a bacteriogenic brine to create the sulfides, which then flocculated to the sea floor. This layered nature suggests a pulsing hydrothermal fluid and/or an intermittent sediment supply, or likely both. The more massive sections of pyrite represent either long periods of starved sediment supply or large amounts of vented fluid. The venting fluid is likely the

same hydrothermal fluid that is responsible for the creation of Pale Beds Ore. The timing of this fluid event can only be constrained by the host rock and any earlier venting would have been removed by erosional events. The location of the hydrothermal vent is currently unconstrained and could be local or as far as several km distant.

The Boulder Conglomerate mineralization lacks massive amounts of pyrite, which distinguishes it from CGO in the SWEX and the main ore body. The large mineralized clasts have many similarities with main mine Pale Beds ore in texture, $\delta^{34}S$ and mineral composition. The massive pyrite in the BC likely formed in situ during periods of quiescence between debris flows, and was not transported as clasts within the flow, based on similarities to pyrite found within the TBU. These clasts were likely sourced from the NW and were mineralized prior to incorporation within the Boulder Conglomerate. The sulfides found within the Boulder Conglomerate matrix and rimming clasts of unmineralized Pale Beds have two potential sources. The first potential source is the dissolution and remobilization of sulfides and metals after deposition of the Boulder Conglomerate. The loss of sulfur during the processes of dissolution and reprecipitation could explain the odd (ca. 0‰) $\delta^{34}S$ values that are atypical of the bimodal distribution found at Navan (Figure 5.25). However similar $\delta^{34}S$ values are known to occur within the Boulder Conglomerate above the main mine and some late-stage Pale Beds sulfides and these numbers could represent this same unknown process (Anderson, 1990, Ford, 1996). The second potential source is a hydrothermal fluid moving through the Boulder Conglomerate after its deposition, a feature of CGO in the main mine (Ford, 1996).

Mineralization within the SWEXS Pale Beds is similar to that found at the main mine and SWEX. The bimodal distribution in sulfur isotopes from the Pale Beds (Figure 5.25) suggests that the same processes of fluid mixing that are at work within the main mine are also present in the SWEXS. The difference in sulfur isotopes seen in between the Terrace and the Pale Beds Trough (Figure 5.25) could be explained by sample bias and the propensity to analyze textures related to heavy $\delta^{34}S$ that has been recognized for some time

(Anderson, 1990, Fallick et al., 2001). It has been shown that hydrothermal sulfur dominates the immediate feeder fault areas in the main mine, suggesting that N02176 is near such a structure (Blakeman et al., 2002). The samples analyzed from N02240 suggest more mixing with the sulfur-rich fluid while still containing the hydrothermal signature of feeder-proximal areas. This implies that each area has a distinct feeder source while showing variable mixing with the surface fluid. The similarities with respect to host lithology, grade, textures, and $\delta^{34}S$ values between the SWEXS and the main mine lend credence to the idea that the SWEXS may contain significant quantities of mineralization.

5.4.2.2 Regional Interpretation

The Pale Beds Trough area, as seen in N02176 and associated holes, yields evidence for three phases of fluid inclusions as well as halite crystals that indicates that boiling fluid was present during their formation (Treloar, 2014). The average fluid inclusion temperature in the Navan area is 120-130 °C, with a maximum of 175 °C (Wilkinson, 2010). Treloar (2014) reported that the liquid-rich fluid inclusion data from the SWEXS is ca. 173-184 °C, which is significantly higher temperature than the main mine. The large quantities of visible Sb sulfosalts and high temperature fluid inclusion data reported by Treloar (2014) point to the likelihood that Pale Beds Trough represents a high temperature feeder vent area. The abundance of heavy $\delta^{34}S$ values in sulfides reported here is consistent with this interpretation.

In the Terrace area, the majority of the few samples taken from N02240 yield light $\delta^{34}S$ values with an average of -15.0 ±3.6‰. These light values are similar to the mine-average $\delta^{34}S$, -13.6 ± 2‰ (Fallick et al., 2001), indicating similar dominance of bacteriogenically-derived sulfide occurred within this area. (The occurrence of some hydrothermal signatures here (at 1374 m), is echoed in the data of Blakeman et al. (2002), where minor, largely clast-centered hydrothermal signatures can be found in areas of otherwise bacteriogenic S dominance.) The difference between the textures, sulfur isotope values, and metal ratios in N02176 and N02240 is consistent with the idea that this Terrace area contains more distal

ore, whereas the Pale Beds Trough contains indications of a hydrothermal feeder. Proximity to feeder areas could be further tested for using a bulk sulfur isotope approach (Fallick et al., 2001). Future work should include taking the pulps of drill core after assay, and leaching for acid volatile sulfides, thus providing a whole rock sulfide "sample". This would yield a $\delta^{34}S$ that would represent the bulk mixing of mono-sulfides (ZnS and PbS) and could be used to quantifiably indicate feeder areas. It is tempting to genetically link the Terrace and the Pale Beds Trough ores as distal ore and feeder, respectively, in the same system. However, it must be recognized that (1) they are separated by nearly 1 km of unexplored space and (2) there is apparent structural complexity which raises doubt as to contiguity, for example, the structures along SE flank of the mine are known to have large strike slip movements (km-scale), which could bring distinct areas together long after mineralization occurred.

The thick units of TBU and Boulder Conglomerate, as well as Shaley Pales found in the Basin Margin suggest that faulting in this area has removed the pre-rift Carboniferous section. The top of the Lower Paleozoics interpreted from the seismic lines shows that all holes stop far above the basement contact and thus a large amount of basin fill is still undrilled (Figure 5.6). The existence of mineralized Pale Beds clasts in the BC and layered pyrite and sphalerite in the TBU indicates that mineralization must have occurred before the filling of the basin and must have been ongoing at the time of deposition.

A single hole, N02223 within the Basin Margin area has intersected siderite for the first time in the Navan area. Siderite is found in Silvermines in the south of Ireland and there it is associated with deep-water areas between the Waulsortian Mud banks. The siderite there is found below the more pervasive pyrite that continues into shallow-water areas (Taylor, 1984). N02223 represents some of the deepest drilling in the Navan area and the siderite could also have formed from hydrothermal fluids, as it is thought to have at Silvermines, because it is stable near the pyrite-hematite transition (Cooke et al., 2000). However this first identification of siderite in the Navan area is coincident with the rare intersection of

methane gas below the siderite, suggesting a possible correlation. Siderite can be formed in early digenesis, by replacement of sulfides or by methanogens overlying a source of hydrocarbons (Curtis et al., 1986, Raiswell, 1987, Raiswell and Fisher, 2000). Siderite nodules are also often found above coal measures. The $\delta^{18}O$ and $\delta^{13}C$ data of the siderite yield no conclusive evidence for geologic setting, as they fall within both continental and marine environment fields (Mozley and Wersin, 1992); a greater variation in C isotopes from future work may strengthen the methanogenesis link (Raiswell and Fisher, 2000). The $\delta^{18}O$ value does indicate that it was in equilibrium with sea water at <50°C and therefore early in the diagenetic history of the rocks. Understanding the relationship of siderite to pyrite and the source and timing of the methane will provide further insight into siderite formation.

5.4.3 Relationship of SWEXS to the main mine and SWEX

The mineralization in the SWEXS is very similar to that in the main mine and SWEX. The mineralization is predominately Pale Beds-hosted and is dominated by sphalerite and galena with very little gangue mineralization. Textures in the SWEXS are more dominated by breccias than those in the main mine, but they are not dissimilar to the 'close-packed conglomerates' of the main mine. The existence of mineralized BC clasts and pyrite within the UDL has long been known, and the examples found in the SWEXS are more extreme but consistent. The proximity of the highly mineralized area (N02240) to the Erosion Surface is consistent with mineralization patterns in both the main mine and the SWEX (see Chapter 2). The $\delta^{34}S$ values for sulfides are within the range of those found in the main mine, suggesting similar mechanisms are at play.

5.5 Potential and development of the SWEXS

The SWEXS is a new area of mineralization within the near-mine area which offers considerable prospectivity. It has pronounced similarity to the main mine and SWEX in

terms of mineralogy, ore grades, intersections, ore texture, lithological disposition, and S isotopes, and thus offers hope for future economic exploitation.

The area is positioned along the edge of the steep slopes and large increases in the depth of the basin. The nature of the formation and location of the SWEXS, and what created its structural complexity, are only just being revealed. Of particular importance to its potential as an economic deposit is the lateral contiguity of the Pale Beds. Two theories, one involving large allochthonous slide blocks (Figure 5.26) and the other a remnant Terrace that has experienced reverse faulting, are being considered as drilling to the north of the existing NW-SE section is undertaken. The massive amounts of layered pyrite (with micro sphalerite and galena grains), and the existence of layered sphalerite, show that the mineralizing fluid was exhaled into the sea during the Chadian extensional event during the basin-filling deposition of the UDL. The timing of the Pale Beds mineralization within the Boulder Conglomerate largely predates the deposition of the Boulder Conglomerate, while the layered pyrite must have formed after the major faulting. The Pale Beds breccia-hosted mineralization has textures indicating a vertically flowing mineralizing fluid. Coupled with the high temperature fluid inclusions and evidence of boiling, this suggests a high temperature shallow emplacement of this mineralization. A genetic link between the in situ Pale Beds mineralization and that in the TBU is compelling, but the possibility of an earlier mineralization of the Pale Beds cannot be dismissed. The $\delta^{34}S$ in the TBU shows that extensive bacteriogenic isotopic fractionation of seawater sulfate to sulfide (60‰) was occurring within the sea at the time of venting. This suggests that microbial communities were living within the area of the SWEXS during formation. Thus the SWEXS shows more properties of a SedEx deposit than those of Mississippi Valley Type deposits. Differences between the SWEXS and the main mine are not sufficiently compelling to suggest a distinct genetic model of emplacement.

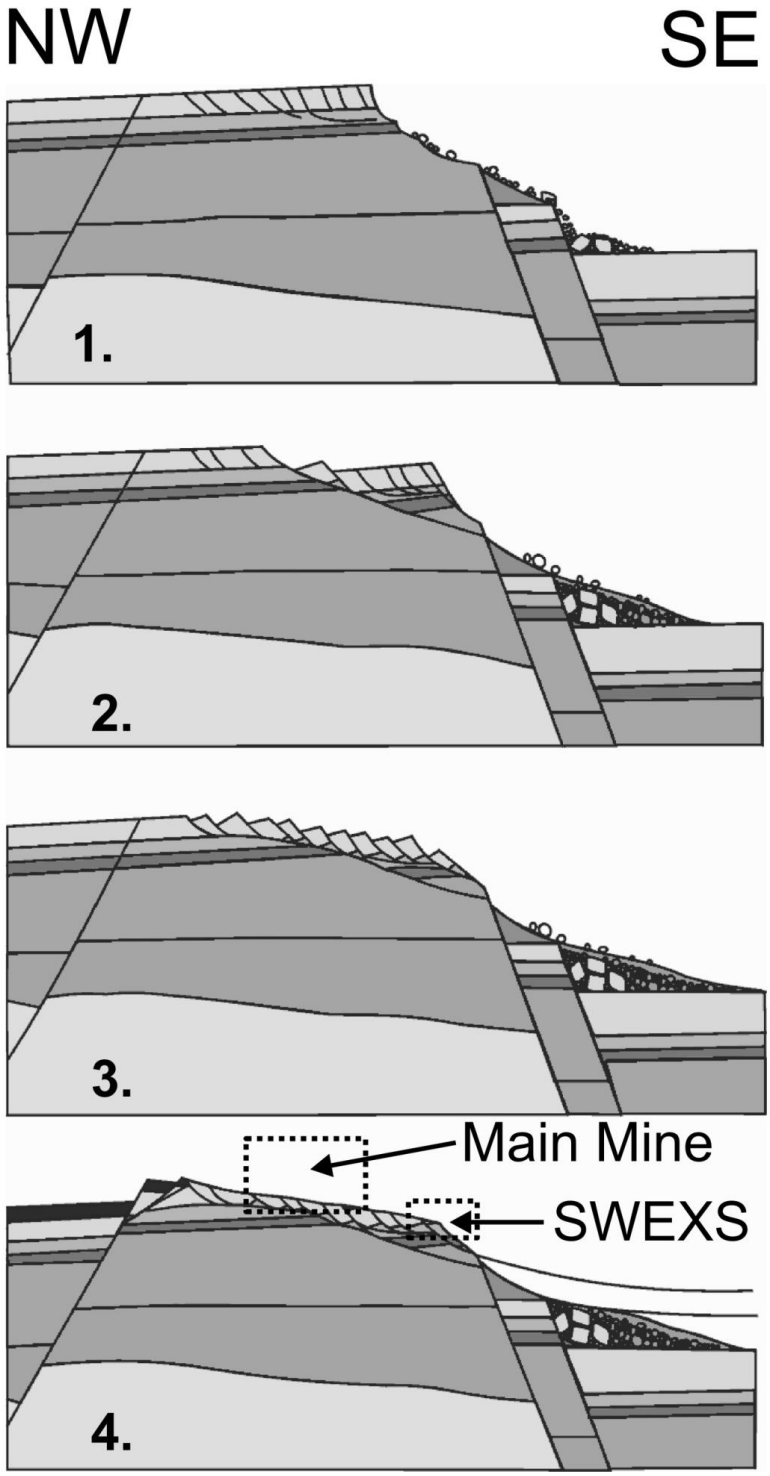

Figure 5.26. A schematic cross-section modified from Ashton et al. (in press) showing the large-scale footwall uplift and degradation that is thought to have occurred during the Chadian. Pane 1 shows the beginning of footwall collapse, with the talus pile to the right representing the Boulder Conglomerate in the undrilled deep basin. Panes 2 and 3 show the creation and progression of listric faulting and further erosion. In pane 4, the Erosion Surface has leveled the tops of the listric faults, creating a planar feature that represents the present-day BC-UDL contact with pre-rift Carboniferous or Lower Paleozoic rocks. Areas are highlighted that are thought to represent the main mine and the new SWEXS.

Chapter 6

Synthesis and Conclusions

6.1 Synthesis

My research into the Navan deposit has led to significantly improved understanding of its history and ore genesis. This chapter synthesizes petrography, geochemistry, noble gases, seismic visualization, and geochronology to elucidate the interactions of fluids with rocks within the Navan deposit.

6.2 A new vector for exploration

Knowledge of the precise location and migration mechanisms of hydrothermal fluid ingress that created the Navan deposit within the Pale Beds would improve drill targeting. By examining large-scale maps of metal concentrations and ratios, I have shown that the hydrothermal fluid escaped the basement and entered the Pale Beds in many locations rather than a single or limited number of points. My work shows that basement faulting does not solely control the ultimate disposition of base metal sulfides. Rather, the location of the most intense mineralization is controlled by the behavior of the fluids (both hydrothermal and sulfur-rich surface) within the Carboniferous lithologies. The presence of numerous basement sources suggests that many areas have similar potential for hydrothermal fluid influx and that exploration should focus on key locations that allow for fluid mixing and sulfur saturation in order to locate large sulfide accumulations.

The style of fluid flow within the Carboniferous lithology governs the types of likely fluid interactions that can occur and is critical in understanding the likelihood of different types of mineralization. The mineralization in the SW main mine has a distinct Pb/Zn ratio (ca 0.66) that moves laterally towards the NE, and is largely focused in the 5 Lens. Conversely, the majority of the north and east main mine (the most intense mineralization in the Navan area), and the entirety of the SWEX, were created by distinct vertical

conduits with a homogeneous Pb/Zn ratio (ca. 0.22). These two areas have different styles of mineralization that have different geometries and grades, and thus require different mining practices.

A key observation from my metal ratio study is that vertical fluid flow at Navan is concentrated in several areas that coincide with topographic lows developed by the Erosion Surface. The Boulder Conglomerate found within the lowest points of these basins is mineralized, while the Boulder Conglomerate found along the basin margins is non-mineralized. Intense Pale Beds mineralization is present in areas where the Erosion Surface has cut down to expose Pale Beds sediments, as noted by previous authors (Ashton et al., in press). By comparing maps of metal concentrations and the Erosion Surface, I have shown that lithologies as high as the Argillaceous Bioclastic Limestone (ABL) are important in understanding the geography of Pale Beds mineralization. For example, I have shown that the long puzzled-over N-striking decrease in 1-5 Lens Zn concentrations coincides with the boundary of non-eroded ABL. This Erosion Surface topographic control on Pale Beds ore indicates that fluid pore pressure focused the hydrothermal fluid to these areas and may also have provided a viable location for sulfide rich brines to pool. The preservation of CGO within these basins is likely due to both preservation and its location in a place where fluids were escaping the Pale Beds. This correlation between high-grade Pale Beds and Boulder Conglomerate mineralization, and valleys in the Erosion Surface, provides a simple exploration test that could lead to the discovery of further high-grade ore.

My research has revealed the existence of two main flow types at Navan: km-scale horizontal flow, and localized vertical flow. These two flow types create mineralization with different potentials for intersection by surface drilling. Large-scale lateral flow exhibits a larger plan map footprint, making an initial intersection by drilling more likely. However mineralized intersections will be thin, and assessing the scale and direction of fluid movement requires many drill holes. Mineralized areas dominated by vertical fluid

flow have a smaller plan map footprint and are thus more difficult to initially discover. However once located, these intersections offer the prospect of stacked lenses of intense mineralization. Understanding the structural and paleotopographic areas that foster vertical fluid flow delivers a new and significant vectoring tool for exploration.

6.3 Mantle Heat: the driving force for convection

Irish type deposits have long been known to be associated with extensional faults. However there has long been a debate over whether the metal-bearing hydrothermal fluids that created the ore bodies were sourced from topographic flow during Hercynian compression (Hitzman and Beaty, 1996) or from the basement during the Chadian extensional event (Russell, 1978).

By measuring $^{3}He/^{4}He$ trapped in fluid inclusions and obtaining an atmospheric-free, supra-crustal value, I have shown that a least some mantle melting occurred during ore genesis. Modern analogues show that mantle melting and high $^{3}He/^{4}He$ values are prevalent in extensional settings, but they are not present in topographically-loaded basins or compressional settings (Oxburgh et al., 1986). Therefore the hydrothermal ore fluids that created the Irish ore deposits must have been coeval with extension, and sulfide minerals containing the fluid inclusions did not grow during a compressional event. The quantity of trapped mantle ^{3}He varies within each deposit and between deposits, with Navan having the smallest mantle component. This work strongly suggests that the driving force for convection that created the Irish Orefield is mantle-derived heat, rather than topographic flow.

6.4 A new date for late Variscan compression in Ireland

The Navan ore deposit has been through a large-scale compressional event that has inverted the stratigraphy in certain areas, particularly in the NW. A syenite intrusion outcrops to the N of this area and has been proposed as a fluid conduit due to its highly

altered nature. In an attempt to constrain the timing of ore deposition, I have analyzed the $^{40}Ar/^{39}Ar$ systematics in feldspars from the Navan Syenite that display patch perthite textures. The data show a complex heating and fluid-rock interaction history. By applying argon diffusion modeling, I have shown that the last fluid heating event in the Navan syenite must have been higher temperature than the ore forming fluid. This work also places a maximum age constraint of 293 ± 3 Ma on this fluid. This places the fluid flow within the expected range of the end of the Variscan compressional event created by the Hercynian Orogeny. This is the first confirmation of a long-held belief that the basin inversion at Navan is related to the Variscan compressional event and produces the first radiogenic age constraint on the timing of this compression in the Irish Midlands.

6.5 Why is Navan a giant?

The reasons behind the size and location of the Navan deposit are fundamental questions for an exploration geologist. In my opinion, several factors combined to make Navan the giant ore body that it is.

1. The basement and source of metals for Navan and the Irish orefield are particularly rich. The basement is composed of volcanoclastic rocks created during subduction of oceanic crust below the continental margin. These rocks have seen little metamorphism during suturing, with Navan sitting on the suture, and thus the magmatic metals were still in place for leaching by a hydrothermal fluid.
2. The slow subsidence over the Carboniferous provided the creation of clean carbonates that provided chemical traps for sulfide-bearing fluids.
3. The paleolatitude during Chadian extension allowed for evaporation and the formation of brines.
4. The Chadian extensional event created crustal thinning that provided heat to drive hydrothermal convection of seawater.

5. Mantle heat thinned the crust and fostered the Chadian extensional event that drove the development of major hydrothermal convection cells.
6. The removal of lithological caps and the surface topography created by the Boulder Conglomerate erosion created three conditions: restricted areas for brines to pool; sulfate reducing bacteria to create sulfide; and focused areas of lower pore pressure. These three conditions created the ideal locations for the fluid mixing that created sulfur saturation and ultimately this giant Irish type deposit at Navan.

6.6 Conclusions

My work has improved our understanding of the fluid migration history of the Navan Orebody. The major findings of each chapter are listed here.

Chapter 2. Mineralization in the Navan area is controlled by faults and lithologies that focused fluids towards areas where clean carbonate lithologies intersected the paleoseawater interface.

Chapter 3. The presence of mantle He in Irish Orefield sulfides shows that these deposits were created in an extensional tectonic setting and involved the presence of mantle heat.

Chapter 4. The compressional event in the Irish Midlands is Variscan in age. This confirms a common assumption and provides the first radiogenic age for Variscan compression in the Irish Midlands.

Chapter 5. The recently discovered SWEXS has many similarities with the main Navan deposit and holds potential for future economic mineralization.

7 References

ALDRICH, L. T. & NIER, A. O. 1948. Argon 40 in potassium minerals. *Physical Review,* 74**,** 876.

ALTINOK, E. 2005. *Zn-Pb-Fe Mineralization Process, Evolution of Sea Water Oxidation State in a Restricted Basin, and Diagenesis of Deep Water Calcareous Sediments: Geochemical and Geological Study of the Navan Deposit, Dublin Basin, Ireland.* Ph. D., Colorado School of Mines.

ANDERSON, G. M. 1975. Precipitation of Mississippi Valley-type ores. *Economic Geology,* 70**,** 937-942.

ANDERSON, G. M. Some geochemical aspects of sulfide preciptation in carbonate rocks. *In:* G. KISVARSANYI, S. K. G., W. P. PRATT, J. W. KOENIG, ed. International Conference on Mississippi Valley Type Lead-Zinc Deposits, 1983. University of Missouri-Rolla, Rolla, Missouri 61–67.

ANDERSON, I. K. 1990. *Ore depositional processes in the formation of the Navan zinc/lead deposit, Co. Meath, Ireland.* Ph. D., The University of Strathclyde.

ANDERSON, I. K., ANDREW, C. J., ASHTON, J. H., BOYCE, A. J., CAULFIELD, J. B. D., FALLICK, A. E. & RUSSELL, M. J. 1989. Preliminary sulphur isotope data of diagenetic and vein sulphides in the Lower Palaeozoic strata of Ireland and southern Scotland: implications for Zn+ Pb+ Ba mineralization. *Journal of the Geological Society,* 146**,** 715-720.

ANDERSON, I. K., ASHTON, J. H., BOYCE, A. J., FALLICK, A. E. & RUSSELL, M. J. 1998. Ore depositional process in the Navan Zn-Pb deposit, Ireland. *Economic Geology,* 93**,** 535-563.

ANDREW, C. J. 1986. *The tectono-stratigraphic controls to mineralization in the Silvermines area, County Tipperary, Ireland,* Dublin, Irish Association for Economic Geology.

ANDREW, C. J. & ASHTON, J. H. 1982. Mineral textures; metal zoning and ore environment of the Navan orebody, Co. Meath, Ireland. *In:* BROWN, A. G. & PYNE, J. (eds.) *Mineral Exploration in Ireland. Progress and Development 1971-1981.* Irish Association for Economic Geology.

ANDREW, C. J. & ASHTON, J. H. 1985. Regional setting, geology and metal distribution patterns of Navan orebody, Ireland. *Institution of Mining and Metallurgy Transactions,* B94**,** 66-93.

ANDREWS, J. 1985. The isotopic composition of radiogenic helium and its use to study groundwater movement in confined aquifers. *Chemical Geology,* 49**,** 339-351.

ANDREWS, J. N. & KAY, R. L. F. 1982. Natural production of tritium in permeable rocks. *Nature,* 298**,** 361-363.

ASHTON, J. H., BLACK, A., GERAGHTY, J., HOLDSTOCK, M. & HYLAND, E. 1992. The geological setting and metal distribution patterns of Zn-Pb-Fe mineralization in the Navan Boulder Conglomerate. *The Irish minerals industry,* 1990**,** 171-210.

ASHTON, J. H., BLAKEMAN, R. J., GERAGHTY, J. F., BEACH, A., COLLER, D., PHILCOX, M. E., BOYCE, A. J. & WILKINSON, J. J. in press. The Giant Navan Carbonate-Hosted Zn-Pb Deposit – A Review. *Economic Geology*.

ASHTON, J. H., DOWNING, D. T. & FINLAY, S. 1986. The geology of the Navan Zn-Pb orebody. *Geology and genesis of mineral deposits in Ireland: Dublin, Irish Association for Economic Geology***,** 243-280.

ASHTON, J. H. & HARTE, G. 1989. *Technical Computerization at Tara Mines, Ltd., Navan, Ireland: Transactions of the Institution of Mining and Metallurgy, Section A, Mining Industry 98(May-August) 1989*.

ASHTON, J. H., HOLDSTOCK, M. P., GERAGHTY, J. F., O'KEEFE, W. G., MARTINEZ, N., PEACE, W. & PHILCOX, M. E. 2003. The Navan orebody–discovery and geology of the South West Extension. *Europe's major base metal deposits: Dublin, Irish Association for Economic Geology***,** 405-436.

BALLENTINE, C. J., BURGESS, R. & MARTY, B. 2002. Tracing fluid origin, transport and interaction in the crust. *Reviews in Mineralogy and Geochemistry,* 47**,** 539-614.

BANKS, D. A., BOYCE, A. J. & SAMSON, I. M. 2002. Constraints on the origins of fluids forming Irish Zn-Pb-Ba deposits: Evidence from the composition of fluid inclusions. *Economic Geology,* 97**,** 471-480.

BANKS, D. A. & RUSSELL, M. J. 1992. Fluid Mixing during Ore Deposition at the Tynagh Base-Metal Deposit, Ireland. *European Journal of Mineralogy,* 4**,** 921-931.
BARKER, C. & ROBINSON, S. 1984. Thermal release of water from natural quartz. *American Mineralogist,* 69**,** 1078-1081.
BARRIE, C. D., BOYCE, A. J., BOYLE, A. P., WILLIAMS, P. J., BLAKE, K., WILKINSON, J. J., LOWTHER, M., MCDERMOTT, P. & PRIOR, D. J. 2009. On the growth of colloform textures: a case study of sphalerite from the Galmoy ore body, Ireland. *Journal of the Geological Society,* 166**,** 563-582.
BETHKE, C. M. 1986. Inverse hydrologic analysis of the distribution and origin of Gulf Coast-type geopressured zones. *Journal of Geophysical Research: Solid Earth,* 91**,** 6535-6545.
BISCHOFF, J. L., RADTKE, A. S. & ROSENBAUER, R. J. 1981. Hydrothermal alteration of graywacke by brine and seawater; roles of alteration and chloride complexing on metal solubilization at 200 degrees and 350 degrees C. *Economic Geology,* 76**,** 659-676.
BLAKEMAN, R. J. 2002. *The compositions and routes of the fluids generating the Navan giant base-metal orebody.* Ph. D., University of Glasgow.
BLAKEMAN, R. J., ASHTON, J. H., BOYCE, A. J., FALLICK, A. E. & RUSSELL, M. J. 2002. Timing of interplay between hydrothermal and surface fluids in the Navan Zn plus Pb orebody, Ireland: Evidence from metal distribution trends, mineral textures, and delta S-34 analyses. *Economic Geology and the Bulletin of the Society of Economic Geologists,* 97**,** 73-91.
BOAST, A. M., COLEMAN, M. L. & HALLS, C. 1981. Textural and stable isotopic evidence for the genesis of the Tynagh base metal deposit, Ireland. *Economic Geology,* 76**,** 27-55.
BOYCE, A. J., ANDERTON, R. & RUSSELL, M. J. 1983a. Rapid subsidence and early Carboniferous base-metal mineralization in Ireland. *Institution of Mining and Metallurgy Transactions,* 92.
BOYCE, A. J., BARRIE, C., SAMSON, I. M. & WILLIAMS-JONES, A. E. in press. Aspects of the geochemistry of zinc – a journey to sphalerite. *Irish Association for Economic Geology,* Irish Association for Economic Geology, Zinc 2010: Decade volume 2000-2010**.,** 19-37.
BOYCE, A. J., COLEMAN, M. L. & RUSSELL, M. J. 1983b. Formation of fossil hydrothermal chimneys and mounds from Silvermines, Ireland. *Nature,* 306**,** 545-550.
BRAITHWAITE, C. J. R. & RIZZI, G. 1997. The geometry and petrogenesis of hydrothermal dolomites at Navan, Ireland. *Sedimentology,* 44**,** 421-440.
BURGESS, R., KELLEY, S. P., PARSONS, I., WALKER, F. D. L. & WORDEN, R. H. 1992. 40Ar39Ar analysis of perthite microtextures and fluid inclusions in alkali feldspars from the Klokken syenite, South Greenland. *Earth and Planetary Science Letters,* 109**,** 147-167.
BURNARD, P. G. & POLYA, D. A. 2004. Importance of mantle derived fluids during granite associated hydrothermal circulation: He and Ar isotopes of ore minerals from Panasqueira. *Geochimica et Cosmochimica Acta,* 68**,** 1607-1615.
CASSATA, W. S. & RENNE, P. R. 2013. Systematic variations of argon diffusion in feldspars and implications for thermochronometry. *Geochimica et Cosmochimica Acta,* 112**,** 251-287.
CAULFIELD, J. B. D., LEHURAY, A. P. & RYE, D. M. 1986. A review of lead and sulphur isotope investigations of Irish sediment-hosted base metal deposits with new data from the Keel, Ballinalack, Moyvoughly and Tatestown deposits. *Geology and genesis of mineral deposits in Ireland: Dublin, Irish Association for Economic Geology***,** 591-616.
CHAMBERS, L. A. & TRUDINGER, P. A. 1979. Microbiological fractionation of stable sulfur isotopes: A review and critique. *Geomicrobiology Journal,* 1**,** 249-293.
CHEN, Y., CLARK, A. H., FARRAR, E., WASTENEYS, H. A. H. P., HODGSON, M. J. & BROMLEY, A. V. 1993. Diachronous and independent histories of plutonism and mineralization in the Cornubian Batholith, southwest England. *Journal of the Geological Society,* 150**,** 1183-1191.
CHESLEY, J. T., HALLIDAY, A. N., SNEE, L. W., MEZGER, K., SHEPHERD, T. J. & SCRIVENER, R. C. 1993. Thermochronology of the Cornubian batholith in southwest England: Implications for pluton emplacement and protracted hydrothermal mineralization. *Geochimica et Cosmochimica Acta,* 57**,** 1817-1835.
COCHRANE, R., SPIKINGS, R. A., CHEW, D., WOTZLAW, J.-F., CHIARADIA, M., TYRRELL, S., SCHALTEGGER, U. & VAN DER LELIJ, R. 2014. High temperature (> 350 °C)

thermochronology and mechanisms of Pb loss in apatite. *Geochimica et Cosmochimica Acta,* 127**,** 39-56.
COLLER, D., BEACH, A., ASHTON, J., GERAGHTY, J., HOLDSTOCK, M., W, O. K., PHILCOX, P. & WALKER, N. Structural Geology and Tectonic Setting of the Navan Zn-Pb Orebody - Inversion of a Degraded Footwall-Uplift Fault Block. Presentation to Mineral Deposits Studies Group Annual Meeting, 2005 Belfast.
CONSTANTINOU, G. & GOVETT, G. J. S. 1973. Geology, geochemistry, and genesis of Cyprus sulfide deposits. *Economic Geology,* 68**,** 843-858.
COOKE, D. R., BULL, S. W., LARGE, R. R. & MCGOLDRICK, P. J. 2000. The Importance of Oxidized Brines for the Formation of Australian Proterozoic Stratiform Sediment-Hosted Pb-Zn (Sedex) Deposits. *Economic Geology,* 95**,** 1-18.
COOMER, P. G. & ROBINSON, B. W. 1976. Sulphur and sulphate-oxygen isotopes and the origin of the Silvermines deposits, Ireland. *Mineralium Deposita,* 11**,** 155-169.
CURTIS, C. D., COLEMAN, M. L. & LOVE, L. G. 1986. Pore water evolution during sediment burial from isotopic and mineral chemistry of calcite, dolomite and siderite concretions. *Geochimica et Cosmochimica Acta,* 50**,** 2321-2334.
DAVIDHEISER-KROLL, B., STUART, F. M. & BOYCE, A. J. 2014. Mantle heat drives hydrothermal fluids responsible for carbonate-hosted base metal deposits: evidence from 3He/4He of ore fluids in the Irish Pb-Zn ore district. *Mineralium Deposita,* 49**,** 547-553.
DIXON, P. R., LEHURAY, A. P. & RYE, D. M. 1990. Basement geology and tectonic evolution of Ireland as deduced from Pb isotopes. *Journal of the Geological Society,* 147**,** 121-132.
DONNELLY, T., WALDRON, S., TAIT, A., DOUGANS, J. & BEARHOP, S. 2001. Hydrogen isotope analysis of natural abundance and deuterium-enriched waters by reduction over chromium on-line to a dynamic dual inlet isotope-ratio mass spectrometer. *Rapid Communications in Mass Spectrometry,* 15**,** 1297-1303.
EDDY, C. A., DILEK, Y., HURST, S. & MOORES, E. M. 1998. Seamount formation and associated caldera complex and hydrothermal mineralization in ancient oceanic crust, Troodos ophiolite (Cyprus). *Tectonophysics,* 292**,** 189-210.
ELLIOT, H. A., GERNON, T. M., ROBERTS, S. & REDMOND, P. B. Diatreme volcanism facilitating Pb-Zn mineralization in the Irish Orefield? Volcanic and Magmatic Studies Group of the Geological Society, 2013.
EVERETT, C. E., RYE, D. M. & ELLAM, R. M. 2003. Source or Sink? An Assessment of the Role of the Old Red Sandstone in the Genesis of the Irish Zn-Pb Deposits. *Economic Geology,* 98**,** 31-50.
EVERETT, C. E. & WILKINSON, J. J. 2001. Fluid Evolution at the Navan Deposit: Preliminary fluid inclusion results.
EVERETT, C. E., WILKINSON, J. J., BOYCE, A. J. & GLEESON, S. A. The role of bittern brines and fluid mixing in the genesis of the Navan Zn-Pb deposit, Ireland. GSA Annual Meeting, November 5-8, 2001, 2001.
EVERETT, C. E., WILKINSON, J. J. & RYE, D. M. 1999. Fracture-controlled fluid flow in the Lower Palaeozoic basement rocks of Ireland: implications for the genesis of Irish-type Zn-Pb deposits. *Geological Society, London, Special Publications,* 155**,** 247-276.
FALLICK, A. E., ASHTON, J. H., BOYCE, A. J., ELLAM, R. M. & RUSSELL, M. J. 2001. Bacteria were responsible for the magnitude of the world-class hydrothermal base metal sulfide orebody at Navan, Ireland. *Economic Geology,* 96**,** 885-890.
FALLICK, A. E., MCCONVILLE, P., BOYCE, A. J., BURGESS, R. & KELLEY, S. P. 1992. Laser microprobe stable isotope measurements on geological materials: Some experimental considerations (with special reference to δ34S in sulphides). *Chemical Geology: Isotope Geoscience section,* 101**,** 53-61.
FOLAND, K. A. 1994. Argon Diffusion in Feldspars. *In:* PARSONS, I. (ed.) *Feldspars and their Reactions.* Springer Netherlands.
FORD, C. V. 1996. *The integration of petrologic and isotopic data from the Boulder Conglomerate to determine the age of the Navan orebody, Ireland.* Ph. D., University of Glasgow.
FRANCHETEAU, J., NEEDHAM, H. D., CHOUKROUNE, P., JUTEAU, T., SEGURET, M., BALLARD, R. D., FOX, P. J., NORMARK, W., CARRANZA, A., CORDOBA, D., GUERRERO, J., RANGIN, C.,

BOUGAULT, H., CAMBON, P. & HEKINIAN, R. 1979. Massive deep-sea sulphide ore deposits discovered on the East Pacific Rise. *Nature,* 277**,** 523-528.
FYFE, W. S., PRICE, N. J. & THOMPSON, A. B. 1978. *Fluids in the Earth's Crust*, Elsevier Amsterdam.
GAGNEVIN, D., BOYCE, A., BARRIE, C., MENUGE, J. & BLAKEMAN, R. 2012. Zn, Fe and S isotope fractionation in a large hydrothermal system. *Geochimica et Cosmochimica Acta,* 88**,** 183-198.
GAGNEVIN, D., MENUGE, J. F., KRONZ, A., BARRIE, C. & BOYCE, A. J. 2014. Minor Elements in Layered Sphalerite as a Record of Fluid Origin, Mixing, and Crystallization in the Navan Zn-Pb Ore Deposit, Ireland. *Economic Geology,* 109**,** 1513-1528.
GARVEN, G., APPOLD, M. S., TOPTYGINA, V. I. & HAZLETT, T. J. 1999. Hydrogeologic modeling of the genesis of carbonate-hosted lead-zinc ores. *Hydrogeology Journal,* 7**,** 108-126.
GIAMBALVO, E. R., FISHER, A. T., MARTIN, J. T., DARTY, L. & LOWELL, R. P. 2000. Origin of elevated sediment permeability in a hydrothermal seepage zone, eastern flank of the Juan de Fuca Ridge, and implications for transport of fluid and heat. *Journal of Geophysical Research: Solid Earth (1978–2012),* 105**,** 913-928.
GILLESPIE, A. 2013. *A petrological and geochemical characterisation of lithologies and hydrothermal alteration in the basement to the Navan Ore Deposit, Ireland.* M. Sci, University of Southampton.
GIZE, A. P. & BARNES, H. L. 1987. The organic geochemistry of two mississippi valley-type lead-zinc deposits. *Economic Geology,* 82**,** 457-470.
GLEESON, S. A., ROBERTS, S., FALLICK, A. E. & BOYCE, A. J. 2008. Micro-Fourier Transform Infrared (FT-IR) and δD value investigation of hydrothermal vein quartz: Interpretation of fluid inclusion δD values in hydrothermal systems. *Geochimica et Cosmochimica Acta,* 72**,** 4595-4606.
GOLDHABER, M. B., CHURCH, S. E., DOE, B. R., ALEINIKOFF, J. N., BRANNON, J. C., PODOSEK, F. A., MOSIER, E. L., TAYLOR, C. D. & GENT, C. A. 1995. Lead and sulfur isotope investigation of Paleozoic sedimentary rocks from the southern Midcontinent of the United States; implications for paleohydrology and ore genesis of the Southeast Missouri lead belts. *Economic Geology,* 90**,** 1875-1910.
GOODFELLOW, W. D. 2004. Geology, genesis and exploration of SEDEX deposits, with emphasis on the Selwyn Basin, Canada. *Attributes and models of some major deposits in India, Australia and Canada: New Delhi, Narosa Publishing House***,** 24-99.
GOODFELLOW, W. D., CECILE, M. P. & LEYBOURNE, M. I. 1995. Geochemistry, petrogenesis, and tectonic setting of lower Paleozoic alkalic and potassic volcanic rocks, Northern Canadian Cordilleran Miogeocline. *Canadian Journal of Earth Sciences,* 32**,** 1236-1254.
GOSSE, J. C. & PHILLIPS, F. M. 2001. Terrestrial in situ cosmogenic nuclides: theory and application. *Quaternary Science Reviews,* 20**,** 1475-1560.
GRADSTEIN, F. M., OGG, G. & SCHMITZ, M. 2012. *The Geologic Time Scale 2012 2-Volume Set*, Elsevier.
HELGESON, H. C. 1965. in "Report on S.E.G. symosium on the chemistry of the ore froming fluids," by Edwin Roedder. *Economic Geology,* 60**,** 1380-1403.
HITZMAN, M. W. 1999. Extensional faults that localize Irish syndiagenetic Zn-Pb deposits and their reactivation during Variscan compression. *Geological Society, London, Special Publications,* 155**,** 233-245.
HITZMAN, M. W. & BEATY, D. W. 1996. The Irish Zn-Pb-(Ba) orefield. *Carbonate-hosted lead-zinc deposits: Society of Economic Geologists Special Publication,* 4**,** 112-143.
HUHTELIN, T. 1994. Mineralogical and chemical study on Tara U Lens samples. *Mining as a process.* Tara internal report.
INDEN, R. F. & MOORE, C. H. 1983. *Beach Environment: Chapter 5: PART 1*, AAPG Memoir.
JOHNSTON, J. D. 1999. Regional fluid flow and the genesis of Irish Carboniferous base metal deposits. *Mineralium Deposita,* 34**,** 571-598.
JOHNSTON, J. D., COLLER, D., MILLAR, G. & CRITCHLEY, M. F. 1996. Basement structural controls on Carboniferous-hosted base metal mineral deposits in Ireland. *Geological Society, London, Special Publications,* 107**,** 1-21.
JOHNSTON, J. D., RAUB, T. D. & ASHTON, J. H. Mineral magnetism identifies the presence of pyrrhotite in the Navan Zn-Pb deposit, Ireland: implications for low temperature pyrite to

pyrrhotite reduction, timing of mineralization and future exploration strategies. *In:* JONSSON, E., ed. Mineral Deposit Research for a Hi-Tech World, 2013 Uppsala. 323-325.
JONES, G. L. I. 1992. Irish Carboniferous conodonts record maturation levels and the influence of tectonism, igneous activity and mineralization. *Terra Nova,* 4**,** 238-244.
JØRGENSEN, B. B., ZAWACKI, L. X. & JANNASCH, H. W. 1990. Thermophilic bacterial sulfate reduction in deep-sea sediments at the Guaymas Basin hydrothermal vent site (Gulf of California). *Deep Sea Research Part A. Oceanographic Research Papers,* 37**,** 695-710.
KENDRICK, M. A., BURGESS, R., LEACH, D. & PATTRICK, R. A. D. 2002. Hydrothermal fluid origins in Mississippi valley-type ore districts: combined noble gas (He, Ar, Kr) and halogen (Cl, Br, I) analysis of fluid inclusions from the Illinois-Kentucky fluorspar district, Viburnum Trend, and Tri-State districts, midcontinent United States. *Economic Geology,* 97**,** 453-469.
KENNEDY, B. M., KHARAKA, Y. K., EVANS, W. C., ELLWOOD, A., DEPAOLO, D. J., THORDSEN, J., AMBATS, G. & MARINER, R. H. 1997. Mantle fluids in the San Andreas fault system, California. *Science,* 278**,** 1278-1281.
KNIGHT, H. 2012. *Seeking The Deep Fluid Feeder Zone of the Navan Zn-Pb Deposit, Republic of Ireland.* MSci, Imperial College London.
LARGE, D. & WALCHER, E. 1999. The Rammelsberg massive sulphide Cu-Zn-Pb-Ba-Deposit, Germany: an example of sediment-hosted, massive sulphide mineralisation. *Mineralium Deposita,* 34**,** 522-538.
LARGE, D. E. 1980. Geological parameters associated with sediment-hosted, submarine exhalative Pb-Zn deposits: an empirical model for mineral exploration. *Geol. Jb. D,* 40**,** 59-129.
LARGE, R. R. 1992. Australian volcanic-hosted massive sulfide deposits; features, styles, and genetic models. *Economic Geology,* 87**,** 471-510.
LEACH, D., SANGSTER, D., KELLEY, K., LARGE, R. R., GARVEN, G., ALLEN, C., GUTZMER, J. & WALTERS, S. 2005. Sediment-hosted lead-zinc deposits: A global perspective. *Economic Geology,* 100**,** 561-607.
LEACH, D. L., BRADLEY, D., LEWCHUK, M. T., SYMONS, D. T., DE MARSILY, G. & BRANNON, J. 2001. Mississippi Valley-type lead–zinc deposits through geological time: implications from recent age-dating research. *Mineralium Deposita,* 36**,** 711-740.
LEACH, D. L., BRADLEY, D. C., HUSTON, D., PISAREVSKY, S. A., TAYLOR, R. D. & GARDOLL, S. J. 2010. Sediment-hosted lead-zinc deposits in Earth history. *Economic Geology,* 105**,** 593-625.
LEE, J.-Y., MARTI, K., SEVERINGHAUS, J. P., KAWAMURA, K., YOO, H.-S., LEE, J. B. & KIM, J. S. 2006. A redetermination of the isotopic abundances of atmospheric Ar. *Geochimica et Cosmochimica Acta,* 70**,** 4507-4512.
LEE, J. W. 1995. Multipath diffusion in geochronology. *Contributions to Mineralogy and Petrology,* 120**,** 60-82.
LEE, M. R. & PARSONS, I. 2003. Microtextures of authigenic Or‐rich feldspar in the Upper Jurassic Humber Group, UK North Sea. *Sedimentology,* 50**,** 597-608.
LEHURAY, A. P., CAULFIELD, J. B. D., RYE, D. M. & DIXON, P. R. 1987. Basement controls on sediment-hosted Zn-Pb deposits; a Pb isotope study of Carboniferous mineralization in central Ireland. *Economic Geology,* 82**,** 1695-1709.
MALLON, A. J. 1997. *Petrological and mineralogical characteristics of the Old Red Sandstone facies rocks beneath base metal deposits as a guide to the setting of mineralisation in the Irish Midlands.* Ph. D., University College Cork.
MARK, D. F., KELLEY, S. P., LEE, M. R., PARNELL, J., SHERLOCK, S. C. & BROWN, D. J. 2008. Ar–Ar dating of authigenic K-feldspar: Quantitative modelling of radiogenic argon-loss through subgrain boundary networks. *Geochimica et Cosmochimica Acta,* 72**,** 2695-2710.
MARK, D. F., PARNELL, J., KELLEY, S. P. & SHERLOCK, S. C. 2007. Resolution of regional fluid flow related to successive orogenic events on the Laurentian margin. *Geology,* 35**,** 547-550.
MARK, D. F., PETRAGLIA, M., SMITH, V. C., MORGAN, L. E., BARFOD, D. N., ELLIS, B. S., PEARCE, N. J., PAL, J. N. & KORISETTAR, R. 2014. A high-precision 40Ar/39Ar age for the Young Toba Tuff and dating of ultra-distal tephra: Forcing of Quaternary climate and implications for hominin occupation of India. *Quaternary Geochronology,* 21**,** 90-103.
MARK, D. F., STUART, F. M. & DE PODESTA, M. 2011. New high-precision measurements of the isotopic composition of atmospheric argon. *Geochimica et Cosmochimica Acta,* 75**,** 7494-7501.

MARTY, B., O'NIONS, R. K., OXBURGH, E. R., MARTEL, D. & LOMBARDI, S. 1992. Helium isotopes in Alpine regions. *Tectonophysics,* 206**,** 71-78.
MATSUHISA, Y., GOLDSMITH, J. R. & CLAYTON, R. N. 1979. Oxygen isotopic fractionation in the system quartz-albite-anorthite-water. *Geochimica et Cosmochimica Acta,* 43**,** 1131-1140.
MCCANN, T., PASCAL, C., TIMMERMAN, M. J., KRZYWIEC, P., LÓPEZ-GÓMEZ, J., WETZEL, L., KRAWCZYK, C. M., RIEKE, H. & LAMARCHE, J. 2006. Post-Variscan (end Carboniferous-Early Permian) basin evolution in Western and Central Europe. *Geological Society, London, Memoirs,* 32**,** 355-388.
MCCUSKER, J. & REED, C. 2013. The role of intrusions in the formation of Irish-type mineralisation. *Mineralium Deposita***,** 1-9.
MCDOUGALL, I. & HARRISON, T. M. 1999. *Geochronology and Thermochronology by the 40Ar/39Ar Method,* New York Oxford, Oxford University Press.
MERRIHUE, C. & TURNER, G. 1966. Potassium‐argon dating by activation with fast neutrons. *Journal of Geophysical Research,* 71**,** 2852-2857.
MILES, A., GRAHAM, C., HAWKESWORTH, C., GILLESPIE, M., DHUIME, B. & HINTON, R. 2013. Using Zircon Isotope Compositions to Constrain Crustal Structure and Pluton Evolution: the Iapetus Suture Zone Granites in Northern Britain. *Journal of Petrology***,** 181-207.
MILLS, H., HALLIDAY, A. N., ASHTON, J. H., ANDERSON, I. K. & RUSSELL, M. J. 1987. Origin of a giant orebody at Navan, Ireland. *Nature,* 327**,** 223-226.
MONTY, C., BOSENCE, D., BRIDGES, P. & PRATT, B. 1995. Carbonate Mud Mounds: Their Origin and Evolution. International Association of Sedimentologists. Special Publication, 23. *Monty537Carbonate mud-mounds: Their origin and evolution1995*.
MORELLI, R. M., CREASER, R. A., SELBY, D., KELLEY, K. D., LEACH, D. L. & KING, A. R. 2004. Re-Os Sulfide Geochronology of the Red Dog Sediment-Hosted Zn-Pb-Ag Deposit, Brooks Range, Alaska. *Economic Geology,* 99**,** 1569-1576.
MOZLEY, P. S. & WERSIN, P. 1992. Isotopic composition of siderite as an indicator of depositional environment. *Geology,* 20**,** 817-820.
MURPHY, F. C., ANDERSON, T. B., DALY, J. S., GALLAGHER, V., GRAHAM, J. R., HARPER, D. A. T., JOHNSTON, J. D., KENNAN, P. S., KENNEDY, M. J. & LONG, C. B. 1991. An appraisal of Caledonian suspect terranes in Ireland. *Irish Journal of Earth Sciences***,** 11-41.
NAKAI, S. I. & HALLIDAY, A. N. 1990. Rb-Sr dating of sphalerites from Tennessee and the genesis of Mississippi Valley type. *Nature,* 346**,** 354-357.
NOLAN, S. C. 1989. The style and timing of Dinantian syn-sedimentary tectonics in the eastern part of the Dublin Basin, Ireland. *The role of tectonics in Devonian and Carboniferous sedimentation in the British Isles,* 6**,** 83-97.
O'NEIL, J. R. & TAYLOR, H. P. 1967. The oxygen isotope and cation exchange chemistry of feldspars. *American Mineralogist,* 52**,** 1414-1437.
O'KEEFFE, W. G. 1986. Age and postulated source rocks for mineralization in central Ireland, as indicated by lead isotopes. *Geology and genesis of mineral deposits in Ireland: Dublin, Irish Association for Economic Geology***,** 617-624.
OHLE, E. L. 1959. Some considerations in determining the origin of ore deposits of the Mississippi Valley type. *Economic Geology,* 54**,** 769-789.
OXBURGH, E. R., O'NIONS, R. K. & HILL, R. I. 1986. Helium isotopes in sedimentary basins. *Nature,* 324**,** 632-635.
OZIMA, M. & PODOSEK, F. A. 2002. *Noble gas geochemistry*, Cambridge University Press.
PANNALAL, S., SYMONS, D. & SANGSTER, D. 2008a. Paleomagnetic Evidence for an Early Permian Age of the Lisheen Zn-Pb Deposit, Ireland. *Economic Geology,* 103**,** 1641-1655.
PANNALAL, S. J., SYMONS, D. T. A. & SANGSTER, D. F. 2008b. Palaeomagnetic evidence of a Variscan age for the epigenetic Galmoy zinc–lead deposit, Ireland. *Terra Nova,* 20**,** 385-393.
PARSONS, I. 1978. Feldspars and fluids in cooling plutons. *Mineral Mag,* 42**,** 1-17.
PARSONS, I., BROWN, W. L. & SMITH, J. V. 1999. 40Ar/39Ar thermochronology using alkali feldspars: real thermal history or mathematical mirage of microtexture? *Contributions to Mineralogy and Petrology,* 136**,** 92-110.
PARSONS, I. & LEE, M. R. 2005. Minerals are not just chemical compounds. *The Canadian Mineralogist,* 43**,** 1959-1992.

PEACE, W. 1999. *Carbonate-hosted Zn-Pb mineralisation within the Upper Pale Beds at Navan, Ireland.* Ph. D., The University of Melbourne.
PEACE, W. M. & WALLACE, M. W. 2000. Timing of mineralization at the Navan Zn-Pb deposit: A post-Arundian age for Irish mineralization. *Geology,* 28**,** 711-714.
PEACE, W. M., WALLACE, M. W., HOLDSTOCK, M. P. & ASHTON, J. H. 2003. Ore textures within the U lens of the Navan Zn-Pb deposit, Ireland. *Mineralium Deposita,* 38**,** 568-584.
PHILCOX, M. E. 1984. *Lower Carboniferous Lithostratigraphy of the Irish Midlands: Based on a Symposium Held at the Athlone Regional Technical College on 11th June 1983*, Irish Association for Economic Geology.
PHILCOX, M. E. 1989. The mid-Dinantian unconformity at Navan, Ireland. *The role of tectonics in Devonian and Carboniferous sedimentation in the British Isles. Yorkshire Geological Society, Bradford***,** 67-81.
PHILCOX, M. E. 2013. *RE: Personal Communication.*
PHILLIPS, W. A., STILLMAN, C. J. & MURPHY, T. 1976. A Caledonian plate tectonic model. *Journal of the Geological Society,* 132**,** 579-605.
PIRAJNO, F. 2008. *Hydrothermal processes and mineral systems*, Springer.
RAISWELL, R. 1987. Non-steady state microbiological diagenesis and the origin of concretions and nodular limestones. *Geological Society, London, Special Publications,* 36**,** 41-54.
RAISWELL, R. & FISHER, Q. J. 2000. Mudrock‐hosted carbonate concretions: a review of growth mechanisms and their influence on chemical and isotopic composition. *Journal of the Geological Society,* 157**,** 239-251.
RAVENHURST, C. E., WILLETT, S. D., DONELICK, R. A. & BEAUMONT, C. 1994. Apatite fission track thermochronometry from central Alberta: implications for the thermal history of the Western Canada Sedimentary Basin. *Journal of Geophysical Research: Solid Earth (1978–2012),* 99**,** 20023-20041.
REED, M. H. & PALANDRI, J. 2006. Sulfide mineral precipitation from hydrothermal fluids. *Reviews in mineralogy and geochemistry,* 61**,** 609-631.
REES, C. E., JENKINS, W. J. & MONSTER, J. 1978. The sulphur isotopic composition of ocean water sulphate. *Geochimica et Cosmochimica Acta,* 42**,** 377-381.
RENNE, P. R., BALCO, G., LUDWIG, K. R., MUNDIL, R. & MIN, K. 2011. Response to the comment by WH Schwarz et al. on "Joint determination of 40K decay constants and 40Ar∗/40K for the Fish Canyon sanidine standard, and improved accuracy for 40Ar/39Ar geochronology" by PR Renne et al.(2010). *Geochimica et Cosmochimica Acta,* 75**,** 5097.
RENNE, P. R., SHARP, W. D., DEINO, A. L., ORSI, G. & CIVETTA, L. 1997. 40Ar/39Ar Dating into the Historical Realm: Calibration Against Pliny the Younger. *Science,* 277**,** 1279-1280.
RICKARD, D. T., WILLDEN, M., MARDE, Y. & RYHAGE, R. 1975. Hydrocarbons associated with lead-zinc ores at Laisvall, Sweden. *Nature,* 255**,** 131-133.
RIZZI, G. & BRAITHWAITE, C. J. R. 1997. Sedimentary cycles and selective dolomitization in limestones hosting the giant Navan zinc-lead ore deposit, Ireland. *Exploration and Mining Geology,* 6**,** 63-77.
ROBB, L. 2009. *Introduction to ore-forming processes*, John Wiley & Sons.
ROBERTS, S., BACH, W., BINNS, R. A., VANKO, D. A., YEATS, C. J., TEAGLE, D. A. H., BLACKLOCK, K., BLUSZTAJN, J. S., BOYCE, A. J. & COOPER, M. J. 2003. Contrasting evolution of hydrothermal fluids in the PACMANUS system, Manus Basin: the Sr and S isotope evidence. *Geology,* 31**,** 805-808.
ROBINSON, B. W. & KUSAKABE, M. 1975. Quantitative preparation of sulfur dioxide, for sulfur-34/sulfur-32 analyses, from sulfides by combustion with cuprous oxide. *Analytical Chemistry,* 47**,** 1179-1181.
ROCK, N. M. S., GASKARTH, J. W. & RUNDLE, C. C. 1986. Late Caledonian Dyke-Swarms in Southern Scotland: A Regional Zone of Primitive K-Rich Lamprophyres and Associated Vents. *The Journal of Geology,* 94**,** 505-522.
ROMANO, M. 1980. The Stratigraphy of the Ordovician Rocks between Slane (County Meath) and Collon (County Louth), Eastern Ireland. *Journal of Earth Sciences,* 3**,** 53-79.
RUSSELL, M., SOLOMON, M. & WALSHE, J. 1981. The genesis of sediment-hosted, exhalative zinc+ lead deposits. *Mineralium Deposita,* 16**,** 113-127.

RUSSELL, M. J. 1978. Downward-excavating hydrothermal cells and Irish-type ore deposits: importance of an underlying thick Caledonian prism. *Transactions of the Institution of Mining and Metallurgy,* 87**,** B168-171.
SAMSON, I. M. & RUSSELL, M. J. 1987. Genesis of the Silvermines zinc-lead-barite deposit, Ireland; fluid inclusion and stable isotope evidence. *Economic Geology,* 82**,** 371-394.
SANGSTER, D. F. Mississippi Valley-type deposits: a geological melange. International Conference on Mississippi Valley-Type Lead-Zinc Deposits, Proceedings Volume: Rolla, Missouri, EUA, University of Missouri-Rolla, 1983. 7-19.
SANGSTER, D. F. 2002. The role of dense brines in the formation of vent-distal sedimentary-exhalative (SEDEX) lead–zinc deposits: field and laboratory evidence. *Mineralium Deposita,* 37**,** 149-157.
SANGSTER, D. F. & HILLARY, E. M. 1998. Sedex lead-zinc deposits; proposed sub-types and their characteristics. *Exploration and Mining Geology,* 7**,** 341-357.
SCOTT, S. D. 1997. Submarine hydrothermal systems and deposits. *In:* BARNES, H. L. (ed.) *Geochemistry of hydrothermal ore deposits.* 3rd ed.: John Wiley.
SHARP, Z. D. 1990. A laser-based microanalytical method for the in situ determination of oxygen isotope ratios of silicates and oxides. *Geochimica et Cosmochimica Acta,* 54**,** 1353-1357.
SHEARLEY, E., REDMOND, P. B., GOODMAN, R. & KING, M. 1995. *Guide to the Lisheen Zn-Pb-Ag deposit,* Littleton, Society of Economic Geology.
SHEPPARD, S. M. F. 1986. Characterization and isotopic variations in natural waters. *Reviews in Mineralogy and Geochemistry,* 16**,** 165-183.
SIBSON, R. H. 1996. Structural permeability of fluid-driven fault-fracture meshes. *Journal of Structural Geology,* 18**,** 1031-1042.
SIM, M. S., BOSAK, T. & ONO, S. 2011. Large sulfur isotope fractionation does not require disproportionation. *Science,* 333**,** 74-77.
SINGER, D. A. 1995. World class base and precious metal deposits; a quantitative analysis. *Economic Geology,* 90**,** 88-104.
SKINNER, B. J., WHITE, D. E., ROSE, H. J. & MAYS, R. E. 1967. Sulfides associated with the Salton Sea geothermal brine. *Economic Geology,* 62**,** 316-330.
STEED, G. M. 1980. Silver in the Tara Mines Mineral Deposit at Navan - with particular emphasis on the ores to the west of the main shaft pillar. Tara Internal Report.
STRACHAN, R. A. 2012. Mid-Ordovician to Silurian subduction and collision: Closure of the Iapetus Ocean. *Geological History of Britain and Ireland***,** 110.
STROGEN, P. 1988. The Carboniferous lithostratigraphy of southeast County Limerick, Ireland, and the origin of the Shannon Trough. *Geological Journal,* 23**,** 121-137.
STROGEN, P., JONES, G. L. & SOMERVILLE, I. D. 1990. Stratigraphy and sedimentology of lower carboniferous (Dinantian) boreholes from West Co. Meath, Ireland. *Geological Journal,* 25**,** 103-137.
STUART, F. M., BURNARD, P. G., TAYLOR, R. P. & TURNER, G. 1995. Resolving mantle and crustal contributions to ancient hydrothermal fluids: He・Ar isotopes in fluid inclusions from Dae Hwa W・Mo mineralisation, South Korea. *Geochimica et Cosmochimica Acta,* 59**,** 4663-4673.
STUART, F. M., LASS-EVANS, S., FITTON, J. G. & ELLAM, R. M. 2003. High 3He/4He ratios in picritic basalts from Baffin Island and the role of a mixed reservoir in mantle plumes. *Nature,* 424**,** 57-59.
STUART, F. M., TURNER, G., DUCKWORTH, R. C. & FALLICK, A. E. 1994. Helium isotopes as tracers of trapped hydrothermal fluids in ocean-floor sulfides. *Geology,* 22**,** 823-826.
STYRT, M. M., BRACKMANN, A. J., HOLLAND, H. D., CLARK, B. C., PISUTHA-ARNOND, V., ELDRIDGE, C. S. & OHMOTO, H. 1981. The mineralogy and the isotopic composition of sulfur in hydrothermal sulfide/sulfate deposits on the East Pacific Rise, 21°N latitude. *Earth and Planetary Science Letters,* 53**,** 382-390.
SUSAK, N. J. & CRERAR, D. A. 1982. Factors controlling mineral zoning in hydrothermal ore deposits. *Economic Geology,* 77**,** 476-482.
SYMONS, D. T. A., PANNALAL, S. J., KAWASAKI, K., SANGSTER, D. F. & STANLEY, G. A. 2007. *Paleomagnetic age of the Magcobar Ba deposit, Silvermines, Ireland,* Dublin, Irish Association for Economic Geology.

SYMONS, D. T. A., SANGSTER, D. F. & LEACH, D. L. 1996. Paleomagnetic dating of Mississippi Valley-type Pb-Zn-Ba deposits. *Carbonate-Hosted Lead Deposits: Society of Economic Geologists Special Publication,* 4**,** 515-526.

SYMONS, D. T. A., SMETHURST, M. T. & ASHTON, J. H. 2002. Paleomagnetism of the Navan Zn-Pb deposit, Ireland. *Economic Geology,* 97**,** 997-1012.

TAYLOR, S. 1984. Structural and paleotopographic controls of lead-zinc mineralization in the Silvermines orebodies, Republic of Ireland. *Enonomic Geology,* 79**,** 529-548.

TORNOS, F., SOLOMON, M., CONDE, C. & SPIRO, B. F. 2008. Formation of the Tharsis massive sulfide deposit, Iberian Pyrite Belt: geological, lithogeochemical, and stable isotope evidence for deposition in a brine pool. *Economic Geology,* 103**,** 185-214.

TRELOAR, M. 2014. *The South West Extension - South (SWEXS) Mineralisation of the Giant Navan Zn-Pb Deposit; Genesis and Relation to the Main Orebody.* Msci, Imperial College London.

VANLANINGHAM, S. & MARK, D. F. 2011. Step heating of 40Ar/39Ar standard mineral mixtures: Investigation of a fine-grained bulk sediment provenance tool. *Geochimica et Cosmochimica Acta,* 75**,** 2324-2335.

VAUGHAN, A. P. M. 1996. A tectonomagmatic model for the genesis and emplacement of Caledonian calc-alkaline lamprophyres. *Journal of the Geological Society,* 153**,** 613-623.

VAUGHAN, A. P. M. & JOHNSTON, J. D. 1992. Structural constraints on closure geometry across the Iapetus suture in eastern Ireland. *Journal of the Geological Society,* 149**,** 65-74.

VELASCO, F., SÁNCHEZ-ESPAÑA, J., BOYCE, A. J., FALLICK, A. E., SÁEZ, R. & ALMODÓVAR, G. R. 1998. A new sulphur isotopic study of some Iberian Pyrite Belt deposits: evidence of a textural control on sulphur isotope composition. *Mineralium Deposita,* 34**,** 4-18.

WAGNER, T., BOYCE, A. J. & FALLICK, A. E. 2002. Laser combustion analysis of δ34S of sulfosalt minerals: determination of the fractionation systematics and some crystal-chemical considerations. *Geochimica et Cosmochimica Acta,* 66**,** 2855-2863.

WALKER, B. 2004. The Nature and Origin of the Carboniferous 'Boudin Shale' at Navan, County Meath. Ireland: Trinity College Dublin.

WALKER, F. D. L., LEE, M. R. & PARSONS, I. 1995. Micropores and micropermeable texture in alkali feldspars: geochemical and geophysical implications. *Mineralogical Magazine,* 59**,** 505-534.

WALSHAW, R. D., MENUGE, J. F. & TYRRELL, S. 2006. Metal sources of the Navan carbonate-hosted base metal deposit, Ireland: Nd and Sr isotope evidence for deep hydrothermal convection. *Mineralium Deposita,* 41**,** 803-819.

WARR, L. N. 2012. The Variscan Orogeny: the Welding of Pangaea. *Geological History of Britain and Ireland.* John Wiley & Sons, Ltd.

WEBBER, A. P., ROBERTS, S., BURGESS, R. & BOYCE, A. J. 2011. Fluid mixing and thermal regimes beneath the PACMANUS hydrothermal field, Papua New Guinea: Helium and oxygen isotope data. *Earth and Planetary Science Letters,* 304**,** 93-102.

WEBER, A. & JØRGENSEN, B. B. 2002. Bacterial sulfate reduction in hydrothermal sediments of the Guaymas Basin, Gulf of California, Mexico. *Deep Sea Research Part I: Oceanographic Research Papers,* 49**,** 827-841.

WHEELER, J. 1996. Diffarg: A program for simulating argon diffusion profiles in minerals. *Computers & Geosciences,* 22**,** 919-929.

WILKINSON, J. J. 2010. A review of fluid inclusion constraints on mineralization in the Irish ore field and implications for the genesis of sediment-hosted Zn-Pb deposits. *Economic Geology,* 105**,** 417-442.

WILKINSON, J. J., BOYCE, A. J., EVERETT, C. E. & LEE, M. J. 2003. Timing and depth of mineralization in the Irish Zn-Pb orefield.

WILKINSON, J. J., CROWTHER, H. L. & COLES, B. J. 2011. Chemical mass transfer during hydrothermal alteration of carbonates: Controls of seafloor subsidence, sedimentation and Zn-Pb mineralization in the Irish Carboniferous. *Chemical Geology,* 289**,** 55-75.

WILKINSON, J. J., EVERETT, C. E., BOYCE, A. J., GLEESON, S. A. & RYE, D. M. 2005a. Intracratonic crustal seawater circulation and the genesis of subseafloor zinc-lead mineralization in the Irish orefield. *Geology,* 33**,** 805-808.

WILKINSON, J. J., EYRE, S. L. & BOYCE, A. J. 2005b. Ore-forming processes in Irish-type carbonate-hosted Zn-Pb deposits: Evidence from mineralogy, chemistry, and isotopic composition of sulfides at the Lisheen mine. *Economic Geology,* 100**,** 63-86.

WILKINSON, J. J. & HITZMAN, M. W. in press. The Irish Zn-Pb Orefield: The View from 2010. *Economic Geology*.

WILKINSON, J. J., STOFFELL, B., WILKINSON, C. C., JEFFRIES, T. E. & APPOLD, M. S. 2009. Anomalously metal-rich fluids form hydrothermal ore deposits. *Science,* 323**,** 764-767.

WOODCOCK, N. H. 2012a. Early Devonian sedimentary and magmatic interlude after Iapetus closure. *Geological History of Britain and Ireland.* John Wiley & Sons, Ltd.

WOODCOCK, N. H. 2012b. Late Ordovician to Silurian Evolution of Eastern Avalonia during Iapetus Closure. *Geological History of Britain and Ireland.* John Wiley & Sons, Ltd.

WORDEN, R. H., WALKER, F. D. L., PARSONS, I. & BROWN, W. L. 1990. Development of microporosity, diffusion channels and deuteric coarsening in perthitic alkali feldspars. *Contributions to Mineralogy and Petrology,* 104**,** 507-515.

ZHENG, Y.-F. 1993. Calculation of oxygen isotope fractionation in anhydrous silicate minerals. *Geochimica et Cosmochimica Acta,* 57**,** 1079-1079.